Investigation of Magnetic States in Molecular Systems in Cryogenic Environments



Simen Olav Njaa Sopp

Wadham College

University of Oxford

A thesis submitted for the degree of

Doctor of Philosophy

Trinity Term 2021

This thesis is dedicated to

my parents, Nils & Kjersti,
for their endless encouragement, support, and love,

my siblings, Nora & Axel,
for their support, enthusiasm and inspiration,

my grandparents, Margareth & Olav, Heidi & Tore,
for their unconditional love and for being my role models.

Acknowledgements

My time as a DPhil candidate at Oxford University has been a beautiful roller-coaster ride thanks to exciting challenges and a vibrant community, but most of all thanks to the inspiring people I have been surrounded by.

Initially, I want to thank the funding bodies that have made my journey possible: The Norwegian State Educational Loan Fund (Lånekassen), the European Research Council, Wadham College and the University of Oslo for awarding funding for my DPhil.

I thank St Cross College for providing a welcoming and friendly environment during my first two years at the University. A particular thanks goes to Wolfson (and St Cross) College Rowing Club for countless of beautiful mornings on the Isis River and the many resulting bumps that we won. The rowing community has been an integral contributor to my wellbeing and enjoyment during my time at the University. In particular, I want to thank Simon, Allison, Giuseppe, Hans-Joachim and the rest of the Wolfson Men's First crew.

I also want to thank my friends from the College and wider community, in particular my house mates over the years Tom, Alex, Toby, Daniel and Michael, who put up with my excessive use of cream in my cooking.

Thank you to Wadham College to which I transferred at the beginning of my third academic year, for honouring me with a Keeley Senior Scholarship and for providing a supportive and vibrant community.

A special thanks goes to my College Advisors Prof Laura Hoyano and Prof Paolo Radaelli for their unconditional and persistent support through challenging times. I am immensely and eternally grateful for all their efforts.

I thank everyone who has contributed to and helped me through my DPhil. In particular, Dr Dimitrios Alexandropoulos, Dr Jennifer Le Roy and Dr Wenjing Yan for sample preparation; Dr Tian Pei and Alessandro Lodi for device fabrication, transport measurements and inspiring physics discussions; Dr Michael Slota for helping me understand magnetic anisotropy; Ming-Yee Tsang for calculations and assistance with programming; Dr Mauro Perfetti for enlightening conversations on cantilever torque magnetometry; Dr Edward Laird for helpful discussions on experiments, experimental setup and interpretation of transport data; Paul Pattinson, Robert Storey and Tony Hickman at the Department of Physics for excellent service and for supporting me in instrumentation development; and many more.

I also want to thank our collaborators: the groups of Prof Akimitsu Narita, Prof Klaus Müllen at MPI for Polymer Science in Mainz, Prof Xinliang Feng Technical University of Dresden and Prof Guido Burkard at the University of Konstanz for productive and engaging collaborations on graphene nanoribbons, and to the group of Prof Harry Anderson at Oxford University for our collaboration on molecular magnets.

I thank all my great colleagues who have contributed to my unforgettable time in the Department: John, Jasper, Dominic, Alex, Anna, and others, and in particular my group mates who all have become good friends: Dimitrios, Fanmiao, Arthur, Michael, Jennifer, Alex, Iago, Tian, Wenjing and Xuelin. A special thanks to Alessandro, Ming-Yee, and Federico who started at the same time as me and who have become great friends.

My greatest gratitudes and appreciations go to Prof Lapo Bogani who has been an absolutely fantastic supervisor. First, for creating a stimulating, tolerant, diverse and exceptionally friendly group environment. Second, for providing constructive and motivating feedback to enable me to become the best version of myself. Most importantly, for providing invaluable and unconditional support, mentoring and guidance far beyond what can be expected. I am forever grateful to him for contributing to my scientific and personal flourishment over the last four years.

Finally, I want to thank my parents, siblings and grandparents for all your support - without your intellectual curiosity, encouragement and love over the years I would never be where I am today. A particular thanks to my father who sowed the seed that lead to the undertaking of my DPhil. A special thanks to my Uncle Thomas who tragically passed away during the final stages of my DPhil and to my Aunt Tove - you have always been so curious about and happy for me and I really appreciate that.

Last and most I thank my beloved Denise for always standing by my side. Your resilience, willpower, morals and unlimited love and affection is my greatest source of inspiration.

Contents

1 Introduction **1**

2 Theory and Concepts **7**

2.1 Molecular Magnetism 7

2.1.1 Single-Molecule Magnets 8

2.1.2 Lanthanide-Based SMMs 9

2.1.3 Time-Reversal Symmetry and Relaxation of Magnetisation . 12

2.1.4 Detection of Molecular Anisotropy 12

2.2 Transport Properties of Graphene 13

2.2.1 Dirac Electrons and Chiral States 14

2.2.2 Conductivity of Graphene 16

2.3 Transport Properties of Graphene Nanoribbons 19

2.4 Single-Spin Electrical Detection in Devices 20

2.4.1 The Single-Molecule Transistor 21

2.4.2 Single-Molecule Magnet Devices 29

2.4.3 Graphene-Based Devices 32

2.4.4 Carbon Nanotube Devices 33

2.5 Quantum Control of Magnetic Single Molecules 34

2.5.1 Single-Molecule Magnets 34

2.5.2 Carbon Nanotubes 36

2.6 Perspectives and Outlook 38

3 Experimental Techniques and Development of Instrumentation **39**

3.1 Introduction 40

3.2 Cantilever Torque Magnetometry 40

3.2.1 Torque Detection of Magnetic Anisotropy 41

3.2.2 Fabrication of Cantilever Torque Magnetometers 45

3.2.3 Sample Preparation 46

3.2.4 Torque Measurement Techniques 47

3.3 Millikelvin Transport Spectroscopy 54

3.3.1 Instrumental Setup 54

3.3.2 Transport-Spectroscopic Technique 57

3.4 Fast-sweeping Superconducting Magnets 62
3.4.1 Magnetic Fields and Forces of Solenoids 64
3.4.2 Degradation and Training of Composite Superconductors . . 67
3.4.3 Coil Construction 68
3.4.4 Design and Fabrication of Fast-Sweeping Superconducting Magnet Systems 69
3.4.5 Testing and Proof-of-Concept Demonstration 71
3.5 Triangular-Waveform Magnetic Field Amplifier 72
3.6 Conclusions 74

4 Magnetic Anisotropy Characterisation of Molecular Nanomagnets using Torque Magnetometry 75
4.1 Introduction 75
4.2 Terbium Porphyrin Monomer Single-Molecule Magnet 76
4.2.1 Theoretical Predictions 78
4.2.2 Characterisation of Magnetic Anisotropy 78
4.2.3 Discussion 87
4.3 Dysprosium Porphyrin Monomer Single-Molecule Magnet 90
4.3.1 Theoretical Predictions of the Ligand Field 91
4.3.2 Characterisation of Magnetic Anisotropy 91
4.4 Fused-Porphyrin Dysprosium Dimer SMM 93
4.4.1 Characterisation of Magnetic Anisotropy 96
4.5 Dy_2-hfac Dimer SMM 100
4.6 Dysprosium Trimer SMM 102
4.6.1 Conclusions 107

5 Comparison of the Magnetic Anisotropy of a Dysprosium SMM in Single-Crystals and Single-Molecule Transport 109
5.1 Introduction 109
5.2 DyP Single-Molecule Transistor 110
5.3 Magnetotransport Spectroscopy of DyP 113
5.4 Comparison of Magnetotransport Spectroscopy with CTM 116
5.5 Discussion 117
5.6 Conclusions 118

6 A Study of a Single-Molecule Graphene Nanoribbon Using Transport Spectroscopy 120
6.1 Introduction 121
6.2 Solubility-Enhancement and Franck–Condon Suppression 121
6.2.1 MGNR Single-Molecule Transistor 122

6.2.2 Millikelvin Transport Spectroscopy 123
6.2.3 Results 124
6.2.4 Discussion 129
6.3 Magnetic States and Observation of Stoner Instability 131
6.3.1 Magnetic Splitting of MGNR Ground States 131
6.3.2 Spin Filling Derived from Excited-State Spectroscopy 133
6.3.3 Stoner Instability and Irregular Spin-Filling Pattern 134
6.3.4 Magnetic Anisotropy in MGNRs 140
6.4 Low-Frequency Noise in MGNR Single-Electron Transistors 144
6.4.1 Theory of Low-Frequency Noise in SETs 144
6.4.2 Low-Frequency Random Telegraph Noise Experiment 146
6.4.3 Results 146
6.4.4 Discussion 148
6.5 Conclusions 151

7 Conclusion **153**

References **156**

Abstract

The aim of this Thesis is to increase the fundamental understanding of magnetic molecules, as the ultimate miniaturisation of the electronic component. The considerable interest in molecular nanoscale systems for quantum technologies is hampered by poor understanding of their behaviour when introduced into electronic nanodevices. We investigate the magnetic and electronic states of molecular systems at millikelvin temperature, with the aim of clarifying their behaviour in extreme conditions, and to develop novel instrumentation to further this cause. We do so by concentrating on single-molecule magnets and molecular graphene nanoribbons, first addressed in single crystals and then as single molecules in electronic nanodevices. We observe clear signatures of true magnetism in graphene nanoribbons and reveal connections between the magnetic anisotropy of molecules and their transport properties. The Thesis ultimately contributes to the unification of magnetic and conductive molecular systems and thus serves to advance the field of molecular spintronics.

We choose to go to the moon in this decade [...], not because [it is] easy, but because [it is] hard, because that goal will serve to organize and measure the best of our energies and skills, because that challenge is one that we are willing to accept, one we are unwilling to postpone, and one which we intend to win.

— John F. Kennedy [1]

1 Introduction

The ultimate limit of miniaturisation of electronic and magnetic component is a single molecule. However, there is still considerable uncertainty about the behaviour of molecular nanoscale systems, especially when they are introduced into non-crystalline environments, such as electronic nanodevices. In this Thesis we investigate the magnetic and electronic states of molecular systems at millikelvin temperature, with the aim of clarifying their behaviour in extreme conditions. We concentrate specifically on the study of lanthanide-based single-molecule magnets (SMMs) and molecular graphene nanoribbons (GNRs). We address these systems in crystals first, and probe their magnetic properties at very low temperatures, comparable to those used for single-molecule electronics. We then investigate the behaviour of lanthanide-based molecules in single-molecule devices, and discover the influence of their magnetic anisotropy on the transport properties. Eventually, we investigate the interplay of magnetic, vibrational and electronic degrees of freedom in molecularly-made graphene nanoribbons, revealing staggeringly clear states and the fundamental differences between such systems and previously-investigated carbon-based nanostructures, such as carbon nanotubes. In order to access the states of the molecular systems of choice we developed novel instrumentation, specifically tailored to the problems posed by these molecular nanostructures. The development of this instrumentation is thus an integral part of this thesis, and reported hereby.

Lanthanide ions can yield SMMs with large magnetic moment and large magnetic anisotropies, and can behave like permanent magnets of purely molecular origin. On the other hand, their physical complexities make them very difficult to rationalise [2]. This work aims to contribute to the field by analysing the magnetic anisotropy of single crystals and single molecules of six compounds based on terbium and dysprosium at millikelvin temperature. We use the relatively uncommon technique of cantilever torque magnetometry (CTM) due to its unparalleled suitability for magnetic-anisotropy detection in single crystals [3], and single-molecule transport spectroscopy. Our main findings are as follows: (i) the magnetocrystalline anisotropy is highly dependent on crystal and molecular symmetries; (ii) terbium and dysprosium behave very differently in the same ligand field; (iii) dipolar and exchange interactions between magnetic centres strongly affect the magnetocrystalline anisotropy; (iv) the magnetocrystalline anisotropy of one dysprosium SMM is approximately the sum of single-molecule anisotropies with different orientations; and (v) slow relaxation of magnetisation manifests in large hysteresis that strongly depend on the magnetic field direction relative to the crystal orientation.

In contrast to graphene, pristine graphene nanoribbons exhibit both band gap and access to free spins through their magnetic edge states [4–7]. Top-down fabrication methods have so far proven unsuitable for producing GNRs of sufficient quality [8–10], but recent advances in bottom-up chemical synthesis solved the problem of forming GNRs with atomic precision [11, 12]. The progress in the investigation of single GNR molecules has been hampered by the inability to produce single-GNR transistors due to their tendency to bundle up with each other. In this Thesis we show that after increasing the solubility of molecular GNRs in solution, single-GNR transistors can be produced and their transport properties studies with an unrivalled level of detail. For the first time we clearly demonstrate access to quantum effects in GNRs, such as the Franck–Condon effect and magnetic exchange interactions between edge states and conduction electrons, and thereby finally elevate GNRs to the list of practically useful quantum units.

Quantum computing as an industry was recently estimated to reach an annual value of $850 million by 2040, primarily by revolutionising simulation, optimisation, machine learning and cryptography [13]. Sectors such as aerospace, automotive, chemistry, energy, manufacturing and pharmacology will strongly benefit from quantum computing through e.g. development of new materials [14], computational fluid dynamics [15] and drug discovery [16, 17]. The financial-technology sector expects game-changing improvements to fraud detection [18] and portfolio [19] and risk management [20] from quantum computing. Quantum computational machine learning can anticipate superior capabilities in search and advertisement optimisation [21] in addition to industry-wide impact through artificial-intelligence applications [22].

These high expectations to quantum computing are reflected in a surging $700 million of investments in 2020 with ∼80% of this going into hardware development [13]. The fundamental unit for quantum hardware is the quantum bit (qubit). The qubit is a physical system that can be initialised in one out of two quantum states that lives long enough to be read out after the computation is completed. Quantum computations requires multiple qubits that are connected through quantum entanglement [23].

There are currently five major hardware systems competing for supremacy: superconducting qubits [24] (IBM, Google, Amazon Web Services), trapped-ion qubits [25] (Honeywell, IonQ), photonic qubits [26] (PsiQuantum, Xanadu), cold-atom qubits [27] (ColdQuanta, Pasqal) and quantum-dot qubits [28] (Intel, SQC). Quantum-dot qubits are based on the quantum properties of charges and spins. the two qubit states can be valley states in graphene [29] or silicon [28], electron orbits in carbon nanotubes (CNTs) [30], zero-field splitting in SMMs [31], or spin qubits in e.g. nitrogen vacancies in diamond where a Kramers' doublet is split by a magnetic field via the Zeeman effect [32].

This Thesis will focus on the two last types of quantum building blocks: SMMs and GNR spin systems. They comprise the two separate branches of magnetic and conducting materials that are often treated separately. In the present work we seek

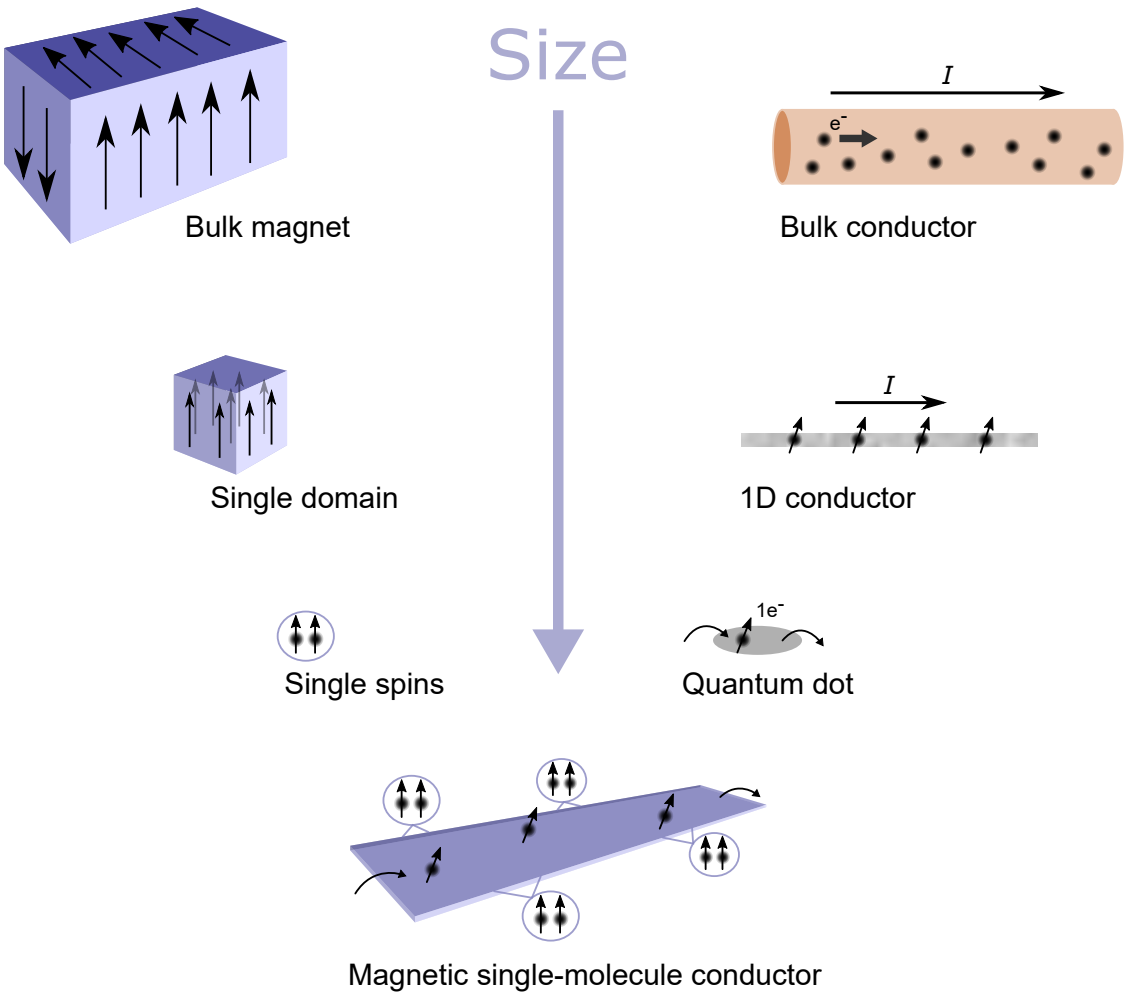


Figure 1.1: Magnetic and conducting materials are generally treated as separate types of building blocks in both physical and technological aspects. By reducing the size down to the nanoscale and ultimately to the single-molecular scale, we gain control of single spins and single electrons. Isolated, these systems are highly interesting for quantum research and application. However, by combining the single-spin and single-electron systems we create a truly unique quantum unit in which quantum information can be manipulated, stored and transmitted.

to bring these two concepts together by experimentally probing combinations of magnets and conductors at the molecular level (Fig. 1.1). We do this by measuring the magnetotransport properties of SMMs engineered to combine conducting units with strongly magnetic building blocks, and GNRs with magnetic edge states.

The purpose of this research is to provide fundamental understanding to the unification of molecular nanomagnets and molecular nanoconductors. These systems are intrinsically difficult to understand - the former due to unusually complex magnetism and the latter for the practical difficulties in measuring their transport

properties. However, because collaborators and coworkers provide us with expertly designed lanthanide-based SMMs and molecular GNRs, and we possess state-of-the-art fabrication facilities and cryogenic magnetotransport setup, we are in a unique position to acquire high quality data, provide new insight to the field and push the art of the possible.

This Thesis is structured as follows: after the present introduction, Chapter 2 will establish the theory and concepts necessary for putting the remainder of the Thesis in context and for understanding the results. First, this Chapter will elaborate on the concepts of molecular magnetism and magnetic anisotropy in molecules. Second, we describe the transport properties of graphene and graphene nanoribbons. Finally, we discuss single-spin detection using single-molecule transistors and the theory behind their operation mechanism before touching on state-of-the-art quantum control of single-molecular spins.

Chapter 3 is dedicated to the experimental techniques used to obtain the results presented in this Thesis. We outline in detail the development of a sensitive cantilever torque magnetometer and of fast-sweeping superconducting magnets. The magnetometer served as the work horse for the experiments reported in Chapter 4. Additionally, we describe the experimental setup used for millikelvin transport magnetospectroscopy that was used for Chapters 5 and 6. We round off with the proposal of a new device concept that utilises all the previously described techniques in generating amplified magnetic fields with triangular waveforms.

In Chapters 4-6 we present our experimental results. Chapter 4 focuses on the detection of magnetic anisotropy in molecular nanomagnets using our home-built torque magnetometer. We report on a range of single-crystalline terbium and dysprosium SMMs and provide novel insights on the complex magnetic anisotropy of these compounds. We discuss in detail molecular monomers with terbium or dysprosium bonded directly to conducting porphyrin ligands, in addition to dysprosium-based dimers and trimers.

In Chapter 5 we report magnetotransport measurements of a single dysprosium porphyrin SMM and compare the observed magnetic anisotropy with that of the

single crystal of the same compound (from Ch. 4). Our results suggest a clear connection between the two sample geometries and the fundamental role of the magnetic anisotropy in shaping the single-molecule elctrical response. To our knowledge such comparison is the first of its kind and has not before been reported in the literature.

Chapter 6 is the final experimental Chapter but arguably the most important Chapter of this Thesis. Here, we present results from transport spectroscopy of single graphene nanoribbons. By using GNRs with enhanced solubility we observe devices with unprecedented detail in their transport features, which gives access to GNR spin states and magnetic anisotropy. Our results pushes the boundary of the possible by clearly demonstrating molecular GNRs potential as new platforms for quantum operations.

The Thesis targets molecular magnets from bulk down to single spins in Chapter 4 (left branch of Fig. 1.1), and the electronic quantum dots in the form of single GNRs in Chapter 6 (right branch of Fig. 1.1). It ultimately allows to unify magnetic and conductive molecular systems into molecular spintronic units, as described in Chapter 5 by dysprosium porphyrin, and in Chapter 6 as molecular GNRs with magnetic edge states. The results obtained will thus, on one hand, shape the field of molecular spintronics, and on the other hand, will provide the basis for the investigation of graphene nanoribbons, and their future use in electronic devices.

2

Theory and Concepts

Contents

2.1 Molecular Magnetism 7
2.1.1 Single-Molecule Magnets 8
2.1.2 Lanthanide-Based SMMs 9
2.1.3 Time-Reversal Symmetry and Relaxation of Magnetisation 12
2.1.4 Detection of Molecular Anisotropy 12
2.2 Transport Properties of Graphene 13
2.2.1 Dirac Electrons and Chiral States 14
2.2.2 Conductivity of Graphene 16
2.3 Transport Properties of Graphene Nanoribbons 19
2.4 Single-Spin Electrical Detection in Devices 20
2.4.1 The Single-Molecule Transistor 21
2.4.2 Single-Molecule Magnet Devices 29
2.4.3 Graphene-Based Devices 32
2.4.4 Carbon Nanotube Devices 33
2.5 Quantum Control of Magnetic Single Molecules 34
2.5.1 Single-Molecule Magnets 34
2.5.2 Carbon Nanotubes 36
2.6 Perspectives and Outlook 38

2.1 Molecular Magnetism

In the field of molecular magnetism magnetic building blocks are synthesised bottom-up through chemical design, to yield magnetic molecules with tailored magnetic

properties. Single molecules of coordination compounds represent the ultimate limit of miniaturisation of molecular magnetic moment, producing molecules with well-defined quantum states available for manipulation. Their quantum properties are highly interesting for quantum technologies such as quantum sensing, quantum information processing and storage [31, 33–40].

2.1.1 Single-Molecule Magnets

Single-molecule magnets (SMMs) are characterised by their high-spin ground states and strong magnetic anisotropy making this group of compounds exhibit permanent magnetism of a purely molecular origin below a certain temperature. The magnetic anisotropy is quantum in nature and stems from orbital angular momentum of electrons. Molecular magnetism has enabled access to investigating the origins of magnetism at the most fundamental scale [41–43].

In SMMs organic ligands are coordinated around ions that carry the magnetic momentum. It is generally assumed that the magnetically active electrons in the ions interact with each other but not with the magnetic moments of other molecules, because of spatial shielding provided by the bulky ligands, although it can happen if large dipolar fields are present (e.g. in lanthanide-based SMMs). A milestone in molecular magnetism was the the discovery of the magnetic properties of Mn_{12}, which effectively is a cluster of manganese oxide which growth is blocked by the presence of carboxylates [43].

Mn_{12} consists of 12 spin centres of which eight Mn^{3+} all have spin up and four Mn^{4+} have spin down resulting in a S=10 ground state. At low temperature the magnetisation of Mn_{12} relaxes slowly and therefore exhibits hysteresis like a small permanent magnet [44]. These phenomena, combined with quantum tunnelling of magnetisation (QTM), were ground breaking when discovered in 1996 [45, 46]. The properties of Mn_{12} lay the cornerstone for molecular magnetism and resulted in an explosion of interest in the field [31, 36–38, 41, 47–49].

The design of SMMs usually focuses on maximising the magnetic moment while quenching the mechanisms that promote magnetisation reversal. Transition

Table 2.1: Basic magnetic information for selected trivalent transition-metal and Ln ions. Adapted from Ref. [43].

Ion	$3d^n/4f^n$	$^{2S+1}L_J$	g_J	SOC (cm^{-1})	$\chi_M T$	μ_{eff} (μ_B)	M (μ_B)
Fe^{3+}	5	$^6S_{5/2}$	2	460	-	5.4	5
Co^{3+}	6	$^5D_4$	3/2	580	-	-	6
Tb^{3+}	8	$^7F_6$	3/2	1705	11.82	9.72	9
Dy^{3+}	9	$^6H_{15/2}$	4/3	1900	14.17	10.65	10

metal ions have 3d valance electrons that strongly interact with the electrons of surrounding ligands which leads to lifting of the orbital degeneracy respective to the symmetry of ligand orientation. Spin–orbit coupling (SOC) in transition metals is typically small and can be treated as perturbations to the ligand field (LF) splitting of the orbitals. However, the transition-metal spin is small, even in high-spin clusters, compared to the total magnetic moment of many lanthanides (Ln).

2.1.2 Lanthanide-Based SMMs

Lanthanide-based SMMs are very promising for spintronic applications because they typically have large spins, large unquenched orbital angular momenta and often larger ligand field splitting than transition metal complexes [50–54]. Particularly interesting are the Ln(III) with more than half-filled shells because they have spin and orbital angular momenta aligned in parallel. The energy of free Ln(III) ions is the sum of the kinetic energy, electron–electron (e–e) repulsion and spin–orbit coupling (SOC) and can be described by the Hamiltonian $H_{\text{free}} = H_{\text{kin}} + H_{\text{ee}} + H_{\text{SOC}}$. The total angular momentum, J, is a 'good' quantum number and describes the Russell–Saunders coupling of total spin, S, and orbital angular momentum, L, of the associated multiplets (Tab. 2.1). Moreover, 4f electrons are well shielded by outer electrons resulting in strongly localised magnetic moment around the Ln ion and ground states are typically hundreds of meVs below electronic excited states [55].

In coordination complexes, the ground state multiplet of the free ion is split by the electrostatic field provided by ligands that interacts with the Ln 4f orbitals. For Ln, the ligand-field effect is treated as a perturbation because it is always smaller than that of e–e repulsion and SOC. This perturbation lifts the degeneracy

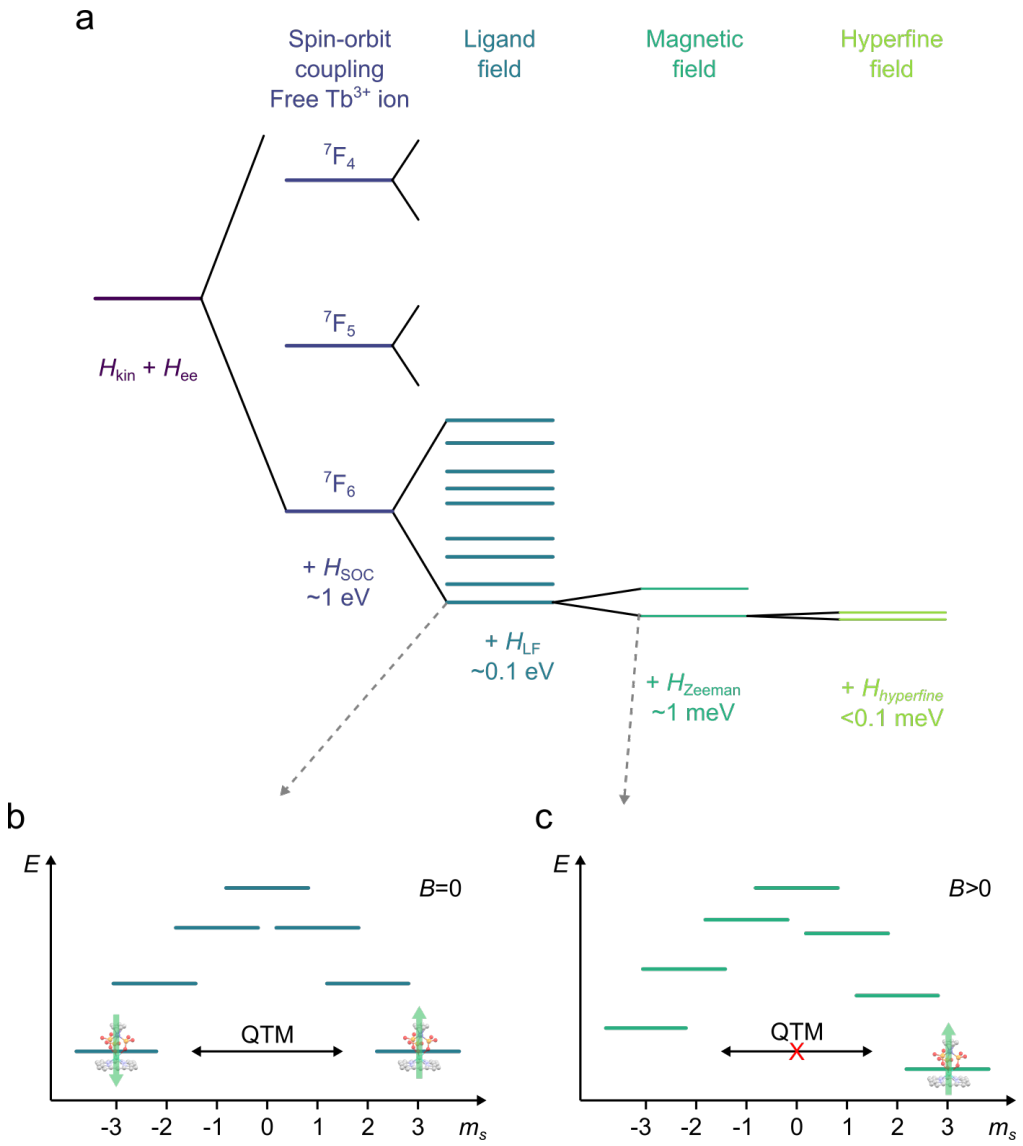


Figure 2.1: **(a)** Energy level scheme of Tb^{3+} illustrating the effects of the different terms of the Hamiltonian with approximate energy scales. Adapted from Ref. [55]. **(b)** At zero magnetic field the ground state doublet of a terbium porphyrin SMM is in resonance and allows QTM. **(c)** For $B > 0$ the degeneracy is lifted and QTM is not favoured. $T < 1$ K is assumed so that QTM is the only available relaxation mechanism. No panels are to scale.

of the electronic multiplet into states with different orbital angular momentum and is what causes strong magnetic anisotropy in Ln SMMs. In comparison, ligand-field effects in transition metal complexes are often smaller and the orbital momentum is often quenched. Adding the ligand field, Zeeman and hyperfine effects to H_{free} yields (Fig. 2.1a): [55]

$$H = H_{\text{free}} + H_{\text{LF}} + H_{\text{Zeeman}} + H_{\text{Hyperfine}}. \tag{2.1}$$

Therefore, to characterise of the magnetic properties of SMMs it is sufficient to characterise the ligand field. A common phenomenological approach for describing the ligand field is by using Stevens operator equivalents, O_k^q, that are functions of the tensor $\mathbf{J}$: [56]

$$H_{LF,J} = \sum_{k,q} B_k^q O_k^q(\mathbf{J}), \tag{2.2}$$

where B_k^q are Stevens parameters and $-q \leq k \leq q$ with $q = 2, 4, 6, ...$ From this we can construct a phenomenological spin-Hamiltonian, H_J:

$$H_J = H_{\text{LF},J} + H_{\text{Zeeman},J} + H_{\text{Hyperfine},J}, \tag{2.3}$$

where $H_{\text{Zeeman},J} = g_J \mu_B \mathbf{J} \cdot \mathbf{B}$, g_J is the Landé g-factor and μ_B is the Bohr magneton. The contribution from hyperfine is usually too small compared with the other terms, but can have a large impact on QTM [55].

There is a total of 27 Stevens parameters that characterise the ligand field, which complicates experimental characterisation. However, symmetries of the ligand field can greatly reduce the number of non-zero Stevens parameters because those that are not invariant under the respective symmetry operations are zero. Consequentially, complexes with high crystal symmetry leave only a few Stevens terms in Equation 2.3 and facilitate simpler characterisation experimentally. By contrast, the presence of low symmetry leaves few or no vanishing coefficients. In these cases multiple experimental methods and first-principles calculations might be necessary to describe the magnetic properties [55].

2.1.3 Time-Reversal Symmetry and Relaxation of Magnetisation

Another important aspect is time-reversal symmetry. Kramers' theorem [57] states that every energy level of a time-reversal symmetric system with half-integer J must be at least two-fold degenerate in a purely electric field such as the ligand field (e.g. Fig. 2.1b). A magnetic field would be required to lift the degeneracy (Fig. 2.1c). This theorem does not apply to integer J systems, which can be nondegenerate in the ligand field. Kramers' theorem has an important impact on the probability of QTM at zero field (that formally requires degenerate levels). However, the hyperfine coupling in Ln SMMs can promote QTM in both integer and half-integer J systems [55].

In SMMs relaxation of magnetisation is the process of returning to equilibrium with the environment after a perturbation. Relaxation is a consequence of coupling between the magnetic moment of the magnetic centre with the crystal lattice or with neighbouring SMMs in the lattice. Therefore, a molecular complex is a SMM only if all relaxation mechanisms are inefficient, so that it can maintain a remanent magnetisation. At millikelvin temperatures, the relaxation mechanism is mainly QTM mediated via hyperfine coupling, and above a few Kelvin spin–phonon coupling adds to available mechanisms [55].

QTM can occur when two states, e.g. $|\uparrow\rangle$ and $|\downarrow\rangle$, are in resonance and non-zero off-diagonal terms of the matrix Hamiltonian are present. Such non-zero terms are typically introduced by dipolar and hyperfine coupling to neighbouring magnetic centres. A requirement for QTM is that the dipolar or hyperfine splitting are equal to or larger than the energy difference between two electronic states. In SMMs, QTM is typically effective around zero magnetic field and often leads to characteristic 'butterfly-shaped' or 'waist-restricted' hysteresis loops [55].

2.1.4 Detection of Molecular Anisotropy

As mentioned above, understanding the magnetic properties of SMMs relies on understanding the effects of the ligand field on the magnetic ion. Popular experi-

mental methods are electron paramagnetic resonance (EPR) [58], inelastic neutron scattering [59] and optical absorption and luminescence spectroscopy [60]. These techniques allow measuring the energy levels of separate multiplets. [55] However, the two former techniques require expensive and complicated facilities, and the latter technique is limited to optical transitions.

Cantilever torque magnetometry (CTM) is a simple but powerful technique to directly measure the magnetic anisotropy of SMMs [3]. For systems with high symmetry, and thus a simple Hamiltonian, the ligand field can often be described solely through CTM. However, for Ln-based SMMs, the crystal symmetry is typically low and the Stevens parameters to be determined are many. Therefore, in this Thesis we attempt to use a combination of CTM, first-principles CASSCF calculations [61] and magnetotransport spectroscopy to describe the magnetic properties of Ln-based SMMs (Ch. 4 and 5) and molecular GNRs (Ch. 6).

2.2 Transport Properties of Graphene

The electronic band theory of monolayer graphite was developed in 1947 [62] although the scientific community considered the material unstable and thus its physical realisation impossible. Despite these negative predictions a single layer of graphene was experimentally isolated and transport spectroscopy was performed by Novoselov, Geim and coworkers in 2004 [63, 64]. Their striking results revealed that the electronic properties of graphene is that of a two-dimensional gas of massless Dirac electrons mimicking relativistic particles moving at the speed of light [65–72] and with a non-zero minimum conductivity [64]. Importantly, and in addition to these intriguing results, they established graphene as an easily accessible platform for investigating the rich physics of quantum electrodynamics, which sparked tremendous efforts in the field of graphene research [29, 73–78].

The mentioned pioneering work was followed by observation of several interesting phenomena in graphene, such as large mean free path at room temperature [63, 64, 79, 80], the absence of weak localisation [81], magnetoresistance [81], the chiral quantum Hall effect [82], topological states [83–85], edge states in nanoribbons [7]

and Hofstadter butterflies [86–88] in van der Waals heterostructures. In this Section we will establish the transport properties of graphene and graphene nanoribbons from the literature, which will be useful for the discussion of our experimental results on molecular graphene nanoribbons in Chapter 6.

2.2.1 Dirac Electrons and Chiral States

The description of the transport properties of graphene starts from its lattice structure. Graphene consists of a single layer of carbon atoms in a hexagonal 'honeycomb' lattice. The unit cell is spanned by vectors $\mathbf{a_1}$ and $\mathbf{a_2}$ and contains two non-equivalent carbon atoms A and B separated by a distance $a_0 = 1.4$ Å (Fig. 2.2a). Thus, only atoms A and B are necessary to describe the electronic structure of graphene. Using a tight-binding Hamiltonian it can be shown that the energy dispersion $E(\mathbf{k})$ at low energies is: [62, 89]

$$E(\mathbf{k}) = \pm t|1 + e^{i\mathbf{k}\cdot\mathbf{a_1}} + e^{i\mathbf{k}\cdot\mathbf{a_2}}|, \tag{2.4}$$

where t is the hopping energy and $\mathbf{k}$ is the fermion momentum vector. $E(\mathbf{k})$ represents electrons in the graphene π orbitals composed by hybridised atomic $2p_z$ orbitals. Equation 2.4 shows that the band structure consists of one band at positive and one band at negative energies [90].

The Brillouin zone reveals two non-equivalent wave numbers, labelled $\mathbf{K}$ and $\mathbf{K'}$ (Fig. 2.2b) which existence stem from the two non-equivalent lattice sites. Because the p_z orbital only contains one electron the system is half-filled and as a consequence the major parts of the transport properties of graphene is determined by the spectrum close to $\mathbf{K}$ and $\mathbf{K'}$. Close to the two Dirac points K and K' $E(\mathbf{k})$ is shaped like two cones commonly known as 'valleys' (Fig. 2.2c). In these valleys $E(\mathbf{k}) = \pm v_F \hbar k$ with $v_F = 3ta_0/(2\hbar)$ and using the widely accepted value of $t \approx -2.7$ eV then $v_F \approx 10^6$ m/s (this value is consistent with experiments [64, 80]). Furthermore, it can be shown that the density of states in graphene can be written $\rho(E) = 2|E|/\pi\sqrt{3}t^2$ and reveals the linear dependence of $\rho(E)$ on the energy, which is a fingerprint of massless[1] Dirac electrons [89, 90].

[1] The effective mass $m^* = \partial^2\rho(E)/\partial(k)^2 = 0$.

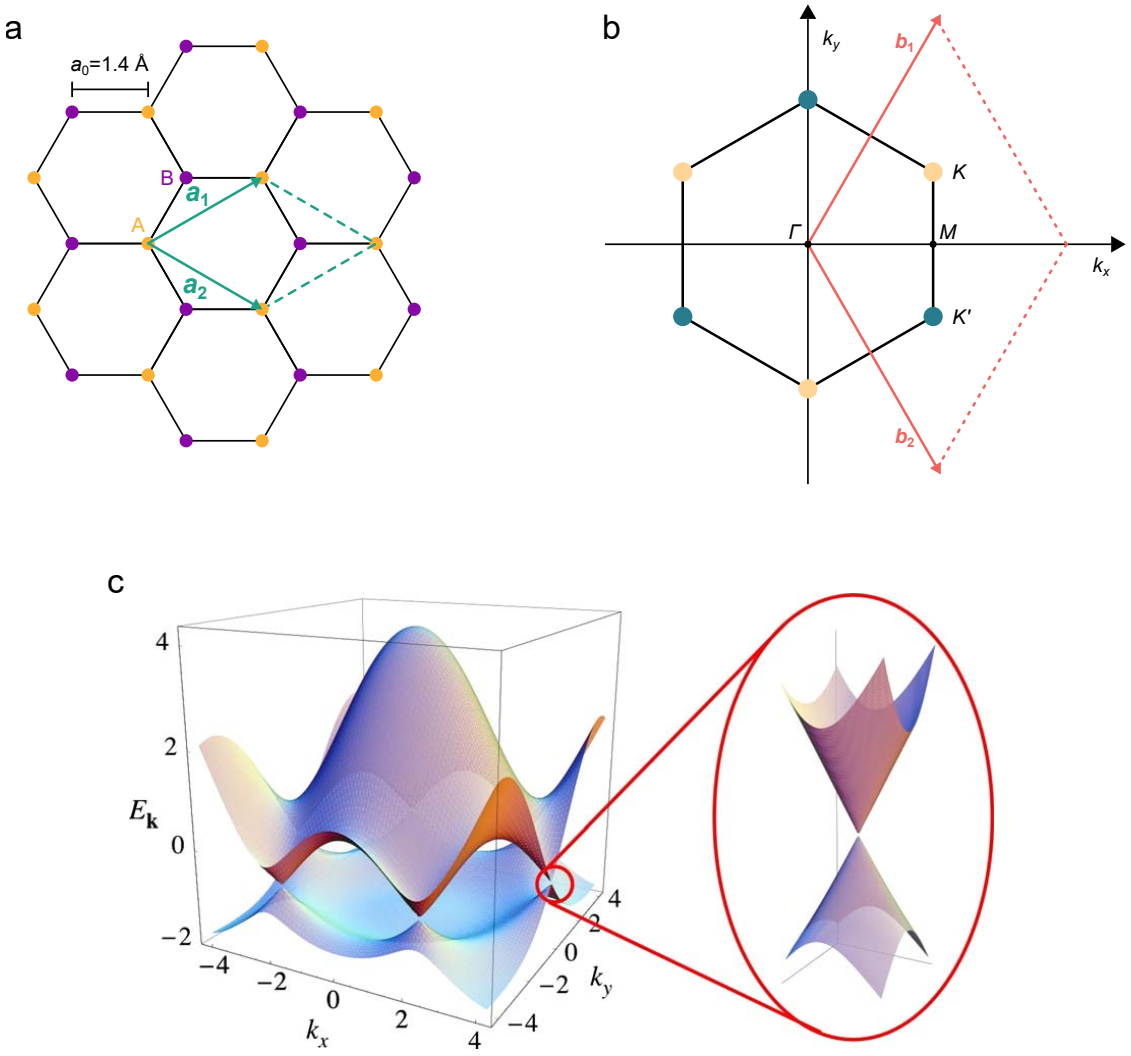


Figure 2.2: **(a)** The honeycomb Bravais lattice of graphene with the unit cell spanned by green arrows and the two non-equivalent carbon atoms (A and B) marked by yellow and purple dots. **(b)** The Brillouin zone of graphene with the non-equivalent points **K** and **K′** marked by yellow and green dots, respectively. **(c)** Energy dispersion (in units of t) in the lattice. The Dirac cones (zoom in) are located at the **K** and **K′** points. Adapted from Ref. [89].

It turns out that particles in the **K** and **K′** valleys also attain a property called chirality. In the **K** valley electrons have positive chirality and holes have negative chirality, and in the **K′** valley it is opposite. An important consequence of the valley physics is so-called Klein tunnelling that causes unity transparency of the potential barrier between **K** and **K′** valleys for head-on collisions, meaning that back-scattering is suppressed [91]. As we will discuss below, much of the uniqueness of graphene transport lies in the presence of chiral and massless Dirac states. From

Table 2.2: Important short-range and long-range scatterer types in graphene.

Short-range scatterers ($r_0 \leq a_0$)	**Long-range scatterers** ($r_0 \gg a_0$)
Adatoms	Ripples
Vacancies	Dislocations
Adsorbed molecules	Edge disorder
Resonant scatterers	Charged scatterers

chirality of electrons in graphene came the observation of the chiral quantum Hall effect where the Hall conductivity is quantized as $\sigma_{xy} = 2e^2(1 + 2n)/h$ (n =1,2,...), and is a consequence of the Landau levels of Dirac electrons combined with the presence of two valleys [80, 92, 93].

2.2.2 Conductivity of Graphene

Non-zero Conductivity at the Dirac Point

The transport properties of graphene is determined by its conductivity, σ. The Fermi energy of neutral graphene is zero and that would suggest that its conductivity should also be vanishing. However, experiments have shown that the conductivity of graphene at the Dirac point is finite and of the order of $\sim 4e^2/h$ [64]. It turns out that the non-zero σ at the Dirac point is a consequence of non-zero density of states at the Dirac point caused by small amounts of disorder [94]. This phenomenon can be understood by looking at how electrons interact with different sources of disorders in graphene[90].

There are two important categories of disorder in graphene: long-range and short-range scatterers (Tab. 2.2). Adatoms bond with the p_z orbital and thus effectively act as a vacancy and do not take part in transport. They also cause conversion of sp^2 to resonant sp^3 orbitals that add to scattering by increased SOC [95]. Experimental observations suggest that disorder in graphene is often dominated by short-range resonant scatterers acting as vacancies and by long-range charged scatterers [96].

For extended graphene systems transport is well described by Boltzmann's transport equation that assumes: [97] (i) scattering is local in space and time, (ii) scattering is weak and electric fields are small and (iii) the electronic de Broglie

wavelength is much smaller than the distance between impurities. For short-range resonant scatterers, such as vacancies or adatoms, the conductivity at the Fermi energy can be written: [98]

$$\sigma(E_F) = \frac{4e^2}{\pi h} K(E_F), \tag{2.5}$$

where $K(E_F)$ is a dimensionless function. It turns out that $K(0) = 1$ at the Dirac point regardless of the impurity concentration and therefore results in $\sigma_{min} = 4e^2/\pi h$. Moreover, if instead long-range, charged scatterers are considered σ_{min} takes a different form: [99]

$$\sigma_{min} = (e^2/h)c\mathcal{L}, \tag{2.6}$$

with $c = 0.5 \pm 0.05$ and $\mathcal{L} = \log\left[1/(4\mathcal{L}/\alpha_g^{eff})\right]$, where α_g^{eff} is the effective fine structure constant of graphene.

Conductivity Minimum of Graphene Ribbons

Graphene ribbons also exhibit a finite minimum conductivity however through different mechanisms than described above. The minimum conductivity of extended graphene systems arise from disorder but in small ribbons, where the electrons can be in the ballistic regime, the transport problem is different. First, conductivity is only a well defined quantity when the system is sufficiently large so that the current is homogeneous and similar in different samples. For systems with dimensions smaller than the mean free path, ℓ, i.e. the mesoscopic regime, the conductance G is the appropriate quantity to describe electron transport. The typical impurity concentration in graphene is $n_i \approx 5 \cdot 10^{11}$ cm^{-2} [100], and the typical distance between impurities is $d \approx \sqrt{n_i^{-1}} = 20$ nm. The typical de Broglie wavelength of electrons at the Fermi surface is $\lambda_F \approx 20$ nm^{-1} is of the same order of magnitude as d, and therefore the current becomes nonhomogeneous, sensitive to the impurity positions and the conductance varies from sample to sample [90].

For a ribbon with width L_y and length L_x and $L_y/L_x \ll 1$ and $L_x, L_y \ll \ell$ (i.e. the ballistic regime), the total transmission, T, at the Dirac point is $T =$

$L_y/L_x\pi$. The conductance can be expressed as $G = \frac{4e^2T}{h} = \sigma\frac{L_y}{L_x}$, [101] and therefore σ=σ_{min}. Note, that this result is only valid when $L_y/L_x \ll 1$, otherwise σ is dependent on the aspect ratio.

Quantum Correction to the Drude Conductivity

The conductivity of classical metals with disorder is described by the Drude model as $\sigma_M = e^2 n\tau/m^*$, where n is the charge density, the relaxation time $\tau = \ell/v_F$ is the average time between elastic collisions with static impurities [102]. However, quantum interference effects such as weak localisation give rise to several relaxation times.

Weak localisation is a quantum correction to the classical conductivity that arises from quantum-mechanical superposition of scattering trajectories. It stems from scattering trajectories where the initial and final points coincide (so-called type II trajectories). Due to time reversal symmetry for type II trajectories (i.e. electrons going around the trajectory either in clockwise or anti-clockwise direction), interference arises between the equal phases. This phenomenon serves to increase the probability of type II scattering trajectories and thereby decrease conductivity [103].

An applied magnetic field perpendicular to type II trajectories break the time reversal symmetry by relatively shifting the phases of clockwise and anti-clockwise trajectories. This phenomenon, called the Aharanov–Bohm effect, serves to suppress the phase interference and thereby increase the conductivity in metals.

In graphene characteristic relaxation times are confounded by chirality and the existence of two valleys because the electron trajectories depend on intra- and intervalley scattering probabilities. It turns out that intervalley scattering (between the $\mathbf{K}$ and $\mathbf{K}'$ valleys) only occurs when electrons enter a strong short-range potential with range $r_0 \leq a_0$ from impurities such as vacancies or adatoms. Intervalley scattering is negligible in the potential from long-range scatterers, where $r_0 \gg a_0$, such as charge impurities, ripples and dislocations (Tab.2.2).

In long-range potentials back-scattering is also suppressed due to Klein tunnelling between valleys of the same chirality [104]. Formally, this effect is explained as the

destructive interference caused by the Berry's phase of massless Dirac electrons performing closed chiral orbits leading to weak antilocalisation [105]. Therefore, Klein tunnelling enhances forward scattering, and consequentially the conductivity in graphene is enhanced compared to the classical Drude's conductivity. Backscattering (weak localisation) can only arise if short-range scatterers are present.

Through application of a B field it has been revealed that graphene can switch between weak localisation and weak antilocalisation. This phenomenon depends on the charge density n and the B magnitude. Small n favours weak antilocalisation where long-range scatterers are dominant. Large n favours weak localisation because screening of charge impurities makes short-range scatterers more dominant [106]. Moreover, B can break the time reversal symmetry and suppress the interference effect that gives rise to weak antilocalisation and thereby switch the system to a weakly localised one [107].

2.3 Transport Properties of Graphene Nanoribbons

While graphene offers exceptional transport properties in extremely large electron mobility even at large charge densities, it lacks the convenient features of band gap and magnetic moment. It is therefore of large excitement that the finite size of graphene nanoribbons (GNRs) results in both these features. Theoretical calculations have predicted the opening of a band gap for ribbon widths below ∼30 nm that increases with decreasing width as a consequence of increasing confinement [4, 5, 108–110].

The electronic properties of GNRs are largely defined by their atomic structure at the edges. While band gaps can open in GNRs with armchair edges, GNRs with zigzag edges exhibit flat bands that turn out to be states localised along the ribbon edges [111–114], and are predicted to be ferromagnetic along the edges and antiferromagnetic between opposite edges [6, 115, 116]. Armchair and zigzag ribbons have been dedicated much attention theoretically but experimental realisation has proven very difficult. Top-down, mainly lithographic, fabrication

methods produce GNRs with large edge disorder that destroys the fragile edge states but promote phenomena such as large magnetoresistance [8, 9, 117, 118]. The top-down approach yielding the GNRs with the cleanest transport features is unzipping of CNTs [10, 119–122]. But not even this approach could produce ribbons of the necessary quality to observe edge states.

Surprisingly, the solution to the problem of atomically defined GNR edges did not come from the cleanroom but instead from the chemistry laboratory in the form of bottom-up chemical synthesis. Through polymerisation of monomer precursors, molecular GNRs (MGNRs) with atomic precision could be engineered, first on metallic surfaces [11, 123–129], and recently also in liquid-phase processable in large quantities [12, 130]. These GNRs can be synthesised with fixed widths and exhibit perfect edges with configurations determined by the synthesis design. The ribbon length is the only parameter that can not easily be controlled and batches therefore contain ribbons with a distribution of lengths.

Before we can investigate the elusive transport properties of MGNRs, they must be isolated and implemented in a transistor geometry (Sec. 2.4.1). MGNRs have proven particularly difficult molecules to integrate because of generally very poor solubility that causes ribbons to bundle up. Nevertheless, in a recent ground-breaking experiment magnetic edge states were detected in MGNRs using pulsed electron paramagnetic resonance (EPR) confirming the theories that free spins can exist in GNRs [7]. This study also revealed µs spin-coherence times.

GNRs intrinsic quantum properties give this class of graphene nanomaterials a great potential for quantum applications. The challenge now remains to investigate these properties of GNRs using transport spectroscopy. In this Thesis, Chapter 6 is dedicated to this aim.

2.4 Single-Spin Electrical Detection in Devices

Moors law has pushed the transistor towards smaller and smaller size to maximise computation-power density and minimise cost. However, miniaturisation pushed to the ultimate limit, i.e. that of a single-molecule transistor, offers more than just

small size. When the transistor channel is a quantum dot that attains discrete energy levels, the transistor itself may become a spectroscopic instrument that can probe its own quantum states. In contrast to the other techniques discussed in this work, these are systems where the internal molecular energy levels can be tuned by the electrostatic potential created by a gate electrode.

The potential of using single molecules as electronic components was first recognised by Aviram and Ratner in 1974 [131] which triggered much effort in the field. The first clear experimental demonstration of a single-molecule transistor was reported by Park and coworkers in 2000 [132]. Theoretical predictions of the transport properties of such devices are encouraging [133, 134]. Important reviews about the possibilities and prospects of using single-molecule transistors for use in future quantum computer technology [135, 136], as well as the characteristic electron transport in such junctions [35, 137, 138], were published during the 00s, and a recent review about the state-of-the-art of single-molecule transistors was published in 2015 [139].

2.4.1 The Single-Molecule Transistor

Single molecules and atoms trapped between three-electrodes constitute a kind of quantum dots at the limit of miniaturisation [141]. Molecules are capacitively coupled to the leads by a coupling energy Γ that allows tunnelling of electrons between the source and drain electron through the dot molecule (Fig. 2.3. The electronic properties of these devices are dominated by (i) discrete molecular energy spectrum and (ii) Coulomb repulsion between dot electrons resulting in an energy cost associated with adding an electron to the dot, called the addition energy, E_{add}. When E_{add} is not paid tunnelling of electrons is suppressed in a phenomenon called Coulomb blockade [142]. Quantum dots with just a few electrons constitute potential building blocks for spintronic processing units [143–150].

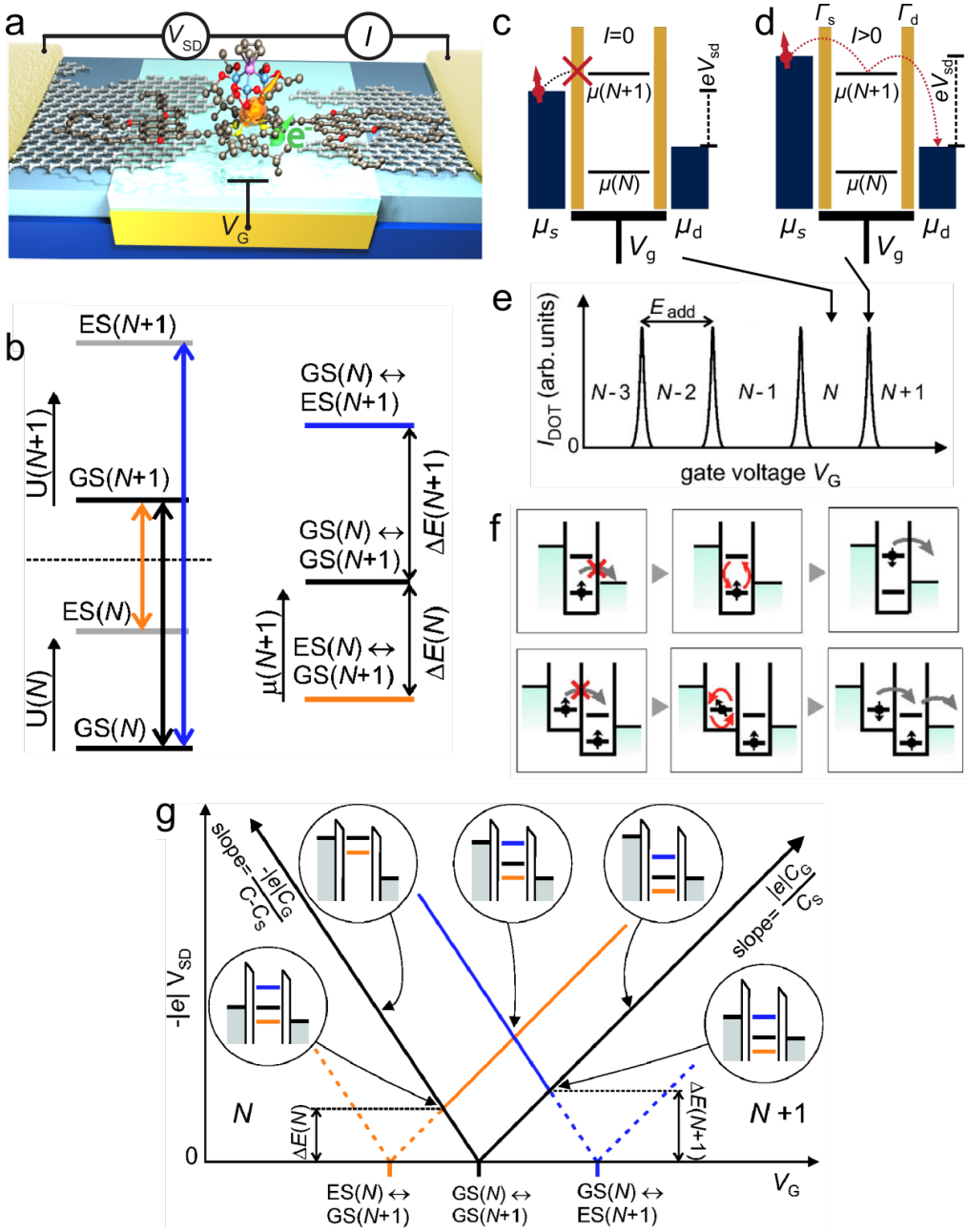


Figure 2.3: The single-electron transistor. **(a)** Scheme of the single-electron transistor electronic circuit. The quantum-dot channel is separated from the source and drain electrodes by Shottky tunnell barriers. Experimentally the tunable parameters are V_g and V_{sd} that shift the lead potentials and dot levels, respectively. The measured quantity is the drain current I. **(b)** Potential energies, U, and molecular levels, μ_i, for ground states (GS) and excited states (ES) of quantum dot charge states N and N+1, and transitions between them. **(c,d)** Chemical-potential diagram of a single-electron transistor in **(c)** Coulomb blocked (I=0) and **(d)** resonant ($I \neq 0$). **(e)** I-V_g peaks whenever resonance allows sequential electron tunnelling, otherwise Coulomb blockade. **(f)** Schemes for coherent spin manipulation in single (top row) and double (bottom row) dots with spin-to-charge conversion read-out. **(g)** Conductance map dI/dV_{sd} versus V_{sd} and V_g. The solid lines correspond to onsets of resonant transport at different electrostatic configurations coloured relative to panel **(b)**. Adapted from Ref. [140].

The Constant Interaction Model

The constant interaction model [142, 151] assumes that all Coulomb interactions among electrons in the dot and with those in the environment can be described by a single, constant capacitance, C, which is the sum of the capacitances between the dot and the source, C_s, the drain C_d, and the gate C_g, so that $C = C_s + C_d + C_g$ [140]. Furthermore, the model assumes that the single-particle level spectrum is insensitive to C and thus independent of the number of electrons N. Consequentially, the total energy, $U(N)$, of the ground state of a quantum dot with N electrons can be written:

$$U(N) = \frac{(-|e|(N - N_0) + C_s V_s + C_d V_d + C_g V_g)^2}{2C} + \sum_{n=1}^{N} E_n(B), \qquad (2.7)$$

where -$|e|$ is the electron charge, N_0 is the background charge. The last term is the sum of all the occupied single-particle levels and depends of the confinement potential. [140]

Electron tunnelling transport is best described through the the chemical potential, $\mu(N)$, of the dot, which denotes the transition GS(N-1)↔GS(N) and is expressed:

$$\mu(N) = U(N) - U(N–1) = -\frac{E_C}{|e|}(C_s V_s + C_d V_d + C_g V_g) + E_N, \qquad (2.8)$$

where $E_C = e^2/C$ is the charging energy (Fig. 2.3b). The addition energy is the energy difference between successive μ and is written:

$$E_{add}(N) = \mu(N) - \mu(N–1) = E_C + \Delta E, \qquad (2.9)$$

where ΔE is the single-particle level spacing and can be zero for degenerate levels. E_{add} is generally dominated by E_C in molecular devices due to the strong confinement [140].

The bias window is defined as, $-|e|V_{sd} = \mu_s - \mu_d$, where $V_{sd} = V_s - V_d$ (Fig. 2.3c,d), and current can only flow when the resonance criterion $\mu_s \leq \mu(N) \leq \mu_d$ is fulfilled (Fig. 2.3c-e). In resonance, one electron can tunnel from the source and into an empty dot state and then from the dot state into the lead before a new electron can tunnel from source to dot. This two-step process is called sequential electron tunnelling because only a single electron at a time is shuttled through

the device. If μ lies outside the bias window no current flows and the number of electrons on the dot remains fixed. This phenomenon is known as Coulomb blockade (Fig. 2.3d,e). The process of sequential electron tunnelling has named this class of transistors single-electron transistors, and single-molecule transistors is a subclass within this class [140].

The dot can be tuned in and out of resonance by either adjusting V_g to shift the dot levels, or changing the bias window. The dot's I-V_g characteristically peaks whenever the resonance criterion is met and remains in Coulomb blockade in between resonances (Fig. 2.3e). Furthermore, we differentiate between the low-bias regime with only the ground state of N is in resonance from the high-bias regime with ground and excited states inside the bias window. There can be one tunnelling current for each resonant state [140].

Devices are typically characterised by mapping I as a function of V_{sd} and V_g, commonly called a stability diagram (SD) (Fig. 2.3g). The SD is directly linked to the dot's chemical potential spectrum (Fig. 2.3b), and each transition results in a V-shaped region that denotes a μ entering the bias window. The slopes, $\alpha_{\pm}$, of the two edges, $\partial(-|e|V_{sd})/\partial V_g$, depend on the capacitances, and can be written (for V_d=0): $\alpha_- = -|e|C_g/(C - C_s)$ and $\alpha_+ = |e|C_g/C_s$. While there is a 1:1 correspondence between the lead potentials and the dot potentials through $\mu = |e|V_{sd}$, the coupling between dot and gate is given by $\mu = \beta V_g$ where $\beta = (|\alpha_+| + |\alpha_-|)^{-1}$ is the gate lever arm.

The GS(N)$\leftrightarrow$GS(N+1) transition (black solid line in Fig. 2.3g) marks the change from Coulomb blockade to resonant transport, and due to their diamond-shape the regions of Coulomb blockade are named Coulomb diamonds. The onset of excited states are indicated with solid lines inside the conducting region. It is often useful to plot the differential conductance $G = \partial I/\partial V_{sd}$ because it can be difficult to recognise small changes in I. While I-V_{sd} is typically step-like in quantum dots, G-V_{sd} has a series of peaks at each step position. Onsets of transitions can thus be easier to distinguish in G than in I [140].

The Coulomb regime requires that both $k_BT \ll \Gamma$ and $k_BT \ll \Delta E$, where $\Gamma = \Gamma_s + \Gamma_d$ ($k_BT = 2.2$ µeV at T=25 mK). In the Coulomb regime, the capacitive lead–dot couplings Γ_s and Γ_d determines the tunnelling rate of electrons through the molecule. Γ can be extracted experimentally from the full-width half maximum (FWHM) of conductance peaks in G-V_{sd} traces or from G-V_g traces at zero bias across the degeneracy point (i.e. where two Coulomb diamonds meet) through Γ = FWHM$\cdot\beta$. The couplings $\Gamma_{s/d}$ depends on the degree of overlap between orbitals in the leads and dot and is thus a fixed device parameter [152].

Rate-Equation Model

Formally, single-electron transport through a weakly coupled molecule can be described using a rate-equation model as reported in Refs. [153, 154]. We assume a single molecular mode and a superohmic phonon bath (accounting for the coupling with the environment) in the model. The current through the junction can be written as:

$$I = |e|\frac{\gamma_{ox}^{s}\gamma_{red}^{d} - \gamma_{red}^{s}\gamma_{ox}^{d}}{\gamma_{red}^{s} + \gamma_{red}^{d} + \gamma_{ox}^{s} + \gamma_{ox}^{d}}, \tag{2.10}$$

where $\gamma_{red/ox}^{s/d}$ denotes the electron-transfer rates at each electrode corresponding to a reduction or an oxidation. $\gamma_{red/ox}^{s/d}$ for N/N+1-type transitions, are given as follows:

$$\gamma_{red}^{s,d} = 2\frac{\Gamma_{s,d}}{\hbar}\int f_{s,d}(\epsilon)k_{red}(\epsilon)d\epsilon, \tag{2.11}$$

$$\gamma_{ox}^{s,d} = \frac{\Gamma_{s,d}}{\hbar}\int (1 - f_{s,d}(\epsilon))k_{ox}(\epsilon)d\epsilon, \tag{2.12}$$

where $\Gamma_{s,d}$ is the electronic coupling between molecule and the electrodes, $f_{s,d}(\epsilon)$ is the Fermi–Dirac distribution at the chemical potential, ϵ, in the respective electrode. $k_{red/ox}(\epsilon)$ is the density of states of the molecule written as:

$$k_{red/ox}(\epsilon) = \frac{1}{\pi}\mathrm{Re}\int_0^\infty e^{\sigma i(\epsilon-\mu)t/\hbar}e^{-t/\tau}B(t)dt, \tag{2.13}$$

where $\sigma = 1$ ($\sigma = -1$) for reduction (oxidation), μ is the molecular energy level, $\tau = 2\hbar/(\Gamma_s + \Gamma_d)$ is the lifetime of the molecular electronic state and $B(t)$ is the phononic correlation function in time, t:

$$B(t) = e^{D_q(t)} \cdot e^{D_{bath}(t)}, \tag{2.14}$$

$$D_q(t) = \left(\frac{g_q}{\omega_q}\right)\left[(\cos\omega_q t - 1)\cdot\coth\left(\frac{\omega_q}{2k_BT}\right) - i\sin(\omega_q t)\right], \tag{2.15}$$

$$D_{bath}(t) = \int \frac{J(\omega)}{\omega^2}\left[(\cos\omega t - 1)\cdot\coth\left(\frac{\omega}{2k_BT}\right) - i\sin(\omega t)\right]dt, \tag{2.16}$$

where D_q is the single-mode contribution and D_{bath} is the contribution from the superohmic bath. g_q is the electron-vibration coupling strength, ω is the vibron frequency and the spectral density, $J(\omega)$, of the phonon bath with reorganisation energy, λ, and cut-off frequency, ω_c, is

$$J(\omega) = \frac{\lambda}{2}\left(\frac{\omega}{\omega_c}\right)^3 e^{-\omega/\omega_c}. \tag{2.17}$$

We use this model in Chapter 6 to reproduce the low-T transport characteristics of a molecular GNR with strong electron–vibron coupling.

Spin Transport

In the low-bias regime, there is only enough energy for ground-state transitions to occur which means that electron transport will always pass through the orbitals that make up the ground state. The Pauli exclusion principle determines that no identical particle can occupy the same quantum state, i.e. only two electrons with opposite spin can occupy each orbital. In the case of an empty non-degenerate ground state orbital, an electron with either spin direction could enter the quantum dot but if the orbital is singly occupied the added electron must be of opposite spin. In the latter case the tunnelling current through the device would be completely spin polarised.

If the ground-state orbital is empty the two spin states can be shifted by a magnetic field. The Zeeman effect will split the up and down spin by about 0.12 meV per Tesla (for $g = 2.0$) which can be detected by high-resolution transport spectroscopy. Thus, single-molecule transistors that operate in the described Coulomb regime exhibit intrinsic single-spin sensitivity through spin-to-charge conversion.

Spins in quantum dots were reviewed in 2007 by Hanson and coworkers [140] and coherent spin manipulation were explained (Fig. 2.3f). The outlined idea is to detect a single electron-spin through its charge and not through its small magnetic

moment. In principle, single-spin detection is possible through a scheme proposed by Engels and Loss in 2001 [155, 156], where the quantum dot is tuned in such a way that only the first excited spin state lies within the bias window while the one-electron ground state does not. Only after flipping the spin (e.g. by using microwaves) the quantum dot would be raised into the bias window lifting Coulomb blockade. This shown in the top row of Figure 2.3f.

In practice, this scheme has proven to be challenging. One issue is that microwave heating of the leads can lift the Coulomb blockade long before enough power to induce resonant spin transitions can be applied [157]. Another is the alternating electric field noise that is unavoidably generated with the microwave-frequency magnetic field, which can kick the electron out of the quantum dot through photon-assisted tunnelling processes [158]. However, there are examples of schemes involving spin-dependent tunnel rates to read out electron spin states of quantum dot, that have been demonstrated experimentally [159]. We also note that schemes involving double quantum dots can circumvent the mentioned issues and has allowed coherent control of single electron spins in gallium arsenide [160], but similarly clear demonstrations in equivalent all-molecular double-dot systems have, to our knowledge, not yet been achieved.

Several types of quantum dots and single molecules have been studied using transport spectroscopy, such as gate-confined quantum dot islands e.g. silicon and gallium arsenide, and single molecules or atomic clusters trapped between two electrodes. This work will focus on the latter: single molecules bridging the gap between two electrodes. In general, silicon-based micro- and nanofabrication techniques can be used to make arrays of transistor device frameworks before single-molecules may be added through various techniques. Compounds, such as SMMs [49], porphyrin-based molecules [161], and carbon-based molecules e.g. single-walled carbon nanotubes [162], fullerenes [132], and graphene nanoribbons [163], have been studied by transport spectroscopy in the single-molecule transistor environment.

Fabrication of Single-Molecule Devices

The challenge of connecting a single molecule to two electrodes is not an easy one. First, the electrodes needs to be fabricated with a suitable spacing depending on the size of the single molecule which may be as small as 1 nm for SMMs (but longer for CNTs and GNRs). Second, for the device to work properly the single molecule must be located exactly at the gap and with a weak coupling Γ to each electrode that puts the device into the desirable Coulomb blockade regime. A common way to place single molecules into such gaps is drop casting where a droplet of a solution (of e.g. 0.1 mM [49]) of the compound is applied to the chip, and whereas a few single molecules stochastically finds their way into the gap of one out of thousands of nanojunctions.

Another way is to deposit single molecules on thin gold wires, which are broken so that the molecule can form a bridge between two gold leads. Such metal–molecule–metal junctions can be fabricated either through electro-migration/electro-burning or mechanical-breaking techniques to create a nanometre-spaced gap in a metal wire. The molecule can be introduced either by drop-casting or as part of the mechanical breaking process. Single-molecule transistors that are fabricated in this way are popular tools for performing transport spectroscopy on very small single-molecules such as SMMs because nanometre gaps are possible to make with decent yields. A drawback with such devices is the high atomic mobility of gold, which causes atomic instability in the electrodes. This effect can rather quickly kill the devices, when a current is applied. Also, their bulky features cause screening of the electric field from the gate electrode, which decreases the importance of the gate–molecule coupling. Therefore, a very small separation distance between gate and molecule may be necessary to compensate for screening effects.

Transport spectroscopy on a tunable single molecule is obviously an interesting concept but it does not come without obstacles. Essential questions regarding single-molecule transistors include how to know that there is a molecule in the gap, and how to know that there is only one. Electromigration may create small metal clusters that may cause spurious electronic signatures that closely resemble those

of single molecules [164]. To ensure transport through a molecule, one has to look for molecule-specific transport features, such as magnetic anisotropy, vibrational modes and Kondo effect, or use fabrication methods that prevent the formation of metal clusters, e.g. by the patterning of graphene leads [139].

Multiple molecules in a junction can be revealed by certain features in the conductance map. If two molecules are electrically connected in series inside the junction, the criterion for resonant transport depend on both molecular levels that are inside the bias window. It is highly unlikely that this will occur at zero bias and thus there should not be a conductance peak at zero bias, if two molecules in series are bridging the gap. When two molecules are bridging the gap in parallel, the conductance of both molecules should be added together, and result in a distinct conductance map with one set of features for each molecule. The characteristic features of each map depend critically on the value of Γ (typically 1-10 meV), and this will usually lead to multiple Coulomb diamond patterns, with different slopes for each bridging molecule. The yield of measurable junctions containing a single molecule is typically below 10% [139].

2.4.2 Single-Molecule Magnet Devices

Extensive efforts have indeed resulted in clean devices of single-molecule transistors. The first clear display of a single-molecule transistor was presented in 2000 by Park and coworkers [132]. They made a single-molecule transistor consisting of a single C_{60} molecule trapped between two gold electrodes, and conducted transport measurements. Their results provided, for the first time, clear evidence of coupling between transport and the motion of the C_{60}, manifest as quantised nanomechanical oscillations of the C_{60} molecule in the junction. Their breakthrough triggered considerable effort in the field.

In 2006, Heersche and coworkers and Ralph and coworkers, independently demonstrated transport measurements on a weakly coupled single Mn_{12} SMM in a single-molecule transistor geometry with gold electrodes [49, 165]. Heersche and coworkers observed both Coulomb blockade and negative differential conductance

using gate spectroscopy of discrete SMM energy levels, whereas Ralph and coworkers distinguished the tunnelling current under an applied magnetic field from the tunnelling current under the absence of magnetic field.

An interesting possibility, made feasible by the single-molecule transistor, is to measure the magnetic anisotropy of SMMs. From 2010, Cornia and coworkers investigated the magnetic anisotropy of a single Fe_4 SMM with this technique [152, 166–168]. By tuning the energy levels of the SMM with the gate, they displayed control of the anisotropy in different charge states. Measurements of the position of the resonance line with changing V_g and B, allowed them to relate the conductance to the non-linear Zeeman splitting of the molecule. Moreover, Burzuri and coworkers were able to extract the spin Hamiltonian of a single Fe_4 SMM through transport spectroscopy in a vector field $\vec{B}$ [169]. Some other examples of phenomena that have been explored include electron–vibron coupling [170] and spin excitations in molecular double quantum dots [171].

In 2012, Vincent and coworkers demonstrated electronic read-out of a single nuclear spin of an individual metal atom embedded in a SMM [172]. In this experiment a single bis(phthalocyaninato)terbium(III) ($TbPc_2$) SMM was incorporated into a transistor environment (Fig. 2.4a), and measured through transport spectroscopy. In $TbPc_2$, strong spin–orbit coupling and ligand fields result in a strong uniaxial magnetic anisotropy and a ground-state doublet of $J_z = \pm 6$, and transverse magnetic anisotropy that caused avoided energy-level crossings [173]. Tb^{3+} has a nuclear spin $I = 3/2$ ($I_z = (-3/2, -1, 2, 1/2, 3/2)$) and strong hyperfine coupling splits each ground state $J_z = \pm 6$ into four states $|J_z, I_z\rangle$ (Fig. 2.4b).

At low temperature (the experiments were performed at 0.1 K) and in low magnetic fields, magnetisation reversal of $TbPc_2$ could only occur through QTM at avoided energy-level crossings between states of the same I_z but opposite J_z. It turned out that the reversal of magnetisation in $TbPc_2$ could be read out electronically by measuring the differential conductance as a function of B which jumped at fields coinciding with those of avoided energy-level crossings (Fig. 2.4c,d). The authors explain that the charge transport does not occur through the Tb^{3+} ion

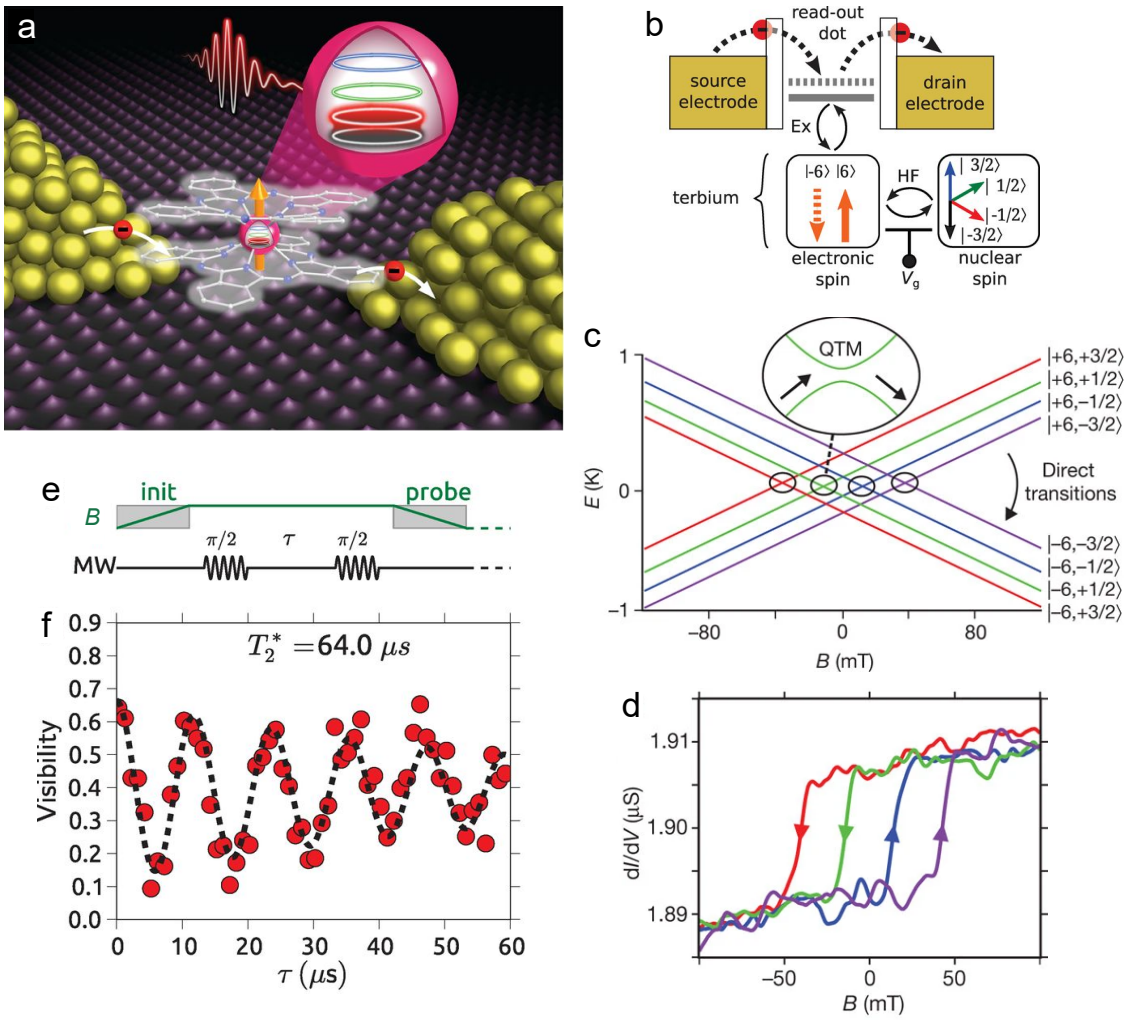


Figure 2.4: Electronic read-out and manipulation of single nuclear spins in a $TbPc_2$ SMM transistor. **(a)** Graphical illustration of a nuclear spin qubit transistor based on a single $TbPc_2$ molecule. The four coloured circles represents the nuclear spin states of Tb^{3+}. **(b)** The three subsystems of the transistor and their coupling: (*i*) a read-out quantum dot (Pc ligand) antiferromagnetically exchange-coupled to (*ii*) the electronic spin which is hyperfine-coupled to (*iii*) The four-level spin qubit. **(c)** Energy-level diagram showing the Zeeman splitting of the two ground states $J_z = \pm 6$ as a function of B. Hyperfine coupling with the nuclear spin of $I = 3/2$ splits the ground states into four sub-states with I_z components equal to $-3/2$, $-1/2$, $1/2$ and $3/2$. Magnetisation reversal can occur through two mechanisms: in small fields QTM at the avoided level crossings with equal I_z but opposite J_z (black circles), or in higher fields a direct relaxation process. **(d)** Measurements of G as a function of B (along the easy axis) with fixed $V_g = -0.9$ V and $V_{sd} = 0$ V, at 0.1 K. The jumps in G are attributed to switching of the magnetic moment of Tb^{3+} with switching fields coinciding with the avoided level crossings from panel **(a)**. Arrows indicate sweep direction of the hysteretic G-versus-B curves. **(e)** Time-dependent B and pulse sequence. The nuclear spin is initialised in the $|3/2\rangle$ state before microwave $\pi/2$ pulses separated by τ coherently manipulates the nuclear spin qubit. The final state is probed by sweeping the field back. **(f)** Ramsey interference fringes obtained using the procedure of **(e)** revealing $T_2^* \approx 64$ μs. Adapted from Refs. [172, 174].

but instead through the π-conjugated Pc ligands which form a molecular quantum dot [172]. The Tb^{3+} couple to the transport channel through its anisotropic magnetic moment mainly via ferromagnetic exchange interaction.

Furthermore, statistics of the magnetisation reversal was obtained by sweeping B back and forth at 0.05 T s^{-1} thousands of times [172]. From these experiments the lifetime of a nuclear spin state was determined to be of the order of tens of seconds. This result introduced $TbPc_2$ as a promising platform for coherent manipulations of a single nuclear spin.

2.4.3 Graphene-Based Devices

As mentioned above, an issue with gold electrodes is the high atomic mobility that causes atomic instability. Moreover, their bulky features cause screening of the electric field from the gate electrode, requiring a very small separation distance between gate and molecule.

Graphene has lower atomic mobility causing higher atomic stability, and causes much weaker screening of the gate electrode than gold, meaning that the separation distance can be much larger [175]. In 2015, Mol and coworkers demonstrated a graphene-porphyrin single-molecule transistor [161]. Electroburning was used to create the nanogap of 1-2 nm in the CVD-grown single-layer graphene sheet [176, 177], on top of a buried silicon back gate separated by a 300 nm thick layer of silicon oxide. The porphyrin molecule was implemented through drop casting. Unlike other relevant electrode materials, graphene showed good compatibility with the molecule because the graphene work-function matches well the discrete molecular energy levels [178].

The authors claim to demonstrate robust single-molecule transistors with high reproducibility and operation at room temperature, and they attribute the enhancement of the technique to the graphene electrodes. The electrode fabrication, single-molecule transistor and measured room-temperature stability diagram is depicted in Figure 2.5; the latter showing signs of Coulomb diamonds indicating that different charge states of the porphyrin can be accessed by tuning V_g. These

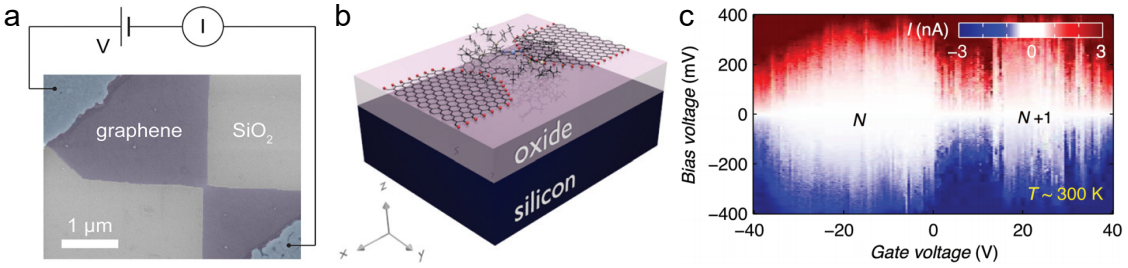


Figure 2.5: **(a)** SEM image of a bow-tie-shaped graphene device with electroburned nanogap. **(b)** Depiction of a graphene-based single-molecule transistor with a heavily doped silicon back gate separated by a 300-nm silicon oxide layer. **(c)** Room-temperature current map as a function of V_g and V_{sd} of a graphene-porphyrin single-molecule transistor. Reproduced from Refs. [161, 177].

results establish graphene-based single-molecule transistors as promising candidates for further transport measurement of single molecules at room temperature, with higher stability than those using metal electrodes. Such graphene-based devices have a central role in this Thesis and will be discussed in detail in Chapters 5 and 6.

2.4.4 Carbon Nanotube Devices

Single-molecule transport spectroscopy on carbon-based nanostructures, and in particular CNTs, have also been dedicated extensive attention. New transport properties of CNTs have been revealed by studying them in the single-molecule transistor geometry. These studies sometimes involve multiple gates with the purpose of confining the long 1D quantum systems into smaller, closed quantum dots.

Using such methods, Cobden and coworkers observed two-fold shell filling in a single-walled CNT quantum dot, and learned that the spin filling of ground states of successive charge states follows a spin pairing pattern, i.e. alternating spin-up and spin-down (Sec. 3.3.2), and observed indications of $K - K'$ subband shells [162, 179]. In contrast, Tans and coworkers observed irregular spin filling in a CNT. They proposed that electrons were always added with spin-up similar to Hund's rule filling (Sec. 3.3.2) to maximise S_z, but compensated by internal spin-flips to avoid gigantic spin polarisations [180].

Such contrasting results on similar physical systems may indicate that spurious effects from sources that are hard to control such as disorder are present, but

which can likely be improved through device fabrication. Moreover, a current misunderstanding at the time was that the spin–orbit coupling in CNTs was negligible. In Section 6.3 we will explore how the interplay between the spin-correlation energy (exchange) and the molecular level spacing impacts on the spin filling of GNRs.

In 2008, Kuemmeth and coworkers discovered spin–orbit coupling in CNTs using single-molecule transport spectroscopy [181]; an important experimental milestone that confirmed theoretical predictions [182]. As shown in Figure 2.6, their results demonstrated how the magnetic field dependence of the one-electron energy levels revealed a spin–orbit-generated zero-field splitting $\Delta_{SO} = 0.37$ meV, and thus deviated from the zero spin–orbit picture. This discovery was mainly attributed to the low degree of disorder in the 'ultra-clean' CNT quantum dot that allowed transport measurement with high energy resolution of about 50 µeV (in contrast to ∼200 µeV in Ref. [179]).

Instead of depositing the CNTs via a solvent, their device was fabricated and cleaned before a defect-free CNT was grown in-situ between the electrodes [181]. This way the CNTs were never in contact with any solvents (which can be sources of contamination) and thus resulted in suspended CNT single-molecule transistors with low internal and external disorder. The low disorder and high energy resolution allowed observing effects that were hidden in the experiments discussed above. In Chapter 6 we present ground-breaking results on non-suspended GNR devices with similar energy resolution as for ultra-clean suspended CNTs that can easily be made using molecular GNRs from solution.

2.5 Quantum Control of Magnetic Single Molecules

2.5.1 Single-Molecule Magnets

With single-nuclear-spin sensitivity established (Sec. 2.4.2) [172], Thiele and coworkers later demonstrated quantum control through coherent manipulation and read-out of a single nuclear spin after implementing microwave-frequency electric fields to an identical single-$TbPc_2$ setup as described above [174]. The experiment (Fig. 2.4e)

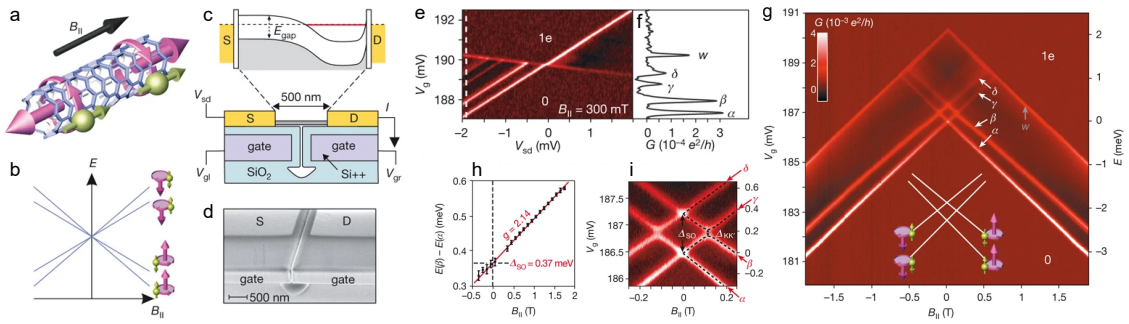


Figure 2.6: Spin–orbit coupling in CNTs. **(a)** The arrows correspond to the current and magnetic moments arising from orbital motion around the CNT (purple) and the magnetic moments due to spin (green). **(b)** Expected energy splitting for a CNT without spin–orbit coupling. All four states are degenerate at zero field but shift as the field $B_{\|}$ increases according to their orbital and spin momentum. **(c)** Schematics of the device. A 500 nm long CNT is connected to source and drain electrodes and is gated from below by two gates. A quantum dot localised over the right gate is created by applying two gate voltages V_{gl} and V_{gr}. **(d)** Scanning electron micrograph of the device without CNT. **(e)** $G = dI/dV_{sd}$ measured as a function of V_g and V_{sd} at $B_{\|} = 0.3$ T, showing the transitions between N=0 and N=1. **(f)** Gate trace obtained with $V_{sd} = -1.9$ mV reveals energy levels α, β, γ and δ. **(g)** G versus V_g and $B_{\|}$ at $V_{sd} = -2$ mV. Inset: observed states with orbital and spin moments assigned to them. **(h)** Energy splitting between α and β extracted from **(g)** (dots). Linear fit yielding factor $g = 2.14$ and Δ_{SO} (red line). **(i)** Magnified view of **(g)** highlighting $\Delta_{SO} = 0.37$ meV and $K - K'$ mixing, $\Delta_{KK'} = 65$ μeV. Dashed lines are calculated. Reprinted from Ref. [181].

involved initialising the nuclear spin qubit in its $I_z = 3/2$ state by sweeping B before manipulating it by pulsing microwaves which couple to the nuclear spin qubit through the hyperfine Stark effect. The final state of the qubit was read out by sweeping back the field. Ramsey fringe experiments (Fig. 2.4f) revealed a qubit dephasing time $T_2^* = 64$ μs which probably was limited by charge noise. The authors predict that more stable gate oxides could increase T_2^* by one to two orders of magnitude.

Their results were the first demonstration of an all-electrical control of a single nuclear spin, and with a concept that should be feasible for transfer to other qubits with large hyperfine interaction. Similar systems without large hyperfine interaction are also interesting provided two subsystems with large exchange interaction are present. In Chapter 5 we explore the magnetotransport properties of such a device based on a dysprosium porphyrin SMM with strong exchange coupling between Dy^{3+} and the porphyrin conduction channel.

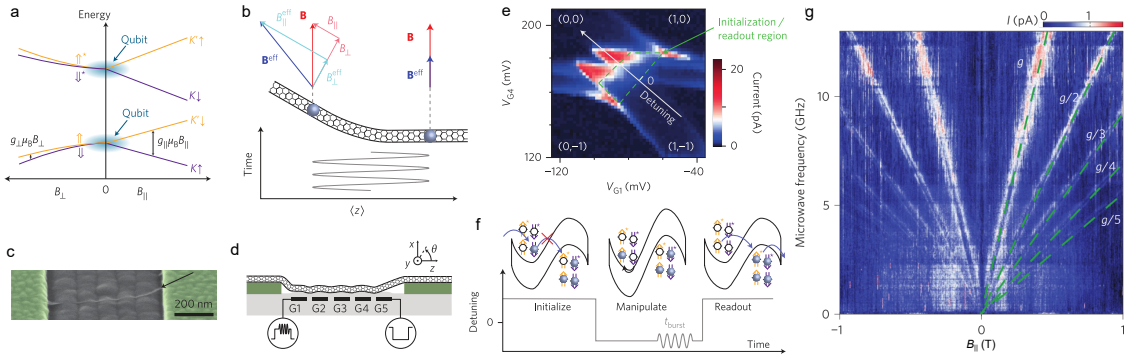


Figure 2.7: EDSR in bent CNT Kramers qubit. **(a)** Single-particle energy levels of a CNT versus $B_{\parallel}$ and $B_{\perp}$ with different splitting of the doublets depending of the field orientation. **(b)** Bend can be used to mediate spin resonance because an electron that is being driven back and forth experiences a periodically varying B^{eff} that can lead to spin resonance. **(c)** Scanning electron micrograph and **(d)** schematic of the CNT device. The electrostatic potential is controlled by gates G1-G5. **(e)** Current through the device versus gate voltages on G1 and G4 close to the (1,-1) $\leftrightarrow$ (0,0) transition. Within the green box Pauli blockade makes the device sensitive to the qubit state. **(f)** Gate voltage pulse cycles for manipulation of qubits and detection of EDSR. **(g)** Current as a function of $B_{\parallel}$ and microwave frequency showing resonance lines at $g \approx 2$ and at subharmonics. Reprinted from Refs. [184] and [185].

2.5.2 Carbon Nanotubes

Quantum control of CNTs have been realised through electrically-driven spin resonance (EDSR) in the transistor geometry. In spin–orbit-coupled systems, time-varying electric fields can substitute the time-varying magnetic fields that can be hard to generate in nanostructures. The idea of EDSR is to use a microwave-frequency electric field to move an electron back and forth, which leads to a spin–orbit-mediated effective magnetic field that can drive resonant spin excitations [30]. Laird and coworkers (and later Pei and coworkers [183]) were first to clearly demonstrate a Kramers qubit in a CNT experimentally [184].

As proposed by Ref. [186], Laird and coworkers used CNTs with bends exhibiting anisotropic splitting of the Kramers doublets with a magnetic field [183, 184]. Each qubit can be regarded as an effective spin+1/2 where the Zeeman splitting depends on the field angle, due to an anisotropic **g** tensor ($g_{\parallel} \neq g_{\perp}$). As shown in Figure 2.7, when an electron is driven back and forth across a bend in the CNT, it experiences a B^{eff} of periodic variation that can lead to spin resonance. At the resonance condition $f = g\mu_B B/h$ a current peak can be observed, indicating spin mixing

(Fig. 2.7g) along with a series of subharmonics possibly due to disorder [187] or anharmonicity of the confinement potential [30, 188].

Quantum coherence in CNTs was demonstrated by measuring Rabi oscillations using pulsed microwaves [184]. The CNT was electrostatically tuned to a double quantum dot (i.e. two qubits in series) initialised at the border between the (1,-1) and (0,0) charge states (see Fig. 2.7e), where the two dots are in resonance but Pauli blockade suppresses the tunnelling current between the dots [140]. As illustrated in Figure 2.7f, the system can then be manipulated by tuning the two qubits out of resonance and into Coulomb blockade before applying a microwave burst that possibly flips one of the qubits. Finally, the system is tuned back to Pauli blockade. Only if a qubit was flipped tunnelling may occur which allows read-out of the event by measuring the current, and by repeating this cycle several times the qubit flip probability can be determined.

Furthermore, qubit dephasing time $T_2^* \approx 13$ ns and the coherence time $T_{echo} \approx 200$ ns have been measured through Ramsey fringe and Hahn echo sequences, respectively [183, 184]. The qubit dephasing rate is attributed to hyperfine interaction with the fluctuating ^{13}C spin bath while T_{echo} is likely limited by charge noise [183]. The large hyperfine coupling strength of ~ 0.16 μeV is consistent with other measurements [185, 189] but is larger than theoretical predictions [190]. Perhaps other dipolar hyperfine interactions, e.g. from nearby magnetic-atom contamination, cannot be ruled out as an additional source of qubit dephasing. The values for T_2^* and T_{echo} are similar to those in InAs and InSb nanowires [191, 192] but shorter than some other semiconductor spin qubits, such as GaAs [193], Si [194] or nitrogen-vacany (NV) centres in diamond [195]. Therefore, although quantum control in CNTs has been demonstrated they can not yet compete with the best qubits available.

Evidently, the electrostatic environment of the CNT quantum dot dictates many of its electromagnetic properties. Based on the discussion above, it seems likely that disorder, in the form of e.g. symmetry-breaking or local defect potentials, has a large impact on the CNTs. It is interesting to observe such contrasting results in

relatively similar experiments because they imply that very small changes in the environment such as defects can lead to very different phenomena.

Vice versa, the results demonstrate these devices' extreme sensitivity to fluctuations in their environments; a feature that can be utilised for sensors that outperform existing technologies. When we fully understand the quantum-dynamical properties of single-molecule devices, we could imagine the ability to manipulate and control them to create devices with tailored quantum properties for applications. One idea could be controlled implementation of defects in the electrostatic vicinity of an ultra-clean quantum dot to tailor its properties in certain voltage ranges. Another highly interesting approach would be the combination of GNRs with SMMs, by decorating GNRs, with weak intrinsic magnetisation, with SMMs to create strongly magnetic and highly conductive hybrid quantum systems (Fig. 1.1).

2.6 Perspectives and Outlook

From the material presented in this Chapter, the reader will have noticed that, because the experiments are extremely challenging, there is still very little connection between the magnetic states of molecular clusters and the electronic conduction properties. In particular, the relation between one central characteristic of single-molecule magnets, namely the magnetic anisotropy, and the resulting spin transport properties remains unexplored. Moreover, while the electronic spin properties of carbon nanotubes have been explored in detail, and their possible usage in quantum systems has been defined, there is still no clarity about the possible existence of ferromagnetic spin states in graphene nanostructures, and in graphene nanoribbons in particular. While carbon nanotubes have shown disappointingly short spin-coherence times, graphene nanoribbons display edge states with coherence times up to microseconds at room temperature, and the interest of their possible applications in quantum devices has thus soared. In the next Chapters we will thus describe the apparata necessary for such investigations, as developed during the course of this thesis, and we will then dedicate ourselves to the investigation of these outstanding scientific problems.

3

Experimental Techniques and Development of Instrumentation

Contents

3.1 Introduction 40
3.2 Cantilever Torque Magnetometry 40
3.2.1 Torque Detection of Magnetic Anisotropy 41
3.2.2 Fabrication of Cantilever Torque Magnetometers 45
3.2.3 Sample Preparation 46
3.2.4 Torque Measurement Techniques 47
3.3 Millikelvin Transport Spectroscopy 54
3.3.1 Instrumental Setup 54
3.3.2 Transport-Spectroscopic Technique 57
3.4 Fast-sweeping Superconducting Magnets 62
3.4.1 Magnetic Fields and Forces of Solenoids 64
3.4.2 Degradation and Training of Composite Superconductors 67
3.4.3 Coil Construction 68
3.4.4 Design and Fabrication of Fast-Sweeping Superconducting Magnet Systems 69
3.4.5 Testing and Proof-of-Concept Demonstration 71
3.5 Triangular-Waveform Magnetic Field Amplifier 72
3.6 Conclusions 74

3.1 Introduction

In this Chapter we will establish the experimental techniques used in the rest of the Thesis, and discuss the development of novel instrumentation. We will start by looking at the development and use of cantilever torque magnetometry (CTM) which is central in Chapters 4 and 5. The following Section will discuss the development of fast-sweeping superconducting magnets, before establishing the experimental technique of millikelvin transport spectroscopy that is central in Chapter 6. Finally, the prospects of a novel magnetic field amplifier will be outlined.

3.2 Cantilever Torque Magnetometry

An accurate understanding of the magnetic anisotropy of molecular nanomagnets is a prerequisite before proceeding to any quantum information applications using such materials. Because magnetic anisotropy by definition is spatially dependent, experimental techniques to unravel its information are often angular-resolved on single-crystals. Several techniques offer such capabilities but less frequently used cantilever torque magnetometry (CTM) offers some unique features that is extremely helpful in measuring magnetic anisotropy in a wide variety of compounds.

The most common technique in the research field is single crystal magnetometry performed in a superconducting quantum interference device (SQUID) magnetometer [196]. This technique offers a good sensitivity but can only resolve magnetic anisotropies that are collinear. Electron paramagnetic resonance (EPR) [197] and nuclear magnetic resonance (NMR) [198] offer better sensitivity but are often limited to low temperatures and solutions, respectively. Polarised neutron diffraction is another powerful technique that can give access to the magnetisation density of individual crystallographic sites [199], but require large crystals and large-scale facilities to produce neutron beams [3].

CTM is an excellent alternative to the techniques mentioned above, especially for measuring samples with high magnetic anisotropy. Its major advantages are its extreme sensitivity to magnetic anisotropy and its ability to disentangle noncollinear

anisotropy contributions. Therefore, CTM enables access to information about all seven crystal systems. Furthermore, all kinds of magnetic ions can be investigated regardless of the parity of the spin which, in contrast, may complicate the use of EPR. The main disadvantage of CTM is that measurements may yield a number of solutions equal to the number of noncollinear anisotropy contributions, and thus require complimentary experiments or theoretical calculations to provide an unambiguous solution [3].

CTM also offers an experimental setup that can be created in many laboratories, with few requirements of instruments for cryogenics and data acquisition. Although this thesis will focus on CTM at low temperature, experiments at higher temperature are possible, up to room temperature, to populate higher energy levels. Moreover, CTM in combination with microwaves have been used to detect electron spin resonance [200, 201].

This Thesis will focus on low-temperature measurement of magnetic anisotropy through the magnetic field dependence of a magnetic torque signal generated in the magnetometer - either as a function of the field angle or the field magnitude. In Chapter 4 studies of a variety of lanthanide-based SMMs will be presented. The present Section will establish the relevant theory and working principles of CTM, discuss the fabrication of a home-built CTM device and different measurement techniques. We begin with the theory.

3.2.1 Torque Detection of Magnetic Anisotropy

Cantilever torque magnetometers generally consist of a cantilever upon which a sample can be placed. In principle, when subjected to a B field the sample will generate a torque (or a force) that will depend on certain magnetic properties of the sample, such as its anisotropy or hysteresis. The generated torque will bend the cantilever. Thus, this deflection contains information about the magnetic properties of the sample that can be measured by detecting the deflection. The two most popular detection methods are optical interferometry and capacitive detection.

Our cantilever torque magnetometer consists of a metal cantilever and an underlying parallel metal plate which are electrically insulated from each other. This design enables capacitive detection of the cantilever deflection. The capacitance, C, between the plates is a function of the electrical permittivity ε, the area, A, of the projection of one plate onto the other, and of the distance, d, between them, and is given by:

$$C = \frac{\varepsilon A}{d}. \tag{3.1}$$

Magnetic torque, ζ, is given by

$$\zeta = \mathbf{M} \times \mathbf{B}, \tag{3.2}$$

where $\mathbf{M} = (M_x, M_y, M_z)$ is the bulk magnetisation and $\mathbf{B} = (B_x, B_y, B_z)$ is the homogeneous magnetic field (with magnitude B). For small deflections, Δd, of the cantilever, ΔC, (causing only a small change from the zero-field distance d_0) it is often assumed that the system approaches a linear-response regime in which ΔC is proportional to ζ: [202]

$$\Delta C = C_B - C_0 \propto -\zeta, \tag{3.3}$$

and

$$\frac{\Delta C}{C_0} = -\frac{1}{d_0/\Delta d + 1}. \tag{3.4}$$

In the linear-response regime: [202]

$$\Delta d = K\zeta, \tag{3.5}$$

where K is a parameter determined by the mechanical properties of the cantilever and the mass of the sample. The relationship between the capacitance and the torque (and thus also the magnetisation) can be obtained by inserting Equation 3.5 into Equation 3.4:

$$\zeta = \frac{d_0}{K}\left(\frac{C_0}{C} - 1\right), \tag{3.6}$$

after the substitution $C_0 + \Delta C = C$. However, the task of determining $\mathbf{M}$ from ΔC requires an accurate estimation of the ratio d_0/K which is challenging for a number of reasons. Mainly because an accurate measurement of the mass of the microgram crystal is difficult, but also because d_0 is difficult to measure with sufficient accuracy. Therefore, it is acceptable to consider only the qualitative behaviour described by the field dependence of the torque given by:

$$\zeta = \frac{C_0}{C} - 1. \tag{3.7}$$

Angle-Resolved Torque Magnetometry

Equation 3.2 suggests that a magnetic torque will be induced in any anisotropic sample in which $\mathbf{B}$ is not aligned with $\mathbf{M}$, which by definition would be pinned by magnetic anisotropy to a certain crystallographic direction. Therefore, such a sample placed on the cantilever in a magnetic field may exert a torque on the cantilever to minimise the free magnetic energy F, in principle by turning $\mathbf{M}$ to align with $\mathbf{B}$. A relationship between the torque magnitude ζ, F and the angle φ between $\mathbf{M}$ and $\mathbf{B}$ is given by Equation 3.8: [41]

$$\zeta = -\left(\frac{\partial F}{\partial \varphi}\right)_B. \tag{3.8}$$

If one chooses a reference frame in which $\mathbf{M}$ and $\mathbf{B}$ lies in the xz plane, $\zeta = (\zeta_x, \zeta_y, \zeta_z)$ must be parallel to y. From Equation 3.2, $\zeta_x = \zeta_z = 0$ and ζ_y can be expressed as:

$$\zeta_y = M_z B_x - M_x B_z = B^2 \left(\frac{M_z}{B_z} - \frac{M_x}{B_x}\right) \sin\theta \cos\theta, \tag{3.9}$$

where θ is the angle between $\mathbf{B}$ and the z axis and can be reduced further as the magnetic susceptibility $\chi_{ii} = M_i/B_i$. Such an experiment can thus measure the magnetic anisotropy in the xz plane given by $(\chi_{zz} - \chi_{xx})$. Note that an isotropic contribution to $\mathbf{M}$ would by definition have $(\chi_{zz} - \chi_{xx}) = 0$ and thus Equation 3.9 would give $\zeta_y = 0$. This property causes the extremely convenient feature of CTM of only detecting the anisotropic part of $\mathbf{M}$ and neglecting the isotropic part [41].

Equation 3.9 holds true for paramagnetic samples where both the magnetic anisotropy and **M** depend on **B** and where **M** is well below saturation so that **M** is linear with **B** (low-field limit). ζ_y goes through zero at $\theta = n\pi/2$ with n integer and has extrema at $n\pi/4$ [202]. Despite these formulas, it is often only the **B** dependence of ζ_y is analysed experimentally and not the absolute values of ζ_y because of difficulties in weighing microgram sample crystals with the necessary accuracy. However, important information about the magnetic anisotropy can be extracted from the shape and zero-crossings of ζ_y as a function of θ. Angles θ where ζ changes sign correspond to hard or easy axes of magnetisation in the sample where the rule of thumb is that the slope of the curve through the zero-crossing is larger for the hard axis and smaller for the easy axis.

Deviations from Equation 3.9 may indicate phenomena such as superparamagnetism. As we will see in Chapter 4, most of the measured compounds in this Thesis exhibit a torque response that deviate from the simple picture outlined by Equation 3.9. Both the ultra-low temperature and the exotic nature of the lanthanide complexes are central reasons for the anomalous torque response.

Field-Resolved Torque Magnetometry

An alternative to angle-resolved CTM is to fix the field direction while changing the magnitude. Estimations of the field necessary to overcome the magnetic anisotropy, the so-called 'breaking field', have been measured by aligning **B** close to a hard axis and measuring the peak of ζ as a function of B.

The fields required to overcome the strong magnetic anisotropy of most SMMs are generally of the order of tens of Teslas, much higher than the 6 Teslas available in our laboratory. However, it is often possible to study the magnetic hysteresis using field-resolved CTM. In molecular magnetism it is generally accepted to select the field direction that produces the largest magnetic hysteresis, and for this purpose CTM works very well. By either rotating the sample in a 1D field using rotator stages, or by using a 3D vector rotate magnet, the field can be applied in any

crystallographic direction to find the optimal field direction. Conversion from torque to magnetisation can be done via the scalar version of Equation 3.2:

$$\frac{\zeta}{B} \propto M, \tag{3.10}$$

but the result implies that only the magnetic field dependence of some unit proportional to the magnetisation can be detected this way. Some researchers refer to this quantity as the transverse magnetisation. In this Thesis we quantify M in units of the extremal values of ζ/B, through the relation:

$$M \propto \zeta B_{max}(B\zeta_{max})^{-1}. \tag{3.11}$$

3.2.2 Fabrication of Cantilever Torque Magnetometers

We made our cantilever torque magnetometer after Dr Fadi el Hallak's design as described in his PhD Thesis. We designed the metal parts of the device using Autodesk Inventor and AutoCAD. A copper beryllium alloy (2% Be) was chosen because it is diamagnetic and stiffer than pure copper. CuBe sheet metal was purchased from Goodyear in thicknesses of 25, 50, 75, 100 and 150 µm.

Initially, we attempted to cut metal parts from the thinnest metal sheets using razors and pliers but it proved difficult not to irreversibly bend them. Instead, we used a wet-chemical photo-etching method administered by Paul Pattinson in the Department of Physics. The AutoCAD designs were converted to photo masks by Micro Lithography Services Ltd, which Mr Pattinson used to etch out arrays of parts from the CuBe metal sheets. The magnetometer was then assembled onto a FR4 composite plate and installed in a loading puck. The process in shown in Figure 3.1.

Over time the CuBe surface may oxidise into paramagnetic copper oxide. Such impurities could cause spurious ζ signals of the similar order of magnitude as a sample (not shown). El Hallak and others solved this issue by depositing a layer of gold around the cantilever. Before use we instead submerged the cantilevers into a copper-oxide micro-etchant for up to 10 s before rinsing in water.

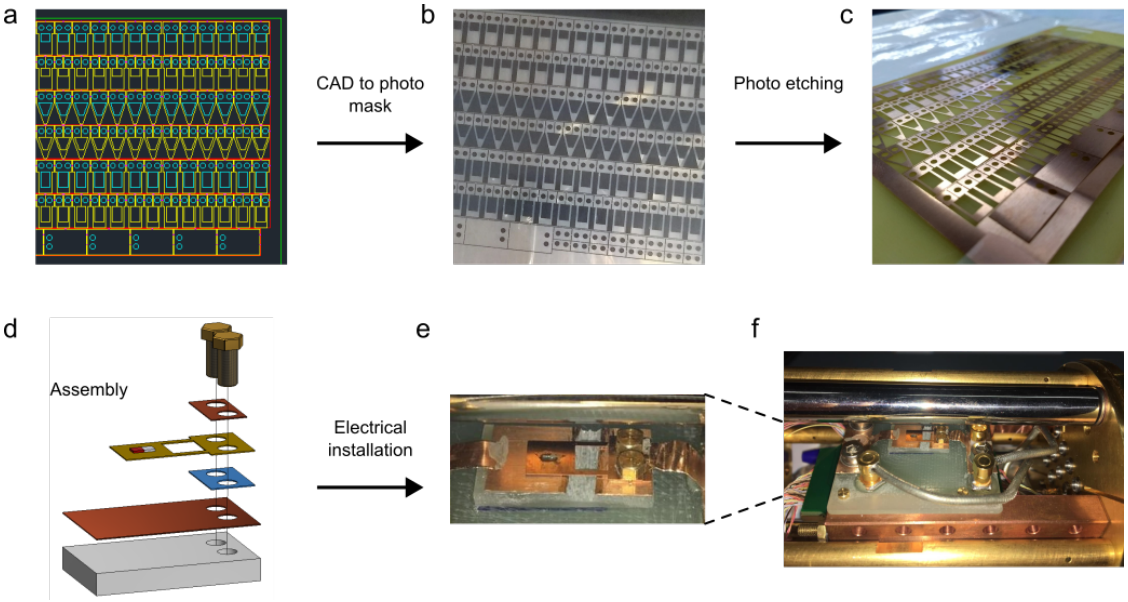


Figure 3.1: Fabrication process of the CTM magnetometer. **(a)** 2D design of photo masks in AutoCAD. **(b)** Photo masks produced from CAD drawings by Micro Lithography Services Ltd. **(c)** Instrument parts were photo etched from copper beryllium metal sheets and photo masks by Paul Pattinson. **(d)** The magnetometer was assembled from the CuBe parts and **(e,f)** onto a home-build FR4 mount providing electrical connection, and finally installed into a refrigerator puck.

3.2.3 Sample Preparation

The nature of magnetic anisotropy demands full spatial control of the unit cell of the sample in order to characterise the phenomenon. Therefore, one sample requirement is that the compounds can be crystallised as single crystals, which must also be of a size that make them possible to handle - typically with a thin needle and cryogenic-grade grease. Special care must be taken when choosing the crystal to measure to ensure that it truly is a single crystal. Any polycrystals, although they may be small, could generate spurious anisotropy signals. Furthermore, the crystal structure of the sample must be resolved and the faces of the single crystal relative to its unit cell must be identified and labelled, typically by face indexing using single-crystal X-ray diffractometry. Finally, the single crystal can be mounted with a suitable crystal orientation on the cantilever, and loaded into a cryostat with a magnet. For the experiments reported in this Thesis, face indexing was performed on a Agilent SuperNova Kappa diffractometer by Dr Dimitrios Alexandropoulos.

3.2.4 Torque Measurement Techniques

General considerations

The important parameters concerning CTM are field direction, field magnitude, field-sweep rate and sample temperature. Field directions can be calculated through a series of intrinsic rotations by proper Euler angles linking the laboratory reference framework with the crystallographic. For example, ZXZ denotes the sequence of a rotation around the z axis, then a rotation around the x axis and finally another around the z axis, relative to the laboratory reference framework. Angular-resolved CTM is usually performed by rotating the field in two or more planes determined by crystallographic arguments which contains magnetically unique axes, e.g. a hard plane and a normal plane which contains the easy axis.

The field magnitude, B, plays more than one part in CTM. First, the level of saturation of magnetisation depends on the field magnitude, as explained above, and angle- and field-resolved measurements are often necessary parts of the anisotropy analysis. Second, from Equations 3.2 and 3.5 the cantilever defection, Δd, is directly proportional to ζ which again is proportional to B. This result is based on the linear-response assumption of the deflection which ultimately serves as an instrumental upper limit on B that depends on the sample and the cantilever thickness. That is, Δd also depends on the susceptibility tensor, χ_{ii}, and the stiffness of the cantilever, and either of these may be changed in order to stay within the linear-response regime at the desired B, by choosing a smaller sample or a thicker cantilever, respectively. It is usually convenient to change the latter because the process of the former can be more involved.

The field-sweep rate has two major consequences. First, higher sweep rates may suppress the number of molecules that undergo QTM, as per the probability of the Landau-Zener tunnelling process. In systems with pronounced QTM, the consequences of increased sweep rates may primarily manifest as larger hysteresis loops with skipped QTM steps. Increased sweep rate also contributes to heat generation in the magnet and the metal parts of the cantilever device. The former is

mainly due to hysteretic losses, and the latter due to ohmic heating in the resistive metal parts caused by eddy currents generated by the changing magnetic field.

The temperature of the sample can have both intrinsic and extrinsic effects on CTM measurements. The intrinsic effects are those of thermal population of molecular energy levels with different anisotropy and probability of magnetisation reversal via thermally activated mechanisms or QTM. Such phenomena could manifest in the torque, as they affect the total magnetization of the crystal.

The extrinsic effect is that of thermal expansion and contraction of the cantilever device which tend to change the separation distance, d, between cantilever and base plate and thereby affect the measured C. There is no simple way of separating the change in d due to thermal expansion and that of magnetic torque, so careful temperature control is key to accurate torque measurements. At millikelvin temperatures accurate control of the sample temperature is challenging and a significant source of error. However, parts of this error can be eliminated by waiting for a suitable time for T to stabilise after sweeping B. This was done throughout for the angle-resolved CTM presented in Chapter 4 and between sweeps in the hysteresis measurements.

All CTM experiments were carried out in an Oxford Instruments Triton dilution refrigerator with a base temperature of 25 mK (see Sec.3.3.1). This cryostat was equipped with a superconducting 3D vector-rotate magnet (VRM) kept at $T = 4$ K consisting of three orthogonal coil pairs, two smaller coil pairs Y and Z capable of generating fields up to 1 T in the yz-plane (see Fig, 3.2), and one large coil pair, X, with a capacity to generate fields up to 6 T along the x-axis. Because B fields are additive, together they can generate B-fields in any direction but limited to $B = 1$ T in a sphere for 360° vector rotation. Each coil pair were powered by a MercuryIPS power supply. The power supply changes the current in the coils to attain a set $\mathbf{B}$ before short-circuiting the coils to maintain a persistent current and thereby a very stable $\mathbf{B}$.

The torque magnetometer was loaded with its cantilever hanging vertically downwards along x to eliminate deflections caused by gravity. In contrast to

commonly reported CTM measurements, the device was always fixed along x while **B** was changed. Cantilever deflections were detected by an Andeen Hagerling 2550 capacitance bridge located outside the refrigerator connected directly to the sample. The bridge measures C by balancing and internal capacitor through applying an AC voltage of up to 15 V to the device. It acquires C values with a sampling rate of 1 kHz and outputs the average value after a user-specified time of one to nine seconds. The highest level of accuracy, nine seconds, was always used for angle-resolved CTM, but for hysteresis measurements four or five seconds were used as a trade-off between acquisition speed and accuracy.

The measurement-control interface was home-written in Python and ran using QTLab. This interface could control both the dilution refrigerator, VRM and capacitance bridge simultaneously. We wrote programmes for analysis and visualisation of all torque data in MATLAB. Visualisations of molecules and crystal structures were produced using Mercury.

Normal-Plane Angle-Resolved CTM

Normal-plane angle-resolved CTM is the technique were B is rotated in the xz-plane as illustrated in Figure 3.2c. This is the standard angle-resolved CTM technique and requires only a 1D magnet and a single-axis rotator. The technique probes the magnetic anisotropy of the crystal plane parallel to xz and requires a manual remounting of the crystal to probe a different crystal plane. Misalignments of the sample may cause significant errors but these can be mitigated by using a 3D VRM that allows adjusting the rotation plane in-situ.

The two planes orthogonal to xz, namely xy and yz, can also be probed if using a 3D VRM (or triaxial rotators). Such experiments have been done for this Thesis to explore transverse anisotropy. An example of normal-plane angle-resolved CTM is shown for a $CoTiO_3$ sample in Figure 3.3. Here **B** was rotated in all three orthogonal planes. In this Thesis, $CoTiO_3$ will only be used for demonstration of CTM because the sample belongs to the group of Prof Radu Coldea at the Department of Physics who will carry out the analysis and characterisation.

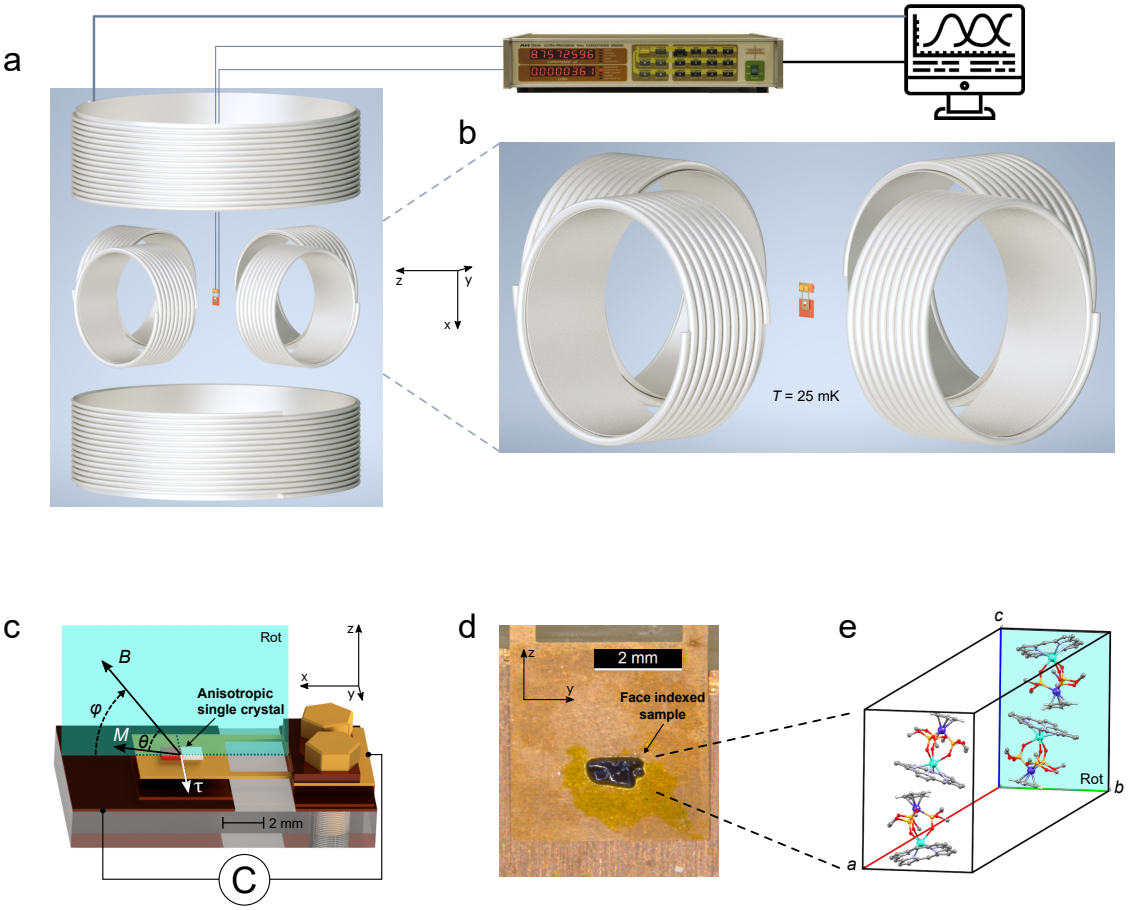


Figure 3.2: Graphical representation and schematics of the CTM experimental setup. **(a)** The 3D VRM consists of three coil pairs. The torque magnetometer is placed in a cylindrical puck (not shown) which is brought up to align with the magnets. The magnetometer is electrically wired directly to an AH2550 capacitance bridge through the top of the fridge. **(b)** Zoom-in of **(a)** highlighting the position of the magnetometer. **(c)** The torque magnetometer capacitively detects the torque-driven deflections of the metal cantilever caused by misalignment of **B** and **M**. These graphics were designed and rendered using Autodesk Inventor. **(d)** Photograph of a terbium complex single crystal mounted with grease onto the cantilever. **(e)** The unit cell of the oriented crystal with a rotation plane, Rot, that corresponds to the one in **(c)**.

Arbitrary-Plane Angle-Resolved CTM

The 3D VRM's ability of generating a field in any direction enables a powerful CTM technique, i.e. to scan any crystal plane of interest. Because the orientation of the unit cell relative to the lab frame is known due to XRD face indexing, field vectors of any arbitrary plane can be calculated using the Euler-angle method described above and sent to the magnet to rotate the field in any crystal plane of choice. This technique was invented for the present Thesis and an example measurement is

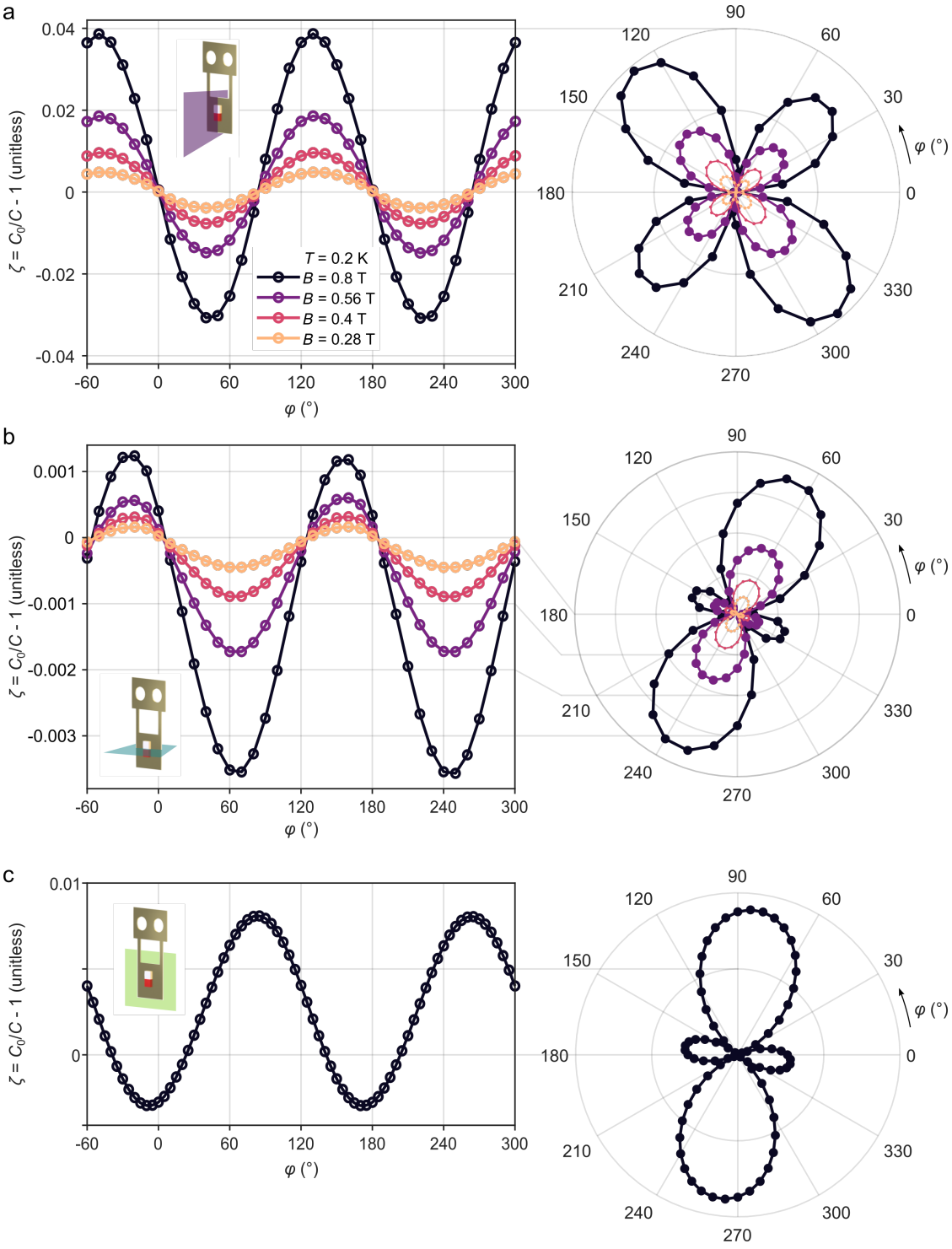


Figure 3.3: Example of torque curves produced through normal-plane angle-resolved CTM of a $CoTiO_3$ compound at $T = 0.2$ K. The panels on the left contains ζ versus ϕ plotted in normal axes and the right panels contain the same data plotted in polar axes. **(a)** shows the torque response detected in the xz plane, **(b)** the yz plane and **(c)** the xy plane.

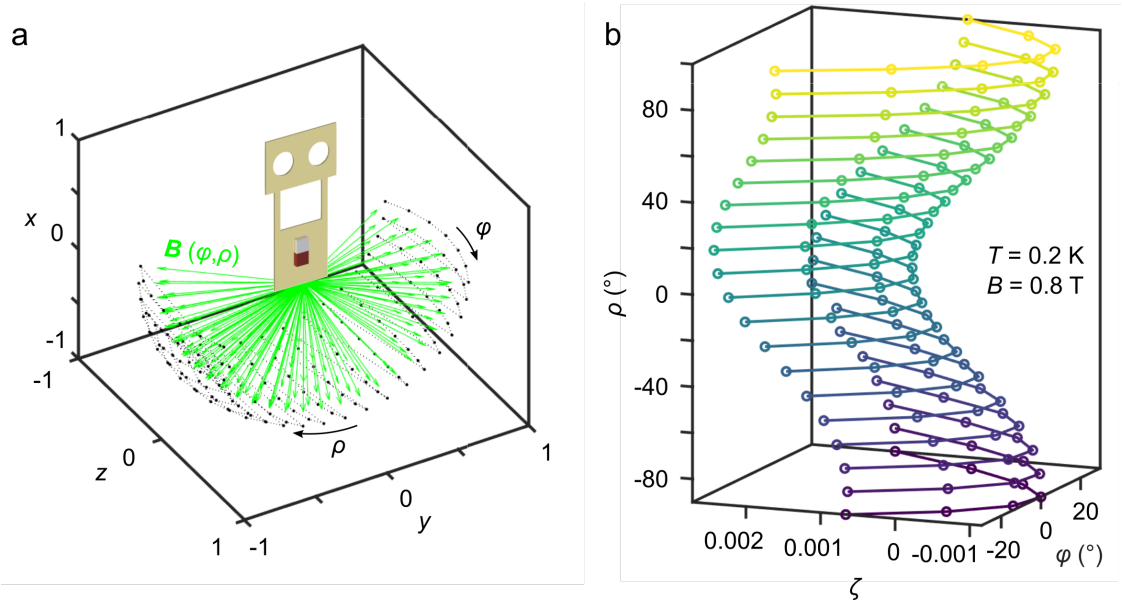


Figure 3.4: Example of arbitrary-plane angle-resolved CTM of a $CoTiO_3$ compound at $T = 0.2$ K. **(a)** Field vectors, $\mathbf{B}(\phi, \rho)$, calculated using the Euler angles ϕ and ρ. $\phi = 0°$ coincides with $z = 0$ and $\rho = 0°$ coincides with $y = 0$. **(b)** The resulting torque curves as functions of ϕ and ρ produce a torque surface that is sinusoidal in both ϕ and ρ and contains a saddle point for $\mathbf{B}(0°, 10°)$.

shown in Figure 3.4. Although novel and unique, the results of this technique has proven difficult to analyse because the total torque is caused by a combination of direct and transverse terms but only ζ_y is detectable. Despite the complex analysis, a terbium complex was investigated using this method (Sec. 4.2).

Field-Resolved CTM

In this Thesis, field-resolved CTM is used for measuring hysteresis. In this technique, the direction of **B** is specified and its magnitude is swept between positive and negative limits, e.g. ± 1 T, at a sweep rate of ≤ 0.125 T/min. C is measured continuously (sampling rate of one measurement per five seconds) and converted to torque using Equation 3.7 and from ζ to M using Equation 3.2. Before starting the hysteresis measurement, $C_0 = \bar{C}$ is calculated where $\bar{C}$ is the average of 25 zero-field measurements of C. To reduce the noise in the obtained M curves, a multiple of B-sweep cycles were usually performed and then averaged using a self-written MATLAB protocol. A demonstration hysteresis measurement is shown in Figure 3.5.

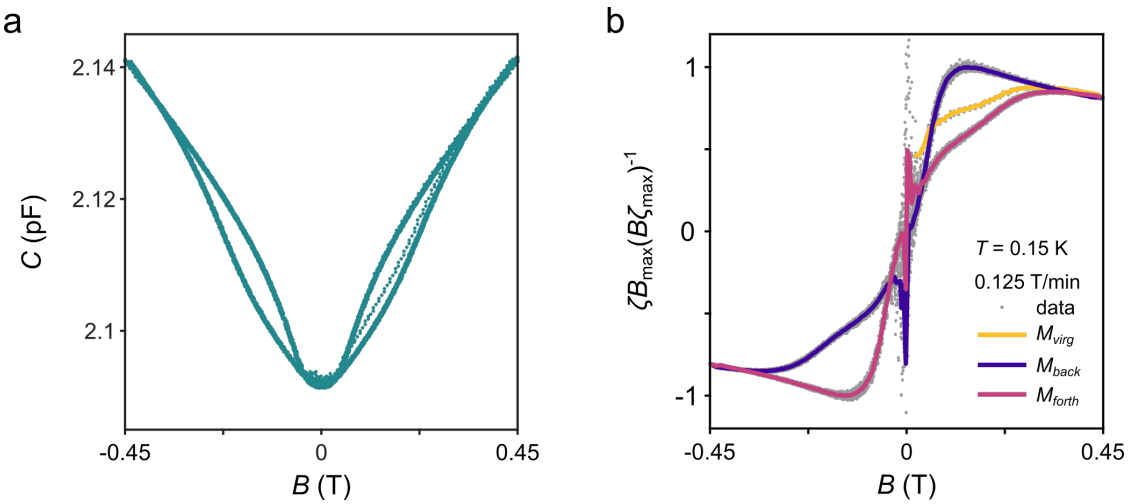


Figure 3.5: Example of a field-resolved hysteresis CTM of a Dy_2-hfac compound at $T = 0.15$ K and at a sweep rate of 0.125 T/min. **(a)** Hysteretic C versus B measured by the capacitance bridge. B was swept back and forth 50 times between ± 0.45 T at an angle, $\phi = -10°$ in the xz plane (see Fig.3.2c). **(b)** Magnetisation versus B calculated from C in **(a)** using Eq.3.2 via Eq.3.7. The quantity on the vertical axis is represented in units of its own maximum value. The window-averaged virginal, back and forth magnetisation curves are plotted in solid lines of different colours on top of the grey data points. This sample is analysed in Section 4.5.

The peaks around $B = 0$ in Figure 3.5b is a consequence of $\zeta = 0$ for $B = 0$ as described by Equation 3.2 and the subsequent division by B (Eq. 3.10) that approaches zero results in diverging magnetisation values. Consequently, resulting zero-field peaks are often removed for clarity because their values are highly prone to noise and does not represent information of physical value. For these reasons, CTM is an unsuitable technique for measuring remanent magnetisation.

Field-resolved CTM can be performed at different T to investigate the presence and size of hysteresis loops below the blocking temperature. The experimental setup allows such measurements between temperatures 25 mK and 30 K although the T control below 100 mK and above 1.5 K is poor. The former range due to heat generation caused inside the sweeping magnet and the latter range due to poor cooling power from the dilution refrigerator above 1.5 K. For $T < 100$ mK the fluctuations in T during the sweeps can be up to 75 mK, which constitutes a large ratio compared to the present thermal energy. We suspect these create spurious C signals due to thermal expansion of the device and T-dependent

susceptibility of the sample.

3.3 Millikelvin Transport Spectroscopy

3.3.1 Instrumental Setup

All transport spectroscopy experiments reported in the present Thesis were done at millikelvin temperature inside a Triton Cryofree dilution refrigerator from Oxford Instruments. This refrigerator was equipped with a superconducting 3D vector rotate magnet (VRM). The electronic measurements were obtained using ultra-low-noise direct-current electronics consisting of DC lines inside the refrigerator and home-built room-temperature electronics and switch boards. We employed standard transport measurement techniques controlled via self-written interface programmes. The following Sections will elaborate on these aspects.

Dilution Refrigeration

The Oxford Instruments Triton dilution refrigerator (DR) uses 80 L of mixture of ^{3}He and ^{4}He (^{3}He concentration around 20%) to reach operating temperatures down to 20 mK. To achieve such extreme temperatures, the cryostat is effectively two refrigerators in one: a pulse-tube cooler (PTC) and a dilution cooler (Fig. 3.6). With a high cooling power at higher T, the PTC is the workhorse of the system. It is situated at room temperature and serves to cool the PT1 plate and PT2 plate to 50 K and 4 K, respectively. The PTC drives the pre-cool circuit until $T < 20$ K below PT1.

When the system is pre-cooled, the helium mixture is transferred from the pre-cool circuit to the dilution circuit. Mixture gas is released in small bursts from a storage tank and each burst of gas is condensed before the next burst is introduced. The pressurised (~ 2 bar) mixture gas is cooled by the PTC before reaching the PT2 plate. The condensation happens in the Joule-Thomson stage were the mixture is allowed to expand isenthalpically and condense inside the highly efficient heat exchanger. Below this stage the mixure is cooled below 0.1 K before reaching the

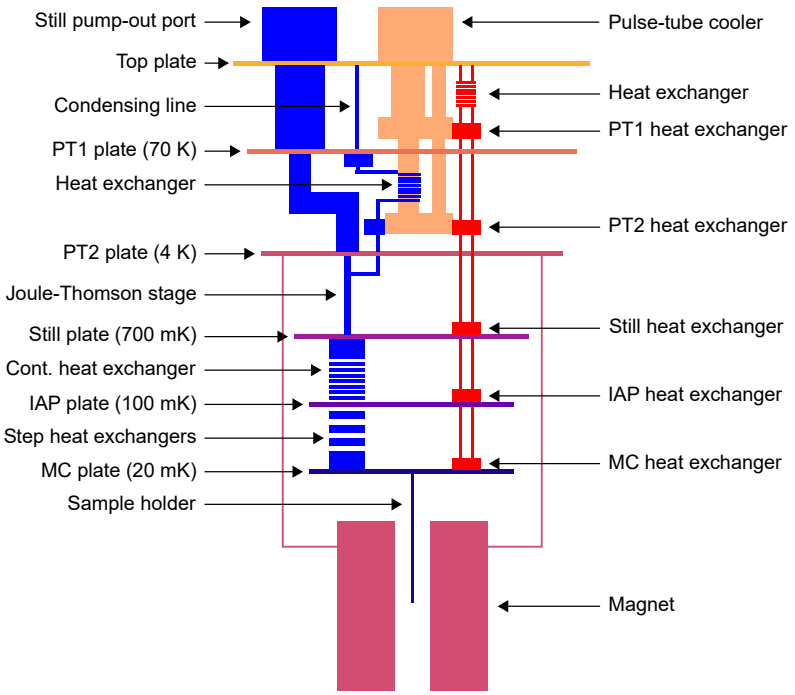


Figure 3.6: Schematics of the Triton DR. The pulse-tube cooler is depicted in orange, the pre-cool circuit in red and the dilution circuit in blue. The different plates and their respective temperatures are also indicated. The magnet (violet) is thermalised via the PT2 plate. Adapted from the Triton User Manual by courtesy of Oxford Instruments.

mixing chamber where dilution cooling takes place. Dilution cooling in the mixing chamber cools the MC plate and the sample holder down to 20 mK.

The ^{3}He-^{4}He phase diagram (Fig.3.7) shows that the mixture separates into two phases below 0.876 K: a lighter phase approaching unity concentration of ^{3}He and a heavier superfluid mixture diluted with 6.6% of ^{3}He below 0.1 K. Inside the mixing chamber therefore, the ^{3}He-rich liquid floats on top of the ^{4}He-rich liquid. ^{3}He atoms acts as a gas in the diluted phase that forces a flow of ^{3}He from the ^{3}He-rich phase into the diluted phase. The enthalpy of diluted ^{3}He is larger than that of pure ^{3}He and must be compensated for by drawing heat from the environment. Such is the working principle of a DR, which explains what happens inside the mixing chamber[203].

Superconducting Vector Rotate Magnet

The superconducting 3D vector-rotate magnet (VRM) is briefly discussed in Section 3.2.4 and depicted in Figure 3.2. Inside the DR, the magnet is placed

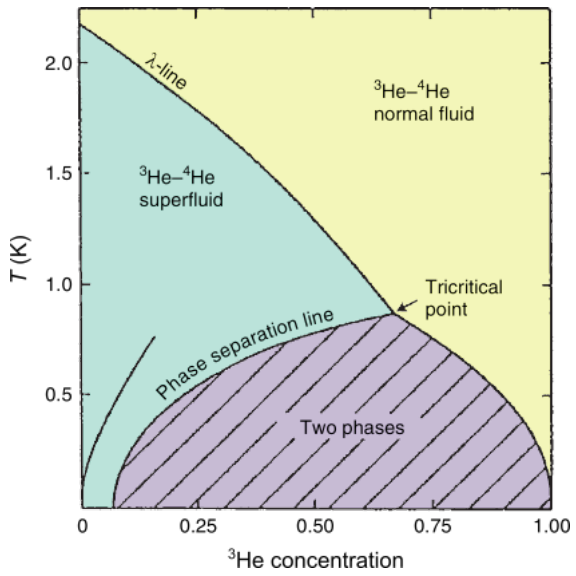


Figure 3.7: Phase diagram for a mixture of ^{3}He-^{4}He at the saturated vapour pressure. Adapted from Ref. [203].

so that its bore and central magnetic field aligns with the sample holder. However, it is thermally connected to the PT2 plate, is mainly cooled by the PTC and therfore holds $T \approx 4$ K. This is necessary because the heat generation in the operating magnet requires the cooling power of the PTC (1.5 W at 4.2 K), higher than what the dilution unit can provide ($\sim$12 μW at 20 mK).

The coil material is copper-clad NbTi filament wires. At zero field and low current densities NbTi is superconducting below 9 K. However, at this temperature the X coil pair readily quenches for $B > 6$ T with its associated current density (Y and Z coils were not tested).

Electronics and Circuitry

The electronic setup used to perform millikelvin transport spectrocopy is shown schematically in Figure 3.8. The circuit begins with the home-written interfacing programme executed by QTLab that signals to the optical signal generator. This unit creates optical pulses of digital information and feeds it to a Delft Box - a home-built low-noise electronics unit. Here, two digital-to-analog converters (DACs) produce input signals as bias voltage, V_{sd}, and gate voltage, V_g. V_{sd} in the range $\pm$0.2 V (less with voltage divider) and V_g in the range $\pm$30 V can be applied to the

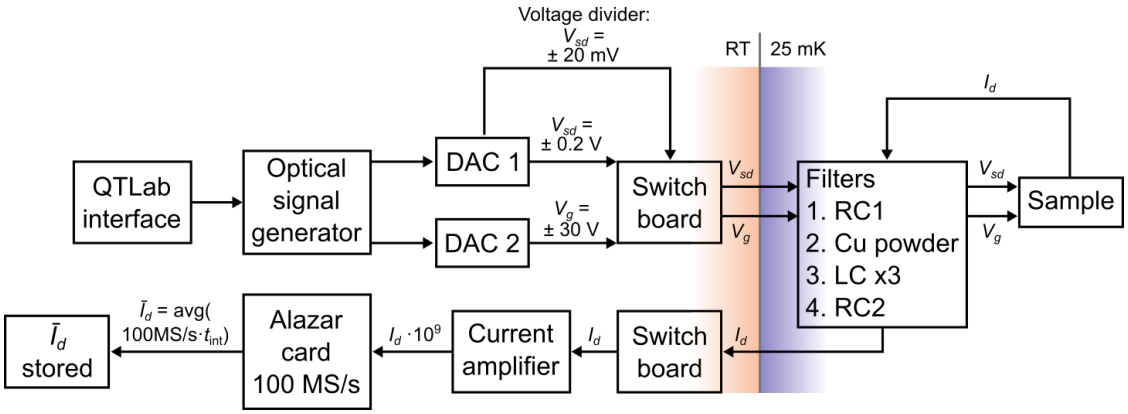


Figure 3.8: Schematic view of the DC electronics setup for mK transport spectroscopy.

switch board. This unit provides simple switching between different devices and crucial protection against voltage spikes that otherwise might destroy the sample.

From the switch board the input signals flows through the internal circuitry of the Delft box before entering the DR. The current is cooled down by two sapphire heat sinks at the PT2 plate and two at the MC plate after which it enters a series of low-pass filters. These consist of an RC filter, a meandering-line copper powder filter, three LC filters (covering different frequency ranges), and another RC filter. The input signals then reaches the sample through a 48-wires NanoD connector. The sample chip is wire-bonded to a 48-pin chip holder that sits on a home-built printed circuit board.

The output current signal, I_d, flows through the described components in reverse order until it reaches a current amplifier (1GAmp/1A amplification) in the Delft Box. The amplified output signal goes through a coax cable to an Alazar data acquisition card with sampling rate 100MS/s. The QTLab interface sets an integration time, t_{int}, for which the Alazar card samples I_d before calculating the average and storing its value.

3.3.2 Transport-Spectroscopic Technique

In this Thesis we performed transport spectroscopy on single-electron transistors (SETs) to probe the energy levels of the single-molecule channel. The underlying physics of this technique was discussed in Section 2.4.1. The present Section will

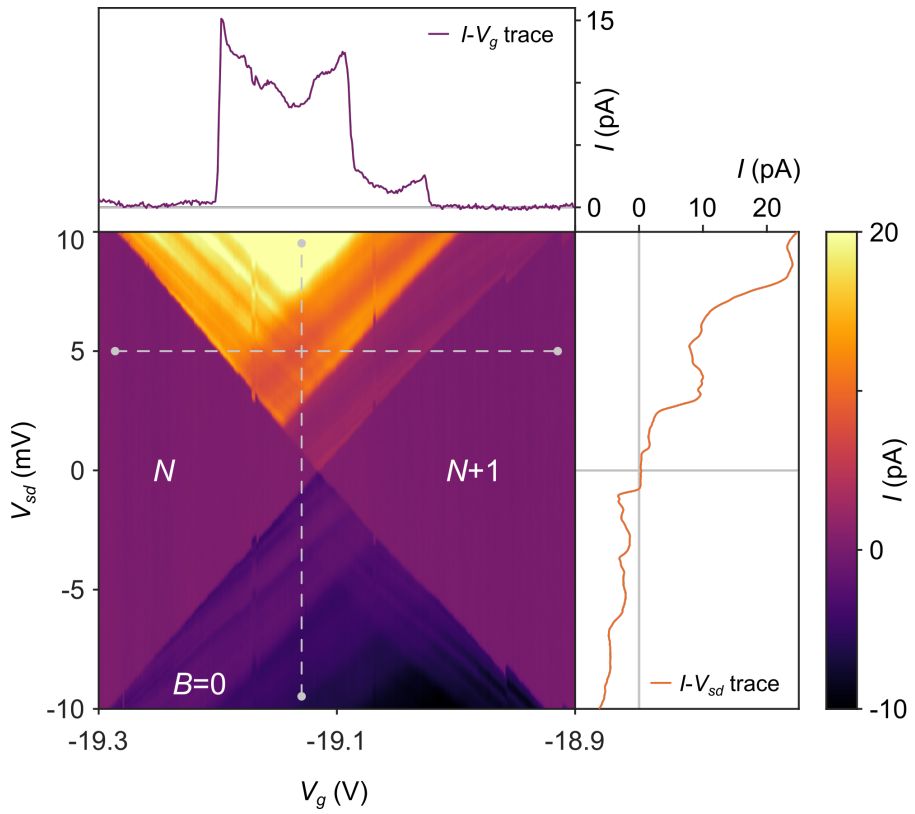


Figure 3.9: Example of a stability diagram of a MGNR transistor (see Ch.6) with I-V_{sd} and I-V_g traces taken along the dashed vertical and horizontal lines, respectively. The data was acquired at zero field and the leakage current, i.e. $I(V_{sd} = 0)$, was subtracted.

outline the specific techniques of the experiments performed in this Thesis. These include obtaining stability diagrams (SDs), measuring I-V_{sd} traces in and without the presence of a B-field and I-V_g traces, which are all exemplified in Figure 3.9. The conductance is calculated from the numerical derivative $G = \partial I/\partial V_{sd}$. The results of such experiments are discussed in Chapter 6.

Bias traces

A I-V_{sd} trace, or bias trace, is a fundamental transport spectroscopic technique. With fixed V_g, V_{sd} is swept in a predefined range with a predefined resolution. At every V_{sd}-setpoint the system remains fixed for a predefined integration time, t_{int}, while the Alazar samples and averages the drain current, I_d, (see Sec.3.3.1) before moving to the next V_{sd} value. In theory, the resulting I-V_{sd} plots as current-steps whenever the bias window overlaps with a new QD level and horizontal elsewhere

(or as peaks if G is shown instead of I), but in practice a superimposed monotone change in I stemming from coupling with the environment is usually observed. Importantly and conveniently, because single-electron transport is measured, the energy of a QD level can be directly obtained from the relationship $\mu = |e|V_{sd}$, e.g. a resonance observed at V_{sd}=1 mV correspond to μ=1 meV.

Series of I-V_{sd} traces over a range of B can reveal how QD levels shift or split with B. Such measurements constitute an important part of this Thesis (see Sec. 6.3. Here, B was set to sweep between -6 and 6 T while I-V_{sd} traces were acquired continuously. Because B was swept slowly (0.05 T/min) and a I-V_{sd} trace is acquired in a few seconds, the field change during each sweep were negligible.

Stability diagrams

SDs are maps generated by multiple I-V_{sd} traces obtained over a range of V_g values displayed side-by-side. The main purpose of SDs in the Coulomb regime is to map out the QD's energy levels. SDs represent the I_d as a function of V_{sd} and V_g where V_{sd} modifies the Fermi energy of the leads and V_g modifies the QD energy levels. In this way resonant sequential electron transport can be initialised either through adjusting V_{sd} so the QD level lies within the bias window, or by V_g-tuning the QD level into the bias window. In practice, V_g is set and held constant before a I-V_{sd} trace is acquired. This process is repeated for the whole range of V_g values and the traces are displayed side-by-side. SDs obtained with a constant B field can reveal magnetic effects in the QD.

Gate traces

I-V_g traces, or gate traces, are similar to I-V_{sd} traces except that V_g is swept while V_{sd} is fixed. There is no 1:1 relationship between V_g and the QD levels but it can be calculated from the lever arm β (see Sec.2.4.1). For this Thesis, I-V_g traces with $V_{sd} = 0$ were mainly used to measure the leakage current (e.g through the dielectric between sample and gate electrode) that was subtracted from the SDs.

Time traces

I-t traces, or time traces, are useful when investigating the noise characteristics of a device. Both V_{sd} and V_g are held constant while I is measured back-to-back for a given time. Such measurements are further discussed in Section 6.4.

Ground-State Spectroscopy

In general, spin filling of quantum dots is determined by the exchange energy (spin correlation) and the inverse density of states. For a QD with discrete states spin correlations smaller than the level spacing (small-correlation regime) results in so-called spin pairing. In this regime the difference in S_z of ground states of successive charge states alternate with $\pm 1/2$ to minimise S_z that often alternates between S_z=0 and S_z=1/2. The added electron alternate between occupying an empty orbital or pairing with a singly-occupied one.

For spin correlations much larger than the level spacing (i.e. fulfilment of the Stoner criterion [204] for a molecule), the system maximises S_z by adding every new electron with spin up leading to an increase in S_z by $+1/2$ for every increase in charge. This large-correlation-regime spin-filling pattern is labelled Hund's-rule filling and is similar to molecular ferromagnetism. An interesting phenomenon arises when the spin correlation is of similar size to the level spacing. In this intermediate-correlation regime competition between the spin correlation seeking to maximise S_z and the level spacing preferring minimised S_z is called Stoner instability [205] and can lead to irregular spin filling.

The changes in S_z associated with adding another electron to the QD, and thus the spin filling, can be analysed using ground-state spectroscopy. The Zeeman energy $g\mu_B S_z B$ of the Nth ground state depends on the spin of the Nth electron, and reflects on the B-field dependence of $\mu(N)$ through: [140]

$$g\mu_B(S_z(N) - S_z(N{-}1)) = g\mu_B B(\Delta S_z(N)). \tag{3.12}$$

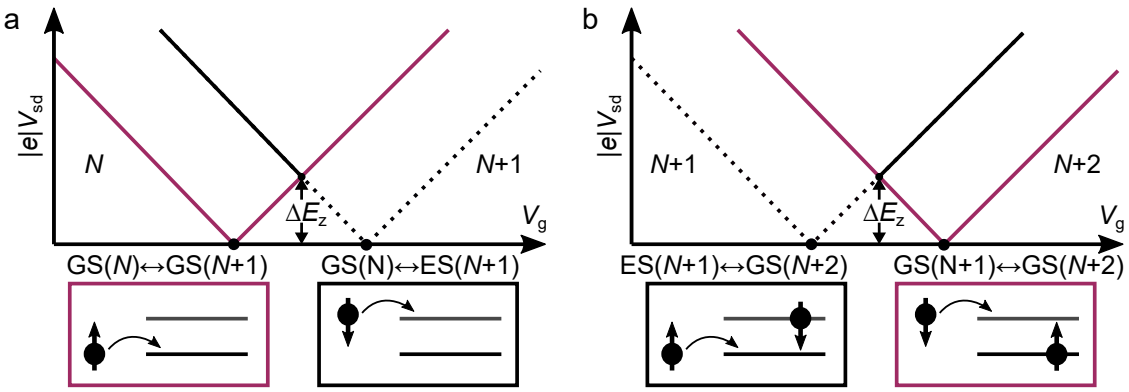


Figure 3.10: Spin filling deduced from excited-state spectroscopy. The schematic stability diagrams consist of lines corresponding to $G = \partial I/\partial V_{sd}$ for the transitions indicated. Adapted from Ref. [140].

However, spin independent shifts with B must be removed by calculating the addition energy, E_{add}, as a function of B: [206]

$$\Delta E_{add}(N) = \mu(N) - \mu(N{-}1) = g\mu_B(\Delta S_z(N) - \Delta S_z(N{-}1)). \tag{3.13}$$

Equation 3.13 implies that $\Delta S_z(N) - \Delta S_z(N{-}1)$ can be read out from the slope of E_{add} versus B in units of $g\mu_B$, and can thus determine the spin filling.

Excited-State Spectroscopy

Excited-state spectroscopy is another powerful technique to deduce spin filling without changing B [162]. A prerequisite is that the Zeeman splitting, $\Delta E_z = g\mu_B B$, can be resolved between electrons with spin up and spin down. The method utilises Pauli's exclusion principle that limits the occupation of a single-particle orbital to maximum two electrons with opposite spins. Then, the $N{+}1$st electron can only enter the QD with N electrons into an empty or a singly occupied orbital [140].

For nonzero B the ground state (GS) splits into a $|\uparrow\rangle$ and a $|\downarrow\rangle$ state. If the orbital is empty (lowest occupied molecular orbital (LUMO)) a spin-up electron enters the GS $|\uparrow\rangle$ at the Coulomb peak (GS(N↔GS($N{+}1$)). First when ΔE_z is added a spin-down electron can move into the excited state (ES) $|\downarrow\rangle$ (GS(N↔ES($N{+}1$); Fig. 3.10a) [140].

If the orbital is half filled (singly occupied molecular orbital (SOMO)) the GS already contains an electron with spin-up. Consequentially, the added electron must

be spin-down (Fig. 3.10b) to obey Pauli's exclusion principle and form the N+2nd ground state (GS(N+1)↔GS(N+2)). Only if the QD is already in ES(N+1), with ΔE_z higher than GS(N+1), can a spin-up electron be added to form the ground state (ES(N+1)↔GS(N+2)). A rule of thumb in excited-state spectroscopy is as follows: the N of the Coulomb diamond that the excited-state conduction line terminates at indicates the N of the ES involved in the transition [140].

Excited-state spectroscopy can thus provide important information on the occupancy of orbitals that take part in low-bias sequential electron tunnelling. At finite B spin filling of the QD can be determined provided the Zeeman splitting of the ground state can be resolved. However, for $B = 0$ and in the absence of ZFS the spin-filling information becomes invalid (because $\Delta E_z = 0$) but the orbital-occupancy information remains valid. Both ground-state and excited-state spectroscopy will be used to extract the spin filling of graphene nanoribbons in Section 6.3.

Data Treatment

The acquired data sets consisted of I, V_{sd}, V_g, t, and T (MC plate). Using MATLAB programmes developed by Dr Nicola Dotti, I traces were lightly smoothed using Gaussian and Savitzky-Golay [207] numerical filters, and then plotted. All subsequent analyses were done using our home-written MATLAB programmes.

3.4 Fast-sweeping Superconducting Magnets

A drawback of our vector rotate magnet is its slow maximum sweep rate of 0.125 T/min. In both CTM and magnetotransport spectroscopy faster field sweeps can be an advantage. E.g. in hysteresis measurements a faster sweep may yield larger hysteresis loops because the system has less time for tunnel-reversal of magnetisation. Moreover, electronic nanodevices are often unstable and prone to charge-jumping events (switching). In these cases fast sweeps may allow probing the whole B range before such switches occur.

Therefore, we set out to build electromagnets for fast-sweep experiments below 4.2 K. Our hypothesis was that by winding small coils using superconducting

multifilament wire impregnated with epoxy, we could create coils ideally capable of generating $B = 1$ T and sweep rate 1 T/s. Compared to the VRM, such magnets would reduce measurement time by a factor of 500. It could for example produce 1000 hysteresis cycles in one hour or a I-V_{sd} versus $-1 < B < 1$ measurement in two minutes.

Electromagnets made from coils of superconducting wire forms the backbone of modern low-temperature magnetic experiments. With zero resistance below a critical temperature, T_c, superconducting magnets can hold large, persistent and loss-less currents in closed coil circuits, which can create large and stable magnetic fields. T_c is usually only a few Kelvin which demands liquid-helium refrigeration. In fact, Onnes' discovery of superconductivity of mercury [208] in 1911 was a consequence of his preceeding research into helium liquefication techniques. He envisaged large electromagnets capable of generating huge magnetic fields while consuming zero power, but quickly discovered that superconductors also have a critical field, B_c, and a critical current density, J_c, at which they become resistive [209].

Not until the late-1950s Onnes' vision of powerful superconducting magnets could become a reality through the discovery of a new classes of superconducting alloys such as niobium titanium that have a high B_c and J_c [210]. In fact, niobium titanium is still often the alloy of choice for superconducting magnets of today, and is indeed the chosen material for those fabricated for this Thesis. While large superconducting solenoids and coil pairs, with thousands of coil winding capable of generating large fields, have become an indispensable part of most low-temperature laboratories, this Thesis is going to focus on small coils with only a few hundreds of windings. These coils were designed for the purpose of fast field sweeps for $B \leq 1$ T. Before discussing coil development, we will outline the necessary theory.

3.4.1 Magnetic Fields and Forces of Solenoids

Magnetic Fields of Single Coils and Coil Pairs

The central field, B_0, of a coil magnet (solenoid) of length, l, and number of turns, N, is proportional to the current I and can be written,

$$B_0 = \frac{\mu N}{l} I, \tag{3.14}$$

where μ is the magnetic permeability and I is the current through the wire. A change in I is followed by a change in B_0 that, by Faraday's Law results in an electromotive force $\mathcal{E} = -NA(dB_0/dt)$, where A is the coil cross section that serves to oppose the B-change. Substituting B_0 using Equation 3.14 yields,

$$\mathcal{E} = -L\frac{dI}{dt}, \tag{3.15}$$

where $L = (\mu N^2 A)/l$ is the coil inductance. On the one hand, the $\mathcal{E}$ opposes the applied voltage, V, when charging the coil as described using Ohm's Law:

$$V = IR - L\frac{dI}{dt}. \tag{3.16}$$

On the other hand, substitution with L in Equation 3.14:

$$B_0 = \frac{L}{NA} I, \tag{3.17}$$

shows that B_0 is proportional to L. Therefore, large L favours large B_0 but opposes fast sweeps. The design of fast-sweeping coils thus rely on an acceptable compromise of L.

Another important factor for practical applications is the degree of homogeneity of **B**. In a homogeneous **B** region a sample will feel the same B wherever it is located. In contrast, in an inhomogeneous **B** the field will differ at different locations, and even within different regions of the sample (which can cause spurious signals from Faraday forces in magnetic samples).

Stray fields generated by single coils are inhomogeneous outside its bore (Fig. 3.11a,b) and this can be problematic for applications where the sample is located outside the coil. However, coil pairs can generate more homogeneous fields in the space

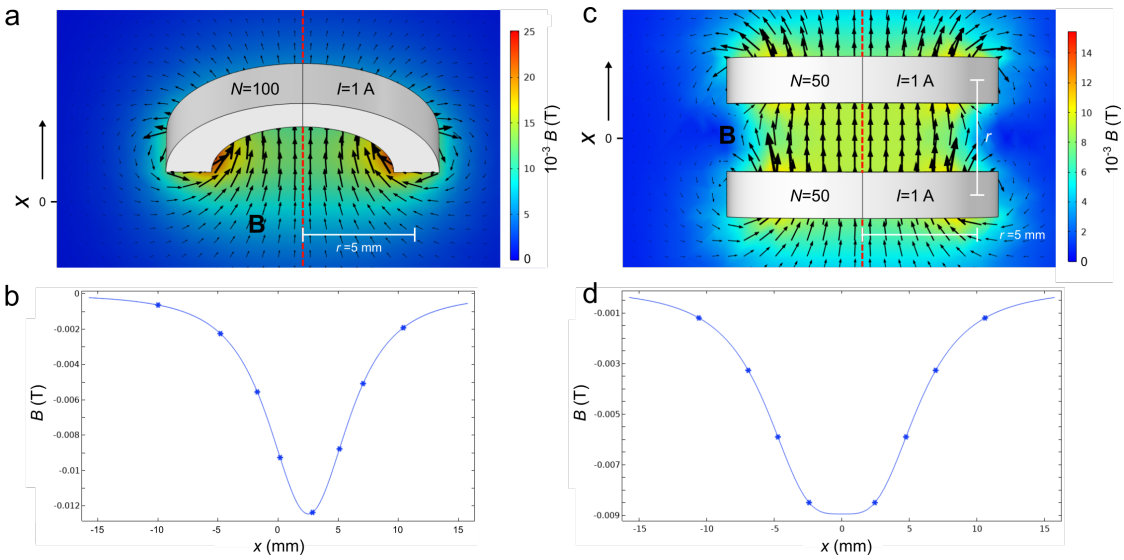


Figure 3.11: Field comparison between a single coil ($N = 100$) and a Helmholtz coil pair ($N = 50$ in each coil). The models were created in COMSOL Multiphysics. **(a)** **B** of the single coil with $r = 5$ mm, $l = 3$ mm. **(b)** The central B (along the red dashed line in **(a)**) is centred on $x = 2.5$. **(c)** **B** of the Helmholtz coil pair each with $r = 5$ mm, $l = 3$ mm and a separation distance equal r. **(d)** The central B (along the red dashed line in **(d)**) clearly shows a plateau of 2.5 mm centred on $x = 0$ where the field is homogeneous (B is insensitive to x). B at this plateau equals B at the same location of the single coil for equal number of total N and I.

separating the coils. A region of perfect homogeneity can be generated by a Helmholtz pair where the coil radius, r, equals the separation distance between the coils (Fig. 3.11c,d). A sample located in this region will experience a homogeneous **B** with equal B per N as a single coil.

Because the field of single coils is the strongest and most homogeneous in the centre of its bore, applications where the sample can be placed inside the bore have an advantage. Figure 3.12 shows that increasing l results in a more homogeneous **B** close to $x = 0$. However, it is not perfectly homogeneous like the Helmholtz configuration so a careful tolerance analysis and potentially corrections for spurious signals (e.g. Faraday forces) may be required in applications using long single coils.

Forces on Single Coils and Coil Pairs

The forces exerted on the solenoid by a magnetic field **B** closely resembles the picture of the pressure of compressed gas in a cylindrical vessel. The force **F** per

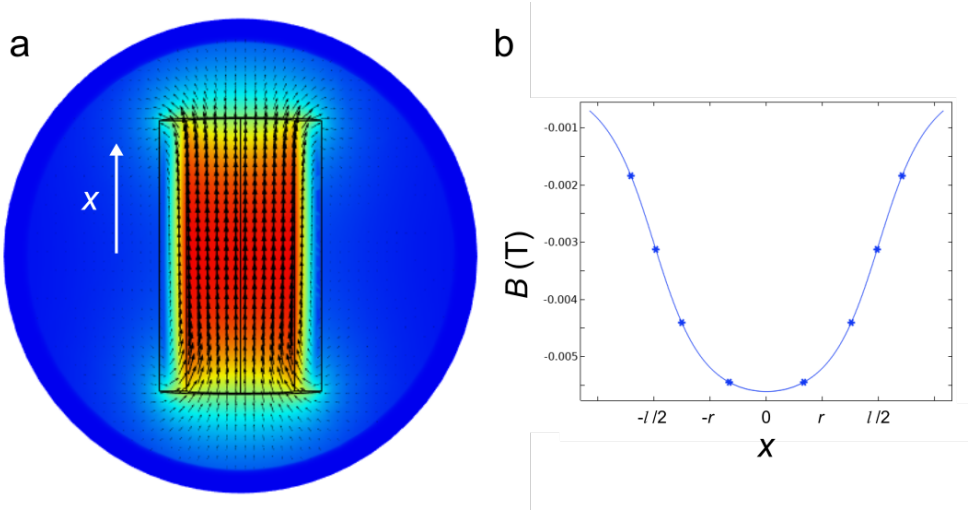


Figure 3.12: **(a)** A long solenoid with $r = 5$ mm, $l = 20$ mm, $N = 100$ and $I = 1$ A generates a more homogeneous **B** inside its bore. **(b)** The central B as function of x showing that close $x = 0$ a long coils generate a more homogeneous **B** than short coils but less than Helmholtz pairs.

unit volume on a current-carrying conductor caused by **B** can be written as:

$$\mathbf{F} = \mathbf{B} \times \mathbf{J}. \tag{3.18}$$

In a direction perpendicular to the flux lines the field exerts a pressure $B^2/2\mu_0$ on the coil which equals 4.0×10^5 N m$^{-2}T^{-1}$ or 4 atmospheres per Tesla. In high-field magnets the magnetic pressures can break the structure and destroy the magnets but for smaller magnets these pressures are less likely to cause problems. However, sudden release of magnetic energy (i.e. quench) may cause mechanical degradation also in small coils [209].

Stresses in solenoids are composed of circumferential and axial contributions and their signs and magnitudes depend on the shape factor and fields. Stress calculations are given in Refs. [209, 211–213] but in this Thesis we will simply note that while solenoids tend to be strong in compression, they should be designed to avoid too large circumferential tension as that may cause fracture and magnet failure at low temperature. Maximum working stress in NbTi composites is around 500 MN m^{-2} [209]. This information will be useful in the discussion of magnet design below.

Split pair coils experience also an attractive force, F_z, between them which may be expressed in terms of their mutual inductance, L_{12}^{mut}, respective currents,

I_i, and separation distance, d: [209]

$$F_z = -I_1 I_2 \frac{\partial L_{12}^{mut}}{\partial d}. \tag{3.19}$$

F_z is a relevant parameter for the coil pair holder, which must be designed to withstand the forces involved. Aluminium coil holders are common for larger magnet systems because it is paramagnetic and remains ductile at cryogenic temperatures. Small systems with small forces involved allow a broader range of materials, e.g as plastics.

3.4.2 Degradation and Training of Composite Superconductors

Coil degradation is the effect of quenching at a much lower current than what could be expected from tests on a perfect sample of the same conductor. The term quenching describes the process which occurs when a small part of the coil goes from the superconducting to the resistive state. During a quench, the high current densities will generate intense local heating in the resistive conductor which quickly will bring the surrounding temperature above the critical. In this irreversible process, all the stored magnetic energy $\frac{1}{2}LI^2$ is dissipated as heat. Surprisingly, new coils often show progressive performance-improvement, i.e. increasing critical current densities, J_c, after multiple quenches; a phenomenon called training [209].

Degradation is attributed to several sources of energy disturbances that cause the magnet to quench before the critical values of the superconductor have been reached. A disturbance may bring a part of the superconductor into its normal resistive state. However, if the resistive part is shorter than a critical length called the minimum propagation zone (MPZ), cooling effects will revert it back to its superconducting state. If longer, the resistive part will grow and cause a magnet quench.

To reduce degradation magnets should be designed to facilitate cooling. Superconducting alloys generally have low thermal conductivity, κ, high resistivity, ρ, (in the resistive state). Therefore, composite conductors with NbTi covered in a layer of copper are much less prone to quench due to Cu's much higher κ and much lower

ρ at low T. When the supercurrent exceeds J_c the superconductor continue to carry J_c while the Cu layer becomes an 'over-pressure valve' that carries the rest [209].

Mechanical disturbances is the major source of quenching. When magnetic forces becomes larger than the friction holding a wire in place, the wire will move and dissipate heat. Therefore, impregnation with resins greatly enhances performance because it prevents the wires from moving. However, the high brittleness of insulators at low temperature favours crack propagation under stress which in fact may generate serious heating as well. Cracking must be avoided by choosing a resin such as Stycast with a high work of fracture. Use of composite conductors and epoxy resin impregnation solves many problems when it comes to quenching in small solenoids.

3.4.3 Coil Construction

We have fabricated small coils for research purposes following standard practice. 0.152-mm thick NbTi in a CuNi matrix (Copper-10% Nickel Alloy) composite wires with 42 filaments insulated with an electrical varnish such as polyvinyl acetate. Coil formers were designed in Inventor and printed in polycarbonate or water-soluble plastic using a Prusa i3 MK3S+ 3D printer. The coils were then made using an ACME Mechatronics AEX-01 winding machine that ensured high packing density and accurate counting of turns N. Gloves were used during the process to keep finger oil off the wire. Additionally, the wire was run through a cotton pad soaked in isopropyl alcohol to remove grease and ensure good adhesion between wire and epoxy.

Impregnation with a resin should be done to prevent magnetic forces from moving the windings and cause a quench. Thus, the coils were submerged in liquid Stycast 1266 epoxy resin and hardened at room temperature. Finally, the water-soluble coil formers were dissolved in water leaving only the epoxy-impregnated coils. Leaving resin-impregnated coils on their coil formers often lead to more degradation and training than when the former is removed [209]. This effect may be a cause of local stresses at the interface between resin and former leading to failure under electromagnetic stress. Therefore, it may be advantageous to to remove the coil former before putting it to use.

3.4.4 Design and Fabrication of Fast-Sweeping Superconducting Magnet Systems

The previous discussion has elaborated on the working principles of small coils of superconducting wire and how they can be fabricated. This Section will report on applications designed for this Thesis by use of such coils. Fast-sweeping systems for both magnetotransport spectroscopy and CTM will be discussed. Because electromagnets require large currents the associated Ohmic losses in resistive leads and connectors are correspondingly large. This issue prevents us from using these systems at mK temperature because the cooling power is too low. Instead such systems are typically used at 4.2 K where the cooling power is larger, e.g. at the PT2 plate in the DR or in a liquid He cryostat.

Small fast-sweeping 3D superconducting magnets for fields up to 0.8 T and sweep rates up to 0.2 T/min at 4.2 K have been developed elsewhere [214]. Instead, we have made multiple simple designs tailored for specific purposes. These were all designed in Autodesk Inventor and either 3D printed in high-quality polycarbonate (PC) or PET-G plastics.

Single Coil for Magnetotransport Spectroscopy

In Figure 3.11a we saw that a macroscopic single coil can generate an inhomogeneous **B** that might be unusable for applications requiring homogeneous fields. However, an inhomogeneous **B** at the macroscale can feel like a homogeneous **B** for a nanoscopic electronic devices used for transport spectroscopy[1]. Therefore, single coils may be sufficient for magnetotransport purposes. Here, the coil should be placed as close to the device as possible to maximise B. Difficulties with calibrating **B** at the nanoscale is a significant drawback of this method that might require a nanoscale calibration magnetometer (e.g. a Hall bar).

[1]Similar to how a navigator with a compass experiences the Earth's inhomogeneous magnetic field as homogeneous for the purposes of her hike.

Single Coil for In-Plane CTM

Figure 3.5 shows how CTM could detect magnetic hysteresis in single crystals. We have also seen that magnetisation reversal is time dependent, i.e. faster field sweeps should lead to less reversal and thus larger hysteresis. Therefore, an apparatus was designed composed of a long superconducting solenoid and a CTM device placed inside its bore with the cantilever direction parallel to the longitudinal solenoid axis (Fig. 3.13d). A rotator stage can rotate the CTM device by $\pm 10°$. In this configuration $\mathbf{B}$ can be applied along the cantilever direction and $\varphi = 10°$ in either direction (not shown).

A major advantage with this system over small coils is that a long solenoid can hold many wire turns and thus generate a larger B. By placing the CTM device inside the bore, this large and nearly homogeneous B can be utilised. The small range of φ is a limitation that can be easily circumvented by first performing CTM using the standard technique presented in Section 3.2.4, and then using the fast-sweeping apparatus to measure hysteresis in a specific direction of interest.

Coil Pair for Out-of-Plane CTM and Magnetotransport

Coil pairs are suitable for applications that require a more homogeneous $\mathbf{B}$ than can be generated by a single coil. Their implementation on both sides of the sample is more complicated and may require specially designed sample holders and circuitry. We have designed a two coil-pair systems for use in CTM and magnetotransport in which B can be applied out-of-plane (Fig. 3.13a-c). Mechanical finite element analysis was performed to assess the structural impact caused by the attractive force, F_z, between the two coils (Eq 3.19). To minimise plastic deformation under compression we chose a compact coil-pair design.

In this design, the two coils are carefully fitted into the coil holder with a coil-pair separation distance approximately equal to the coil radius. A CTM or transport device can be placed in the open space between the coils. To allow a minimised coil-pair separation distance (and thus a maximised B) the sample holder should be made as thin as possible.

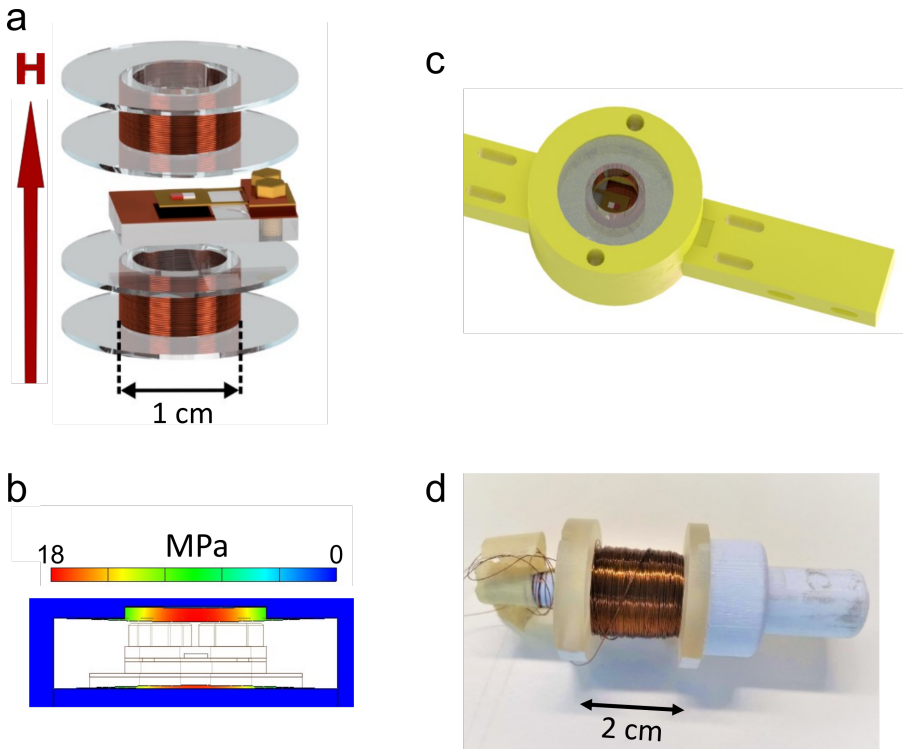


Figure 3.13: **(a)** Graphical illustration of a fast-sweeping coil pair for use with out-of-plane CTM. **(b)** Finite-element mechanical stress simulation of the stress exerted on the coil-pair holder by the mutually attracting coil pair. **(c)** Graphical illustration of the 3D printed coil-pair holder. **(d)** Photo of a long coil for fast-sweeping in-plane CTM directly after winding of the coil.

3.4.5 Testing and Proof-of-Concept Demonstration

The aim of producing fast-sweeping superconducting coils was to push the magnetic sweep environment in which we perform experiments to the limit. The scope of this project was to demonstrate proof-of-concept experiments on both CTM and magnetotransport spectroscopy, and to add this capability to our experimental toolbox.

To test the fast-sweeping superconducting coils we designed and produced a dipstick for liquid helium cryostats, with help from Tony Hickman at the Cryomagnetics Group in Oxford Physics. The dipstick head was fitted with a single-coil holder and a holder for a Hall probe in the centre of the coil bore. The coil was wired through the dipstick and connected to a Cryomagnetics 4G Superconducting Magnet Power Supply. The 3D vector Hall probe was used to detect the true **B** in the coil centre and was wired to a Keithley 2450 SourceMeter. Due to severe disruptions caused by the Covid-19 pandemic, neither the testing

of the coils nor the proof-of-concept demonstrations could not be done within the timeframe of the present DPhil project.

3.5 Triangular-Waveform Magnetic Field Amplifier

This Section will outline the invention of a magnetic field amplifier that can be used to generate a triangular-waveform alternating magnetic fields to a nanoelectronic device. This instrument would constitute another pushed environment to our millikelvin single-electron transistor setup. The instrument relies crucially on all the components discussed in this Chapter: CTM, anisotropic single crystals, fast-sweeping superconducting magnets and single-electron magnetotransport. Its working principle is illustrated in Figure 3.14.

The explanation of the instrument starts with a strongly anisotropic single crystal on a thin CuBe cantilever. The crystal must have a strong hard plane oriented along the x direction and an easy axis along z, and it must be superparamagnetic at low T. Then, the magnetisation, M, will strongly prefer the $\pm x$ direction (Fig. 3.14a). A large, constant B-field, B_1, is applied along x. Because B_1 aligns with the hard plane the resulting magnetic torque $\zeta = 0$ and thus the cantilever deflection $d = 0$ (Fig. 3.14d). However, a small change in field angle, φ, will cause M to flip and induce a large torque and deflection as M seeks to align with B.

The key component of this instrument is the stray field of M, B_M, which changes direction with M. A strongly magnetic crystal such as a Dy-based SMM can generate a large B_M close to itself. B_M could be utilised by fabricating an electronic device, e.g. a single-electron transistor, on the other face of the cantilever, as close as 25 μm away from the crystal. The field experienced at the device site as a function of time, t, is $B_d(t) = B_m(t) + B_M(t)$, i.e. stronger than what one could achieve with the coil only ($B_m(t)$: coil field). Capacitive detection of d would be useful for calibrating the instrument.

The necessary φ-change can be produced by a small coil nearby the crystal. For a 1° change, $B_m(\varphi = 1°) = B_1 \tan\varphi \approx 0.02 B_1$, or around $B_m = 20$ mT per

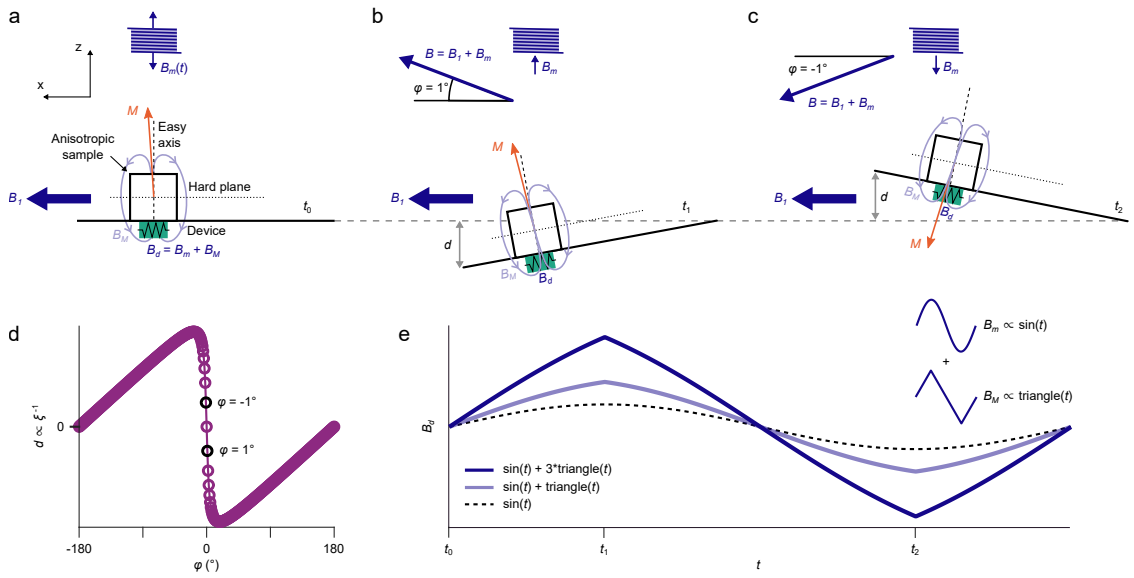


Figure 3.14: Triangular-waveform magnetic field amplifier. **(a)** A strongly anisotropic single crystal on a cantilever subjected to B_1 along x and a perpendicular $B_m(t)$. The system provides a field B_d to an electronic device fabricated on the opposite cantilever face. **(b,c)** B_m oscillations induce torque-driven deflections that assist in reversing M and thus generate an oscillating B_d at the device site. **(d)** $d \propto \zeta^{-1}$ versus φ for a typical crystal where the difference in d associated with $\varphi = \pm 1$ is highlighted. **(e)** B_d versus time, t, where the ratios between sinusoidal and triangular wave forms are 1:3 (dark blue), 1:1 (light blue) and 1:0 (dashed). B_d at times t_0 to t_2 correspond to the configurations depicted in **(a-c)**.

$B_1 = 1$ T. Coils similar to those discussed in Section 3.4 could easily generate the required B_m with fast sweeps taking a sinusoidal form. From Figure 3.14d the region close to $\varphi = 0°$ is approximately linear, i.e. B_M also changes linearly with small φ producing triangular wave forms. Thus, B_d would take the form of a triangular wave superimposed on a sinusoidal wave. Figure 3.14e shows three such curves with different ratios between the contributions.

The advantage of this instrument is its ability to generate oscillating B fields of large magnitude for magnetotransport spectroscopy experiments. As discussed earlier in this Chapter, the amplitude of B-field oscillations is limited by the heat generation associated and potential coil quenching associated with fast sweeps. The present instrument seeks to add B-oscillation amplitude to what can be generated by the coil ($B_m(t)$) by utilising the stray field of the crystal that reverses in synchronisation with $B_m(t)$. If the B_d is dominated by the stray field, its

oscillations in time will take a triangular form.

3.6 Conclusions

In this Chapter we have discussed the design, fabrication, testing and experimental use of the instruments used in this Thesis. In addition, the foundations are laid for high-performance instruments that will soon be fully realised in the laboratory. In the next Chapter, we will show how to use these setups to explore hitherto unknown information about the magnetic anisotropy of paramagnetic and superparamagnetic molecular compounds at very low T.

4

Magnetic Anisotropy Characterisation of Molecular Nanomagnets using Torque Magnetometry

Contents

4.1 Introduction 75
4.2 Terbium Porphyrin Monomer Single-Molecule Magnet 76
4.2.1 Theoretical Predictions 78
4.2.2 Characterisation of Magnetic Anisotropy 78
4.2.3 Discussion 87
4.3 Dysprosium Porphyrin Monomer Single-Molecule Magnet 90
4.3.1 Theoretical Predictions of the Ligand Field 91
4.3.2 Characterisation of Magnetic Anisotropy 91
4.4 Fused-Porphyrin Dysprosium Dimer SMM 93
4.4.1 Characterisation of Magnetic Anisotropy 96
4.5 Dy_2-hfac Dimer SMM 100
4.6 Dysprosium Trimer SMM 102
4.6.1 Conclusions 107

4.1 Introduction

In Chapter 3 we looked at the different experimental techniques used for this Thesis. The principles of detecting magnetic anisotropy through the magnetic torque $\zeta =$

$\mathbf{M} \times \mathbf{B}$ using cantilever torque magnetometry (CTM) were discussed. Furthermore, the design and fabrication of a CTM device was described. The present Chapter will discuss the results of experiments performed using our home-built CTM device to characterise the magnetic anisotropy of several molecular compounds. We will begin with the treatment of a terbium porphyrin SMM and a dysprosium porphyrin SMM before proceeding with dysprosium based dimeric and trimeric SMMs. To our knowledge, none of these systems have been investigated using CTM in the past.

Several of these SMMs consist of trivalent Tb or Dy ions bound to a porphyrin molecule. These combinations introduce interesting couplings between the large magnetic moment of the Ln ions and the delocalised electron spins in the porphyrin backbone. It can be expected that the delocalised electrons are strongly affected by the Ln magnetic state, and in dimers the might even transfer magnetic information between Ln ions. Herein, we will attempt to disentangle the roles of the mentioned components on the magnetic anisotropy of the compounds.

4.2 Terbium Porphyrin Monomer Single-Molecule Magnet

Molecular materials with graphene-like π-delocalised elements, combined with spin-bearing ions constitute a promising path towards novel electronics and spintronics [215, 216]. A prerequisite for molecular spintronics is molecular hysteresis, which has been frequently observed in SMMs below their blocking temperature [217, 218]. The first observed lanthanide-based SMM that exhibits hysteresis is the $TbPc_2^-$ that consists of a Tb^{3+} sandwiched between two phthalocyanine dianions (Pc^{-2}) [173].

Here, we investigate single crystals of a terbium(III) porphyrin SMM (**TbP**) synthesised by Dr Jennifer Le Roy (Fig. 4.1a) [219]. Porphyrins exhibit strong π-conjugation and can host a metal atom in its centre. While transition metals tend to sit in the porphyrin plane, lanthanides, such as Tb^{III} and Dy^{III}, sits out of plane [219]. A Kläui capping ligand provides chemical stability, high solubility in organic solvents and results in neutral compounds [220]. While the lanthanide in $LnPc^-$ is 8-fold coordinated, it is only 7-fold coordinated in LnP. The different

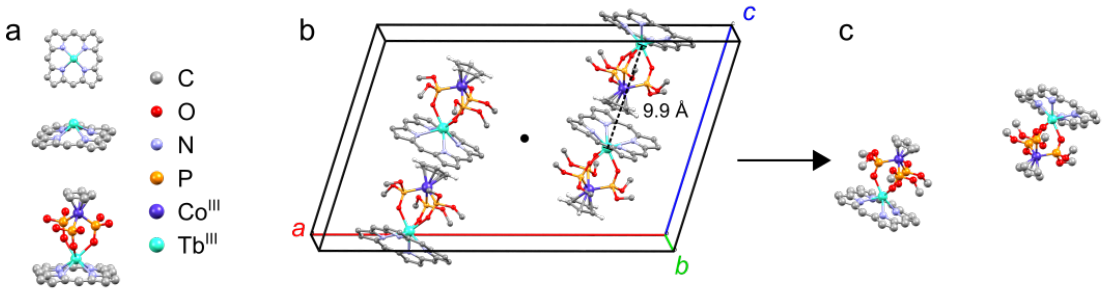


Figure 4.1: **(a)** A porphyrin building block bonds with a lanthanide metal centre (here Tb) sitting out of plane and is protected by a Kläui capping ligand. **(b)** The monoclinic unit cell of the TbP crystal structure contains four molecules and **(c)** reduces to two inequivalent units due to the presence of an inversion centre (black dot) located in the centre of the unit cell. The molecules are tilted by 24° (between Tb–Co axes) which means that the molecular anisotropies are noncollinear.

coordination environment leads to a different crystal field and thereby alters the magnetic anisotropy of the molecular ground state.

TbP crystallises in the monoclinic crystal system and contains four molecules per unit cell (Tab. 4.1; Fig. 4.1b). A screw axis along the b axis serves to eliminate any paramagnetic component of $\mathbf{M}$ that is not parallel to b and therefore b must be a unique magnetic axis. Due to the presence of an inversion centre the unit cell reduces to two inequivalent molecules. The molecular Tb–Co axes are tilted by 24° relative to each other and the anisotropies of the two molecules are therefore non-collinear. Thus, we expect CTM measurements to reflect a crystal anisotropy that consists of two non-collinear spin centres.

Table 4.1: Crystallographic information for **TbP**.

Crystal system (number)	Space group	Unit cell parameters						Noncollinear angle (°)
		a (Å)	b (Å)	c (Å)	α (°)	β (°)	γ (°)	
Monoclinic (14)	$P2_1/c$	31.47	16.11	19.51	90.0	107.3	90.0	24

We assume that only Tb^{III} contributes with magnetic moment because the Co^{III} in the capping ligand is diamagnetic. However, the magnetic centre may interact with the delocalised porphyrin electrons. The static magnetic susceptibility, χ,

Table 4.2: Stevens coefficients B_k^2 and B_k^4 in units of cm^{-1} for **TbP** calculated by Ming-Yee Tsang using MOLCAS.

k	-4	-3	-2	-1	0	1	2	3	4
B_k^2			0.40	-2.88	-3.92	-1.78	0.57		
B_k^4	-0.049	-0.0087	0.012	-0.0036	-0.016	0.013	0.0023	0.22	-0.047

of **TbP** has been measured elsewhere [219] to $\chi T = 11.19$ cm^3 $kmol^{-1}$ at room temperature. This value is in good agreement with the theoretical value for a single Tb^{III} ion with term symbol $^7F_6$, S=3, L=3 and g_J=3/2. An increase in χT was observed below 10 K and might indicate a ferromagnetic interaction between Tb ions in different molecules (Tb–Tb = 9.9 Å). AC susceptibility studies revealed an effective energy barrier $U_{eff} = 7$ K and we thus expect superparamagnetic behaviour below this temperature. Strong spin–orbit interactions cause large line-width broadening and zero-field splitting (ZFS) in **TbP** and render techniques such as electron paramagnetic resonance infeasible.

4.2.1 Theoretical Predictions

Ming-Yee Tsang performed ab-initio calculations of **TbP** in MOLCAS. This software was used to calculate the spin Hamiltonian that describes the symmetries of the magnetic anisotropy. The resulting Stevens operators of significance are reported in Table 4.2. The calculations identify the crystallographic b axis as a hard axis. Isoenergy surfaces are doughnut shaped, with small modulations, for both the molecular and crystal anisotropies (not shown). We will see in the next Sections that the calculated anisotropy deviate from experiments by an inexplicable rotation of 90°.

4.2.2 Characterisation of Magnetic Anisotropy

Crystal Orientation and Device Testing

To characterise the magnetic anisotropy of **TbP** we performed CTM on single crystals. Two crystals were face indexed to identify how their crystallographic axes related to their crystal faces (Fig. 4.2a; Sec. 3.2.3). Crystals were then mounted

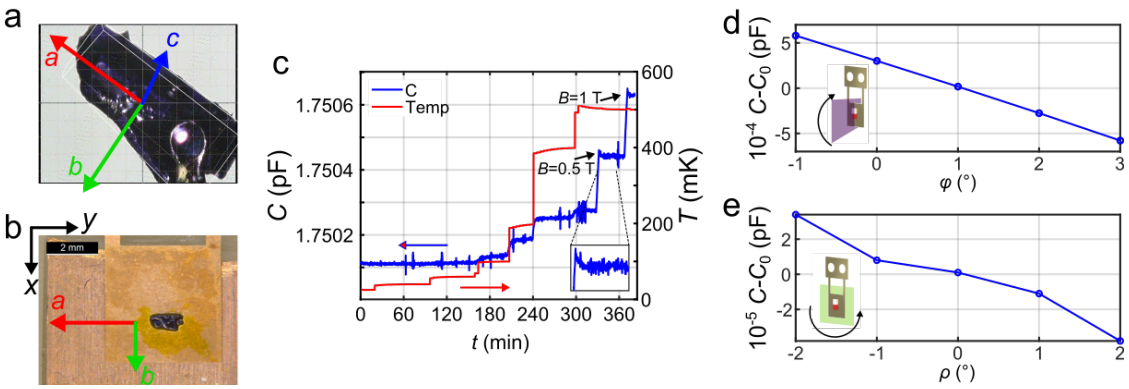


Figure 4.2: Mounting of the **TbP** sample and CTM testing of T dependence and crystal orientation. **(a)** Photo of the **TbP** single crystal inside the X-ray diffractometer with the crystallographic axes indicated. **(b)** Photo of the **TbP** sample mounted with its b axis parallel to the the laboratory x axis on a 100-µm CuBe cantilever. **(c)** Testing of T dependence on C by continuously sampling C while step-wise increasing T. The two last steps in C are due to B sweeps up to 1 T. The inset shows a relaxation of C after a B sweep. **(d)** $C-C_0$ crosses zero at $\phi = 1$ and **(e)** at $\rho = 0$.

on 25- and 100-µm thick CuBe cantilevers, Crystal 1 with its ab plane facing the cantilever and its b axis aligned with the laboratory x axis (Fig. 4.2b) and Crystal 2 on its a^*b face with b pointing along $-y$.

We start our analysis with Crystal 1. To control for misalignment angle-resolved CTM was performed close to $\varphi = 0°$ ($\rho = 0°$) in the xz (xy) plane (Fig. 4.2d,e). Because b must be a unique axis, due to symmetry, ζ must equal 0 when **B** is aligned with b. From Figures 4.2d and e we see that this is the case for $\varphi = 1°$ and $\rho = 0°$. This observation confirms that the misalignment of the crystal on the cantilever is very small.

As shown in Figure 4.2c the capacitance C (related to ζ through Eq. 3.7) increases with T. The change in C is largest for low T and decreases with higher T when the heat capacity of the device is higher. Furthermore, the round shapes of the steps in C indicates that it took around seven minutes before the device thermalises with the thermometer on the MC plate. Moreover, for time $t < 320$ min B is zero and the T-dependency must be one of the device itself as the sample cannot generate a torque at zero field. Around $t = 320$ min the field was swept to $B = 0.5$ T with a rate of 0.125 T/min and induced further steps in C. Notably, when B had reached its set point, C peaks and then decreases exponentially for

5-10 min. This effect is likely caused by heat generation in the CTM device due to eddy currents induced by the sweeping field. The observed peak width of around seven minutes agrees with the thermalisation time discussed above.

Angle-Resolved CTM

First, angle-resolved CTM was performed on the crystallographic *bc* plane. This was done by creating a rotation plane in the xz plane and then rotating it around x by an angle equal to $\beta - 90°$. The CTM measurements were performed at 0.5 K and at three different B up to 1 T. The results are shown in Figure 4.3.

The main observations from Figure 4.3 are as follows: (i) that $\zeta_y < 0$ for $\varphi < 0$ means that the cantilever bends towards **B** and this would only happen if **M** pointed along b. Therefore, b is an easy axis in the bc plane; (ii) the magnitude of the slope of ζ is larger around $\varphi = 90°$ and 270°, where **B** aligns with c, than around 0° and 90°, where **B** aligns with b. This is in agreement with (i) that b is an easy axis and also identifies c as a hard axis; (iii) the period of the ζ oscillation is 180°; (iv) $|\zeta|$ is approximately equal at every extrema as expected for a paramagnetic sample i.e. there is no indication of magnetic hysteresis in the bc plane.

It turned out that B rotations in the ab and ac plane also generated a torque along y (Fig. 4.4). It is evident that b is an easy axis also in the ab plane, and that a seems to be hard. ζ_y has a similar shape as in the bc plane but the magnitude is less by a factor of 20.

The anisotropy of the ac plane differs from the other planes because ζ_y crosses zero four times for every 180° (in contrast to two times for bc and ab). This four-fold symmetry indicate that anisotropy in the ac plane is of higher symmetry than the other planes, and that the free energy contains more local maxima and minima. Moreover, $|\zeta|$ is a factor of 10 less than in the bc plane and the largest negative values are about 1.4 times larger than positive values. This magnitude asymmetry indicate that superparamagnetic effects are present. Furthermore, the sign of the slopes of ζ_y when zero is crossed indicate that both a and c are close to easy directions in this plane and that the hardest directions lie around 50°/230° and

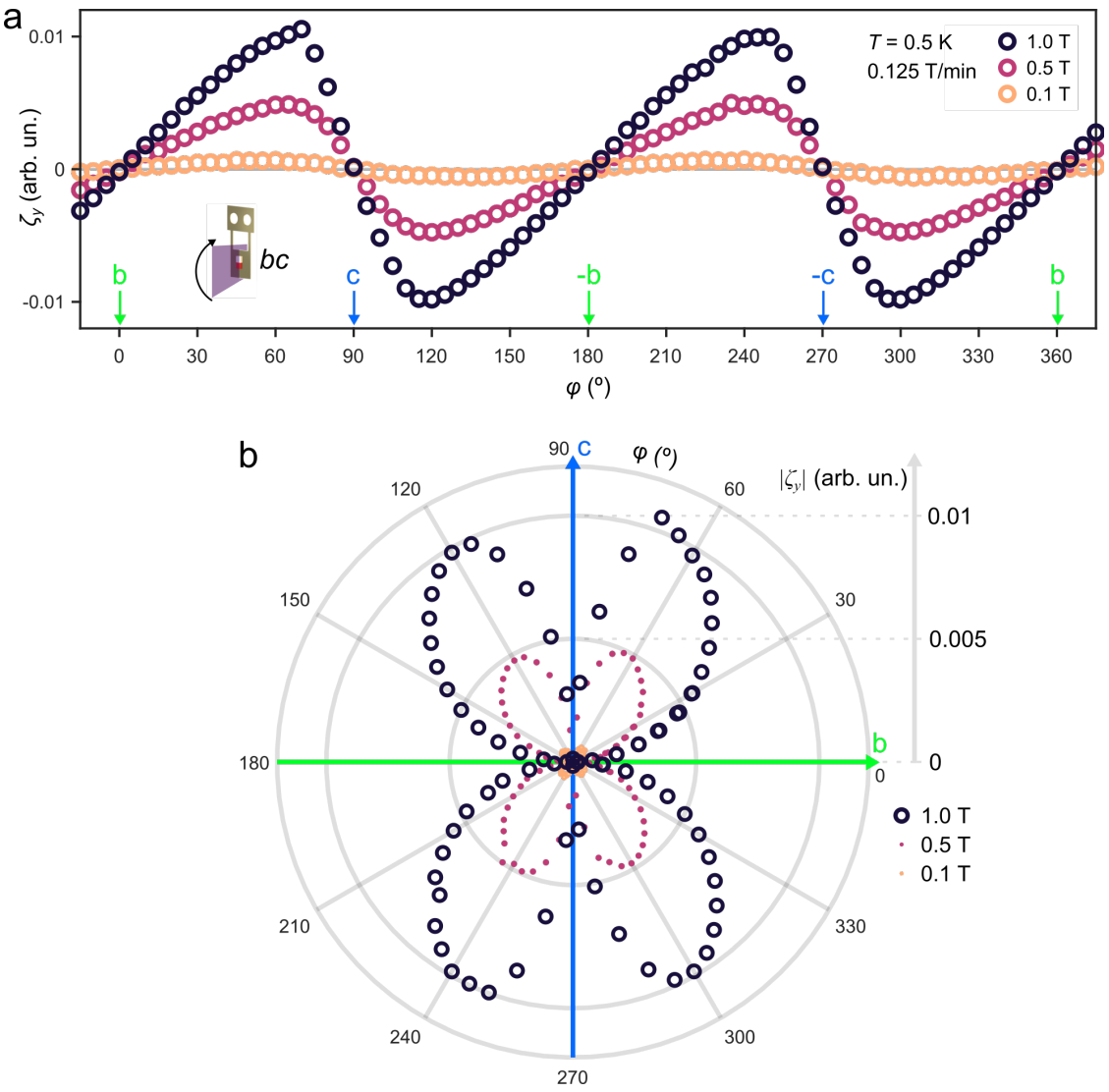


Figure 4.3: Angle-resolved CTM of the *bc* plane of **TbP**. **(a)** ζ_y plotted as a function of rotation angle φ for three different B. ζ crosses zero every 90° corresponding to the *b* and *c* axes, as indicated. **(b)** $|\zeta_y(\varphi)|$ plotted in polar coordinates.

150°/330°. Note, that the ζ measured at different B crosses zero at different φ, which is a further indication of hysteresis.

We proceed with the analysis of **TbP** Crystal 2. We experienced two issues with this sample: (i) we were uncertain if the crystal face indexing is correct but we assumed the orientation depicted in Figure 4.5a; (ii) the initial idea was to scan the crystallographic plane that contains all the Tb^{3+} ions, i.e. the [4,4,-1] plane, and a plane perpendicular to it. But because we initially assumed the wrong crystal orientation (and did a mistake in calculating **B** vectors for the [4,4,-1] plane) we

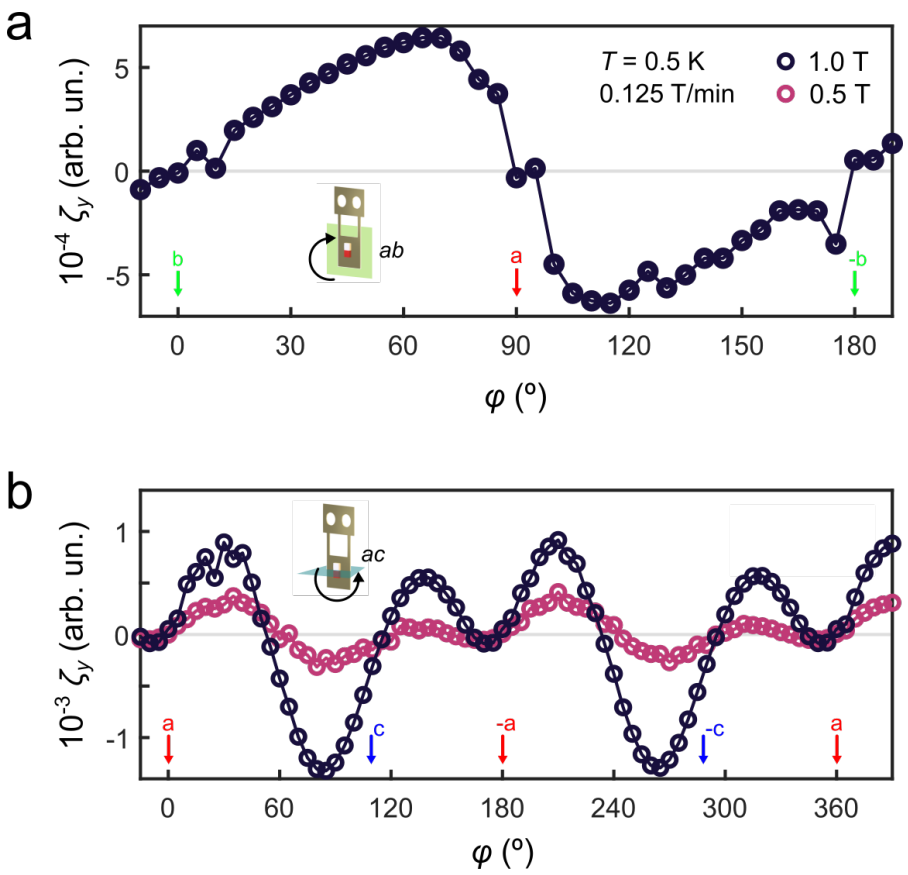


Figure 4.4: Angle-resolved CTM of **TbP** showing the ζ_y response of B rotation in the **(a)** ab plane and **(b)** ac plane. The B rotation directions are indicated in the cartoon.

could not complete this analysis. However, the scanned planes lie close to the xy and yz planes, respectively, and the torque can be analysed with respect to the projections (Proj) of the crystallographic axes on the scanned planes.

In this way, angle-resolved CTM was performed by rotating **B** close to the a^*b plane (Rot_c) and the bc plane (Rot_{a^*}) (Fig. 4.5a-c). Rot_c scans close to the porphyrin plane and Rot_{a^*} scans close to the Tb–Co molecular axes. ζ_y as a function of φ in Rot_c was plotted in normal and polar coordinates (Fig. 4.5e,f). In stark contrast to Crystal 1, ζ is positive for all φ. ζ takes a shape of seemingly 360° periodicity but instead of torque inversion every 180° it increases and starts a new 180° cycle. The only explanation for such behaviour is that of a superparamagnet that reverses its magnetic moment at certain φ preventing ζ from taking negative values.

ζ seems to peak close to the projection of the b axis (Proj(b)) which is surprising as we earlier estimated b as an easy axis and a permanent magnet should exhibit

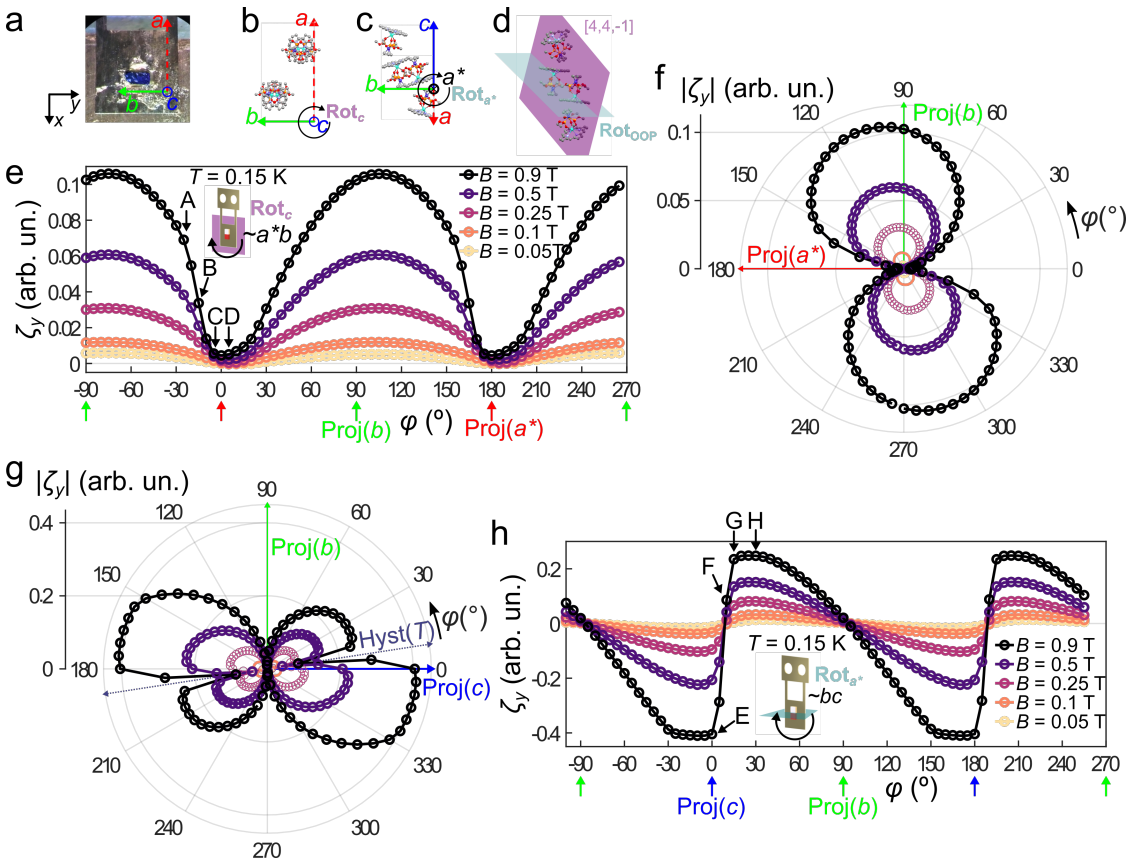


Figure 4.5: Angle-resolved CTM of **TbP** (Crystal 2) for B between 0.05 and 0.9 T at 0.15 K. **(a)** The crystal is oriented with its a^*b face facing the cantilever and b axis pointing along $-y$. **(b,c)** The unit cell viewed along c and a^*. **(d)** The plane [4,4,-1] contains the Tb^{3+} ions. **(e)** Angle-resolved CTM near the a^*b plane (i.e. rotation approximately around c: Rot_c). The angles corresponding to Proj(a^*) (Proj(b)) is indicated by red (green) arrows. **(f,g)** $|\zeta_y|$ from **(e)** and **(h)**, respectively, presented in polar coordinates. The dotted blue line indicates the angles used in the hysteresis measurements mentioned below. **(h)** Angle-resolved CTM near the bc plane (i.e. rotation approximately around a^*: Rot_{a^*}).

zero torque at its easy axis and maximum torque perpendicular to it. However, this picture may be too simplistic for our strongly superparamagnetic molecular terbium system, and it is difficult to determine the direction of the superparamagnetic magnetic moment from simple CTM measurements. The reversal of magnetisation occurs close to Proj(a^*)) which is close to the direction where **B** points from one molecule to the other (Fig. 4.5b). At this field interactions between the two noncollinear spin centres allow reversal of **M** through tunnelling.

When **B** is rotated in Rot_{a^*}, the observations are more similar to that seen in Crystal 1 with 180° periodicity (Fig. 4.5g,h). Although less pronounced than

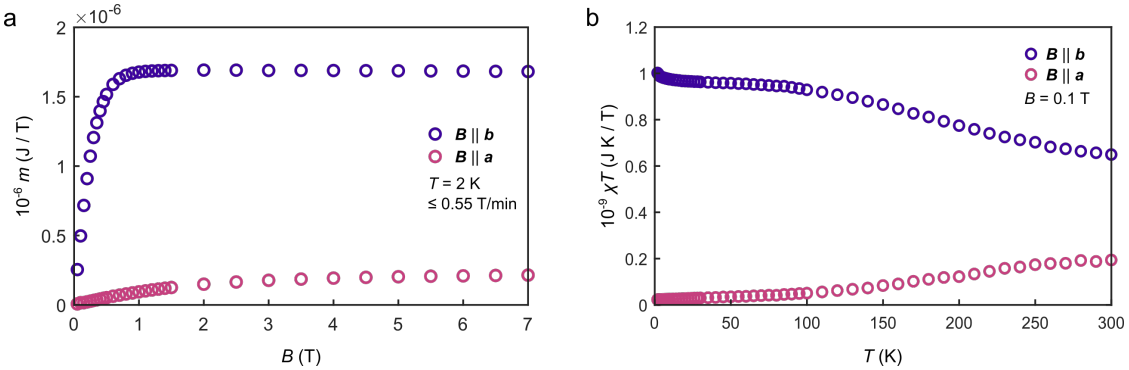


Figure 4.6: SQUID magnetometry of **TbP**. **(a)** m as a function of B when **B** is aligned with b (purple) and aligned with a (violet) at 2 K. **(b)** χT as a function of T. The measurements were performed by Dr Michael Slota.

for Rot_c, the negative ζ-magnitudes are larger than the positive ones and indicate minor superparamagnetism also in this plane. A steep slope as ζ crosses zero is present close to Proj(c) indicating a hard axis and a less steep slope around Proj(b) indicates an easy axis. These observations fit with the results of Crystal 1.

To summarise, the results from angle-resolved CTM were used to characterise the magnetic anisotropy of different **TbP** planes. b was identified as an easy axis and the planes bc and ab both have a two-fold 180° rotation symmetry. ac appears to be a hard plane with four-fold 180° symmetry and minor signs of superparamagnetism. Preliminary results using ab-initio MOLCAS calculations, performed by Ming-Yee Tsang, seem to reproduce the shape of the experimental torque signals (not shown) but not the orientation. Evidence of strong superparamagnetism with reversal of magnetisation was detected in the a^*b plane, and smaller similar effects were seen in the ac and bc planes. Only the a^*b plane behaved like a superparamagnet (with reversal) and the other measured planes were dominated by paramagnetic anisotropy.

SQUID Magnetometry

Because the experimental and theoretical results did not agree on whether b was an easy or hard axis, single-crystal SQUID magnetometry was performed with **B** applied along b and a. These measurements were done by Dr Michael Slota. The hypothesis was that the magnetic moment, m, of the crystal would be larger and saturate faster when **B** was applied along an easy axis than a hard axis.

At 2 K, it turned out that m is a factor of 8 larger when $\mathbf{B}$ is applied along b than along a and saturates around 1 T (Fig. 4.6a). This behaviour shows that b is an easy axis, in agreement with the CTM measurements and in contrast to the ab-initio calculations. Moreover, direct-current susceptibility measurements (Fig. 4.6b) confirmed easy b (χT decreases with T; purple) and hard a (χT increases with T; violet). Note that χT increases below ~ 10 K for $\mathbf{B} \parallel b$ which indicates ferromagnetic exchange interactions and could be explained by a magnetic phase transition from paramagnetic to superparamagnetic at low T. This was not observed for $\mathbf{B} \parallel a$.

Field-Resolved CTM

A criterion for certain SMM spintronics, e.g. as spin-valves, is molecular magnetic hysteresis. In Section 3.2.4 we explored how field-resolved CTM is capable of detecting magnetic hysteresis derived from torque through Equations 3.10 and 3.11. The angle-resolved CTM discussed above indicated the presence of strong superparamagnetism in the a^*b plane. To further investigate the superparamagnetic properties, field-resolved CTM was performed by sweeping $\mathbf{B}$ back and forth in selected directions labelled A-D and E-H in Figure 4.5e,h, in the a^*b and bc planes, respectively.

Figure 4.7 shows that the hysteresis in the a^*b plane changes drastically depending on the field direction. All loops close (i.e. go to zero M) at zero field but while A yields horizontal curves B and C show anisotropy-breaking effects manifest through decreasing M with increasing B. Surprisingly, D shows a complete inversion of M for $|B| < 0.26$ T indicating magnetisation reversal during the sweep possibly as a consequence of the interplay between the two non-collinear anisotropies. It is around the directions of C and D (close to the ac plane) that we expect the reversal of magnetisation through tunnelling, and the observed inversion observed in D confirms this.

Figure 4.8 reveals very large hysteresis in the bc plane when the field direction is close to the hard ac plane. The largest loops were observed (directions F and G) when $\mathbf{B}$ was aligned close to the Tb–Co axis and the hard axis. In F, the remanent

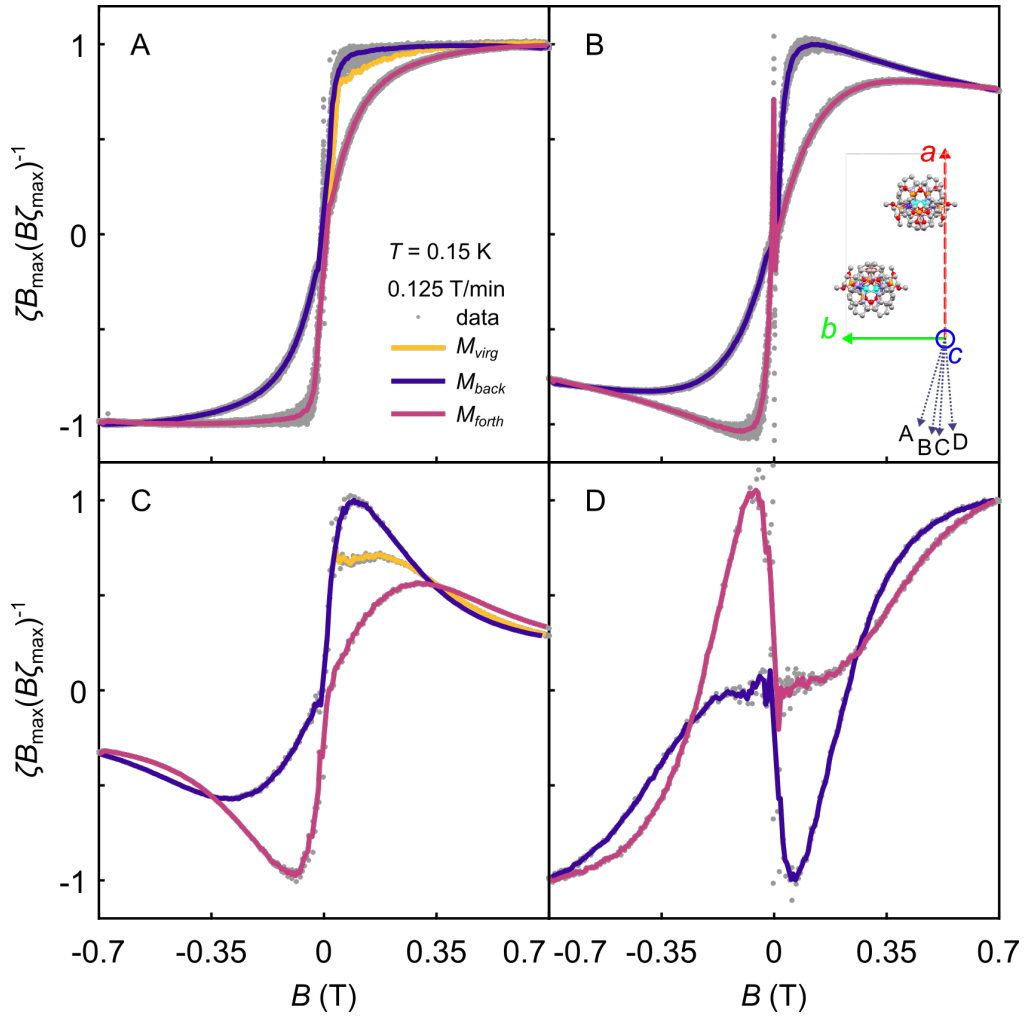


Figure 4.7: The magnetic hysteresis in the a^*b plane. Different directions of **B** are indicated by the letters A-D and correspond to the same letters in Figure 4.6e and is also shown relative to the unit cell in the inset. The dotted arrows in the inset correspond to the positive **B** direction.

magnetisation is around 0.7 and the coercive field is larger than 0.9 T. The sign of M changes between directions E and F because the sign of ζ also changes (Fig, 4.5h).

Moreover, we measured the T dependence of the hysteresis along direction G, i.e. $\varphi = 10°/\varphi = 190°$ in the a^*b plane (Fig. 4.5e). The resulting curves for T between 50 mK and 12 K are displayed in Figure 4.9. The hysteresis is clearly visible below 2 K and is large below 150 mK. At 2 K and above M decreases and the hysteresis disappears due to relaxation through thermal-assisted tunnelling. At 50 mK the remanent magnetisation is between 0.2 and 0.5 $\zeta B_{max}(B\zeta_{max})^{-1}$ and the coercive field is around 160 mT. Notably, the field is applied in the G

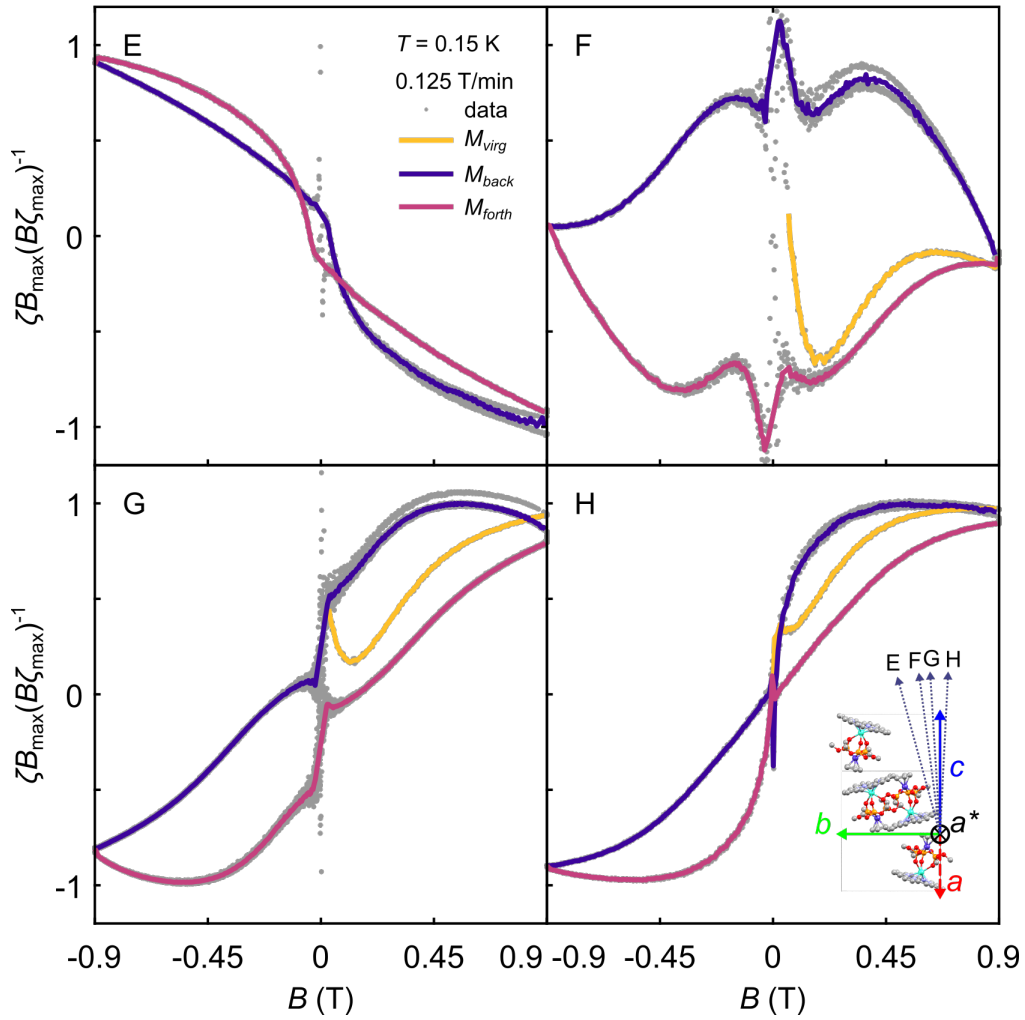


Figure 4.8: The magnetic hysteresis in the *bc* plane. Different directions of **B** are indicated by the letters E-H and correspond to the same letters in Figure 4.6h and is also shown relative to the unit cell in the inset. The dotted arrows in the inset correspond to the positive **B** direction.

direction and corresponds to the minima of the ζ curve in Figure 4.9e,f, i.e. where we assume magnetisation reversal.

4.2.3 Discussion

Through angle-resolved CTM and SQUID magnetometry we have confirmed *b* as an easy anisotropy axis and *ac* as a hard plane. This new information adds to that discovered by Le Roy and coworkers [219]. Furthermore, using field-resolved CTM we have revealed hysteresis in the a^*b and *bc* planes of **TbP** that is several times larger than what has been observed in monolayer $TbPc_2^-$ [221]. The hysteresis

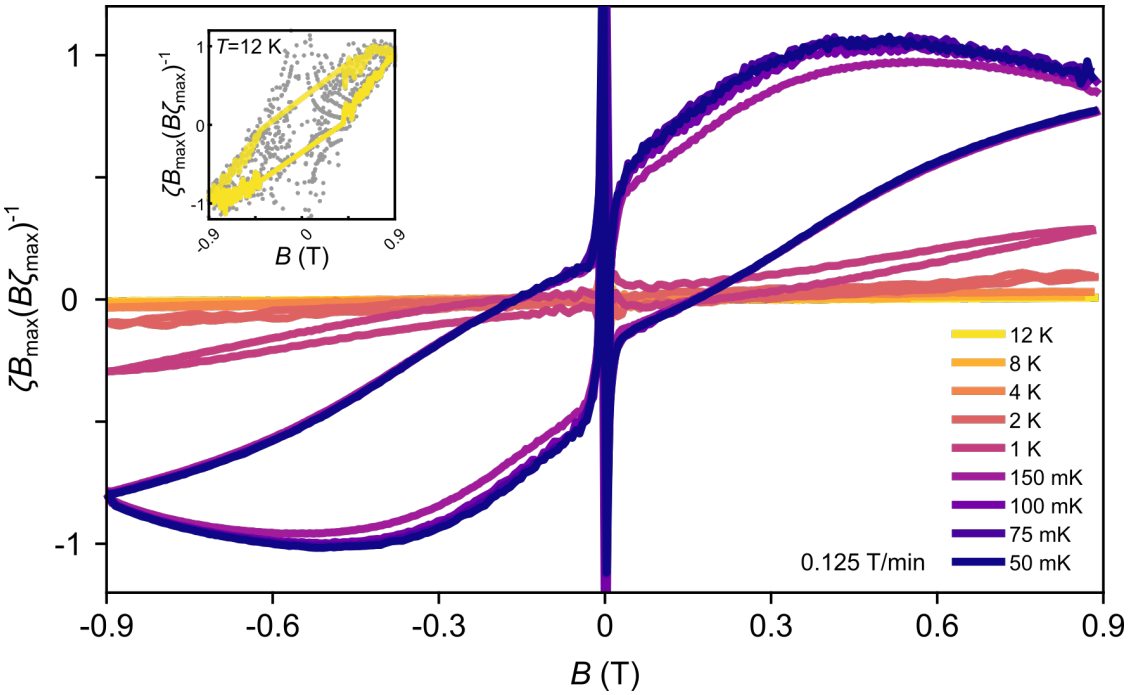


Figure 4.9: TbP exhibits large molecular hysteresis below 150 mK along the **B** direction labelled G in Figure 4.5h. Coloured lines are averages of multiple B sweeps. The inset shows that hysteresis is still present at 12 K.

grew large below 1 K but was visible up to 12 K i.e. 5 K higher than expected from U_{eff} reported in Ref. [219].

A possible explanation for the large hysteresis observed in **TbP** is that the two noncollinear spin centres flip at different φ and, similarly to a ferromagnet, that their interactions with each other breaks time-reversal symmetry. Furthermore, the presence of remanent M and a non-zero coercive field indicate a system that does not allow significant zero-field tunnelling of magnetisation, at least not at 0.125 T/min. Such elongation of magnetic relaxation times has also been observed in variants of $TbPc_2$ that was attributed to interactions between Tb spin centres [222].

Here, we have seen signs of different degrees of superparamagnetic behaviour for different **B** directions. From the direct-current susceptibility data (Fig. 4.6b) a does not stand out as a superparamagnetic axis at low T even though CTM reveals hysteresis close to a^*. Therefore, crystal orientation should always be considered when interpreting single-crystal susceptibility data to determine the presence of magnetic interactions.

While ab-initio calculations suggested easy c and hard ab the experimental data, from both CTM and SQUID, identified b as the easy axis. Therefore, the calculations are likely wrong. However, the shape of the torque curves were strikingly similar to experiments apart from the 90° shift in φ, and suggest that at least the shape of the crystal isoenergy surface should be accurate. In that case **TbP** has a doughnut shaped, easy axis anisotropy, where the transverse terms are dominated by the second B_2^2 coefficient of the series of Stevens operator equivalents.

Our results in this Section confirm that **TbP** exhibit crystal hysteresis. However, single-molecule spin-valves will require molecular hysteresis [38], which our results have not strictly confirmed, although, it is most likely that **TbP** does also exhibit molecular hysteresis. Further research using CTM on terbium porphyrin crystal systems that, through symmetry, reduce to a single molecular anisotropy can confirm the presence of molecular hysteresis.

We note that Crystal 1 and 2 are from different synthesis batches but were assumed identical. A limitation of the study is that no control measurements of the same planes in the two samples were performed to confirm that the anisotropy of compounds were identical. We can therefore not exclude differences in the samples due to synthesis parameters or decomposition over time that could explain the deviations between theoretical calculations and experiments.

Table 4.3: Crystallographic information for **DyP**

Crystal system	Space group	Unit cell parameters						Non-collinear angle (°)
		a (Å)	b (Å)	c (Å)	α (°)	β (°)	γ (°)	
Triclinic	P-1	16.2	23.4	25.5	73.8	89.3	87.0	100

4.3 Dysprosium Porphyrin Monomer Single-Molecule Magnet

We proceed by investigating a dysprosium(III) porphyrin (**DyP**) SMM synthesised by Dr Jennifer Le Roy [219]. Le Roy and coworkers reported that Dy^{3+} ion is seven-fold coordinated by four N atoms of the porphyrin and three O atoms of the Kläui capping ligand, which gives **DyP** a strong anisotropy. Moreover, the Dy^{3+} ion sits 1.21 Å out of the porphyrin plane and and 4.24 Å from the Co^{3+} ion in the capping ligand. Furthermore, the room-temperature $\chi T = 14.16$ cm^3 kmol^{-1} and is in agreement with theoretical values of the Dy^{3+} ion ($^6H_{15/2}$, $S = 5/2$, $L = 5$, $g_J = 4/3$). A dip in χT at low T indicates strong anisotropy but unlike **TbP** no peak below 10 K was observed and therefore no indication of intermolecular ferromagnetic interactions (see Ref. [219] for these data).

DyP is structurally almost identical to **TbP** (Sec. 4.2) with the only morphological difference being that Tb^{3+} is swapped by Dy^{3+}. However, whereas **TbP** crystallises in the monoclinic crystal system **DyP** has a triclinic lattice (Tab. 4.3 that, in contrast to monoclinic, does not require b to be a unique magnetic axis of the crystal. Furthermore, both crystal systems contain an inversion centre that serves to reduce the number of non-equivalent molecules per unit cell from four to two (Fig. 4.10a). The distance between Dy sites in the two non-equivalent molecules is 13.3 Å, i.e. $\sim$ 34% longer than that of **TbP**. On the other hand there are some important differences in the magnetic behaviour: the two molecular anisotropies in **DyP** are non-collinear with an angle of 100° versus 24° for **TbP**, and Dy^{3+} is a Kramers ion, while Tb^{3+} is not.

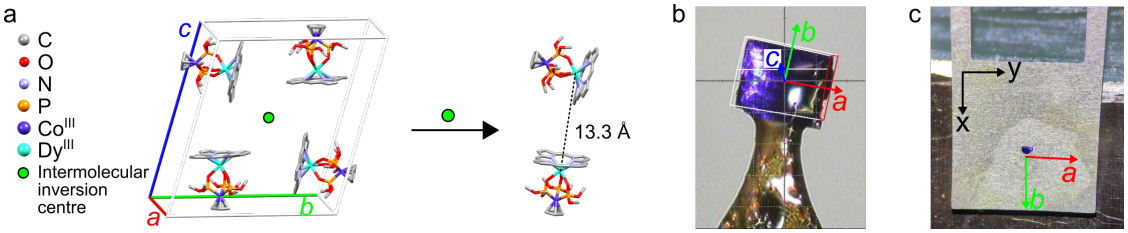


Figure 4.10: (a) DyP crystallises in a triclinic crystal system with four molecules per unit cell. Due to an inversion centre the crystal anisotropy reduces to that of two molecules. **(b)** A **DyP** single crystal labelled with its unit cell axes during face-indexing. **(c)** The face-indexed crystal mounted on a CuBe cantilever for CTM measurements.

4.3.1 Theoretical Predictions of the Ligand Field

Ab-initio calculation were performed for a single **DyP** molecule by Ming-Yee Tsang using MOLCAS. The seven-fold Dy^{3+} coordination environment obtained from the crystal structure was used as active space for the calculation. The calculated Stevens parameters (Tab. 4.4) can be used to simulate torque curves for comparison with experimental CTM data using the Easy Spin toolbox for Matlab [223] (not shown).

Table 4.4: Stevens parameters B_k^q in units of cm^{-1} for **DyP** calculated by Ming-Yee Tsang using CASCSF (MOLCAS). B_k^8 are excluded for brevity but are all below $6.7{\cdot}10^{-7} \cdot 10^{-4}c$.

k	-6	-5	-4	-3	-2	-1	0	1	2	3	4	5	6
B_k^2					-0.15	-0.77	-1.88	-2.87	-0.91				
B_k^4			$-1.3{\cdot}10^{-4}$	-0.033	0.0066	0.011	0.0046	0.039	0.016	-0.017	-0.042		
B_k^6	$4.81{\cdot}10^{-5}$	$2.39{\cdot}10^{-4}$	$3.96{\cdot}10^{-5}$	$2.64{\cdot}10^{-4}$	$-6.44{\cdot}10^{-5}$	$8.15{\cdot}10^{-6}$	$-3.61{\cdot}10^{-6}$	$9.94{\cdot}10^{-5}$	$1.86{\cdot}10^{-5}$	$-2.23{\cdot}10^{-4}$	$2.85{\cdot}10^{-4}$	0.0013	$1.47{\cdot}10^{-4}$

4.3.2 Characterisation of Magnetic Anisotropy

To characterise the magnetic anisotropy of **DyP** single crystals we performed CTM. The crystal was face indexed to relate its crystal faces to its crystallographic axes (Fig. 4.10b) before mounted on a 25-µm thick CuBe cantilever with its bc plane facing the cantilever and b pointing along the x direction and a pointing approximately along y (Fig. 4.10b,c).

Angle-resolved CTM was performed in the bc plane by rotating the field around a^* ($\mathbf{Rot}_{a^*}$) and in the ac plane by rotation around b^* ($\mathbf{Rot}_{b^*}$). The results of $\mathbf{Rot}_{a^*}$ is reported in Figure 4.11a and 4.11b and reveals that the anisotropy in the bc plane has a 180° periodicity with four torque inversions per period. The latter deviates

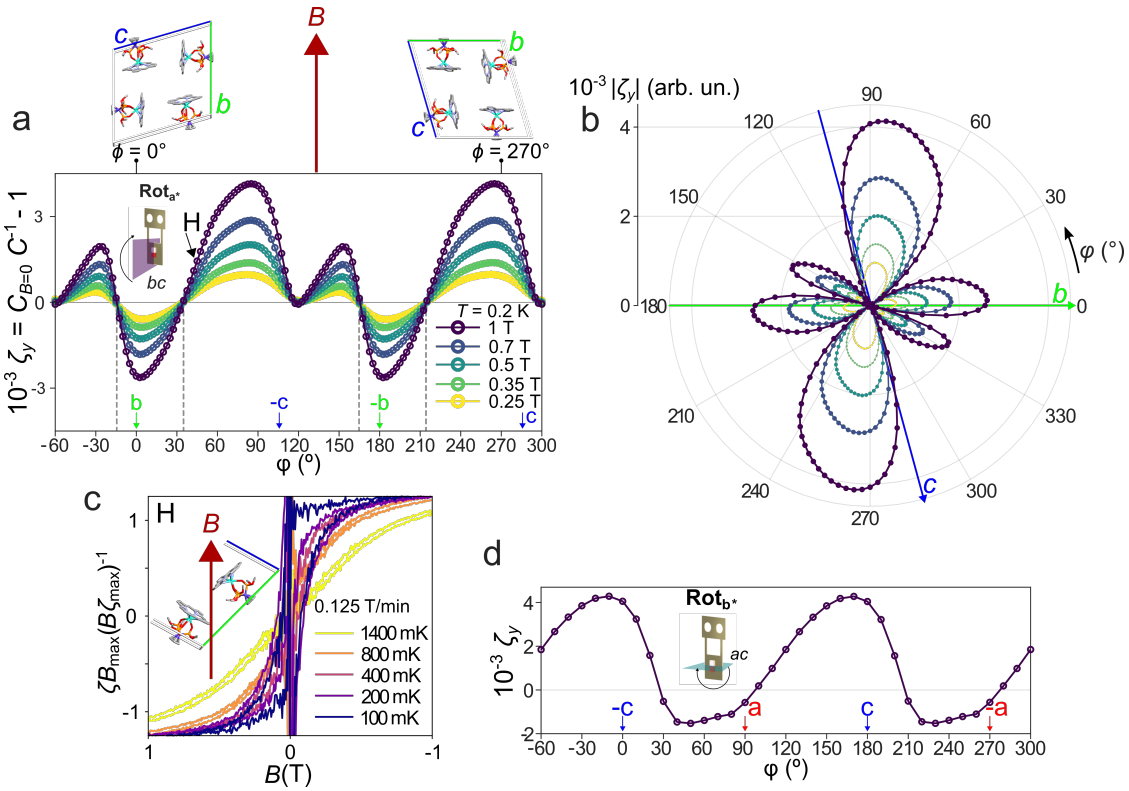


Figure 4.11: Angle-resolved CTM of **DyP**. **(a)** ζ_y vs. φ in the *bc* crystallographic plane for different B at 0.2 K. Cartoons above the panel shows the orientation of the unit cell relative to **B**. **(b)** $|\zeta(\varphi)|$ in polar coordinates highlighting the two-fold symmetry of the anisotropy. **(c)** Hysteresis loops open for $T \leq 400$ mK for **B** along direction H. **(d)** $\zeta(\varphi)$ in the *ac* plane for $B = 1$ T and $T = 0.2$ K.

from the simple picture of a paramagnet with uniaxial anisotropy which only exhibits two torque inversions per period. This effect is likely due to the presence of two non-equivalent anisotropies that manifests as two superimposed torque signals.

Furthermore, hard axes can be identified at $\varphi = -15°$ and 165°, and easy axes at $\varphi = 35°$ and 215°. Between 35° and 110° there is a broad lobe followed by a region of a few degrees where ζ is negative before starting a new period. We observed similar behaviour in Section 4.2 above for **TbP** and attributed it to angle-selective QTM. Moreover, ζ is shifted towards positive values which indicates the presence of superparamagnetism in M. Figure 4.11b highlights the two-fold symmetry of the anisotropy in the **Rot**$_{a^*}$. **Rot**$_{b^*}$ reveals a two-fold anisotropy with 180° periodicity characteristic of a paramagnet but with a shift to positive values that indicates the presence of superparamagnetism.

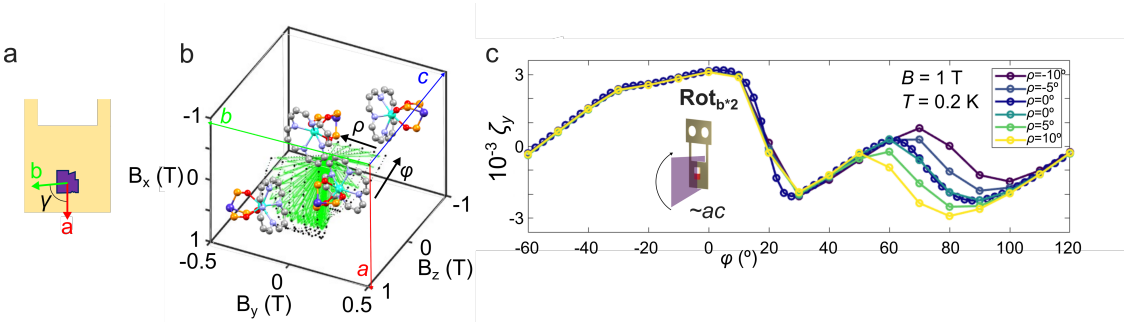


Figure 4.12: Angle-resolved CTM of **DyP** after **(a)** rotating the sample of the cantilever. **(b)** **B** was scanned several times using $\varphi = 180°$ rotations around y plus a small rotation ρ around z. **(c)** The resulting $\zeta(\varphi)$ (only one period is shown) shows large sensitivity to ρ in only one region of φ.

The largest hysteresis in $\mathbf{Rot}_{a^*}$ was observed 45 degrees relative to b (Fig. 4.11c). Hysteresis loops open for $T \leq 400$ mK and increases in size as expected when relaxation mechanisms become less likely with decreasing T. The presence of hysteresis shows that **DyP** is superparamagnetic below 400 mK and is in line with the angle-resolved measurements. The observed hysteresis is significantly smaller than for **TbP** (compare with Figs. 4.7-4.8).

The sample was rotated clockwise by $\sim 90°$ on the cantilever to align a with x and facilitate scans of different crystal planes (Fig. 4.12a). Subsequently, angle-resolved CTM was performed by rotating **B** around $\mathbf{Rot}_{b^*2}$ in the ac plane plus a small rotation ρ around a^* ranging from $\rho = -10°$ to $\rho = 10°$ (Fig. 4.12b). Interestingly, the results shown in Figure 4.12c reveals that only a small range of φ between 50° and 110° seems to be sensitive to ρ, and is another indication that we are observing the manifestation of at least two anisotropies with different behaviour.

4.4 Fused-Porphyrin Dysprosium Dimer SMM

In Section 4.2 we discussed the magnetic properties of a compound in which the Ln ion was sandwiched between a porphyrin and a Kläui capping ligand - a LnP building block. In the present Section we will discuss the magnetic anisotropy of two different isomers of a compound consisting of two dysprosium porphyrin building blocks **DyP** fused together into a dimer. The porphyrins of the two **DyP** are fused

together and are identical in their molecular structures except: (i) the **Z-2**·$\mathbf{Dy_2}$ isomer have both **DyP** pointing in the same direction; (ii) The **E-2**·$\mathbf{Dy_2}$ isomer have their **DyP** point in opposite directions 4.13. Our hypothesis was that the different molecular symmetries of these isomers would cause significantly different molecular anisotropy, despite the isomers being otherwise identical.

Another aspect of the fused-porphyrin Dy dimers is that the electrons in the fused porphyrins are strongly π-conjugated [224]. We expect that these π electrons can move easily inside the porphyrin backbone and therefore couple with their spins to the magnetic moments of both Dy^{3+} sites. Thus, the system contains three quantum systems with assosiated couplings between each other: one for each Dy^{3+} and one for the spins in the π-conjugated conduction channels. These magnetic compounds have obvious potential for molecular-spin-valve applications provided that the single-ion anisotropies within a single molecule are sufficiently different. For this Thesis we characterised the anisotropy to test the mentioned prerequisite.

Herein, we investigate single crystals of the *anti* and *syn* isomers synthesised by Jeff van Raden from the group of Prof Harry Anderson at the Department of Chemistry. **E-2**·$\mathbf{Dy_2}$ crystallises in the triclinic lattice system, and contains two molecules per unit cell (Tab. 4.5; Fig. 4.14a). Each molecule consists of two **DyP** building blocks fused together with the Dy–Ligand axes pointing in the opposite directions. Due to the presence of an intermolecular inversion centre the crystal magnetocrystalline anisotropy effectively reduces to that of a single molecule. Furthermore, the presence of an intramolecular inversion centre effectively reduces the molecular anisotropy to that of a single **DyP** building block. For these reasons the anisotropies on each Dy sites must be perfectly collinear. Moreover, the anisotropy characterisation of the single crystal will reflect the anisotropy of a **DyP** building block.

The **Z-2**·$\mathbf{Dy_2}$ isomer crystallises in the monoclinic lattice system, and also contains two molecules per unit cell (Tab. 4.5; Fig. 4.14b). Each molecule consists of two **DyP** building blocks fused together with the Dy–Ligand group on the same side as the porphyrin backbone. The two Dy–Ligand axes are non-collinear

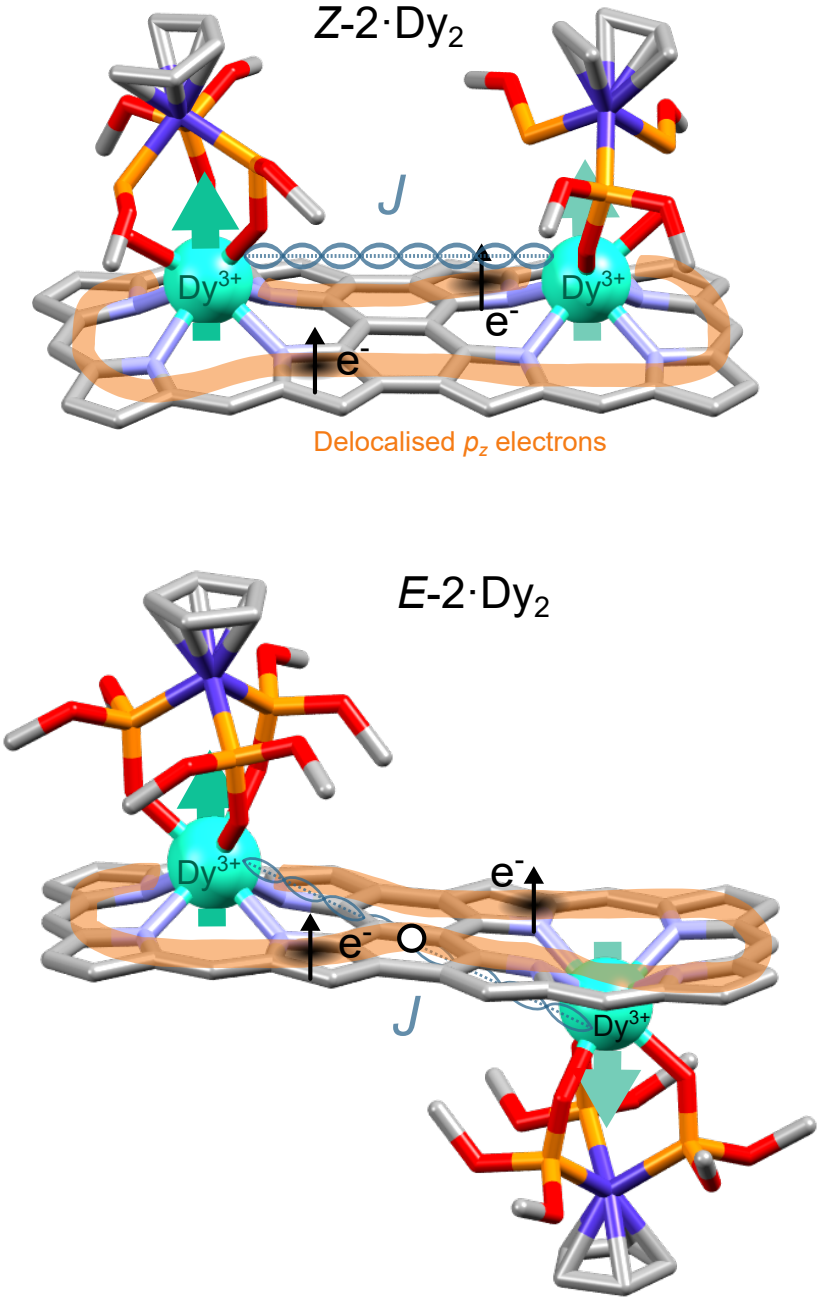


Figure 4.13: Graphical presentation of two isomers of a Dy dimer on a fused porphyrin backbone. Delocalised p_z electrons carry isotropic spins in the delocalised fused porphyrin system. Trivalent Dy ions sit slightly out of plane in the porphyrin centre protected by a Klaui capping ligand. In the **Z-2·Dy$_2$** isomer the Dy centres sits on the same side of the fused porphiren plane, while in the **E-2·Dy$_2$** isomer they sit on opposite sides. The magnetic moments of the Dy^{3+} ions 'feel' each other through the coupling J. The two isomers differ in symmetry as **E-2·Dy$_2$** contains an inversion centre between the **DyP** building blocks with crucial consequences for the magnetic properties (see text).

Table 4.5: Crystallographic information for two fused-porphyrin Dy dimer isomers.

Isomer	Crystal system	Space group	Unit cell parameters						Non-collinear angle (°)
			a (Å)	b (Å)	c (Å)	α (°)	β (°)	γ (°)	
E	Triclinic	P-1	10.53	19.89	20.79	113.2	103.2	100.9	0
Z	Monoclinic	$P2_1/m$	10.35	24.47	29.68	90.0	92.0	90.0	5.4

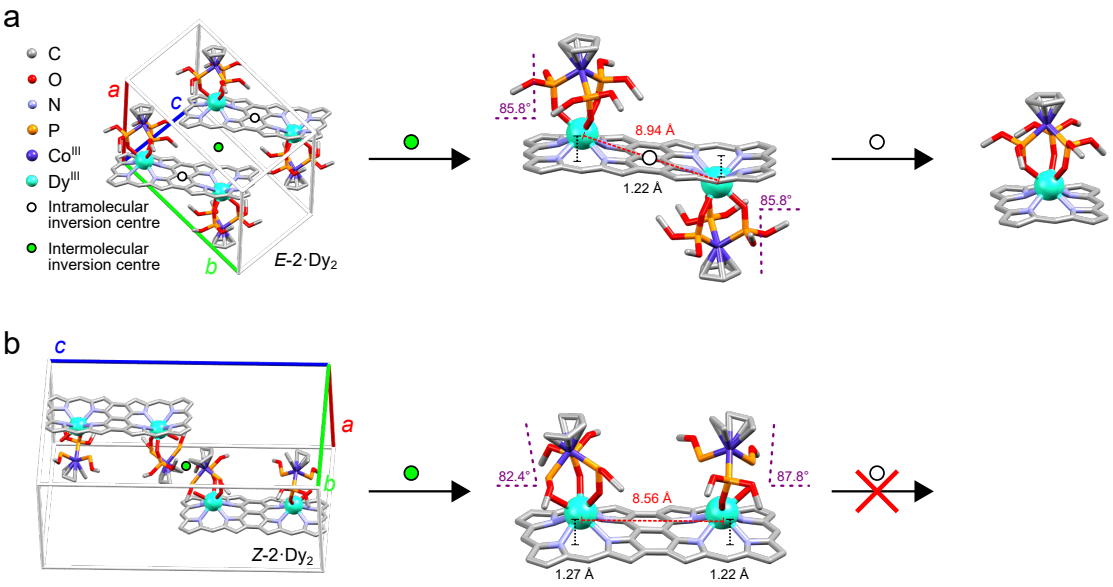


Figure 4.14: The symmetry elements of the two isomers reduce their magnetocrystalline anisotropies. **(a)** The **E-2·Dy$_2$** unit cell contains an intermolecular and an intramolecular inversion centre that effectively reduces the magnetic anisotropy to that of a single **DyP** building block. **(b)** The unit cell of **E-2·Dy$_2$** contains only an intermolecular inversion centre and thus effectively reduces the magnetic anisotropy to that of a single molecule with two non-collinear anisotropies.

with an angle equal 5.4°. The crystallographic unit cell contains a two-fold screw axis along b and consequently an intermolecular inversion centre. In contrast to **E-2·Dy$_2$** it does not contain an intramolecular inversion centre. Therefore, the magnetocrystalline anisopropy of **Z-2·Dy$_2$** reduces to the molecular anisotropy but not to that of **DyP**. As discussed below, this difference in symmetry bears large consequences for the magnetic properties of the isomers.

4.4.1 Characterisation of Magnetic Anisotropy

To characterise the magnetic anisotropy of the two fused-porphyrin Dy dimer isomers we performed single-crystal CTM. The crystals were face indexed to relate their

crystallographic axes to their crystal faces, and subsequently mounted on 50-µm thick CuBe cantilevers. CTM on different crystal orientations was performed by changing the crystal orientation on the cantilever.

Angle-Resolved CTM

We start our analysis with **E-2·Dy$_2$**. Angle-resolved CTM (Fig. 4.15a) was performed in both *ab* and *bc* planes for B in the range 0.25 to 1 T at 200 mK. The results are shown in Figure 4.15b and c. The results show that the anisotropy in the *ab* plane has a 180° periodicity with an easy axis at $\varphi = 90°$, i.e. when **B** points along the porphyrin plane (Fig. 4.15b). There is a plateau of $\sim 10°$ around $\varphi = 0°$ where the torque, ζ, is insensitive to φ. The ζ maxima and minima.

Figure 4.15c shows that the anisotropy in the *bc* plane also has a 180° periodicity with an easy axis at $\varphi = 112°$ that points along the porphyrin plane and close to the *b* axis, and a hard axis at $\varphi = 22°$ also in the porphyrin plane but with a 90° rotation relative to the easy axis (along c^*). Common for both rotation planes is that they produce torque with similar magnitudes for positive and negative torque, as the typical behaviour of a paramagnet.

We proceed with the analysis of **Z-2·Dy$_2$**. On this isomer angle-resolved CTM was performed in the *ab* and *bc* planes for B in the range of 0.35 to 1 T at 200 mK (Fig. 4.15d,e). In stark contrast to **E-2·Dy$_2$**, the ζ of these planes exhibit regions of nearly 180° without torque inversion and is almost always positive. Such behaviour is a fingerprint of superparamagnetic M that are allowed to reverse via tunnelling for certain φ.

The difference in anisotropy between the two isomers can be explained by their different symmetries. As mentioned above, the anisotropy of **E-2·Dy$_2$** is effectively that of one **DyP** building block, while that of **Z-2·Dy$_2$** is the sum of two non-collinear **DyP**. The non-collinearity introduces off-diagonal terms to the anisotropy tensor that promotes tunnelling of magnetisation. For collinear anisotropies the off-diagonal terms must be zero and tunnelling of M is therefore suppressed.

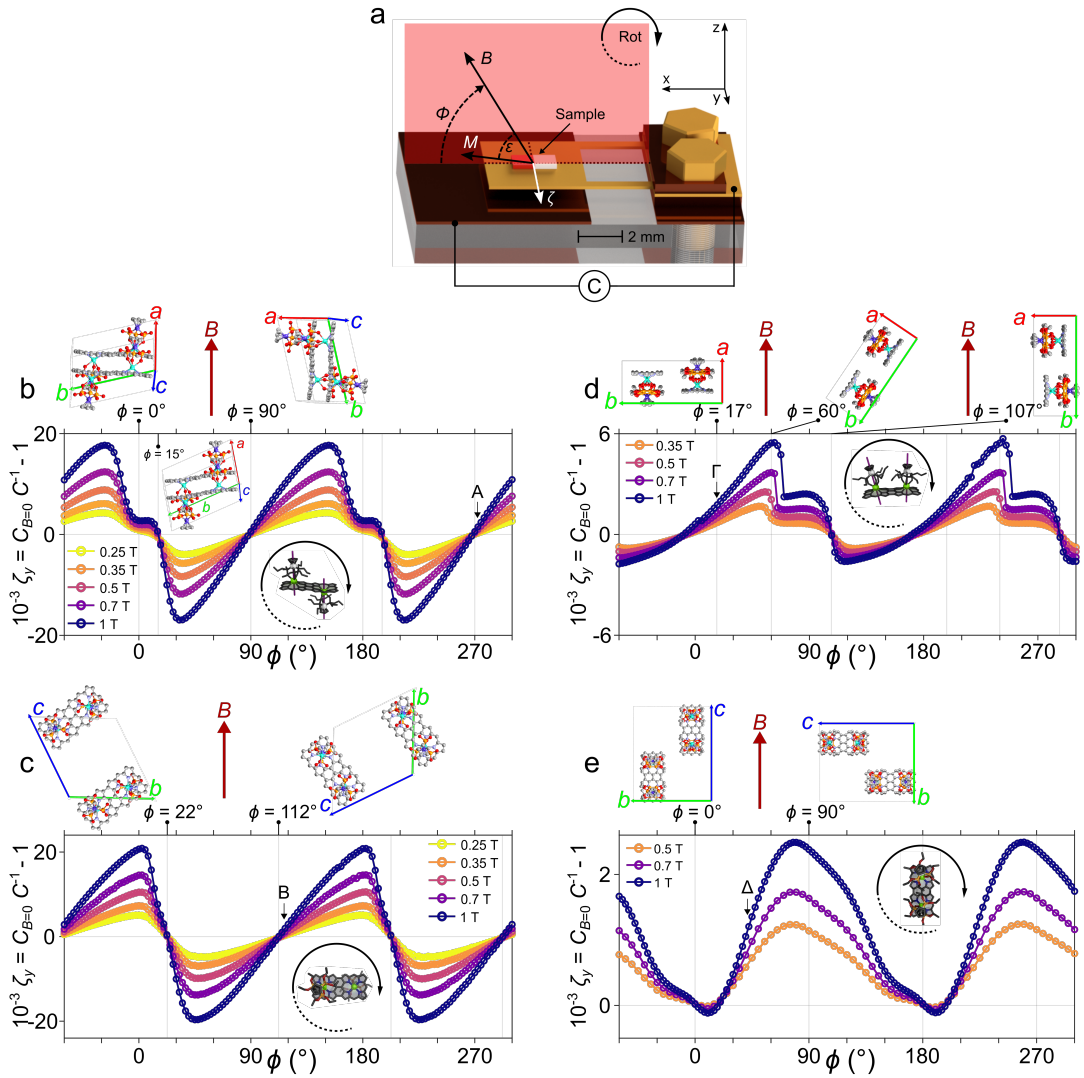


Figure 4.15: Angle-resolved CTM on the two Dy fused porphyrin dimer isomers **Z-2·Dy$_2$** and **E-2·Dy$_2$**. **(a)** The CTM device configuration with the rotation direction indicated on the rotation plane plane **Rot** (red). **(b),(c)** Angle-resolved CTM in the **(b)** *ab* plane, **(c)** *bc* plane of **E-2·Dy$_2$**. **(d),(e)** Angle-resolved CTM in the **(d)** *ab* plane, **(e)** *bc* plane of **Z-2·Dy$_2$** for different B. A cartoon in each panel illustrates the direction of the **B** rotation relative to the molecule. Cartoons above each panel illustrate the orientation of the unit cells relative to **B** for different φ. The symbols A-Δ indicate the value of φ used in the hysteresis measurements presented in Fig. 4.16.

Field-Resolved CTM

The SMM behaviour of both isomers was investigated using field-resolved CTM. **B** was swept between ±1 Tesla along directions specified by symbols A-Δ that correspond to values of φ as indicated in Figure 4.15. A hysteresis loop opens below 1.4 K for both compounds with the cycles increasing with lower T, as expected for SMMs (Fig. 4.16). **E-2·Dy$_2$** exhibits larger hysteresis than **Z-2·Dy$_2$** and is expected based on the two non-collinear anisotropies that suppress tunnelling of M thorugh transverse anisotropy terms. In contrast, the non-collinear anisotropies in **Z-2·Dy$_2$** allow non-zero off-diagonal anisotropy terms that promotes tunnelling of M and result in smaller hysteresis loops.

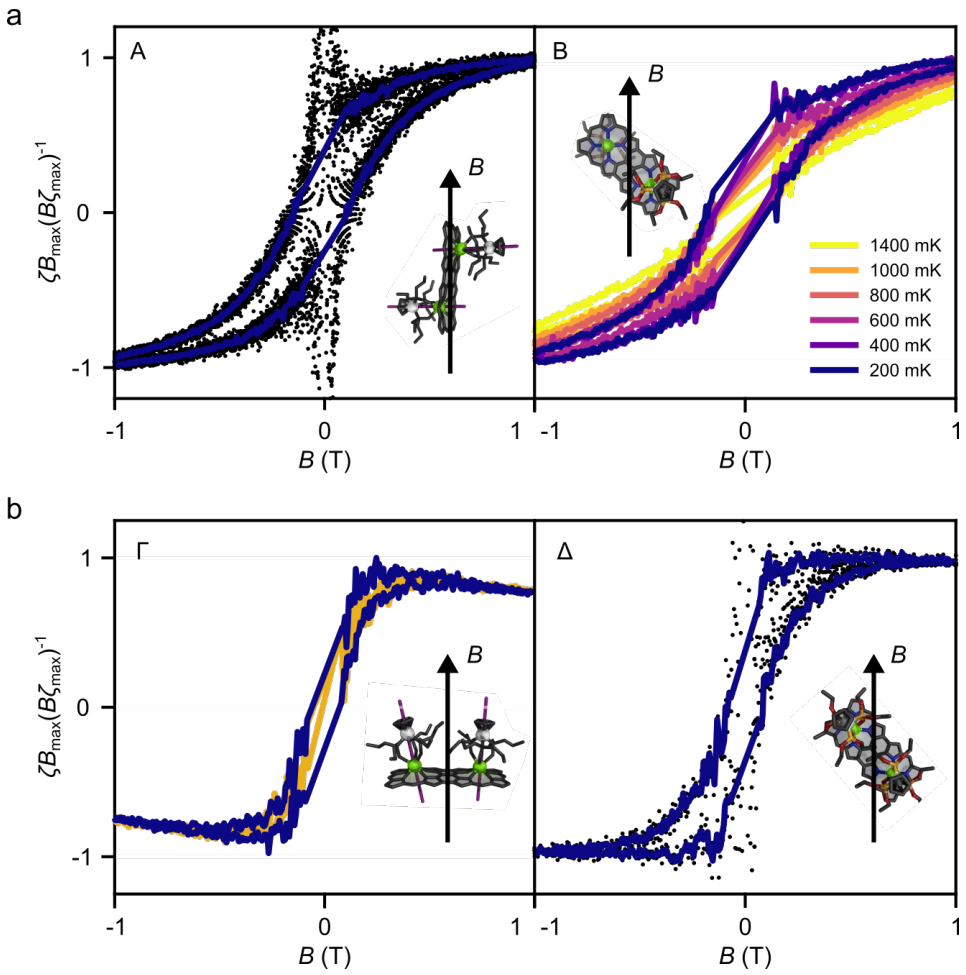


Figure 4.16: Field-resolved CTM revealing different hysteresis in **(a) E-2·Dy$_2$** and **(b) Z-2·Dy$_2$** measured by sweeping between $B = -1$ and $B = +1$ T at φ corresponding to the respective symbols A-Δ. The in-panel cartoons indicate the relative orientation between the molecule and **B**. The blue lines are windowed averages of the data points (black dots) obtained at 200 mK. Lines in other colours represent other T as shown in the legend. The zero-field peaks are replaced with straight lines to guide the eye.

4.5 Dy$_2$-hfac Dimer SMM

In this Section we briefly report our findings on a Dy$_2$-hfac single crystal of unknown crystal structure (see molecular structure in the inset of Fig. 4.18). This sample is the first that we measured and therefore the results are incomplete. The Dy–Dy length is around 4 Å and should lead to a significant dipolar interaction between them. As shown in Figure 4.18 these interaction leads to the opening of large hysteresis loops below 2 K with increasing loop size with decreasing T, as expected when relaxation mechanisms become less effective. Large butterfly-shaped hysteresis

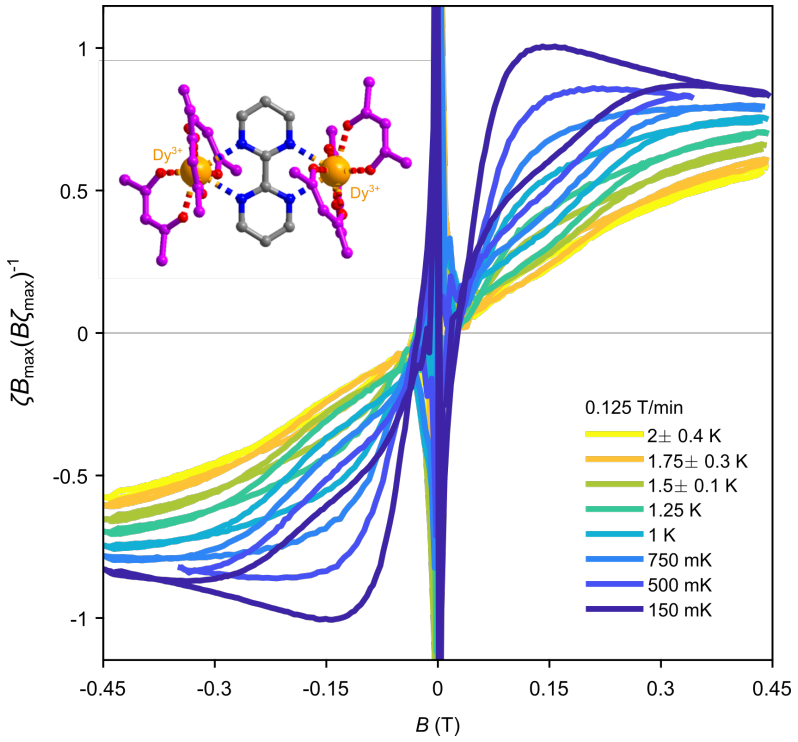


Figure 4.17: Field-resolved CTM on **Dy_2-hfac** reveals large hysteresis below 2 K. Divergence of ζ around zero field is an artefact of the experimental technique.

at 150 mK indicates inefficient relaxation mechanisms at this T when $B \neq 0$ but highly efficient QTM when $B = 0$.

All planes exhibit anisotropy with 180 degree periodicity and two torque inversions per period (Fig. 4.18). While both xy and yz planes generate large signals that are more or less equal extremal values, xz plane shows a small signal that is shifted towards negative torque. Thus there is signature of hysteresis in the xz but because of large uncertainty is the value of C_0 we cannot conclude with hysteresis in this plane only based on this result.

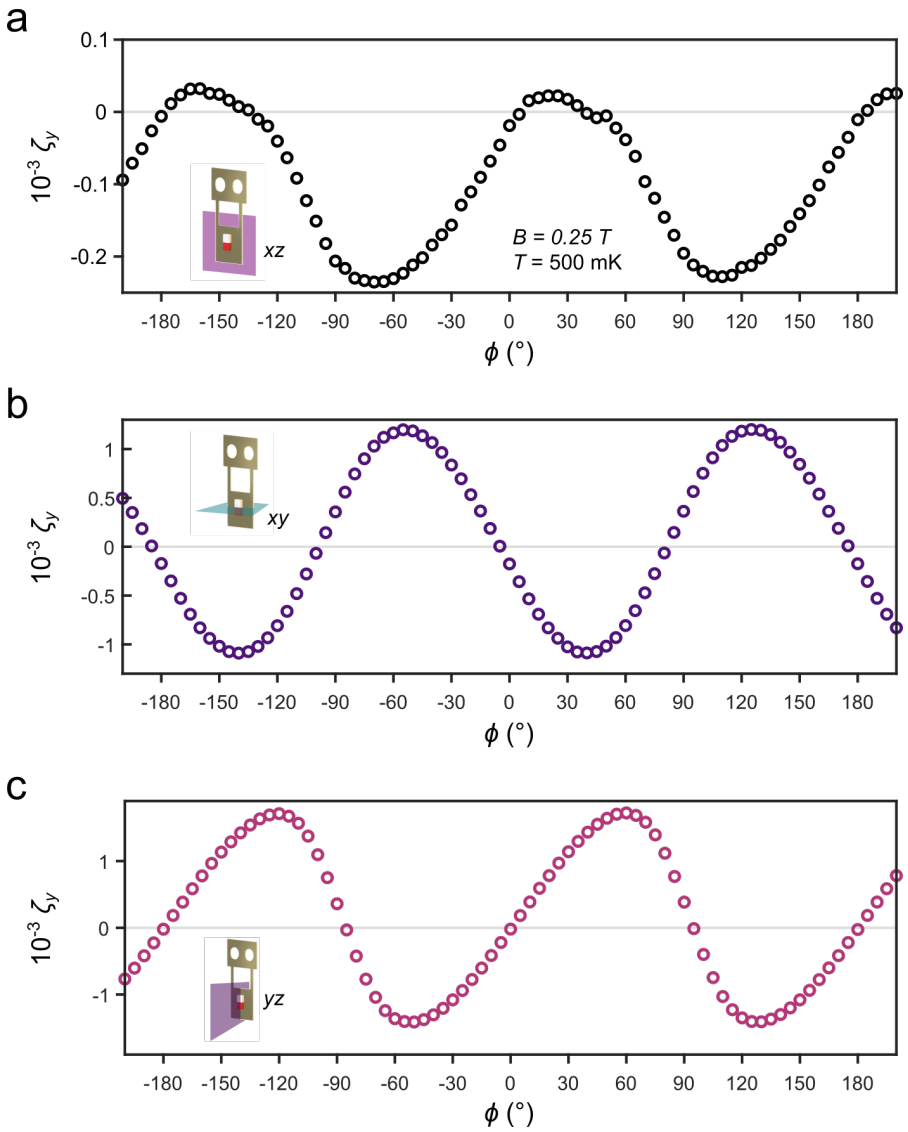


Figure 4.18: Angle-resolved CTM of a **Dy_2-hfac** single crystal of unknown crystal structure acquired using $B = 0.25$ T and at $T = 500$ mK. $\zeta(\varphi)$ is plotted for **(a)** the xz, **(b)** the xy and **(c)** yz plane in the laboratory frame.

4.6 Dysprosium Trimer SMM

In the previous Sections we investigated Tb and Dy monomer and dimer SMMs. Millikelvin torque magnetometry was used to identify the direction of the anisotropy, and the possible presence of interactions between spin centres as the causes of SMM behaviour. Molecular materials that are placed between electrodes, as for single-molecule transport experiments, undergo charging and discharging, as the quantum dots discussed in the introductory chapters. It is thus useful to study the torque

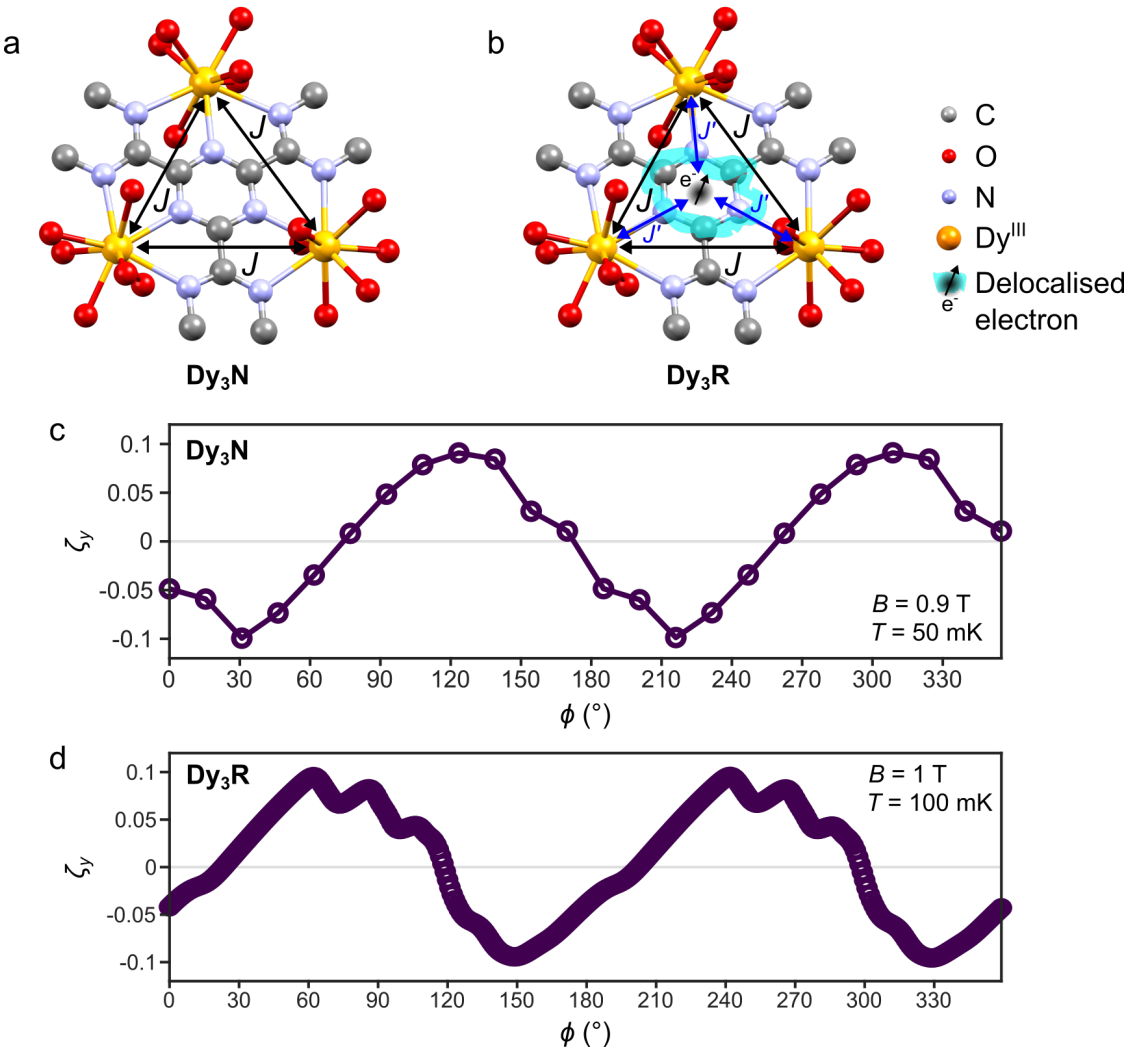


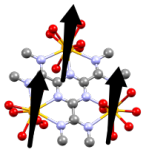
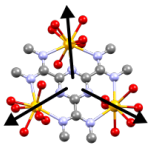
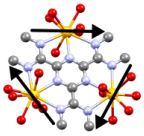
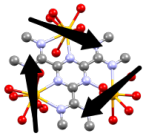
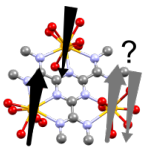
Figure 4.19: Molecular structure of **(a)** $\mathbf{Dy_3N}$ and **(b)** $\mathbf{Dy_3R}$. J (J') indicate the magnetic interaction between Dy^{3+} and Dy^{3+} (Dy^{3+} and delocalised electron). **(c)** $\zeta(\varphi)$ for $\mathbf{Dy_3N}$ for $B = 0.9$ T and $T = 50$ mK, and **(d)** $\zeta(\varphi)$ for $\mathbf{Dy_3R}$ for $B = 1$ T and $T = 100$ mK.

behaviour of a molecular system that can be prepared in differently-charged states.

To this aim, in the present Section, we will study two Dy trimer SMMs: one with neutral charge, $\mathbf{Dy_3N}$, and one radical, $\mathbf{Dy_3R}$, that contains an additional electron that is delocalised on the molecular backbone (Fig. 4.19a,b). Both molecules have planar backbones and a three-fold rotational symmetry of the Dy^{3+} ions, so that that all three Dy spin centres are equivalent.

The exchange and dipolar interactions between Dy^{3+} centres determine the single-ion orientation. For this molecule there are several options: (i) Ferromagnetic,

Table 4.6: Possible magnetic ordering of the Dy^{3+} ions in $\mathbf{Dy_3N/R}$.

Magnetic ordering	Ferro-magnetic	Radial	Tangential	Spin spiral	Frustrated antiferro-magnetic
Illustration					

i.e. all spins collinear and pointing in the same direction; (ii) radial, i.e. non-collinear spins pointing along the disc-shaped molecular's radial direction; (iii) tangential, i.e. non-collinear spins pointing along the tangential direction; (iv) spin spiral, i.e. a combination of ferromagnetic and tangential where spins have a tangential and an out-of-plane component; (v) frustrated antiferromagnetic, i.e. when the three spins prefer to align antiferromagnetically but is prevented by the odd number of moment carrying centres (Tab. 4.6). Our hypothesis is that the additional delocalised electron in the radical will alter the magnetic anisotropy relative to the neutral compound. This difference should thus be manifest in CTM measurements.

Angle-resolved CTM was performed on both compounds to map their magnetic anisotropy as functions of the angle φ of $\mathbf{B}$. Indexed crystal were not available, so CTM was performed on arbitrarily-oriented single crystals. Both compounds display similar torque shapes with 180° periodicity and two torque inversions per period (Fig. 4.19c,d).

The first major difference between $\mathbf{Dy_3N}$ and $\mathbf{Dy_3R}$ was observed in the finer details of $\zeta_y(\varphi)$ (Fig. 4.19c,d). The torque of $\mathbf{Dy_3R}$ displays three shoulders around 60°, 80° and 110° that are not discernible for $\mathbf{Dy_3R}$ and could indicate the presence of three different, non-collinear spin moieties. These shoulders indicate partial breaking of the anisotropy when an increase in φ results in $\mathbf{M}$ and $\mathbf{B}$ moving closer together. Interestingly, the only one shoulder reappears when the torque is negative indicating that they must arise from hysteresis in a superparamagnetic $\mathbf{M}$. However, there are signs of smaller kinks in the torque of $\mathbf{Dy_3N}$ too between 135° and 220° that are hard to interpret due to the low angular resolution of the data.

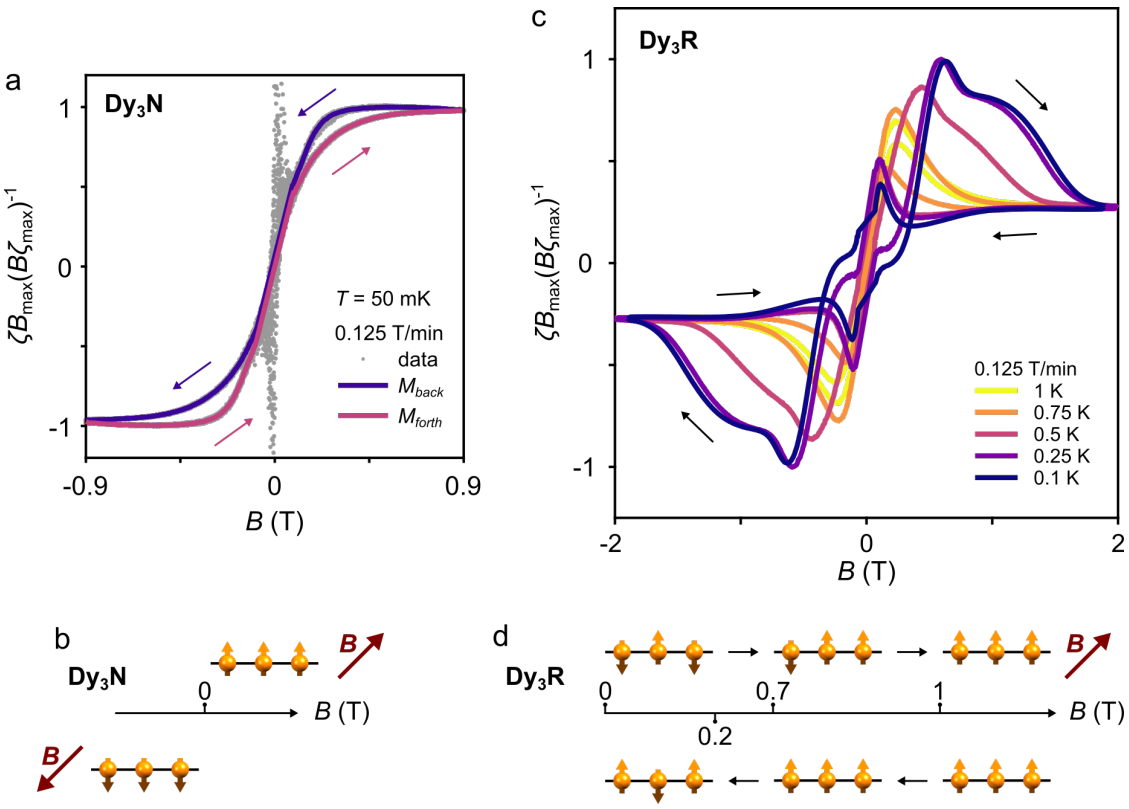


Figure 4.20: Field-resolved CTM reveals small magnetic hysteresis in **(a)** $\mathbf{Dy_3N}$ and **(b)** large hysteresis in $\mathbf{Dy_3R}$. **(c)** Spin configuration of the Dy^{3+} ions in $\mathbf{Dy_3N}$ for positive and negative B. **(d)** Step-wise reversal of Dy^{3+} spin as a function of B for $\mathbf{Dy_3R}$. **B** is displayed at an arbitrary angle as the crystal orientation relative to **B** is unknown.

$\mathbf{Dy_3N}$ exhibits a small 'butterfly-shaped' hysteresis loop at 50 mK (Fig. 4.20a). This behaviour could be explained by a ferromagnetic ordering of three magnetically equivalent Dy^{3+} ions that reverse via strong QTM at zero field (Fig. 4.20b).

In stark contrast, $\mathbf{Dy_3R}$ displays large and complex hysteresis (Fig. 4.20c). At 100 mK the signal increases sharply at low B before a Dy^{3+} spin flip causes a peak at around 0.7 T (Fig. 4.20d). After a plateau at around 1 T the spin of another Dy^{3+} flips and results in saturation at 2 T with all three Dy^{3+} ions ordered ferromagnetically. It seems that this ordering is particularly stable at higher B because the signal remains insensitive to B on the 'back' sweep until about 0.2 T where another flip occurs. At higher T QTM is thermally assisted and results in earlier spin flips, saturation at lower B and smaller hysteresis loops.

The peculiar hysteretic behaviour of $\mathbf{Dy_3R}$ could indicate a frustrated anti-ferromagnetic ordering of the Dy^{3+} ions (Tab. 4.6). In this picture the ions do

not readily flip at zero field but rather inside regions of B where QTM is not suppressed. In contrast to $\mathbf{Dy_3N}$, such behaviour indicate multiple non-equivalent spin moieties that require different magnetic environments to be able to reverse through QTM. This observation is in agreement with the three shoulders observed in the $\zeta(\varphi)$ signal (Fig. 4.19d).

These results reveal a striking difference between $\mathbf{Dy_3N}$ and $\mathbf{Dy_3R}$. The two molecules are seemingly identical except for the radicals' additional electron. However, the presence of this additional electron has huge impact on the magnetic anisotropy. One reason for the large difference is the additional exchange parameter J' in $\mathbf{Dy_3R}$. While the exchange in $\mathbf{Dy_3N}$ could be that of super-super-super exchange (three atoms between Dy^{3+} ions; typically very small in energy), one could envisage that the delocalised electron in $\mathbf{Dy_3R}$ provides a shortcut across the backbone and facilitates an effective super-exchange path between Dy^{3+} ions (typically much larger in energy). Another possible explanation is that the added electron in $\mathbf{Dy_3R}$ distorts the molecular away from its three-fold symmetry rendering the Dy^{3+} ions non-equivalent. Such distortion could propagate into the crystallographic packing arrangement. We do not know if crystal symmetry reduces the effective magnetocrystalline anisotropy to that of a single molecule and we must therefore be cautious in drawing conclusions.

It is fascinating that the two compounds with different charge exhibit such different anisotropy. Although our limited analysis cannot disentangle all the anisotropy information, it stimulates further research on these compounds. Further studies should include CTM and SQUID magnetometry on samples oriented relative to their crystal structure. While CTM is useful to disentangle magnetic anisotropy SQUID could detect ions ordered in spin spirals. Moreover, ab-initio calculations using CASSCF would be invaluable in quantifying the contributions of the Stevens operators to the magnetic anisotropy.

4.6.1 Conclusions

In this section we have shown how angle-resolved CTM, sometimes in conjunction with SQUID magnetometry and ab-initio calculations, can be used as a fundamental tool to explore the magnetic anisotropy of molecular magnets. Because of reasons that will appear evident in the upcoming chapters, we have paid particular attention to porphyrin based molecular magnets such as **TbP** and **DyP** SMMs and their dimers. The experimental results suggest that the crystal anisotropy is dominated by uniaxial, easy-axis contributions.

In **TbP** and **DyP** SMMs the SMM behaviour is confirmed by hysteresis below 12 K that grows as T decreases and becomes particularly large below 1K. The size of the hysteresis loops and manifestations of superparamagnetism in CTM curves are strongly dependent on the direction of **B**. The a^*b plane, which lies close to the porphyrin plane, exhibits the behaviour of a superparamagnet with complete reversal of M every 180°. Contrary to naive expectation based on the molecular shape, we find the largest hysteresis close to the ac plane where **B** is pointing close to the non-collinear Tb–Co molecular axes. Using CTM we have discovered that **DyP** is a SMM below 400 mK that has a magnetocrystalline anisotropy likely consisting of at least two contributions of different nature that responds differently to **B**. Moreover, the component of **M** that is detectable with CTM is predominantly paramagnetic but with a smaller superparamagnetic component at low T.

The hysteresis is smaller than what we observed for **TbP** but arises below similar T. Moreover, through smaller vertical shifts in $\zeta(\varphi)$ and less hysteresis, **DyP** displays less manifestation of superparamagnetism than **TbP**. The presumably smaller dipolar interaction between Dy centres caused by longer Dy–Dy distance than that of **TbP** could be one reason. Another reason could be the larger non-collinearity in **DyP** that could increase the overlap of transverse (off-diagonal) anisotropy terms and thus increase the probability of magnetisation reversal through QTM. A third reason could be differences in the single-ion anisotropies of the Kramer's ion Dy^{3+} and the non-Kramer's ion Tb^{3+}.

The difference in dipolar coupling in the two compounds could be quantified using single-crystal continuous-wave EPR [58]. The impact of non-collinearity could be assessed by comparing the present results with those of a crystal with a higher symmetry that reduces the number of non-equivalent molecules in the unit cell to one because in that case the anisotropies must be collinear. The latter would also yield information about the single-ion anisotropies and could be analysed together with ab-initio CASSCF calculations to provide better understanding.

DyP will be revisited in Chapter 5 where we will investigate the differences between the magnetocrystalline anisotropy of the single crystal and the molecular anisotropy of the single molecule on a surface. This analysis will demonstrate how CTM and magnetotransport spectroscopy can compliment each other in unravelling the magnetic anisotropy of lanthanide-based SMMs.

5

Comparison of the Magnetic Anisotropy of a Dysprosium SMM in Single-Crystals and Single-Molecule Transport

Contents

5.1 Introduction 109
5.2 DyP Single-Molecule Transistor 110
5.3 Magnetotransport Spectroscopy of DyP 113
5.4 Comparison of Magnetotransport Spectroscopy with CTM 116
5.5 Discussion 117
5.6 Conclusions 118

5.1 Introduction

In Chapter 4 we saw how the strong magnetic anisotropy in **M** of SMM single-crystals manifests in the magnetic torque and how CTM is an excellent tool to study this phenomenon. However, we also faced the limitation posed by the crystal environment that restricts the analysis to the magnetocrystalline anisotropy and prevents the access to the anisotropy of the single molecule. Fortunately, state-of-the-art nanofabrication techniques allow the realisation of single-electron transistors with

single SMM molecules as gated transport channels (Sec. 2.4.2). In this configuration, the energies of SMM charge states can be accessed electronically, as well as ground and excited states within each charge state. The magnetic anisotropy of these states can be probed by subjecting the sample to magnetic fields in different directions. In this Chapter we will study the single-molecule magnetic anisotropy of a dysprosium porphyrin SMM as a single-molecule using magnetotransport spectroscopy, and compare it to our CTM analysis of the single-crystal **DyP** from Section 4.3. We will do this to answer the question: how does the magnetic anisotropy of **DyP** differ in the single-crystal and single-molecule environments?

For this project, Dr James Thomas synthesised the chemical compounds, and the device fabrication and magnetotransport measurements were done by Dr Tian Pei, and Dr James Thomas and Prof Lapo Bogani treated the transport data presented in Figures 5.2c, 5.3a,b and 5.5a and Table 5.1. For this Thesis we extended their analysis by comparing the magnetic anisotropy of the single-molecule with that of the single-crystal. Figures 5.3a,b and 5.5a are adapted with additional fits, markers and CTM data to guide the comparison.

5.2 DyP Single-Molecule Transistor

In Section 4.3 we studied the anisotropy of the magnetisation of **DyP** using CTM, and treated the system as two non-collinear easy-axis anisotropies each with a ${}^6H_{15/2}$ ground state. Here, the molecule under testing is a single **DyP** modified with one anchor group at both ends of the porphyrin ligand (Fig. 5.1a). The anchor groups forms π bonds with the p_z orbitals of the graphene leads and thereby facilitate stable electrical connection between molecule and leads.

A **DyP** single-molecule transistor was fabricated to probe the molecular states using magnetotransport spectroscopy. The integrated circuit of the device was made from graphene patterned to a bow-tie shape (Fig. 5.1b) forming the source and drain electrodes. A few-nanometres long tunnelling junction was created in the graphene constriction using a feedback-controlled electro-burning method.

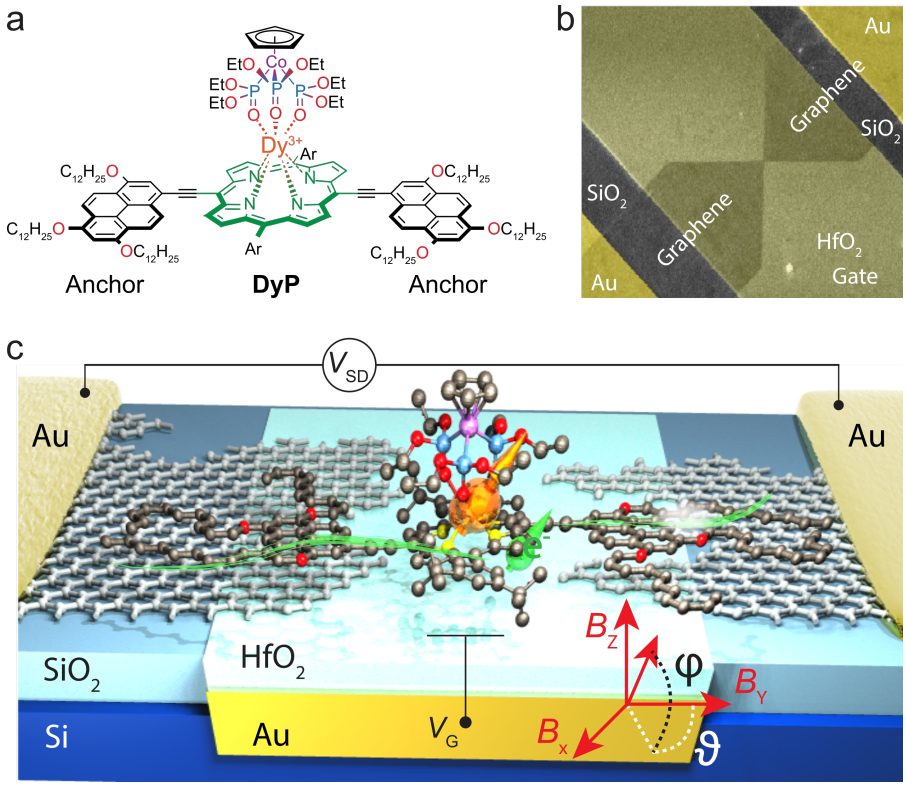


Figure 5.1: **(a)** Schematic drawing of the **DyP** molecule modified with anchor groups. **(b)** Electron micrograph of one device showing graphene leads, SiO_2 and HfO_2 substrates, and Au leads. **(c)** Graphical illustration of the single-molecule transistor. **DyP** bridges the nanogap between the graphene leads. When a molecular level lies between the chemical potentials of the leads sequential electron tunnelling takes place through **DyP**, one electron at a time. Adapted from Ref. [225].

Finally, single-molecule transistors were made by drop-casting **DyP** from a 2-mM solution onto the nanogaps.

An Au local gate separated by 10 nm of HfO_2 served to apply an electrostatic gate voltage, V_g, to the tunnel junction [226]. This shifted the differently charged molecular states $\mu(\mathrm{DyP}^+)$ and $\mu(\mathrm{DyP})$ relative to the chemical potentials of the graphene leads by an amount $\beta e V_g$ (β: gate lever arm) and enabled gating of the single-molecule transistor. The bias voltage, V_{sd}, applied across the source and drain electrodes served to change their respective chemical potentials by $\mu_s = eV_{sd}/2$ and $\mu_d = -eV_{sd}/2$. Only when the criterion for resonant transport was fulfilled namely,

$$eV_{sd} > \mu(\mathrm{DyP}^+) + \beta e V_g > -eV_{sd}, \tag{5.1}$$

a tunnel current I_{sd} will flow through the device (Fig. 5.2).

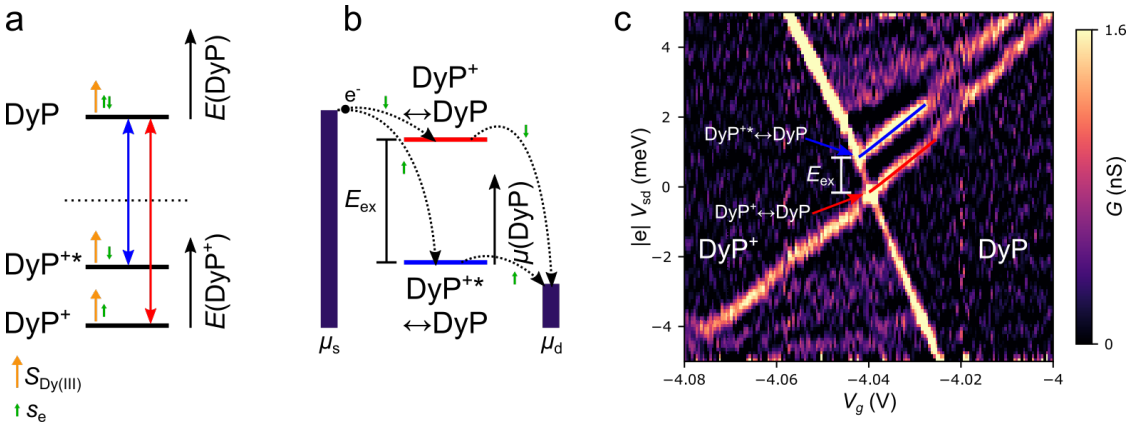


Figure 5.2: **(a)** Energy level diagram for $\mathbf{DyP^+}$/**DyP** with two transitions indicated by red and blue arrows (involving ground and excited states) and **(b)** their corresponding chemical potentials, $\mu = E(\mathbf{DyP}) - E(\mathbf{DyP^+})$, separated by the exchange energy, E_{ex}. The moleculare states lie within the bias window spanned by the lead potentials μ_s and μ_d which allows resonant charge transport. The orange (green) arrows indicate the spin of the Dy^{3+} (e^- on the porphyrin). **(c)** The experimental conductance stability diagram showing resonant transport between $\mathbf{DyP^+}$ and **DyP**, with lines corresponding to the two transitions. Panel **(c)** is adapted from Ref. [225].

In the single-molecule transistor environment different **DyP** charge states can be probed by adjusting V_g. The porphyrin ligand is the redox active part of the molecule because its redox potential is much lower than that of Dy^{3+} [227]. The conduction channel is therefore through the conjugated porphyrin system and no Dy orbitals are directly involved. Instead, the role of the Dy^{3+} ion is that of a SMM with an effective spin $S_{eff} = 1/2$ with a large Landé factor $G_{eff} = 18$ [219] that interacts with the conduction channel via exchange and dipolar coupling. The oxidised cation $\mathbf{DyP^+}$ has one unpaired electron on the porphyrin ligand with spin $s = 1/2$ and Landé factor $g = 2$. Thus, the $\mathbf{DyP^+}$ spin system can be described as $|S_{eff}, s\rangle$ where s can align either ferromagnetically or antiferromagnetically with the Dy spin, i.e. $|\uparrow,\uparrow\rangle$ or $|\uparrow,\downarrow\rangle$. The exchange interactions give rise to a zero-field splitting between the ground state (GS) $|\uparrow,\uparrow\rangle$ named $\mathbf{DyP^+}$ and the excited state (ES) $|\uparrow,\downarrow\rangle$ named $\mathbf{DyP^{+*}}$.

When the resonance criterion for $\mathbf{DyP^+}\leftrightarrow\mathbf{DyP}$ is fulfilled, conduction through the molecule happens as follows: first an electron in the porphyrin HOMO tunnels out through the right anchor ligand and then the drain. This process oxidises **DyP** to $\mathbf{DyP^+}$ and the porphyrin's HOMO to a SOMO. Then an electron from the

source tunnels into the left anchor and then into the SOMO left by the original electron and thereby reduces the molecule back to **DyP**. The measured conductance value is proportional to the probability of this multi-step process. The spin-1/2 electron in the porphyrin channel feels the magnetic moment of the $\mathbf{DyP}^+$ via the exchange interaction that splits the channel into $|\uparrow,\uparrow\rangle$ and $|\uparrow,\downarrow\rangle$. Therefore, the electron must be $|\uparrow\rangle$ for the $\mathbf{DyP}^+\leftrightarrow\mathbf{DyP}$ (GS↔GS) transition and $|\downarrow\rangle$ for the $\mathbf{DyP}^{+*}\leftrightarrow\mathbf{DyP}$ (ES↔GS) transition, i.e. I_{sd} associated with the two transitions are spin polarised (Fig. 5.2b).

Figure 5.2c shows the conductance $G = \partial I_{sd}/\partial V_{sd}$ in the resonant region between $\mathbf{DyP}^+$ and **DyP**. The ZFS is a result of the exchange interaction imposed by the strongly anisotropic Dy^{3+} ion on the isotropic porphyrin spin. It manifests in the energy difference, $E_{ex} = 0.8$ meV, between the conductance lines produced by the $\mathbf{DyP}^+\leftrightarrow\mathbf{DyP}$ (GS↔GS; red line) and $\mathbf{DyP}^{+*}\leftrightarrow\mathbf{DyP}$ (ES↔GS; blue line).

5.3 Magnetotransport Spectroscopy of DyP

We proceed by investigating the anisotropy of this exchange interaction through magnetotransport spectroscopy performed by Dr Tian Pei. I_{sd}-V_g traces were obtained between $V_g = -4.05$ and -4.01 V, with V_{sd} fixed at 1.5 mV, and $\mathbf{B}(\varphi)$ of 1 T applied along φ in the yz plane (see Fig. 5.1c) for $\varphi = 0°$ to 360°. The resulting plots (Fig. 5.3a,b) shows that the energies of both $\mathbf{DyP}^+$ and $\mathbf{DyP}^{+*}$ varies with φ and therefore indicate that the exchange interaction is anisotropic. The positions of the transitions $\mathbf{DyP}^{+*}\leftrightarrow\mathbf{DyP}$ and $\mathbf{DyP}^+\leftrightarrow\mathbf{DyP}$ were fitted using a sum of cosine terms given by Equation 5.2:

$$E(\varphi) = A\sum_{n=0}^{N} C_n \cos(2n\varphi), \tag{5.2}$$

where C_n indicate the weights of the cosine terms and A is a scaling parameter (Tab. 5.1). As expected, the amplitude of the ferromagnetic configuration $\mathbf{DyP}^+$ is substantially larger than that of the antiferromagnetic $\mathbf{DyP}^{+*}$. As expected for antiferromagnetic spin configuration, $\mathbf{DyP}^{+*}$ has significantly lower energy when $\mathbf{B}(180°)$ points along the porphyrin plane.

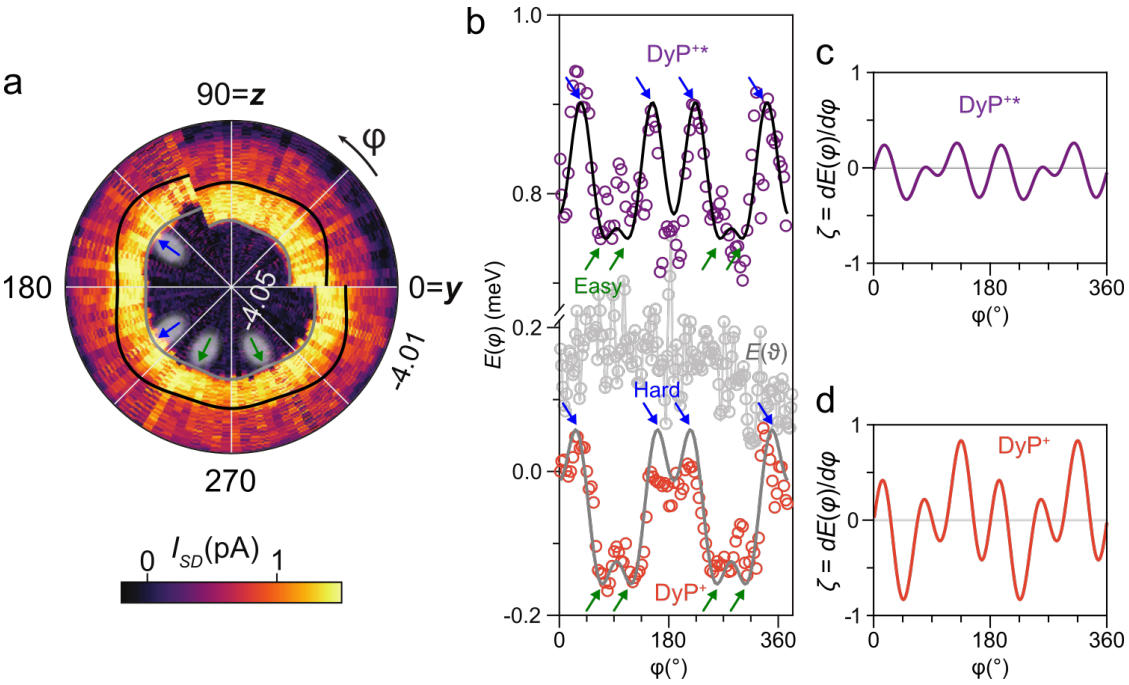


Figure 5.3: **(a)** I_{sd} versus V_g between -4.05 and -4.01 V and magnetic-field angle φ and at $V_{sd} = 1.5$ mV upon rotating **B** in the yz plane at 1 T and plotted in polar coordinates. The green (blue) arrows indicate easy (hard) axes. The radial shift observed between 0° and 100° is due to a spurious charge switch. Solid grey (black) lines correspond to fits calculated using Eq. 5.2. **(b)** Circles correspond to the positions of the I_{sd} steps in panel **(a)** versus φ calculated using $E = \beta e V_g$. Solid lines are fits using Eq. 5.2 (equivalent to **(a)**). The rotation in the xy plane (grey circles) were largely insensitive to ϑ. **(c,d)** Torque for **DyP**$^{+*}$ and **DyP**$^{+}$ calculated from the fits of $E(\varphi)$ using Eq. 3.8. Panels **(a)** and **(b)** are adapted from Ref. [225].

Table 5.1: Fitting parameters used for fitting data in Fig. 5.3b using Eq. 5.2.

	A	C_0	C_1	C_2	C_3	C_4
DyP^{+}	0.444	–0.128	0.151	–0.020	–0.069	–0.003
DyP^{+*}	0.875	0.936	0.034	–0.038	-0.028	0.002

Interestingly, multiple maxima and minima of $E(\varphi)$ indicate multiple hard and easy axes, respectively. Both **DyP**$^{+}$ and **DyP**$^{+*}$ exhibit $E(\varphi)$ with 180° periodicity and two easy axes and two hard axes per period at positions reported in Table 5.2. Such behaviour can be caused by a set of cone shaped anisotropies along the axis normal to the porphyrin plane with apertures equal to Δeasy and Δhard (Fig. 5.4). This hypothesis is supported by $E(\vartheta)$ obtained by rotating $\mathbf{B}(\varphi)$ in the xy plane, which is largely insensitive to ϑ (i.e. isotropic) because the projections of the

Table 5.2: Values of φ corresponding to easy and hard axes of $E(\varphi)$ and the differences Δ for $\mathbf{DyP}^{+}$ and $\mathbf{DyP}^{+*}$.

	easy (°)	**hard (°)**	**Δeasy (°)**	**Δhard (°)**
$\mathbf{DyP}^{+}$	68 112	26 154	44	128
$\mathbf{DyP}^{+*}$	73 107	34 146	34	112

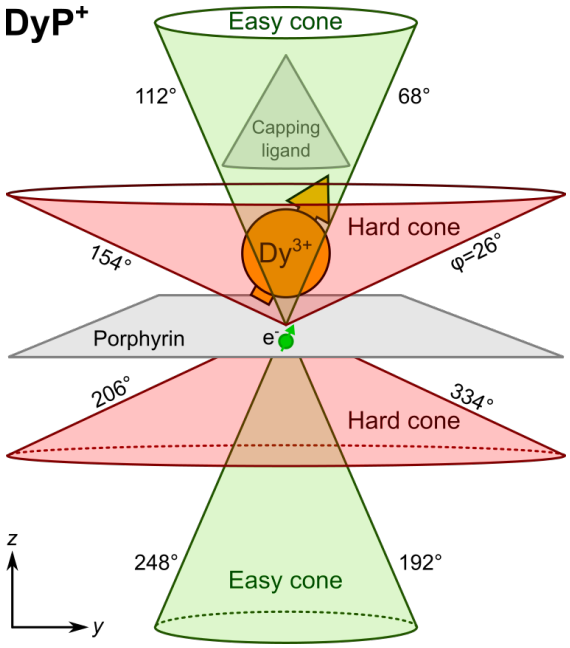


Figure 5.4: Cone shaped magnetic anisotropy of $\mathbf{DyP}^{+}$. Easy cones (green) and hard cones (red) point along the axis perpendicular to the porphyrin plane (z) with cone edges given by φ constituting easy and hard axes in the yz plane, in accordance with Tab. 5.2.

anisotropy cones on the xy plane are isotropic.

Through the relationship $\zeta_x = \partial E(\varphi)/\partial\varphi$ (Eq. 3.8) we can calculate and study qualitatively the magnetic torque generated by $\mathbf{B}(\varphi)$ (Fig. 5.3c,d). The presence of intermediate hard and easy axes (local maxima and minima of $E(\varphi)$ between easy and hard axes, respectively), reflects in a series of torque inversions and varying torque amplitude. As expected, the torque shapes for $\mathbf{DyP}^{+}$ and $\mathbf{DyP}^{+*}$ are similar except for the larger relative amplitude around 180° for the antiferromagnetic $\mathbf{DyP}^{+*}$.

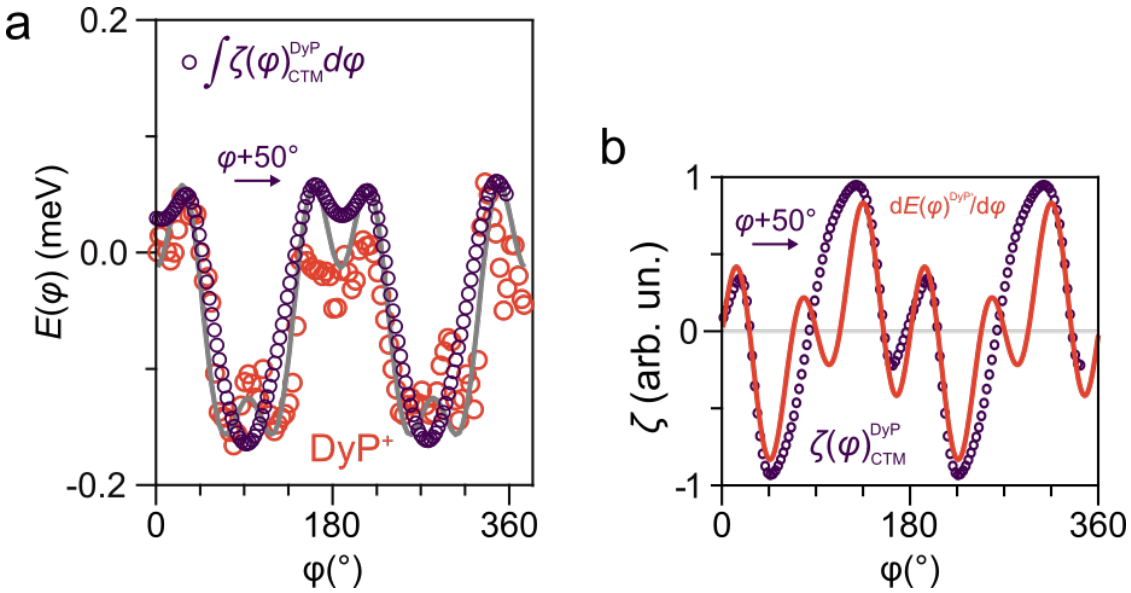


Figure 5.5: Qualitative comparison of $E(\varphi)$ and $\zeta(\varphi)$ curves for $\mathbf{DyP}^+$ (orange) and **DyP** (purple) obtained from transport spectroscopy and CTM (Fig. 4.11a; Rot_{a^*}; $B = 1$ T), respectively. The CTM data are scaled for comparison. **(a)** The orange circles and grey line are the data and fits of $E(\varphi)$ $\mathbf{DyP}^+$ from Fig. 5.3b, and the purple circles are the integral of the experimental $\zeta(\varphi)$ from CTM of **DyP** shifted by +50°. **(b)** The orange line is the calculated torque for $\mathbf{DyP}^+$ and the purple circles are data points from CTM of **DyP**.

5.4 Comparison of Magnetotransport Spectroscopy with CTM

We now compare the torque calculated from magnetotransport spectroscopy of $\mathbf{DyP}^+$ with the experimental data from CTM of **DyP** (see Sec. 4.3; Fig. 4.11a; Rot_{a^*}; $B = 1$ T), and vice versa for $E(\varphi)$. In Figure 5.5 we have plotted these data sets in the same graphs for qualitative comparison. We calculated $E(\varphi)^{\mathrm{DyP}}_{\mathrm{CTM}} \propto \int \zeta(\varphi)^{\mathrm{DyP}}_{\mathrm{CTM}} d\varphi$ where $\zeta(\varphi)^{\mathrm{DyP}}_{\mathrm{CTM}}$ is scaled to yield $E(0°) = E(360°)$ ($E(\varphi)^{\mathrm{DyP}}_{\mathrm{CTM}}$ actually increases with φ due to hysteresis). Interestingly, the anisotropy of the energy calculated from CTM is very similar to the magnetotransport data (Fig. 5.5a). The locations of the hard axes match perfectly but the CTM data indicate one easy axis at 45° instead of two. This observation indicates that the **DyP** single crystal displays easy axis and hard cone anisotropy while $\mathbf{DyP}^+$ exhibits easy cone and hard cone anisotropy.

It is striking how well the positions of easy and hard axes match, i.e. where ζ changes sign. Indeed, the CTM data were shifted by +50° to find the best

fit with the magnetotransport data but this angle does not seem arbitrary. The magnetocrystalline anisotropy of **DyP** consists of two non-equivalent contributions with a relative non-collinear angle of 100° between them, exactly twice as much as the CTM data was shifted (in Fig. 5.5) to best fit $\zeta(\mathbf{DyP}^+)$. This observation suggests that the magnetocrystalline anisotropy of **DyP** is similar to the vectorial sum of the two non-collinear anisotropies in addition to the effect of intermolecular dipolar interactions. The change from single-molecule easy cone to magnetocrystalline easy axis anisotropy is likely a consequence of the mentioned intermolecular dipolar interactions in the crystal. Alternatively, the presence of easy cone anisotropy in the single molecule could be an effect of the anchor groups, interactions with the substrate or with the leads.

5.5 Discussion

Considering how different single-molecule magnetotransport spectroscopy is to single-crystal CTM, it is very interesting to see how similar results they yield. Our results indicate that the magnetocrystalline anisotropy of **M** is very similar to the anisotropy of the molecular exchange interaction experienced by the unpaired porphyrin electron. We have therefore revealed that the anisotropy of **M** in **DyP** is dominated by the same anisotropy as the exchange interaction in $\mathbf{DyP}^+$, i.e. the Dy^{3+} ion. Moreover, it seems that the dipolar interactions present between molecules in the crystal environment reduces the single-molecule easy cone anisotropy to an easy axis anisotropy.

The local maxima at 90° and 270° and local minima at 0° and 180° in $E(\varphi)$ for $\mathbf{DyP}^+$ could be explained by assuming that the spin on the porphyrin ligand is weakly anisotropy with a hard axis perpendicular to the porphyrin plane and an easy axis parallel to the plane. The absence of the intermediate hard axis and a less pronounced intermediate easy axis in the CTM data could be an effect of slow relaxation of magnetisation that prevents **M** to relax with $\mathbf{B}(\varphi)$.

It is worth commenting on the special configuration of **DyP** with the porphyrin being the redox active component and the Dy^{3+} ion playing only a passive part.

Although the system is a SMM, for purposes of magnetotransport spectroscopy it is more suitable to compare our results to a SMM on a graphene constriction [228] or multiple SMMs on a CNT [53] than to a SMM transistor in which the channel involves the orbitals of magnetic ions [168].

Candini and coworkers [228] detected the easy axis of multiple $TbPc_2$ molecules grafted onto constricted graphene through the magnetoconductivity of the graphene spaced 5 Å away from the Tb^{3+} ion. In contrast, our setup reduces the distance between Dy^{3+} ion and conduction electrons to only $\sim$1.2 Å [219], increasing the Dy^{3+} stray field felt by the porphyrin by a factor of $\sim$70 as $\mu_0 H$ scales with $\sim 1/r^3$. The larger field causes a larger ZFS between $|\uparrow,\uparrow\rangle$ and $|\uparrow,\downarrow\rangle$.

Figure 5.2c shows that the large ZFS makes $\mathbf{DyP}^+$ and $\mathbf{DyP}^{+*}$ easy to distinguish and access experimentally. Indeed, in the resonant region between the red and blue conductance line I_{sd} is completely spin polarised because only $\mathbf{DyP}^+ \leftrightarrow \mathbf{DyP}$ is permitted. Above the blue line both channels are accessible and I_{sd} loses spin polarisation. This property enables rapid electrostatic V_{sd}-switching between spin-polarised and normal I_{sd} in this high-fidelity single-molecule spin valve.

5.6 Conclusions

In this Chapter we have shown how single-molecule transport experiments can reveal fundamental links between the molecular magnetic anisotropy and the electron and spin conductance through molecular states. Our study provides a rare example of using single spins to acquire information on the molecular anisotropy for different charge and spin states of a single molecule. In contrast to Misiorny and coworker's similar study on an Fe_4 SMM [168] the transport channel in **DyP** does not involve the orbitals of the magnetic ion. Thus, it is tempting to assume that the anisotropy of the channel is very different to that of the magnetic ion, but our CTM measurements instead suggest that they are similar. We can consider that the anisotropy of single SMMs is insensitive to whether or not the magnetic-ion orbitals forms the channel as long as the channel is sufficiently exchange-coupled to the ion. If true, this

finding is important for the design of future SMMs for spintronic applications that normally depend strongly on the molecular anisotropy.

6

A Study of a Single-Molecule Graphene Nanoribbon Using Transport Spectroscopy

Contents

6.1 Introduction 121
6.2 Solubility-Enhancement and Franck–Condon Suppression 121
6.2.1 MGNR Single-Molecule Transistor 122
6.2.2 Millikelvin Transport Spectroscopy 123
6.2.3 Results 124
6.2.4 Discussion 129
6.3 Magnetic States and Observation of Stoner Instability 131
6.3.1 Magnetic Splitting of MGNR Ground States 131
6.3.2 Spin Filling Derived from Excited-State Spectroscopy . 133
6.3.3 Stoner Instability and Irregular Spin-Filling Pattern . . 134
6.3.4 Magnetic Anisotropy in MGNRs 140
6.4 Low-Frequency Noise in MGNR Single-Electron Transistors 144
6.4.1 Theory of Low-Frequency Noise in SETs 144
6.4.2 Low-Frequency Random Telegraph Noise Experiment . 146
6.4.3 Results 146
6.4.4 Discussion 148
6.5 Conclusions 151

6.1 Introduction

Graphene nanoribbons with the required cleanliness to be used for quantum experiments have so far been unattainable. While staggering quantum properties of carbon nanotubes have been observed in ultra-clean suspended devices [181], GNRs have lagged behind due to inadequate fabrication methods yielding ribbons with too large edge disorder. Recently new and vastly superior synthetic techniques [11, 12, 130] that allow bottom-up fabrication of molecular GNRs (MGNRs) with perfect edges have been developed. This progress brings optimism towards the realisation of clean GNR single electron transistors. However, the low solubility of many MGNRs causes them to bundle up making it difficult to place only a single one across a nanogap. Thanks to our collaborators' efforts to increase solubility through edge functionalisation, we have succeeded in fabricating single-MGNR single-electron transistors exhibiting transport properties of unprecedented quality and accessibility. Through transport spectroscopy at millikelvin temperatures and in magnetic fields, we have observed Coloumb blockade, Franck–Condon suppression, Stoner spin polarisation, negative differential conductance, conductance blinking and other quantum phenomena. This Chapter will investigate these observations.

6.2 Solubility-Enhancement and Franck–Condon Suppression

The first step in making MGNR devices with the high resolution necessary to perform quantum experiments, is to de-bundle the ribbons by increasing their solubility. Otherwise, multiple GNRs from agglomerated bundles of ribbons will constitute the transport channels in devices making it practically impossible to isolate a single ribbon. Our collaborators in Dresden succeeded in functionalising the ribbon edges with evenly spaced bulky side groups yielding MGNRs with much higher solubility. We defined such ribbons pleio-soluble, after the ancient Greek word for "more", $\pi\lambda\epsilon\tilde{\iota}o\nu$. The bulky side groups of these ribbons hinder interribbon π-stacking and thus prevent bundling of MGNRs in solution.

The aims of this project was two-fold: mainly we sought to demonstrate the impact of solubility enhancement on the transport properties and additionally how this improvement enables the detection of elusive quantum effects. We compared devices made before and after the solubility enhancement and the effect was immediate and clear: pleio-soluble MGNRs produce single-electron transistors of unprecedented quality. Next, we showed that these devices were capable of detecting the Franck–Condon effect, which in CNTs have only been observed in ultra-clean suspended systems. This Section therefore demonstrates how solubility enhancement of MGNRs enables access to completely new information on rich GNR transport properties, and thereby pushes the field of GNR electronics and spintronics past old boundaries and into new and exciting frontiers. The Sections that follow will investigate some of these properties.

6.2.1 MGNR Single-Molecule Transistor

To study the difference in quality of MGNRs with different solubility, we prepared single-molecule transistors of two types of MGNRs with the same aromatic backbone but with different side groups (Fig. 6.1a,b). The backbone was 1.12 nm wide [11, 12]. Long alkyl chains were used as side groups for the low-soluble ribbons and bulky three-dimensional side groups with diameter of 0.5 nm were used for the pleio-soluble ones. 0.5 nm is much longer than the typical distance between π stacked graphitic layers and thus prevent ribbons from bundling. Our collaborators Wenhui Niu, Prof Akimitsu Narita, Prof Yiyong Mai and Dr Junzhi Liu from TU Dresden, Shanghai Jiao Tong University and MPI for Polymer Science synthesised the MGNRS.

The devices were made using graphene leads connected to Au pads on top of an n-doped Si wafer separated by 300 nm of SiO_2 (Fig. 6.1c). Using a feedback-controlled electro-burning technique nanogaps were created between the graphene leads. Solutions of MGNRs were drop casted and a sharp increase in the real-time conductance detected that the gap had been bridged by one or more MGNRs. A bias voltage V_{sd} controlled the source and drain potentials and a back-gate voltage V_g could shift the MGNR levels (Fig. 6.1a). See also Section 3.3.2. Alessandro

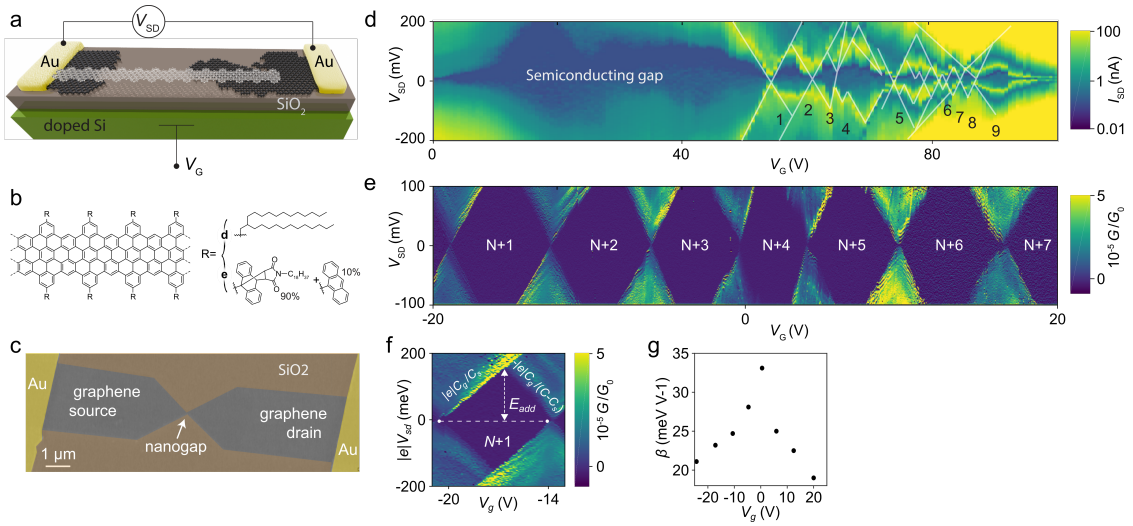


Figure 6.1: Scheme of the device: (a) a MGNR bridges a nanogap between graphene leads connected to Au pads built on top of an n-doped Si wafer separated by a 300 nm insulating layer of SiO_2; (b) Two different MGNRs shown schematically: **d**: low-soluble and **e**: pleio-soluble MGNR; (c) False-colours micrograph of a typical device. The resulting stability diagrams of the MGNR-based single electron transistors are presented corresponding to (d) low-soluble and (e) pleio-soluble MGNR. (f) Visualisation of the quantities E_{add} and α on a stability diagram showing the Coulomb diamond of the N+1 charge state. (d) β depends on V_g for the different Coulomb diamonds in (e). β peaks around $V_g = 0$ and decreases nonlinearly on either side.

Lodi, Dr Chit Siong Lau, Dr Ji Ma (TU Dresden) and Dr Tian Pei fabricated the single-molecule transistors.

6.2.2 Millikelvin Transport Spectroscopy

Magnetotransport spectroscopy was performed on the MGNR single-molecule transistors. We measured the current, I, and calculated the numerical differential conductance, $G = dI/dV_{sd}$, over the device as a function of V_{sd} and V_g to map out the MGNR transitions using the techniques described in Section 3.3.2. We measured large conductance maps spanning the maximum bias and gate voltage ranges, and smaller sections with high resolution around the degeneracy points. The former measurement to get an electrostatic overview of the device, and the latter for a detailed study of ground and excited states at low V_{sd}. The measurements were carried out both in zero magnetic field and in a constant $B_{\|}$ (in-plane) up to 6 T. All experiments were carried out in a dilution refrigerator at 25 mK.

6.2.3 Results

Figure 6.1d and e shows stability diagrams of devices with low-solubility ($T \leq 0.35$ K) and pleio-solubility ($T = 25$ mK), respectively. The low-solubility-MGNR device[1] (Fig 6.1d) shows a large region of suppressed conductance that corresponds to the bandgap. Coulomb diamonds are observed where conducting states comes into resonance with the leads but they are overlapping and have different sizes. Such features indicate that multiple MGNRs, possibly a bundle of ribbons, span the nanogap and takes part in conduction.

In stark contrast, the pleio-soluble-MGNR device (Fig 6.1e) shows exceptionally clean conductance features comparable to those seen in ultra-clean CNTs (e.g. Ref. [181]). The diamonds are periodic and of the same size indicating a single conduction channel, i.e. conduction through a single MGNR. We do not observe a semiconductor gap (i.e. a Coulomb diamond much larger than the others) so the neutral state lies outside our V_g window. Therefore, the charge states N+i are unknown but we assume we are operating in the multi-electron regime.

The addition energy $E_{add} = 156$ meV was extracted from the average of the top point of all diamonds. E_{add} was used to predict the ribbon length, $\ell = 33$ nm, as follows: [229]

$$\ell = \frac{e^2 \ln(4h/w)}{4\pi\epsilon_0\epsilon_r E_{add}} = 33 \text{ nm}, \tag{6.1}$$

where e is the elementary charge, ϵ_0 is the electric permittivity in free space, $\epsilon_r = 3.9$ is the relative permittivity of the SiO_2 [230] layer of thickness $h = 300$ nm between the gate electrode and the MGNR of width $w = 1.12$ nm.

The height and width of the Coulomb diamonds provide the relationship $\beta|e|V_g = |e|V_{sd}$ and is given by the lever arm $\beta = 1/(|\alpha_+|^{-1} + |\alpha_-|^{-1})$, from the slopes of the diamond edges. For negative slopes $\alpha_- = -|e|C_g/(C - C_s)$ and for positive slopes $\alpha_+ = |e|C_g/C_s$, where the total capacitance to the dot $C = C_s + C_d + C_g$ is the sum of the capacitances to the source, drain and gate, respectively. We find that β

[1]This device was fabricated and measured by Tian Pei and Nicola Dotti. For this Thesis we only analysed their results for comparison with our results.

differs between 19 and 33 meV/V for different diamonds and seem to peak around $V_g = 0$ (Fig. 6.1g), and decrease nonlinearly and symmetrically on either side of $V_g = 0$. This V_g dependency may be caused by nonlinear electrostatic saturation effects in the dielectric. The mean value of $\bar{\beta} = 24.5$ meV/V.

Manifestations of several interesting phenomena are present in the conducting regions of the stability diagram, such as negative differential conductance and dark states. Slanted conductance lines within the conducting regions is a feature of interference effects in the graphene leads [231]. The conductance peaks were fitted with Lorentzian functions (Eq. 6.2; Fig.6.2b) with line widths $\Gamma \approx 0.8$ meV (full-width half-maximum (FWHM) at $T = 25$ mK) were extracted. At low T, G is limited by life-time broadening and is proportional to the Lorentzian function: [232]

$$G(\mu) \propto \frac{\Gamma/2\pi}{(\mu - \mu_{\mathrm{GNR}})^2 + (\Gamma/2)^2}, \tag{6.2}$$

where $\mu_s = |e|V_{sd}$ is the chemical potential of the source electrode and μ_{GNR} is an MGNR state. It turns out that the line widths are much smaller than the energies of excited electronic, vibrational and spin states, and thus enable the detection of these phenomena. The remainder of this Section will explore the electronic coupling to MGNR vibrational states in the framework of the Franck–Condon principle.

Franck–Condon theory describes the coupling between electrons and vibrons, i.e. how the addition of an electron changes the electronic wave function and produces a shift in the equilibrium coordinate of the vibronic oscillator. If the electron–vibron coupling, γ, is large it can suppress charge transport through low-lying vibronic MGNR states (Fig.6.2a). Furthermore, Franck–Condon theory predicts that the peak conductance of the vibronic transitions, G_n^{max}, follows the sequence,

$$G_n^{max} = \frac{\gamma^n}{n!} e^{-\gamma}, \tag{6.3}$$

where n is the vibron quantum number. A hint of Franck–Condon suppression apparent from Figure 6.2b where an increase in T from 25 mK to 0.5 K is followed by an increase in G. A further increase to 1 K decreases G due to significant temperature broadening. The same figure was used to deduct the coupling energy

to the leads from the FWHM of the G peaks: 0.8, 1.06 and 1.18 meV for $T = 25$ mK, 0.5 K and 1 K, respectively. Moreover, G seems to increase with a magnetic field, $B_{\parallel} = 6$ T (Fig.6.2f), possibly due to B-induced localisation of the electronic wave function decreasing the Franck–Condon effect [233].

To investigate the Franck–Condon phenomenon, we analysed the conducting regions $N \leftrightarrow N+1$ and $N+1 \leftrightarrow N+2$. Figure 6.2c shows a set of excited states inside the conducting region spaced $\sim$7 meV apart. Using DFT we confirmed the existence of edge-localised vibrons with energy $E_V = 7.8$ meV. To distinguish between conductance lines parallel (vibrational or electronic) and slanted (from leads) with respect to the diamond edge, G was averaged over traces of data points parallel to the diamond edge (see magenta dashed lines in Fig 6.2c) and plotted as a function of V_{sd} (Fig.6.2d,e). The result was a series of peaks with a 7-meV periodicity. A linearly increasing background stemming from the increasing number of conduction channels with V_{sd} was subtracted from G.

Fits with Equation 6.3 are in good agreement with the peak values of G in Figure 6.2d and e for $\gamma = 1.4 \pm 0.2$ which indicates a strong electron–vibron coupling ($\gamma > 1$). For $\gamma < 1$ the highest value of G_n^{max} would be for $n = 1$, i. e. the diamond edge peak (GS$\leftrightarrow$GS), whereas for $\gamma > 1$ this value shifts towards higher n, i.e. stronger Franck–Condon suppression of conductance. In this device Franck–Condon suppression manifests mainly in the three first peaks where $G_1^{max} < G_2^{max} > G_3^{max}$.

γ is mainly determined by the ratio between the first and second conductance peak. Therefore, it is important to check whether the the magnitude of G depends on V_{sd} and V_g. Figure 6.3 shows that there is a small voltage dependence on the first two G peak on the left side of the $N+2$ diamond at low bias for different T. To minimise this error, we restrict the analysis to the least voltage sensitive ranges of V_g.

Using the rate-equation model discussed in Section 2.4.1 for a single-phonon mode $\hbar\omega_q = 7$ meV and a superohmic phonon bath, we calculated a SD (Fig. 6.4). Using Equations 2.10-2.17 we reproduced our experimental data by using the set of parameters reported in Table 6.1. The calculated SD exhibit the same regularly spaced conductance peaks as observed experimentally. These result from the

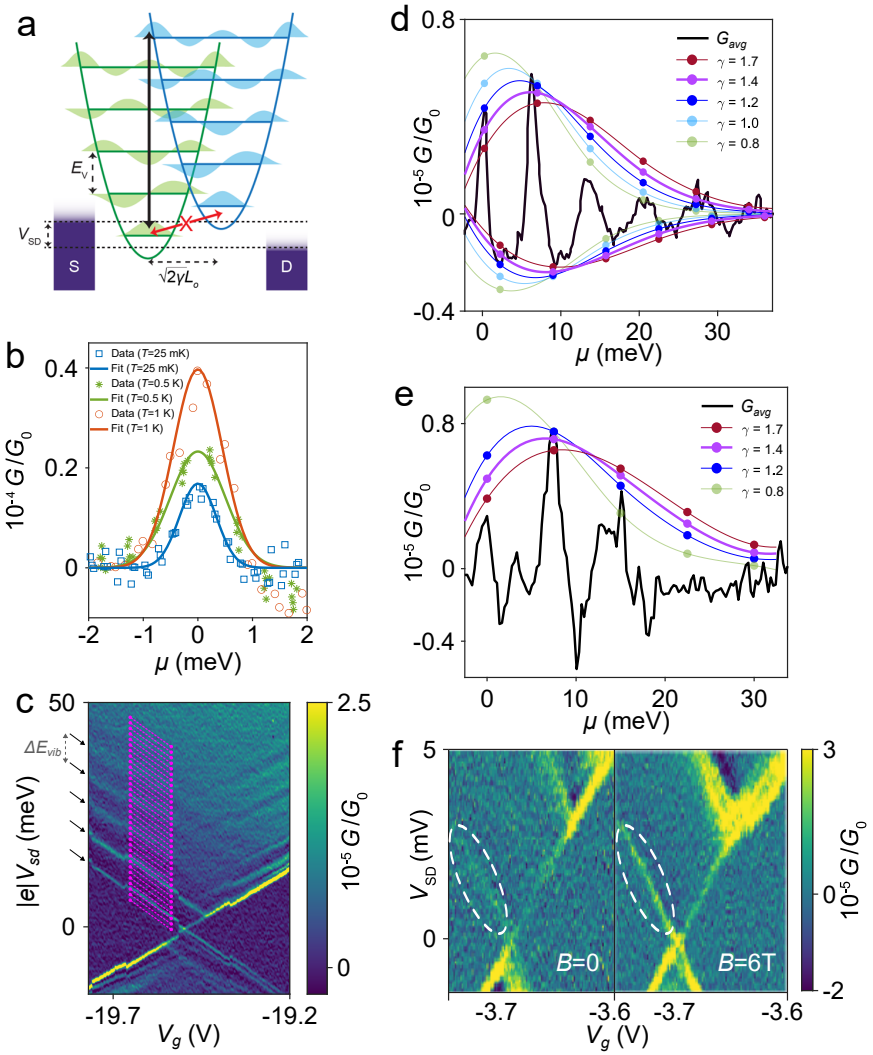


Figure 6.2: Franck–Condon analysis. (a) Scheme of the Franck–Condon blockade in the transport properties of nano-devices, with the equilibrium coordinates represented horizontally for two adjacent charge states (green and blue). Strong electron–vibronic coupling suppresses ground-to-ground-state transitions, while ground-to-excited-state ones become available at higher bias. (b) Lifting of the Franck–Condon suppression for a transmission channel upon increasing the temperature from 25 mK (blue squares) to 500 mK (orange circles), followed by thermal broadening at 1 K (green stars). Lines are Gaussian fits to the data. (c) Conductance values ($N \leftrightarrow N+1$) along the magenta dashed lines were extracted from the SD and averaged to suppress contributions from conductance ridges that are not parallel to the diamond edge. (d) The averaged conductance values, G_{avg}, from (c) are plotted as a function of $\mathfrak{t} = |e|V_{sd}$ after subtraction of the linear part of G_{avg}. Curves of $G^{max}_{(n,0)}$ (see Eq.6.3) with peak spacing $E_{vib} = 7$ meV are plotted for different values of γ. (e) Equivalent analysis as in panel (d) for the $N+1 \leftrightarrow N+2$ transition at $V_g \approx -13$. $\gamma = 1.4$ yields a good fit of the data in both (d) and (e). (f) The intensity of the diamond edge changes without and with a magnetic field ($B_{\|} = 6$ T), at $T = 25$ mK, with circles highlighting the magnetic-field-induced lifting of the blockade.

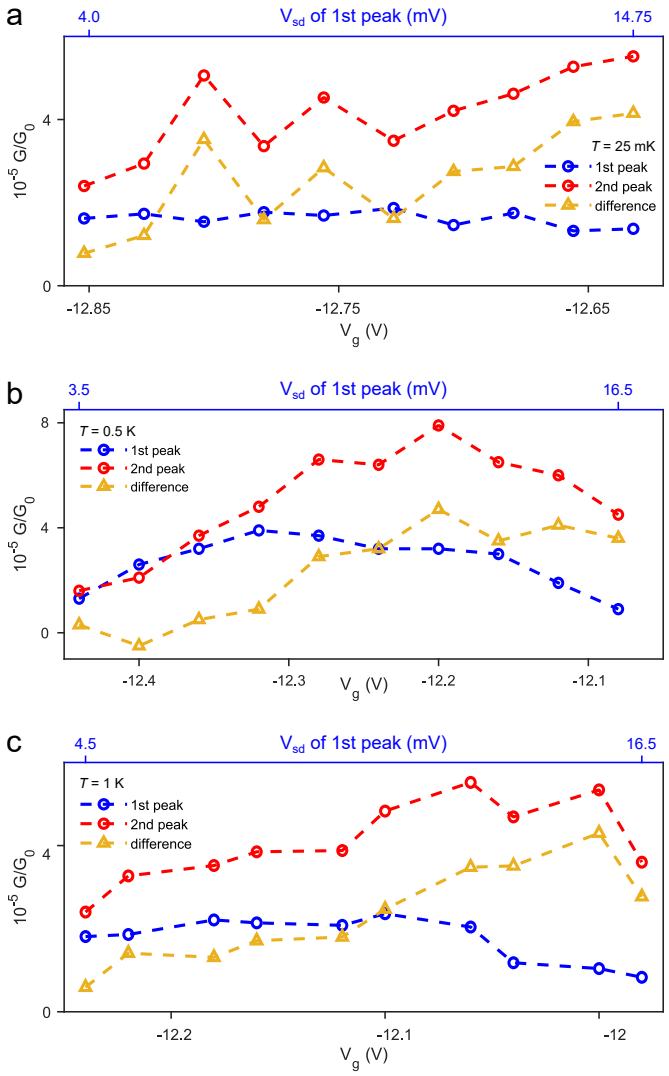


Figure 6.3: Analysis of conductance peak intensities in V_{sd} traces at different V_g for different T. The figures show G_1^{max} (diamond edge) (blue), G_2^{max} (red) and the difference between them (yellow) at temperatures (a) $T = 25$ mK, (b) $T = 0.5$ K and (c) $T = 1$ K.

strongly coupled single-mode that generates multiple peaks in the DOS at low energies (Fig. 6.4c,d). At higher bias the background conductance increases due to the coupling with an increasing number of phonon modes in the bath. Moreover, the strong V_{sd} asymmetry is caused by $\Gamma_D \gg \Gamma_S$ and may be caused by larger overlap between the MGNR and the drain than the source lead. The model does not take into account the slanted conductance lines originating from the leads and does therefore not reproduce these.

Table 6.1: Parameters used with Equations 2.10-2.17 to calculate the stability diagram shown in Figure 6.4b.

T (mK)	$\hbar\omega_q$ (meV)	$\hbar\omega_c$ (meV)	$\hbar g_q$ (meV)	λ (meV)	Γ_s (meV)	Γ_d (meV)	C_s	C_g
25	7	8.5	20	150	0.0012	0.5	0.54	0.025

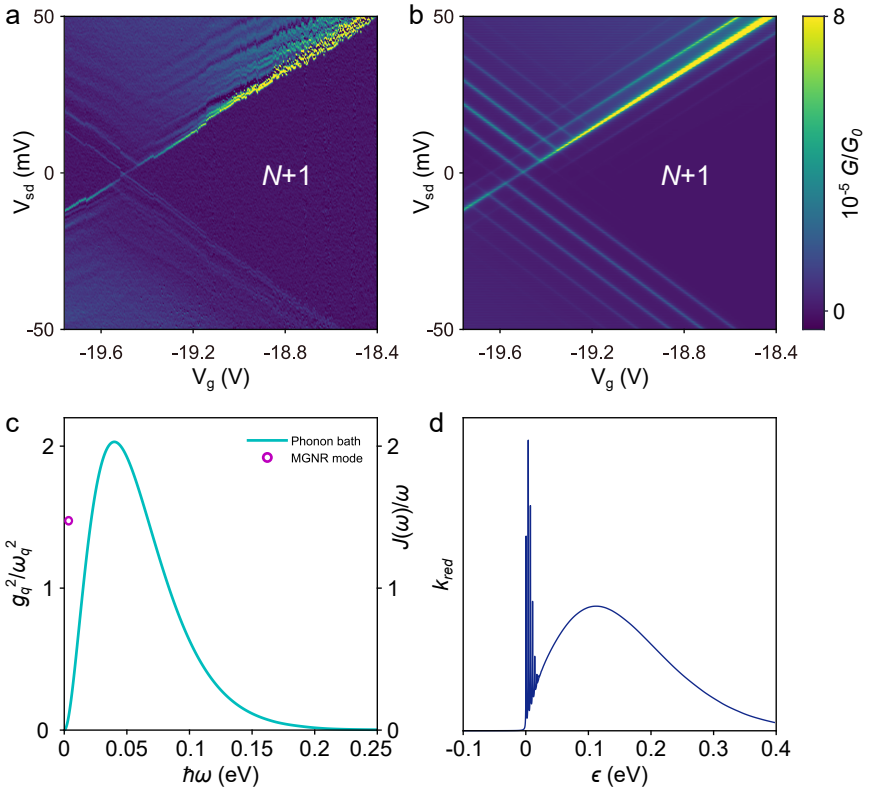


Figure 6.4: Conductance maps of the same transition as in Figure 6.2c plotted on the same colour scale. Panel (a) shows the experimental data and panel (b) shows the conductance calculated using Equations 2.10-2.17 with the parameters from Table 6.1. (c) Calculated spectral densities of the phonon bath (right axis) and the single mode (left axis). (d) Molecular density of states as a function of ϵ (Eq. 2.13).

6.2.4 Discussion

Compared to values of γ reported for suspended CNTs grown in-situ, our observations fall below some observed values: $\gamma = 3.3$ [234] but above other: $\gamma = 0.5$-1.1 [235] (Tab. 6.2). Considering that our system is in close contact with the substrate and still exhibit large γ relative to suspended systems, favours the hypothesis of high electron–vibron coupling in GNRs [236]. Furthermore, our γ is comparable to that observed in single- C_{140} junctions [237], much higher than that of single-C_{60}

Table 6.2: Comparison of electron–vibron couplings for different device types. Values of γ are sorted in ascending order from left to right.

Device type	C_{60}	CNT (in-situ)	C_{140}	MGNR	C_{60} (in graphene junction)	CNT (in-situ)	Fe_4 SMM
γ	$\ll 1$	0.5-1.1	~ 1.4	1.4±0.2	3	3.3	4.2
Reference	[132]	[235]	[237]	This work	[238]	[234]	[170]

junctions ($\gamma \ll 1$) [132], but smaller than that of a single molecule suspended between gold electrodes ($\gamma = 4.2$) [170] and a fullerene in a graphene junction (γ=3) [238]. We may consider that low-energy modes in the phonon bath of the substrate can assist transport at the diamond edges and thereby mask the true magnitude of the Franck–Condon effect. Therefore, de-coupling the GNR from the substrate environment through suspension should result in γ-values much larger than for CNTs, in closer agreement with theoretical limits [236].

The electronic and vibrational properties of CNTs rely strongly on their chirality, length and radius [30, 239], which are difficult to control and one can expect large variation between different devices. In contrast, the properties of GNRs can be designed and engineered with molecular precision, which facilitates the fabrication of large numbers of identical devices. Currently, the main obstacle is to produce GNRs of equal lengths because the energy of longitudinal modes that couple with electronic states at low T strongly depend on the GNR length. Solving this issue would enable further studies of Franck–Condon suppression in a large number of GNR devices and provide a general understanding of electron–vibron coupling in GNRs.

Savin and co-workers [240] calculated the existence of edge-localised nonlinear modes in armchair GNRs with energies exclusively in the range ∼6.8-8.7 meV (∼55-70 cm^{-1}), perfectly matching our observations and DFT calculations (not shown). Several reports states that the electronic wave function is edge-localised in GNRs, and can overlap and couple with the edge-localised vibrational states. The edge-vibrons couple much stronger than other vibrons to the electronic edge state, which may explain why the conductance intensity of the $E_{vib} = 7$ meV vibrational state is so strong compared to lower lying vibrons. Perhaps this observation

explains why the MGNR E_{vib} observed herein is larger than that of 65-nm-long suspended CNTs (∼1 meV) [234].

We have shown that introducting solubilising groups on the MGNR edges enables simple fabrication to create devices of similar quality to that of ultra-clean suspended CNTs grown in-situ. The simplicity of the present technique combined with its remarkable outcomes propose that pleio-soluble MGNR can become part of the small and highly exclusive family of useful building blocks for quantum electronic devices. Our observations strengthen the assumption of the MGNR edge states' importance, both electronic and vibrational, on the physics of GNR systems. Thanks to our demonstration of MGNR states resolved at µeV energies, it is now possible to access the predicted spin states with transport spectroscopy. The next Section will cover our investigation of these spin states through magnetotransport, and show that the spins interact with each other in an unusual way.

6.3 Magnetic States and Observation of Stoner Instability

In the previous Section we discussed how solubility-enhancing side groups drastically improved the quality of MGNR-based single-electron transistors, and how this improvement enables the study of hypothesised spin states. In this Section we will present, to our knowledge, the first detailed observations of magnetic MGNR ground states and their spin filling sequence. Using millikelvin magnetotransport spectroscopy on the ground states of multiple successive charge states of a MGNR, we reveal an unusual ground-state spin selectivity. We theoretically explain this phenomenon as a Stoner instability caused by spin–spin exchange interactions of intermediate strength. In our humble opinion, this result represents the most important discovery in this Thesis.

6.3.1 Magnetic Splitting of MGNR Ground States

In this study we performed magnetotransport spectroscopy at $T = 25$ mK and parallel magnetic fields, $B_{\parallel}$, up to 6 T on charge states N to N+6. The device

under testing was the same as presented in Section 6.2 (Fig.6.1a-c), but with a significant difference: the presented device was heated up from 25 mK to 50 K in a matter of seconds due to an accidental magnet quench and then cooled down again. This thermal cycle has likely disturbed the MGNR and altered the capacitive environment felt by the MGNR transport channels. Therefore, we should not assume that a charge state probed in the present device at a certain V_g is the same as before the thermal cycle.

While Section 6.2 focused on the MGNR ground states and excited vibrational states at zero field in the high-bias regime, the present Section will mainly focus on the effects of $B_{\|}$ on the ground states at low bias. We first mapped out the SD of charge states N to N+7 (Fig. 6.5a before zooming in on the degeneracy point (Fig. 6.5b). The extreme resolution and level of detail in these SDs are unprecedented for GNRs and are comparable to ultra-clean suspended CNTs [181]. Ground and excited states, including slanted lines stemming from lead-interference are easily recognisable.

Interestingly, the resolution of the resonance lines is so high that splittings of the ground states (Coulomb diamond edges) were observed when $B = 6$ T was applied (Fig. 6.5c). I-V_{sd} traces were measured across the $N \leftrightarrow N$+1 ground-states transition along the white lines in Figure 6.6a and b at zero field and at 6 T. Traces A and B show the Zeeman splitting of ∼0.5 meV of the doublet ground state for $B = 6$ T (Fig. 6.6c). This splitting corresponds to an effective g factor, $g_{eff} = 1.4$, through the associated Zeeman energy $E_Z = \mu_B g_{eff} B_{\|}$. Traces C and D show the same splitting for higher V_{sd} when the excited state at 1.7 mV is included (Fig. 6.6d). We note that G for positive V_{sd} of the ground state only (A and B) are suppressed. Interestingly, conductance is promoted for these states in C and D when the excited state is involved in the transport. The coupling energies to the leads, $\Gamma_s = 100$ μeV and $\Gamma_d = 150$ μeV, were extracted from the FWHM of the Lorentzian peaks.

Figure 6.7 reveals Zeeman splitting of ground states of several N_i. We observe three-fold splitting of a triplet for large N_i indicating the presence of high-spin ground states at zero field (Fig. 6.7). Zeeman splitting of excited states are also visible.

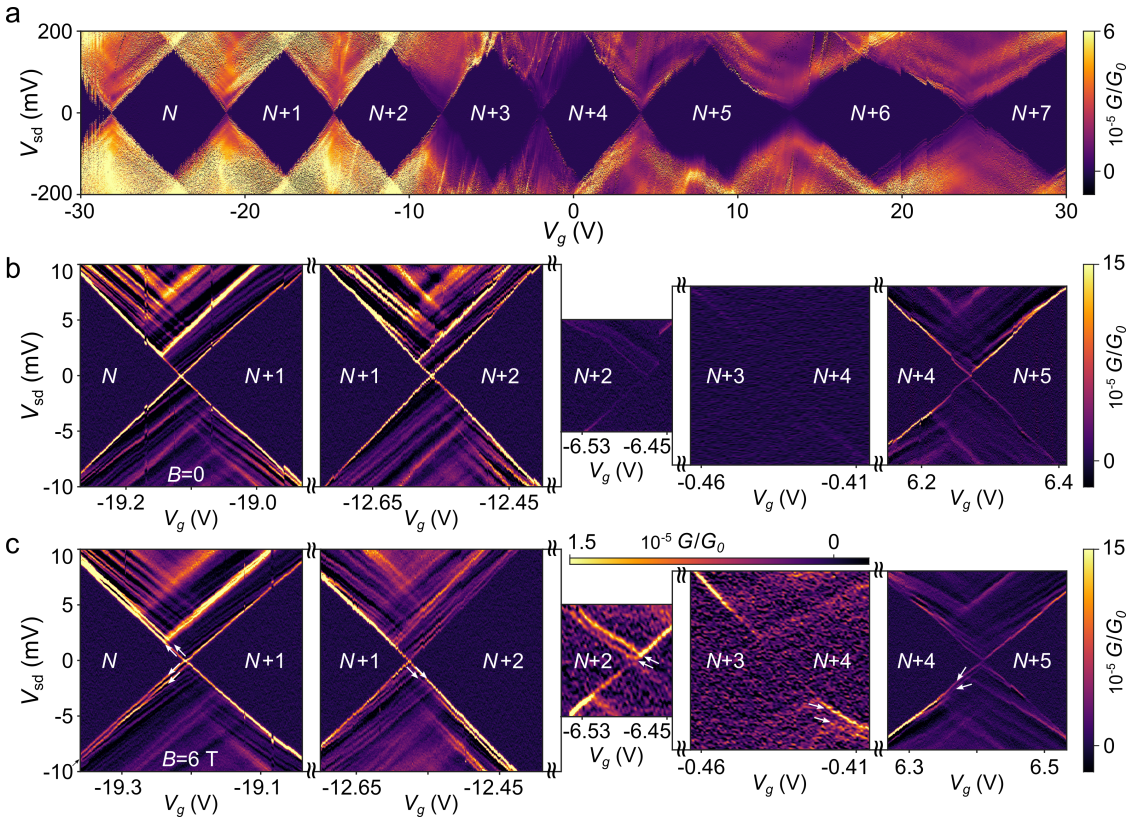


Figure 6.5: Coulomb blockade and magnetic splitting of ground states. (a) Stability diagram (SD), i.e. G as a function of V_g and V_{sd}, for MGNR charge states N to $N+7$. (b) High-resolution SDs at low bias mapping the transitions from N to $N+5$ at zero field, and (c) at $B_{\parallel} = 6$ T. The conductance ridges that form the edge of Coulomb diamonds split in two, as indicated by white arrows, only for diamonds N, $N+2$ and $N+4$.

6.3.2 Spin Filling Derived from Excited-State Spectroscopy

The spin-split ground states observed in Figure 6.5c gives information on the spin filling of the MGNR [162, 179]. Vibrational excitations can be ruled out due to the magnetic field behaviour [153, 241]. As explained in Section 3.3.2, Pauli's exclusion principle allows at most two electrons with opposite spin in any single-particle orbital. If the excited state of the spin-split ground state terminates at the right edge the added electron enters an empty orbital, and if it terminates at the left edge the electron enters a half-filled orbital.

The spin-split ground and excited states are marked with white arrows in Figure. 6.5c. Only the diamonds N, N+2 and N+4 splits and thus indicate that electron N+1, N+3 and N+5 enter empty orbitals while N, N+2 and N+4 enter

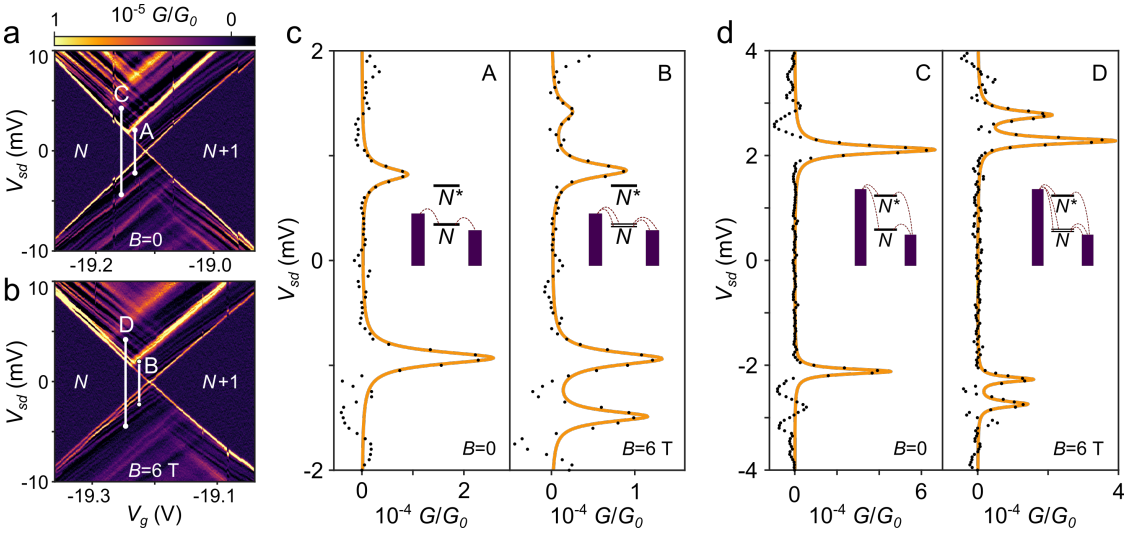


Figure 6.6: Magnetic splitting of ground states. V_{sd} traces (c,d) were obtained across the N-diamond edges at $B_{\|} = 0$ and $B_{\|} = 6$ T along the white lines drawn onto the SDs in (a,b). (c,d) The black dots are data points and the yellow lines are Lorentzian fits. The differences between the left and right panels of (c) and (d) are caused by magnetic splitting of the N ground state. Insets show the potential energy configuration for positive V_{sd} of each trace.

half-filled ones. At $B = 6$ T, the implication is the spin filling pattern $\downarrow, \uparrow, \downarrow, \uparrow, \downarrow, \uparrow$ for electrons N to N+5. However, the splitting of the N+2↔ N+3 ground state is much larger than for the other transitions and indicate a high-spin ground state, which will be investigated below.

6.3.3 Stoner Instability and Irregular Spin-Filling Pattern

In Section 3.3.2 we explained how the spin filling in quantum dots relies on the ratio between the spin correlation energy, ξ, and the level spacing. The magnetic edge states in GNRs are predicted to fulfil the Stoner criterion and form high-spin ground states due to spin correlation energy comparable to the spacing between the quasi-degenerate levels, $\epsilon_2 \approx \epsilon_3$, of graphene valleys. However, the strong lateral confinement in GNR makes in unclear whether pure valley states can be assigned to the quasi-degenerate pair. Therefore, Dr Federico Lombardi performed spin-resolved density functional theory (DFT) calculations for N=1,3,4 and 5. These showed that the quasi-degeneracy was preserved for low N for edge states that progressively intermix with N (Fig. 6.9).

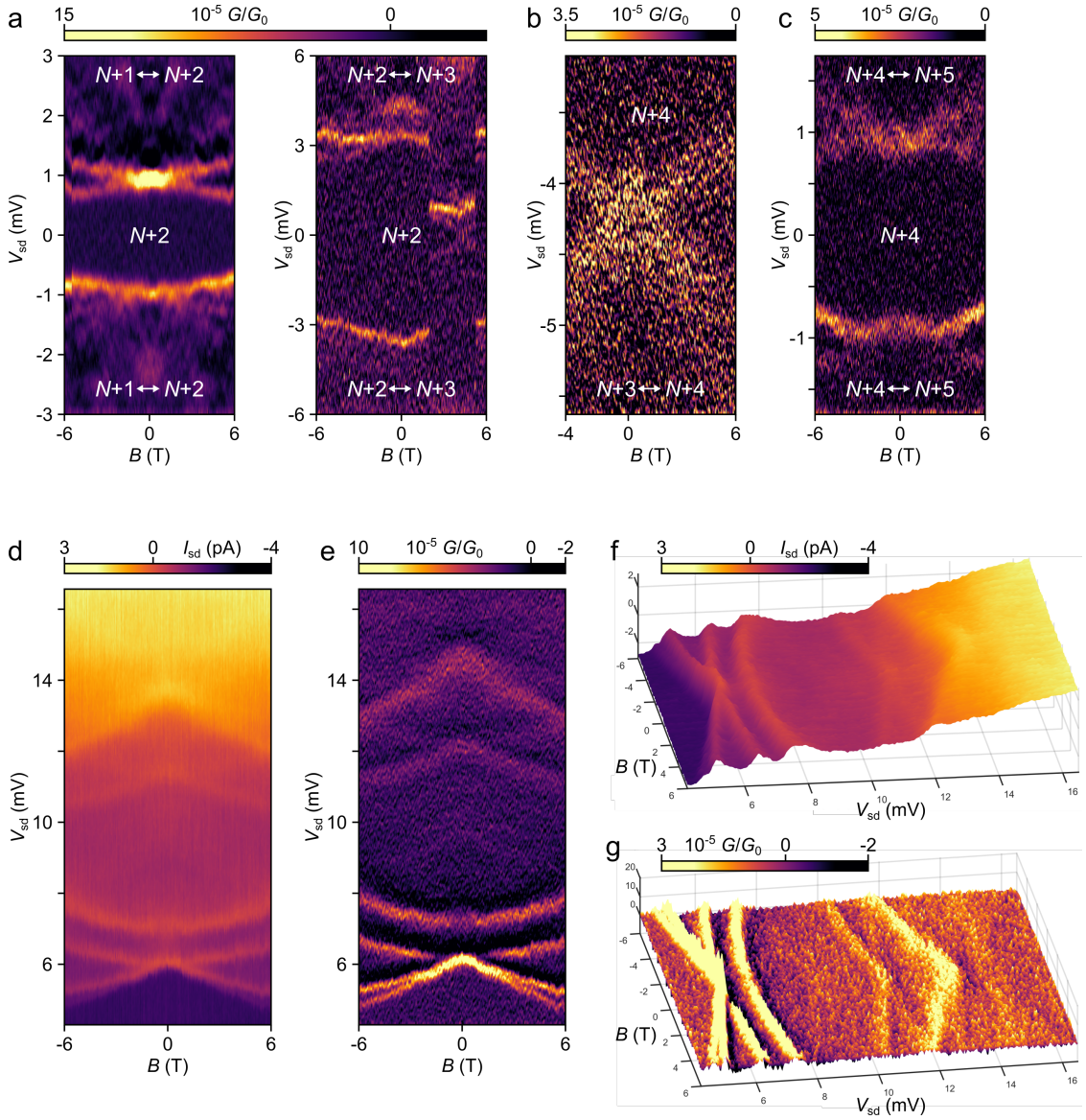


Figure 6.7: **(a-c)** V_{sd} traces vs. $B_{||}$ revealing the shift in $\mu(N{+}2)$ to $\mu(N{+}5)$. These were used to obtain $\Delta E_{add}(N{+}2)$ to $\Delta E_{add}(N{+}4)$ (Fig. 6.10i). **(d,e)** I_{sd} and G/G_0 from V_{sd} traces versus $B_{||}$ for a transition of unknown charge taken at $V_g = 14.6$ V before the device was thermally cycled. A ground state triplet is visible. Excited states at higher bias also split. **(f,g)** The same data in three-dimensional plots.

The DFT calculations estimated $\xi \sim 5$ meV, which is of the same order of magnitude as the single-particle energies, ϵ_i, observed experimentally. Therefore, we predict that the MGNR is in the intermediate-correlation regime characterised by irregular spin filling patterns caused by Stoner instability. We can analyse the Stoner instability by considering the following Hamiltonian: [242]

$$\mathcal{H} = \frac{U}{2}N(N-1) + \sum_{i\sigma} \epsilon_i c_{i\sigma}^{\dagger} c_{i\sigma} - \frac{\xi}{2}\mathbf{S}^2 + g\mu_B B S_z, \tag{6.4}$$

where U is the on-site Coulomb repulsion, ϵ_i is the single-particle energies, $c_{i\sigma}^{\dagger}$ ($c_{i\sigma}$) create (annihilate) an electron in orbital $i = 1, 2, 3, ...$ with spin $\sigma = \uparrow, \downarrow$. $\mathbf{S} = (\hbar/2)\sum_{i\sigma\sigma'} \sigma_{\sigma\sigma'} c_{i\sigma}^{\dagger} c_{i\sigma'}$ where σ is the vector of Pauli matrices. The last term is the Zeeman splitting of the spin states along the z direction and S_z is the projection of $\mathbf{S}$ on the z axis. We developed this theory in collaboration with Prof Guido Burkard at the University of Konstanz.

Equation 6.4 describes the competition between $\Delta\epsilon_i$, which favour a low-spin state, and ξ and B which favour high-spin. The parameter space spanned by the quasi-degeneracy separation, $\Delta\epsilon_3$, and ξ, both normalised by the single-particle level spacing, $\Delta\epsilon_2$, produces a rich spin-filling phase diagram (Fig. 6.8a). Herein, the orange region correspond to the configuration resulting in spin pairing, while the white region results in Hund's-rule filling. The regions in between result in irregular spin filling (Stoner filling) due to competition between ξ and $\Delta\epsilon_3$ (Fig. 6.9). We assume in the first approximation that $\xi/\Delta\epsilon_2$ is a device constant.

The analogous map with the magnetic energy and ξ also reveal phases with irregular spin filling patterns (Fig. 6.8b). Here, the orange/red and purple phases mark irregular spin filling. While it is possible to cross phase boundaries by applying B, the accessible phase space is mainly determined by device characteristics. The green lobes in Figure. 6.8b indicate the phase space accessed with Si nanowire [243], Si [244, 245] and graphene QDs [246]. Seemingly, the orange/red and purple phases have not been explored in the literature but it turns out that our MGNR device lies in this parameter space.

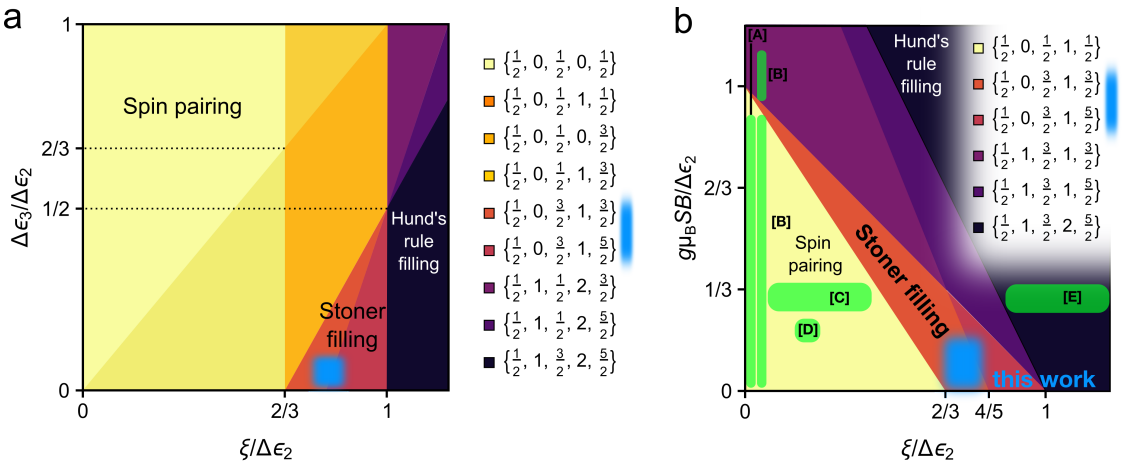


Figure 6.8: Spin-filling phase diagrams of the parameter spaces **(a)** $\Delta\epsilon_3/\Delta\epsilon_2$ and **(b)** $\Delta\epsilon_3/\Delta\epsilon_2$ as functions of $\xi/\Delta\epsilon_2$ yielding regions of different spin filling labelled by the MGNR's total spin, S_{N_i} for $i = N$ to N+4. Our MGNR device (blue lobes) lies within the Stoner filling phases (red) of intermediate $\xi/\Delta\epsilon_2$. Attempts to place systems reported in literature are indicated by green lobes ([A]: Si nanowire QD [243], [B]: Si QD (bottom: $B < 2.7$ T; top: $B > 2.7$ T) [244], [C]: Si QD ($N = 1$) [245], [D]: graphene QD [246], [E]: Si QD ($N = 24$) [245]. This Figure was developed in collaboration with Prof Guido Burkard.

Using ground-state magnetospectroscopy we investigate the change in the total spin, S, of the MGNR ground-states associated with successive charge states (see Sec. 3.3.2). This method relies on measuring how the addition energies $E_{add}(i) = \mu(i)-\mu(i–1)$ changes with B. The experimental method is outlined in Figure 6.10b-i, and starts with obtaining G-V_{sd} traces as functions of B between ±6 T to detect the evolution of the ground states $\mu(i-1)$ and $\mu(i)$ with B. The V_{sd} traces were fitted with Lorentzian functions (Eq. 6.2) to extract the peak positions of $G(V_{sd})$ (Fig. 6.10f,g). Finally, $\Delta E_{add}(i) = \Delta\mu(i) - \Delta\mu(i-1)$, where $\Delta\mu(i) = \mu(i) - \mu(i)_{B=0}$, was calculated for i=N+1 to N+4 (Fig. 6.10h,i).

Our first approximation of constant $\xi/\Delta\epsilon_2$ did not yield good fits with $\Delta E_{add}(i)$. Therefore, we have assumed that only the two first terms in Eq. 6.4 cancel out when calculating $\Delta E_{add}(i)$, which then only depends on the spin-correlation term and the Zeeman term. Using only $\xi/\Delta\epsilon_2$ as fitting parameter (Tab. 6.1), we fit Equation 6.4 to the experimental data (Fig. 6.10i). The fits show that the experimental data is in good agreement with our model. The variation in $\xi/\Delta\epsilon_2$

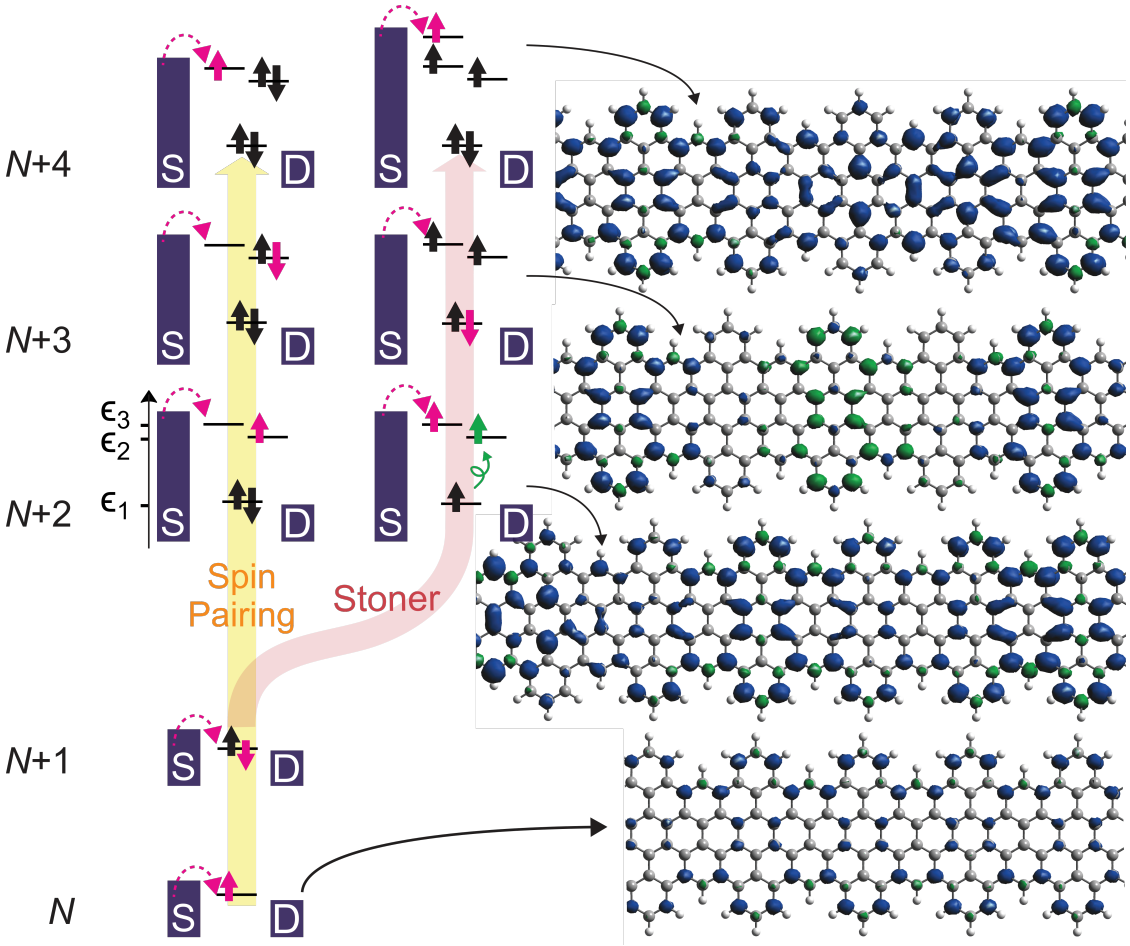


Figure 6.9: Spin pairing (yellow) and Stoner filling (red) paths with DFT-calculated spin densities (difference between positive and negative spin) for the corresponding MGNR charge states. Pink arrows indicate the spin of the added electron, black arrows label the excising spins and the green arrow highlights the internal spin flip associated with adding electron N+2. The Stoner path correspond to the orange region in Figs. 6.8 with progression $S = \{1/2, 0, 3/2, 1, 3/2\}$.

Table 6.3: Values of the parameter $\xi/\Delta\epsilon_2$ fitted to the experimental data in Fig. 6.10i using Eq. 6.4. *The model produced a poor fit for N+3 and this value is likely underestimated.

	N+1	N+2	N+3	N+4
$\xi/\Delta\epsilon_2$	0.34	0.65	0.17*	0.50

suggest that this quantity is not a device constant for MGNRs due to variations in ξ and/or $\Delta\epsilon_i$ with different charge states.

The slopes of $\Delta E_{add}(i)$ imply that our device falls within the elusive Stoner-filling phase with S changing by more than 1/2 upon adding a single electron. We observe

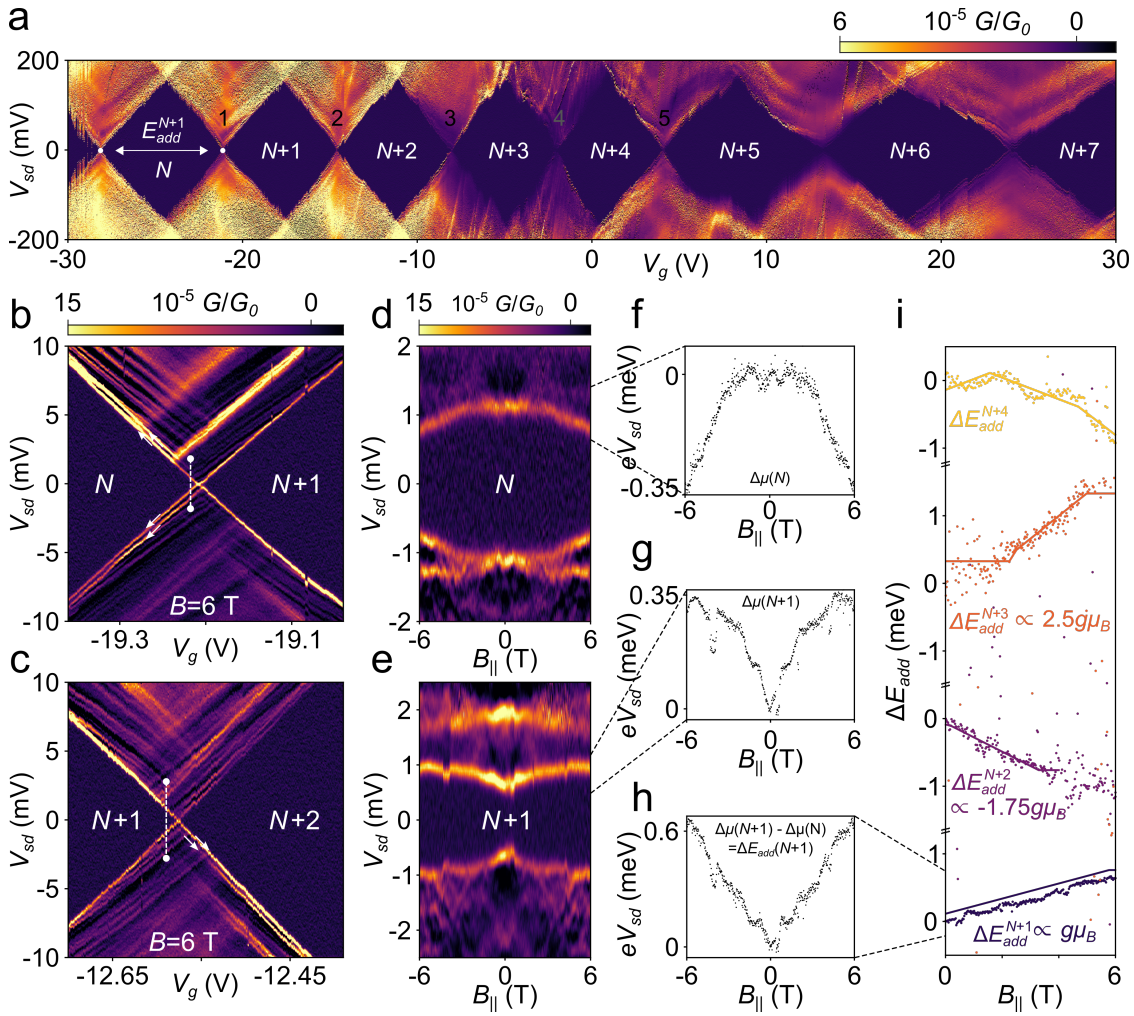


Figure 6.10: Procedure for finding the change in addition energy, $\Delta E_{add}(i)$, as a function of $B_{||}$ through measurements of G as a function of V_{sd} and $B_{||}$. **(a)** Stability diagram showing the definition of the addition energy $E_{add}(N+1)$. **(b,c)** Low-bias stability diagrams for $N \leftrightarrow N+1$ and $N+1 \leftrightarrow N+2$ with white dashed lines indicating where V_{sd} traces vs. $B_{||}$ were taken. **(d,e)** V_{sd} traces vs. $B_{||}$ revealing a shift in the involved chemical potentials, $\mu(N+1)$ and $\mu(N+2)$. **(f,g)** Peak positions found by fitting Lorentzian functions to each V_{sd} trace in the range indicated by dotted lines. **(h)** $\Delta E_{add}(N+1)$, as a function of $B_{||}$ (see text). **(i)** $\Delta E_{add}(i)$ vs. $B_{||}$ for $i = N+1$ to $N+4$, with slopes indicated in units of $g\mu_B$ and solid lines representing fits to Eq. 6.4 with parameters given in Tab. 6.1.

Table 6.4: Comparison between theoretical and experimental values for the slopes of $\Delta E_{add}(i)$ corresponding to the Stoner-filling path (orange phase).

	$\Delta E_{add}(N{+}1)$	$\Delta E_{add}(N{+}2)$	$\Delta E_{add}(N{+}3)$	$\Delta E_{add}(N{+}4)$
Theory (Eq. 3.13)	1 $g\mu_B$	2 $g\mu_B$	-2 $g\mu_B$	-1 $g\mu_B$
Experiment (Fig. 6.10i)	$\sim$1 $g\mu_B$	-1.75 $g\mu_B$	2.5 $g\mu_B$	QPT?

this behaviour for the transition to the $N{+}3$ charge state and the effect manifests in the slope of -1.75$g\mu_B$ in $\Delta E_{add}(N{+}2)$ and 2.5$g\mu_B$ in $\Delta E_{add}(N{+}3)$. From our model, these slopes suggest that $\Delta S(N{+}2) = 3/2$ and $\Delta S(N{+}3) = -1/2$. ξ overcoming $\Delta\epsilon_2$ leads to spontaneous spin polarisation including internal spin-flips that produces a high-spin $N{+}2$ ground state. However, ξ is not strong enough to maintain the spin polarisation for $N{+}3$ which sees a decrease in S by -1/2. Such behaviour deviates from both spin pairing and Hund's-rule filling, and is a fingerprint of Stoner instability [205, 242, 247] and constitutes the most important finding of this Chapter because it shows for the first time the existence of true magnetism in GNRs.

We stress that despite any variation in $\xi/\Delta\epsilon_2$ with N_i, the slopes of the experimental $\Delta E_{add}(i)$ are close to the theoretical values predicted for a system in the Stoner filling phase (Fig. 6.8). If a constant $\xi/\Delta\epsilon_2$ is assumed, we have $\Delta E_{add}(i) = g\mu_B(\Delta S(N_i) - \Delta S(N_{i-1}))$ (Eq. 3.13). Table 6.4 shows good agreement between experimental and theoretical slope values. $E_{add}(N{+}4)$ contains several kinks that can not be satisfactory explained by our simple model. The presence of kinks may suggest B induced quantum phase transitions (QPTs) as the quantity $g\mu_B SB/\Delta\epsilon_2$ increases with B (Fig. 6.8b).

6.3.4 Magnetic Anisotropy in MGNRs

The magnetic anisotropy of the nanoribbon can be assessed using magnetospectroscopy similar to the technique used in Sec. 5.3. We measured V_g traces as a function of $B(\varphi)$ with $B = 1$ T at 40 mK across the ground-state transitions $N{+}1 \leftrightarrow N{+}2$ and $N{+}3 \leftrightarrow N{+}4$. For anisotropic molecular magnetisation the nanoribbon should exhibit a chemical potential that fluctuates periodically with

φ. Our measurements took place before the device was thermally cycled and its stability diagram and corresponding charge states are shown in Figure. 6.1e.

Figure 6.11 reveals that charge states N+2 and N+4 both exhibit strong uniaxial anisotropy with an energy difference of 0.6 meV between hard and easy axes at 1 T. Interestingly, while $\mu(N+2)$ displays an in-ribbon-plane easy axis and an out-of-plane hard axis, $\mu(N+4)$ has opposite anisotropy with in-plane easy axis and out-of-plane hard axis. This important result show that the magnetic anisotropy of MGNRs are highly sensitive to their charge state.

For charge state N+2 the fit of βV_g requires six terms from Equation 5.2 and a linear term, and consists of several local extremal points, but largely follows a uniaxial pattern with 180° periodicity (Fig. 6.11a. The downwards linear trend could be due to hysteretic loss or random charge switches (e.g. at ∼280°). The anisotropy of N+4 is well fitted (Fig. 6.11d) with only one term (n=1) from Equation 5.2, which is typical for purely uniaxial systems. In the fitting procedure, outliers were excluded manually, in order to avoid that the algorithm would fall into a local minima. The result is that, in contrast to N+2, the chemical potential after one full rotation is the same and hysteresis if therefore not present.

Given our previous demonstration of spontaneously spin-polarising Stoner states giving rise to high-spin ground states for some charge states but not other, it is not surprising that only certain charge states display hysteresis. Moreover, perhaps our discovery of charge-dependent anisotropy can provide clues to unravel the mechanisms behind the Stoner instability. Furthermore, we saw in Chapter 5 that the exchange interaction between the nearby SMM and the conduction electrons was highly sensitive to the magnetic anisotropy. Therefore, perhaps charge-dependent anisotropy can explain the variation in spin-correlation energies observed in Section 6.3.3 above (Fig. 6.10i; Tab. 6.3).

The presence of charge-dependent anisotropy can also explain why not all MGNR ground states shift linearly with $B_\parallel$ (e.g. Fig. 6.7c and 6.10d,e). Nonlinear behaviour can simply indicate that B is applied along a hard axis, analogous to what we observed for **DyP** in Chapter 5. Spin–orbit coupling can also cause nonlinear

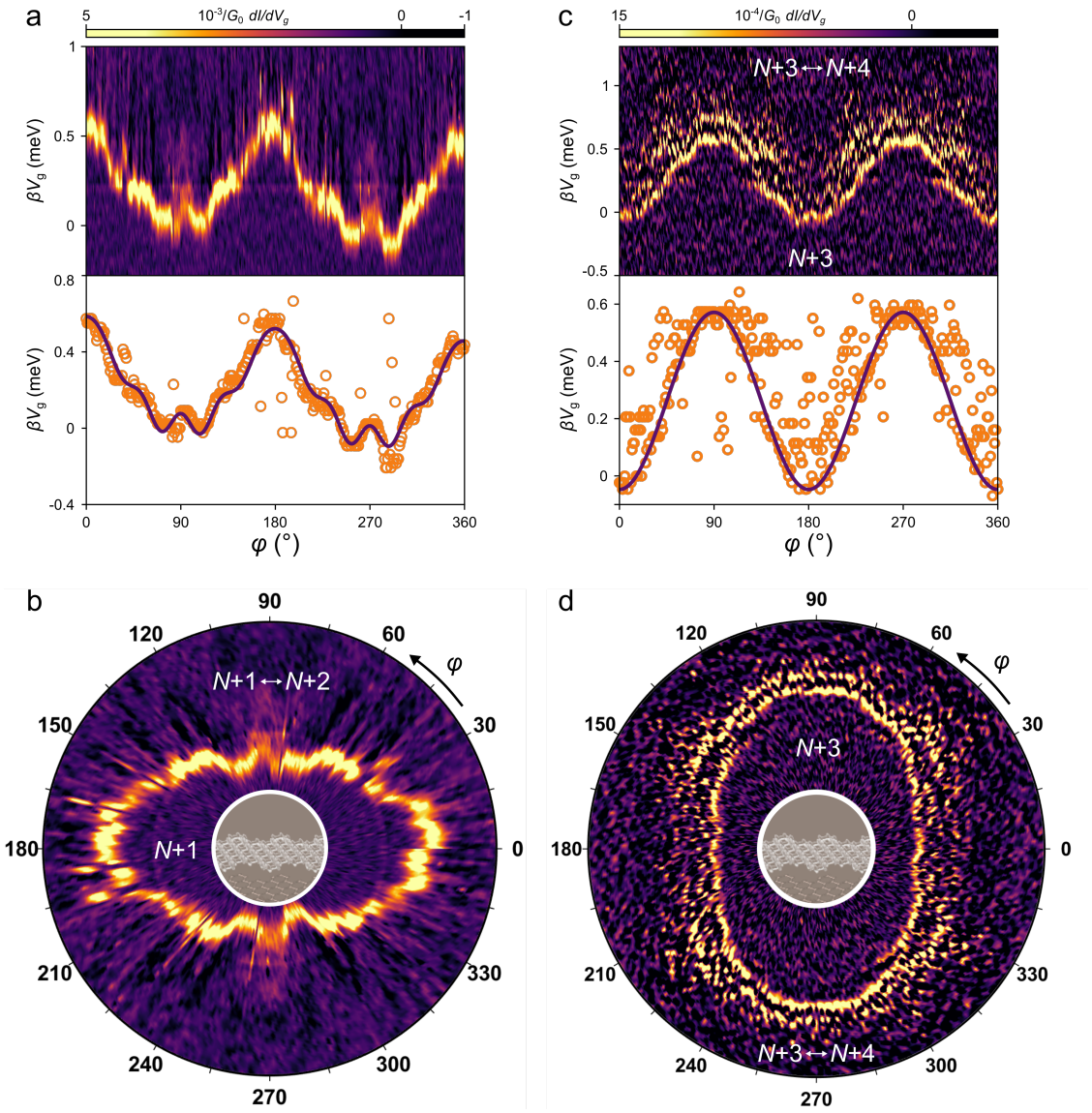


Figure 6.11: Magnetic anisotropy of the nanoribbon of two unknown charge states **(a,b)** N+1↔N+2 and **(c,d)** N+3↔N+4 based on V_g traces versus $B(\varphi)$ presented in polar and Cartesian coordinates. The data were obtained using $V_g = -11.98$ to -11.65 V and $V_{sd} = 5.62$, $V_g = 0.42$ to 0.6 V and $V_{sd} = 5.5$ mV, respectively, and B=1 T. $\varphi = 0°$ equals $B_{\parallel}$ and $\varphi = 90°$ equals $B_{\perp}$. The relative MGNR orientation is shown inside the polar plot. **(a,b)** The chemical potential $\mu(N+2) = \beta V_g$ (circles) is extracted by fitting Lorentzian functions to each trace. $\mu(\varphi)$ is fitted with Eq. 5.2 with the parameters in Tab. 6.5. The ground state of N+2 has a hard axis of magnetisation in-plane of the ribbon and easy out-of-plane. **(c,d)** Analogous plots showing $\mu(N+4)$ versus $B(\varphi)$. The ground state of N+4 has an in-plane easy axis and hard out-of-plane, i.e. the anisotropy is opposite to that of $\mu(N+2)$.

Table 6.5: Fitting parameters used for fitting the data in Fig. 6.11 to Eq. 5.2. $N{+}1 \leftrightarrow N{+}2$ was fitted to an additional linear term $a\varphi + b$.

Transistion	A	C_0	C_1	C_2	C_3	C_4	C_5	C_6	a	b
$N{+}1 \leftrightarrow N{+}2$	0.158	0.809	1.61	0.336	0.088	0.224	0.189	0.024	0.0022	0.807
$N{+}3 \leftrightarrow N{+}4$	0	0	0.309	0	0	0	0	0	0	0.262

Zeeman shift [162, 179, 181] but we expect negligible spin–orbit contributions in graphene nanostructures without curvature.

6.4 Low-Frequency Noise in MGNR Single-Electron Transistors

Random telegraph fluctuation (RTF) is a common noise-phenomenon in micro and nanoelectronics. A good understanding of RTF and other contributions to low-frequency noise is critical to device reliability. In this Section we have analysed the current, I, in a particularly noisy region of the stability diagram of the MGNR single-electron transistor at $T = 25$ mK. We discovered that the enhanced noise in this region stems from RTF, likely due to interplay between single electrons (or holes) in the MGNR channel and nearby charge traps that cause switch-like fluctuations in I. The large signal-to-noise ratio demonstrates the high sensitivity of the device to the environment, where fluctuations of single charges cause very large steps in I.

In this Section we will first establish from the literature the theory that is necessary to analyse the acquired data. We will proceed with the experiments carried out to acquire I as a function of time, t, capturing the RTF in the MGNR single-electron transistor (SET). The results and discussion of the analysis will reveal RTF of high amplitude and long average relaxation times of $\sim$100 s, and noise spectral density at low frequencies dominated by a single two-step fluctuator. Finally, we discuss underlying mechanisms of the RFT and compare the signal-to-noise ratio and noise spectral density to other SETs from the literature, as well as significant limitation of our study.

6.4.1 Theory of Low-Frequency Noise in SETs

RTF is a common phenomenon observed in single-electron transistors at low T. It is commonly caused by population of charge traps near to the transistor channel, and contributes to the low-frequency noise. When RTF is present, it usually is superimposed on the commonly observed $1/f$-noise that dominates low frequencies. RTF can be detected by measuring the current, I, as a function of time, t, (I-t traces) [248, 249].

RTF, also known as generation-and-recombination noise, is produced by charge-traps that capture and emit carriers with charge q from the conduction channel with carrier mobility μ. This process causes $I = q\mathcal{N}\mu$ fluctuations:

$$\delta I \propto q(\delta\mathcal{N}\mu)\mu + q\mathcal{N}\delta\mu, \tag{6.5}$$

where $\delta\mathcal{N}$ is the fluctuations of the charge density, $\mathcal{N}$, in the channel [248]. The current noise spectrum density of a single two-level fluctuator, i.e a charge trap, can be expressed as: [250]

$$S_I^P(f) = \frac{2\Delta I^2\langle\tau\rangle}{4 + (2\pi f\langle\tau\rangle)^2}, \tag{6.6}$$

where $\Delta I = I_{top} - I_{bottom} \approx 0.2$ of the normalised I and $\langle\tau\rangle$ is the mean relaxation time of the fluctuator.

The superposition of two-level fluctuators that cover a continuous spectre of values of $\langle\tau\rangle$ produces a power-law dependency of S_I on f: [248]

$$S_I^L(f) = kf^n, \tag{6.7}$$

with prefactor k and exponent n. n is usually around -1 and thus produces the well-known $S_I \propto 1/f$, also known as flickering noise, that characterises the noise below the white-noise frequency, f_0. This is shown in Figure 6.12g.

The noise power spectral density of an I-t trace can be obtained via the discrete Fourier transform, $\mathcal{F}(I,t)$, of I from time to frequency domain:

$$S_I(f) = \frac{1}{f_s\mathcal{N}_I}|\mathcal{F}(I,t)|^2, \tag{6.8}$$

where $f_s = 5$ Hz is the instrumental sampling rate of I, $\mathcal{N}_I$ is the number of samples of I.

The relaxation time of the system is described by the Poisson distribution: [251]

$$P(\tau) \propto \exp\left(-\frac{\tau}{\langle\tau\rangle}\right), \tag{6.9}$$

and can be used to extract the average relaxation times, $\langle\tau\rangle_l$, for the different I_l levels.

6.4.2 Low-Frequency Random Telegraph Noise Experiment

A low-frequency noise experiment was performed to assess the region $V_g > 15.8$ V that exhibit large I fluctuations close to the Coulomb diamond edge (Fig. 6.12a,b). To investigate these fluctuations the device was tuned to and fixed at $V_{sd} = 15.2$ mV and $V_g = 16.2$ V while measuring I for a time, $t = 48000$ s, resulting in $\mathcal{N}_I \approx 2.4 \cdot 10^5$ observations. The acquisition hardware sampled I values at a rate of 1 MHz and calculated the average value every 0.2 s which was then stored as a data point. Thus the effective sampling rate was 5 Hz.

6.4.3 Results

Intervals of a resulting I-t trace resulting from this experiment is shown in Figure 6.12c and e. The current noise is characterised by higher-frequency noise on a background of switch-like fluctuations between three distinct I levels, also called random telegraph fluctuations (RTFs). The signal-to-noise ratio (SNR) between the RTF signal amplitude, ΔI and the noise floor, Δi, is approximately SNR $= 10 \cdot \log_{10}(\Delta I/\Delta i) = 7$ dB. Figure 6.12d displays the histogram of I that reveals three distinct I levels with Gaussian distributions. The number of bins needed to create the histogram was estimated using Sturge's Rule: [252] $1 + 3.322 \log N_I$, where N_I is the number of observations of I.

The average relaxation times, $\langle\tau\rangle_l$, for I levels l: t, m, b (t: top; m: middle; b: bottom) were extracted from the I-t traces. Relaxation times, τ_i^l, were extracted through the process shown in Figure 6.12e and sorted by l. A histogram of τ_l was created for the three states, which revealed a Poisson distribution (Fig. 6.12g). The fit using Equation 6.9 yielded the avergage relaxation times $\langle\tau\rangle_t = 101$ s, $\langle\tau\rangle_m = 88$ s and $\langle\tau\rangle_b = 100$ s, which are approximately equal within the analysis error.

The current noise spectral density, S_I, was obtained via Fourier transform (Eq.6.8) from the I-t trace. When plotted in log-log axes (blue line in Fig. 6.12h), S_I is constant with f up to around $\cdot 10^{-3}$ Hz where a corner is present followed an approximately linear regime up to the limiting Nyquist frequency at $f = 2.5$ Hz. S_I was fitted to a power-law (Eq. 6.7) with parameters $k = 1.7 \cdot 10^{-8}$ and $n = -1.6$.

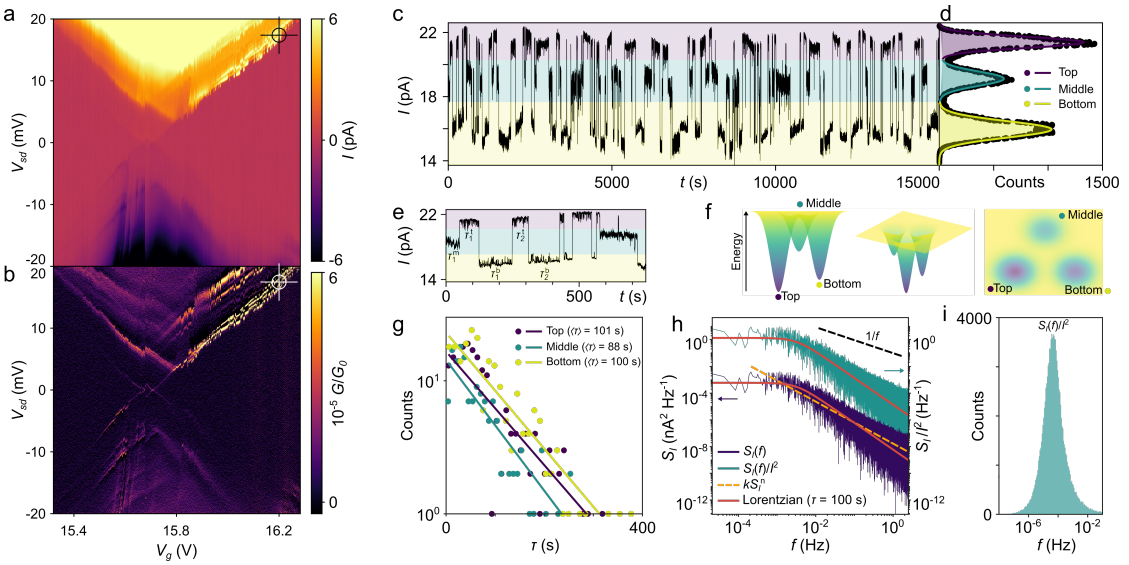


Figure 6.12: V_g-dependent random telegraph signals in a MGNR single-electron transistor. **(a,b)** I and G stability diagrams that show increased current instability for $V_g > 15.8$ V. **(c)** The device was tuned into this region (fixed $V_{sd} = 15.2$ mV and $V_g = 16.2$ V) and I was measured over time, t, with a sampling rate of 5 Hz. Only the first 15000 s are shown. The noise in I is of higher frequency with a low-frequency background of random telegraph noise between three I levels. **(d)** Histogram of I revealing three distinct I levels with Gaussian distributions. **(e)** The first 750 seconds of **(a)** showing the relaxation times τ_i^l of the level l (t: top; m: middle; b: bottom). **(f)** Illustration of the potentials of three charge traps that could explain the observed three-level fluctuations. **(g)** Distribution of relaxation times, t, in each I level fitted with Poisson distributions. **(h)** The current noise spectral density, S_I (blue), and its normalised version, S_I/I^2 (green), as functions of f, below the Nyquist frequency, obtained via Fourier transform of the I-t trace. $S_I(f)$ is fitted with a power-law on the form kx^n (orange line; $k = 1.7 \cdot 10^{-8}$; $n = -1.6$) and a Lorentzian (red line; see Eq. 6.6) with $\tau = 100$ s centred around $3 \cdot 10^{-3}$ Hz. **(i)** Histogram of the normalised noise spectral density S_I/I^2 revealing a log-normal distribution.

The corner was fitted to a Lorentzian (Eq. 6.6 with $\langle\tau\rangle = 100$ s. Above the corner frequency the slope of the the Lorentzian fit is proportional to $1/f^2$ and the power-law fit is $1/f^{1.6}$, i.e. in between the slopes expected for RTF and flickering noise ($1/f$). This observation indicates a superposition of flickering noise and noise generated from the two-level flucuator with a mean relaxation time of 100 s. The slope of S_I can be expected to shift from $1/f^2$ towards $1/f$ for higher f. The normalised spectral density, S_I/I^2, was calculated using the average value of I (green line in Fig. 6.12h). The noise amplitude, $A = fS_I/I^2 = 1 \cdot 10^{-5}$, at $f = 1$ Hz.

Figure 6.12i shows histograms of S_I (blue), S_I/I^2 and the noise amplitude,

fS_I/I^2. These reveal a log-normal distribution of all quantities with noise values spread over 4-5 orders of magnitude. The noise values are centred around $1 \cdot 10^{-8}$, $4 \cdot 10^{-5}$ and $7 \cdot 10^{-5}$ for S_I, S_I/I^2 and fS_I/I^2, respectively.

6.4.4 Discussion

We have shown that the MGNR single-electron transistor shows strong RTF in I with long average relaxation times of $\langle\tau\rangle = 100$ s. The observed three-level RTFs may originate from two or more different charge traps in close proximity to the MGNR conduction channel. Carriers from the MGNR may tunnel in and out of these traps and effectively cause two effects through Equation 6.5: (i) change the MGNR carrier density, $\mathcal{N}$ and (ii) locally modifying the electrostatic potential felt by the conduction channel and altering its alignment with the lead Fermi levels [248]. This effect is equivalent to an abrupt change in V_g and an effective change of carrier mobility, μ.

It seems unreasonable that small fluctuations in $\mathcal{N}$ could cause RTF with the magnitude that we observe. In contrast, modification of the mobility, μ, caused by either tunnelling between the channel and a trap or tunnelling of a trapped charge between distinct charge traps in close proximity to the channel, are more likely mechanisms. The spatial movement of the charge to the trap would alter the electrostatic potential felt by the channel and thereby the MGNR Fermi energy. This process effectively modifies the V_g-tuning of the MGNR levels relative to the Fermi energy of the leads that in turn affects the highly nonlinear conductivity.

There are several examples in the literature where RTF phenomena in QDs are attributed to tunnelling between charge traps. RTF has been observed in CTNs [253], Al single-electron transistors (SETs) [254] and Si MOSFETS [255] at $T < 4.2$ K, graphene tunnel junctions at 77 K [256], and even at room temperature in graphene [257]. However, direct comparisons of the present result with these studies are difficult because our sampling frequency is below their range. Reports often operates with a lower f-limit of around 1 Hz, which is our upper limit.

Despite the f-band limitation, the RTF SNR as a measure of the SETs sensitivity to nearby single charges can be directly compared with other reports. RTF with

relaxation times in the range $\tau : 10 - 1000$ s was reported for Si MOSFETS at $T = 2$ K [255]. The RTF SNR in these devices was around 10 dB compared to 7 dB in our device. In Al SETs at $T < 0.1$ K SNR ≈ 5 dB was observed [254]. When it comes to graphene-based SETs, SNR ≈ 11 dB was observed in a CNT FET at $T = 4.2$ K [258], SNR ≈ 3 dB in graphene tunnel junctions at $T = 77$ K [256], and SNR < 2 dB in graphene QDs at room temperature [257]. To date, there are no reports of RTF in GNRs to our knowledge.

The 7 dB SNR between RTF and the higher frequency noise demonstrates the high sensitivity to the local environment exhibited by MGNR single-electron transistors. Through gating, the device can be tuned into the RTF regime, where the trap potentials are brought to resonance. The strong RTF phenomenon serves as a demonstration of its sensitivity to nearby single-charge fluctuators. The large RTF SNR proposes such devices for highly sensitive single-charge sensors at low T.

The RTF phenomenon is only observed in certain regions of V_g, here $V_g > 15.8$ V. This V_g-dependency could impose that the transition rates between charge traps are also V_g dependent, possibly through V_g tuning of their potentials. In this picture, the onset of RTF could simply be a consequence of V_g-tuning the trap states into resonance with the channel or each other. For this to be possible each trap state must feel a coupling with the gate potential that is different to that of the others, otherwise all trap states would be shifted by the same amount by V_g. Such anisotropic coupling could be a result of electrostatic shielding of the traps by nearby charges.

We can also consider that the RTF is caused by the excitation of vibrons in the GNR side groups. We saw in Section 6.2 that vibrons can affect the electronic wave function through strong electron–vibron coupling. This mechanism would contrast the fluctuating-charge model that is usually found in the literature but proposes an interesting alternative considering the small magnitude of the involved I-fluctuations.

Through the Poisson distribution we showed that the fluctuating system has a long mean relaxation time of $\langle\tau\rangle = 100$ s for all three I levels (Fig. 6.12g). $\langle\tau\rangle$ is determined by the transmission probability between two traps, which depends on the tunnel barrier and coupling between them. However, we can not rule

out RTFs with shorter relaxation times than $1/f_s = 0.2$ s like seen in other graphene-based SETs [256–258].

Chen and coworkers reported the current noise spectral density of electron-beam etched GNRs with different widths [8]. At $T = 4$ K they observed that a device with GNR-width $w = 20$ nm produced 10 times as large noise amplitude, A, as a GNR of $w = 200$ nm; $A \approx 5 \cdot 10^{-4}$ and $A \approx 5 \cdot 10^{-5}$ at $f = 1$ Hz, respectively. If the value of A is dominated by w then we should observe $A \approx 5 \cdot 10^{-3}$ for our MGNR with $w = 1.12$ nm. However, we observe $A \approx 1 \cdot 10^{-5}$ at $f = 1$ Hz, i.e. two orders of magnitude smaller. On the other hand, we measured at $T = 25$ mK, i.e. two orders of magnitude lower than $T = 4$ K.

We found no convincing hints in the literature on whether the deviation from the w-dependent trend of A proposed by Chen and coworkers are due to the lower T. The literature on the noise characteristics of SETs is particularly scarce for mK measurements and therefore the expected T dependence of the noise in our device is hard to predict. However, this lack of evidence opens an attractive path for further investigations.

A significant limitation of this study is that I-t traces of only the high-noise RTF region at $V_g > 15.8$ V were obtained. No I-t traces were taken within the low-noise region. This lack of data makes comparison between the two regions impossible. It would have been valuable to observe whether the high-noise region only marks the onset of RTF or if the flickering noise also changes. Moreover, in the absence of RTF one would expect $S_I \propto 1/f$ noise characteristics for small f. Furthermore, I-t traces in the low-noise region would facilitate a more proper noise comparison with existing literature.

In addition to the V_g-dependence of the noise, further studies could investigate the V_{sd} and T dependence. The former has been studied to identify the approximate location of the charge trap(s) relative to the leads. The latter would, to our knowledge, be the first T analysis of the noise of graphene-based SETs at mK, which could bring information about underlying mechanisms driving RTF in MGNR SETs.

Another limitation is the small sampling frequency, $f_s = 5$ Hz. Comparable nanodevices usually samples at $f_s > 1$ kHz. Optimally, $f_s > f_0$ where f_0 is the threshold frequency for the f-independent (white) noise floor should be used to allow for a full characterisation of the low-frequency noise over several orders of magnitude of f. Such values of f_s are easily achievable in the current experimental setup and is just a matter of selecting it. Unfortunately, this was not done in our experiments.

6.5 Conclusions

In this chapter we have investigated the transport properties of molecularly-precise graphene nanoribbons, which can be created with perfect widths and edges. The electron scattering issues, which usually dominate the behaviour of graphene quantum dots and ribbons, are here almost non-existent, and the systems can be characterised in detail including their vibrational and spin levels. We could thus not only evidence the presence of spin states and their magnetic field evolution, but demonstrate the long-predicted Stoner interaction between spin states, and observe the anisotropy of their behaviour.

Increasing the solubility of MGNRs by switching to bulky side groups greatly enhances the yield of single-GNR transistors, and lifts the quality of those devices to unprecedented quality. The weak electrode-molecule coupling and large signal-to-noise ratio enables the detection of Franck–Condon suppression of conductance - a phenomenon that requires very low disorder to be detectable and thus has never before been observed in graphene nanoribbons. Even in our substrate-coupled GNR system we observe an electron–vibron coupling comparable to that of suspended ultra-clean carbon nanotubes, which confirms the predictions of much stronger electron–vibron coupling in graphene nanoribbons than in carbon nanotubes. Future research can then make use of the strong electron–vibron coupling in GNRs suspended over trenches, e.g. for electro-mechanical resonators, with the possibility of obtaining even stronger couplings.

Most importantly, the observed Stoner instability in graphene nanoribbons leading to the emergence of spin-polarised states, unequivocally fulfils the fundamental ingredient for true magnetism in graphene. This property enables the switching between low-spin and high-spin states simply through electrostatic gating of the nanoribbon. The Stoner instability arises as a consequence of competition between spin-correlation (exchange) energy and molecular level spacing of similar magnitudes, which is unique compared to other carbon nanosystems. This opens the path to the investigation of electron–electron and spin–spin correlations in graphene nanosystems, where theories of correlations remain largely unverified.

We have observed that the molecular magnetic anisotropies of the graphene nanoribbons are uniaxial but may change drastically from in-plane to out-of-plane with different charge states. As we learned in Chapter 5, the anisotropy of the transport channel is strongly linked to the anisotropy of the exchange interaction. Therefore, it seems clear that the observed transition in the anisotropy of the transport channel is interlinked with the Stoner instability. This can produce fingerprint features that may open up the possibility of investigating the edge–edge spin interactions and their possible use in spintronic and quantum devices.

Through noise spectroscopy we have discovered and quantified the high sensitivity of graphene nanoribbons to nearby resonant fluctuators, and provided device-noise characteristics at a temperature that is scarcely reported in the literature. We observed strong random telegraph fluctuations that could be switched on and off by electrostatic gating. These fluctuations were manifest in three distinct current magnitudes that are determined by the fluctuator state.

These results demonstrate graphene nanoribbons for the first time as molecular spintronic units, and provide the basis for the investigation of their future use in electronic devices. Next, quantum control of graphene nanoribbons must be assessed to determine the spin-coherence time, which is predicted to be much longer than in carbon nanotubes. Suspended graphene systems also present interesting opportunities to further enhance the quality of transport features and to increase spin-coherence times.

7
Conclusion

In this Thesis we have characterised the magnetic and electronic states of molecular nanoscale systems, comparing the properties of single-crystals and isolated single-molecules, e.g. as obtained in electronic nanodevices. We developed and used a novel millikelvin torque magnetometry setup, as required to produce side-by-side comparison with magnetotransport spectroscopy at millikelvin temperatures.

We have described the design, fabrication, testing and experimental use of a millikelvin cantilever torque magnetometer. This device proved invaluable in detecting the magnetic anisotropy of the lanthanide-based SMMs studied for this Thesis, and thereby provided new and important insights to this poorly understood group of compounds. The development of fast-sweeping superconducting magnets will, once completed, provide another component to both cantilever torque magnetometry and transport spectroscopy, for investigating hysteresis and quantum tunnelling phenomena in an additional pushed environment.

Through millikelvin magnetotransport spectroscopy on a dysprosium porphyrin single-molecule magnet, we provide a rare example of using single-electron read-out of the molecular anisotropy of a single molecule. We find a strong relationship between the molecular anisotropy of the SMM and the anisotropy of the conduction channel despite no orbitals of the magnetic ion being involved in the channel. We consider this an effect caused by the strong exchange interaction imposed on

the channel spins by the magnetic ion, which if true has important consequences for the design of molecular systems for spintronic applications. Moreover, the connections between intramolecular exchange interactions, molecular anisotropy, and molecular transport properties provide clues to the mechanisms behind the Stoner instability observed in graphene nanoribbons.

Using cantilever torque magnetometry and complimentary techniques, we have characterised the crystal and molecular anisotropy of several terbium and dysprosium-based single-molecule magnets at millikelvin temperature. Our results suggest that the magnetocrystalline anisotropies of these compounds are dominated by non-collinear uniaxial easy-axis contributions. We confirm the SMM behaviour of terbium porphyrin and dysprosium porphyrin SMMs by revealing magnetic hysteresis of a purely molecular origin below 12 K, and manifestations of superparamagnetism that strongly depends on the magnetic field direction.

The development of these techniques later opened up the way for the investigation of the electronic, magnetic and vibrational states of molecular graphene nanoribbons. The final parts of the Thesis show, importantly, that the predicted spontaneous spin-polarisation by the Stoner interaction does occur in graphene nanoribbons. This information was accessible with remarkable simplicity from high quality devices produced from bottom-up synthesised graphene nanoribbons with perfect structure and edges, and solubilising side-groups that promote de-bundling from other ribbons. These results thus open the path to the use in spintronic devices not only of localised magnetic centres, as in single molecule magnets, but also of the magnetic states of delocalised electronic systems, such as graphene nanoribbons.

The magnetic behaviour of such systems is revealed to be fundamentally different from that of carbon nanotubes, and other known carbon nanosystems. Together with the previous observation of long coherence times in graphene edge states, our result opens the possibility of using the magnetic states for quantum applications. The energy scales of the magnetic excitations observed do fall within the GHz region that is accessible by using coaxial cables in dilution refrigerators. We thus think that single-nanoribbon pulsed spectroscopy will soon be the path forward. Future

inclusion of microwaves combined with millikelvin magnetotransport would also enable electron paramagnetic resonance experiments on single-molecule magnets. Such a capability could greatly benefit future research in the area of spintronics, and thus comprises a natural next challenge in instrumentation development for this line of research.

Moreover, our experimental confirmation of the long-standing predictions of true magnetism in graphene nanoribbons will spur additional theoretical work on the subject, with the possibility of validating or falsifying future predictions about these magnetic states using our electronic nanodevices. In this sense, these results may soon establish a paradigm shift in the field of carbon nanoelectronics, by providing a basis for graphene nanoribbons to be further explored for their future use in electronic devices.

We encourage efforts towards the aim of increasing the reproducibility of single-molecule electronic devices. Currently, the morphological synthetic control of graphene nanoribbons is limited to the widths and edges while the length parameter is free, and this limits the opportunity to fabricate identical devices. Moreover, low device yield is a major challenge and therefore advances in the nanofabrication technique to increase yields would proportionally accelerate the throughput of experimental single-molecule studies.

Finally, and in line with the theme of this Thesis, we propose efforts to increase the magnetism of graphene nanoribbons by combining them with single-molecule magnets. Decoration of the nanoribbon edges with lanthanide-based single-molecule magnets that couple with the magnetic edge states, can not only introduce large additional magnetic moments to the system, but also spin–orbit coupling into the edge states. This is a fundamental ingredient for topologically-interesting states, and our synthetic laboratories have already started producing such magnetic ribbons, in a true unification of magnetic and conductive molecular systems, producing molecular pathways towards quantum topological systems.

References

[1] John F Kennedy. *President John F. Kennedy's Rice Stadium Moon Speech*. Sept. 1962. URL: https://er.jsc.nasa.gov/seh/ricetalk.htm.

[2] Javier Luzon and Roberta Sessoli. "Lanthanides in molecular magnetism: so fascinating, so challenging". *Dalton Transactions* 41.44 (2012), pp. 13556–13567.

[3] Mauro Perfetti. "Cantilever torque magnetometry on coordination compounds: from theory to experiments". *Coordination Chemistry Reviews* 348 (2017), pp. 171–186.

[4] Young-Woo Son, Marvin L Cohen, and Steven G Louie. "Energy gaps in graphene nanoribbons". *Physical Review Letters* 97.21 (2006), p. 216803.

[5] Verónica Barone, Oded Hod, and Gustavo E Scuseria. "Electronic structure and stability of semiconducting graphene nanoribbons". *Nano Letters* 6.12 (2006), pp. 2748–2754.

[6] Oleg V Yazyev and MI Katsnelson. "Magnetic correlations at graphene edges: basis for novel spintronics devices". *Physical Review Letters* 100.4 (2008), p. 047209.

[7] Michael Slota et al. "Magnetic edge states and coherent manipulation of graphene nanoribbons". *Nature* 557.7707 (2018), pp. 691–695.

[8] Zhihong Chen et al. "Graphene nano-ribbon electronics". *Physica E: Low-dimensional Systems and Nanostructures* 40.2 (2007), pp. 228–232.

[9] Jingwei Bai et al. "Very large magnetoresistance in graphene nanoribbons". *Nature Nanotechnology* 5.9 (2010), pp. 655–659.

[10] Dmitry V Kosynkin et al. "Longitudinal unzipping of carbon nanotubes to form graphene nanoribbons". *Nature* 458.7240 (2009), pp. 872–876.

[11] Jinming Cai et al. "Atomically precise bottom-up fabrication of graphene nanoribbons". *Nature* 466.7305 (2010), pp. 470–473.

[12] Akimitsu Narita et al. "Synthesis of structurally well-defined and liquid-phase-processable graphene nanoribbons". *Nature Chemistry* 6.2 (2014), pp. 126–132.

[13] Jean-François Bobier et al. *What Happens When 'If' Turns to 'When' in Quantum Computing?* Tech. rep. BCG Global, July 2021.

[14] Bela Bauer et al. "Quantum algorithms for quantum chemistry and quantum materials science". *Chemical Reviews* 120.22 (2020), pp. 12685–12717.

[15] Yudong Cao et al. "Quantum algorithm and circuit design solving the Poisson equation". *New Journal of Physics* 15.1 (2013), p. 013021.

[16] Matthias Evers, Anna Heid, and Ostojic Ivan. *Pharma's digital Rx: Quantum computing in drug research and development*. Tech. rep. McKinsey & Company, June 2021.

[17] Colin P Williams. *Explorations in quantum computing*. Springer Science & Business Media, 2010.

[18] Nana Liu and Patrick Rebentrost. "Quantum machine learning for quantum anomaly detection". *Physical Review A* 97.4 (2018), p. 042315.

[19] Patrick Rebentrost and Seth Lloyd. "Quantum computational finance: quantum algorithm for portfolio optimization". *arXiv preprint arXiv:1811.03975* (2018).

[20] Stefan Woerner and Daniel J Egger. "Quantum risk analysis". *npj Quantum Information* 5.1 (2019), pp. 1–8.

[21] Michel Boyer et al. "Tight bounds on quantum searching". *Fortschritte der Physik: Progress of Physics* 46.4-5 (1998), pp. 493–505.

[22] Vedran Dunjko and Hans J Briegel. "Machine learning & artificial intelligence in the quantum domain: a review of recent progress". *Reports on Progress in Physics* 81.7 (2018), p. 074001.

[23] John Preskill. "Quantum computing in the NISQ era and beyond". *Quantum* 2 (2018), p. 79.

[24] Morten Kjaergaard et al. "Superconducting qubits: Current state of play". *Annual Review of Condensed Matter Physics* 11 (2020), pp. 369–395.

[25] Christopher Monroe and Jungsang Kim. "Scaling the ion trap quantum processor". *Science* 339.6124 (2013), pp. 1164–1169.

[26] Pieter Kok et al. "Linear optical quantum computing with photonic qubits". *Reviews of Modern Physics* 79.1 (2007), p. 135.

[27] Mark Saffman. "Quantum computing with atomic qubits and Rydberg interactions: progress and challenges". *Journal of Physics B: Atomic, Molecular and Optical Physics* 49.20 (2016), p. 202001.

[28] Floris A Zwanenburg et al. "Silicon quantum electronics". *Reviews of Modern Physics* 85.3 (2013), p. 961.

[29] AH Castro Neto et al. "The electronic properties of graphene". *Reviews of Modern Physics* 81.1 (2009), p. 109.

[30] Edward A Laird et al. "Quantum transport in carbon nanotubes". *Reviews of Modern Physics* 87.3 (2015), p. 703.

[31] Michael N Leuenberger and Daniel Loss. "Quantum computing in molecular magnets". *Nature* 410.6830 (2001), pp. 789–793.

[32] MS Grinolds et al. "Subnanometre resolution in three-dimensional magnetic resonance imaging of individual dark spins". *Nature Nanotechnology* 9.4 (2014), p. 279.

[33] SA Wolf et al. "Spintronics: a spin-based electronics vision for the future". *Science* 294.5546 (2001), pp. 1488–1495.

[34] Alexandre R Rocha et al. "Towards molecular spintronics". *Nature Materials* 4.4 (2005), pp. 335–339.

[35] NJ Tao. "Electron transport in molecular junctions". *Nature Nanotechnology* 1.3 (2006), p. 173.

[36] Stefano Sanvito and A Reily Rocha. "Molecular-spintronics: The art of driving spin through molecules". *Journal of Computational and Theoretical Nanoscience* 3.5 (2006), pp. 624–642.

[37] Arzhang Ardavan et al. "Will spin-relaxation times in molecular magnets permit quantum information processing?" *Physical Review Letters* 98.5 (2007), p. 057201.

[38] Lapo Bogani and Wolfgang Wernsdorfer. "Molecular spintronics using single-molecule magnets". *Nature Materials* 7.3 (2008), p. 179.

[39] C Schlegel et al. "Direct observation of quantum coherence in single-molecule magnets". *Physical Review Letters* 101.14 (2008), p. 147203.

[40] Filippo Troiani and Marco Affronte. "Molecular spins for quantum information technologies". *Chemical Society Reviews* 40.6 (2011), pp. 3119–3129.

[41] Dante Gatteschi, Roberta Sessoli, and Jacques Villain. *Molecular nanomagnets*. Vol. 5. Oxford University Press on Demand, 2006, pp. 64–65.

[42] Song Gao et al. *Molecular nanomagnets and related phenomena*. Vol. 164. Springer, 2015.

[43] Cristiano Benelli and Dante Gatteschi. *Introduction to molecular magnetism: From transition metals to lanthanides*. John Wiley & Sons, 2015.

[44] Roberta Sessoli et al. "Magnetic bistability in a metal-ion cluster". *Nature* 365.6442 (1993), p. 141.

[45] Jonathan R Friedman et al. "Macroscopic measurement of resonant magnetization tunneling in high-spin molecules". *Physical Review Letters* 76.20 (1996), p. 3830.

[46] L Thomas et al. "Macroscopic quantum tunnelling of magnetization in a single crystal of nanomagnets". *Nature* 383.6596 (1996), pp. 145–147.

[47] W Wernsdorfer and R Sessoli. "Quantum phase interference and parity effects in magnetic molecular clusters". *Science* 284.5411 (1999), pp. 133–135.

[48] Constantinos J Milios et al. "A record anisotropy barrier for a single-molecule magnet". *Journal of the American Chemical Society* 129.10 (2007), pp. 2754–2755.

[49] HB Heersche et al. "Electron transport through single Mn_{12} molecular magnets". *Physical Review Letters* 96.20 (2006), p. 206801.

[50] Naoto Ishikawa et al. "Lanthanide double-decker complexes functioning as magnets at the single-molecular level". *Journal of the American Chemical Society* 125.29 (2003), pp. 8694–8695.

[51] Jeffrey D Rinehart and Jeffrey R Long. "Exploiting single-ion anisotropy in the design of f-element single-molecule magnets". *Chemical Science* 2.11 (2011), pp. 2078–2085.

[52] Lorenzo Sorace, Cristiano Benelli, and Dante Gatteschi. "Lanthanides in molecular magnetism: old tools in a new field". *Chemical Society Reviews* 40.6 (2011), pp. 3092–3104.

[53] Matias Urdampilleta et al. "Supramolecular spin valves". *Nature Materials* 10.7 (2011), pp. 502–506.

[54] Daniel N Woodruff, Richard EP Winpenny, and Richard A Layfield. "Lanthanide single-molecule magnets". *Chemical Reviews* 113.7 (2013), pp. 5110–5148.

[55] J Dreiser. "Molecular lanthanide single-ion magnets: from bulk to submonolayers". *Journal of Physics: Condensed Matter* 27.18 (2015), p. 183203.

[56] KWH Stevens. "Matrix elements and operator equivalents connected with the magnetic properties of rare earth ions". *Proceedings of the Physical Society. Section A* 65.3 (1952), p. 209.

[57] HA Kramers. "General theory of paramagnetic rotation in crystals". *Proc. Acad. Sci. Amsterdam.* Vol. 33. 1930, p. 959.

[58] Anatole Abragam and Brebis Bleaney. *Electron paramagnetic resonance of transition ions.* OUP Oxford, 2012.

[59] Albert Furrer and Oliver Waldmann. "Magnetic cluster excitations". *Reviews of Modern Physics* 85.1 (2013), p. 367.

[60] Markus P Hehlen and Hans U Güdel. "Optical spectroscopy of the dimer system Cs3Yb2Br9". *The Journal of Chemical Physics* 98.3 (1993), pp. 1768–1775.

[61] Francesco Aquilante et al. "Molcas 8: New capabilities for multiconfigurational quantum chemical calculations across the periodic table". *Journal of Computational Chemistry* 37.5 (2016), pp. 506–541.

[62] Philip Richard Wallace. "The band theory of graphite". *Physical Review* 71.9 (1947), p. 622.

[63] Kostya S Novoselov et al. "Electric field effect in atomically thin carbon films". *Science* 306.5696 (2004), pp. 666–669.

[64] Kostya S Novoselov et al. "Two-dimensional gas of massless Dirac fermions in graphene". *Nature* 438.7065 (2005), pp. 197–200.

[65] Gordon W Semenoff. "Condensed-matter simulation of a three-dimensional anomaly". *Physical Review Letters* 53.26 (1984), p. 2449.

[66] Eduardo Fradkin. "Critical behavior of disordered degenerate semiconductors. II. Spectrum and transport properties in mean-field theory". *Physical Review B* 33.5 (1986), p. 3263.

[67] F Duncan M Haldane. "Model for a quantum Hall effect without Landau levels: Condensed-matter realization of the" parity anomaly"". *Physical Review Letters* 61.18 (1988), p. 2015.

[68] Adriaan MJ Schakel. "Relativistic quantum Hall effect". *Physical Review D* 43.4 (1991), p. 1428.

[69] J González, F Guinea, and MAH Vozmediano. "Unconventional quasiparticle lifetime in graphite". *Physical Review Letters* 77.17 (1996), p. 3589.

[70] EV Gorbar et al. "Magnetic field driven metal-insulator phase transition in planar systems". *Physical Review B* 66.4 (2002), p. 045108.

[71] MI Katsnelson. "Zitterbewegung, chirality, and minimal conductivity in graphene". *The European Physical Journal B-Condensed Matter and Complex Systems* 51.2 (2006), pp. 157–160.

[72] MI Katsnelson, KS Novoselov, and AK Geim. "Chiral tunnelling and the Klein paradox in graphene". *Nature Physics* 2.9 (2006), pp. 620–625.

[73] Andre K Geim and Konstantin S Novoselov. "The rise of graphene". *Nanoscience and Technology: a collection of reviews from Nature Journals*. World Scientific, 2010, pp. 11–19.

[74] Keun Soo Kim et al. "Large-scale pattern growth of graphene films for stretchable transparent electrodes". *Nature* 457.7230 (2009), pp. 706–710.

[75] Andre Konstantin Geim. "Graphene: status and prospects". *Science* 324.5934 (2009), pp. 1530–1534.

[76] Konstantin S Novoselov et al. "A roadmap for graphene". *Nature* 490.7419 (2012), pp. 192–200.

[77] Andrea C Ferrari et al. "Science and technology roadmap for graphene, related two-dimensional crystals, and hybrid systems". *Nanoscale* 7.11 (2015), pp. 4598–4810.

[78] Christian Cervetti et al. "The classical and quantum dynamics of molecular spins on graphene". *Nature Materials* 15.2 (2016), pp. 164–168.

[79] Kostya S Novoselov et al. "Two-dimensional atomic crystals". *Proceedings of the National Academy of Sciences* 102.30 (2005), pp. 10451–10453.

[80] Yuanbo Zhang et al. "Experimental observation of the quantum Hall effect and Berry's phase in graphene". *Nature* 438.7065 (2005), pp. 201–204.

[81] Sergei V Morozov et al. "Strong suppression of weak localization in graphene". *Physical Review Letters* 97.1 (2006), p. 016801.

[82] Konstantin S Novoselov et al. "Room-temperature quantum Hall effect in graphene". *Science* 315.5817 (2007), pp. 1379–1379.

[83] Alberto Cortijo and Maria AH Vozmediano. "Effects of topological defects and local curvature on the electronic properties of planar graphene". *Nuclear Physics B* 763.3 (2007), pp. 293–308.

[84] Alberto Cortijo and Maria AH Vozmediano. "Electronic properties of curved graphene sheets". *Europhysics Letters* 77.4 (2007), p. 47002.

[85] Federico Lombardi et al. "Quantum units from the topological engineering of molecular graphenoids". *Science* 366.6469 (2019), pp. 1107–1110.

[86] Cory R Dean et al. "Hofstadter's butterfly and the fractal quantum Hall effect in moiré superlattices". *Nature* 497.7451 (2013), pp. 598–602.

[87] LA Ponomarenko et al. "Cloning of Dirac fermions in graphene superlattices". *Nature* 497.7451 (2013), pp. 594–597.

[88] Benjamin Hunt et al. "Massive Dirac fermions and Hofstadter butterfly in a van der Waals heterostructure". *Science* 340.6139 (2013), pp. 1427–1430.

[89] Antonio H Castro Neto et al. "The electronic properties of graphene". *Reviews of Modern Physics* 81.1 (2009), pp. 109–162.

[90] NMR Peres. "Colloquium: The transport properties of graphene: An introduction". *Reviews of Modern Physics* 82.3 (2010), p. 2673.

[91] Vadim V Cheianov and Vladimir I Fal'ko. "Selective transmission of Dirac electrons and ballistic magnetoresistance of n-p junctions in graphene". *Physical Review B* 74.4 (2006), p. 041403.

[92] VP Gusynin and SG Sharapov. "Unconventional integer quantum Hall effect in graphene". *Physical Review Letters* 95.14 (2005), p. 146801.

[93] NMR Peres and Eduardo V Castro. "Algebraic solution of a graphene layer in transverse electric and perpendicular magnetic fields". *Journal of Physics: Condensed Matter* 19.40 (2007), p. 406231.

[94] NMR Peres, F Guinea, and AH Castro Neto. "Electronic properties of disordered two-dimensional carbon". *Physical Review B* 73.12 (2006), p. 125411.

[95] AH Castro Neto and Francisco Guinea. "Impurity-induced spin-orbit coupling in graphene". *Physical Review Letters* 103.2 (2009), p. 026804.

[96] ZH Ni et al. "On resonant scatterers as a factor limiting carrier mobility in graphene". *Nano Letters* 10.10 (2010), pp. 3868–3872.

[97] David Ferry and Stephen Marshall Goodnick. *Transport in nanostructures*. 6. Cambridge university press, 1999.

[98] T Stauber, NMR Peres, and AH Castro Neto. "Conductivity of suspended and non-suspended graphene at finite gate voltage". *Physical Review B* 78.8 (2008), p. 085418.

[99] Michael M Fogler. "Neutrality point of graphene with coplanar charged impurities". *Physical Review Letters* 103.23 (2009), p. 236801.

[100] EH Hwang and S Das Sarma. "Single-particle relaxation time versus transport scattering time in a two-dimensional graphene layer". *Physical Review B* 77.19 (2008), p. 195412.

[101] Jakub Tworzydło et al. "Sub-Poissonian shot noise in graphene". *Physical Review Letters* 96.24 (2006), p. 246802.

[102] John M Ziman. *Principles of the Theory of Solids*. Cambridge university press, 1972.

[103] CWJ Beenakker and Henk van Houten. "Quantum transport in semiconductor nanostructures". *Solid State Physics* 44 (1991), pp. 1–228.

[104] CWJ Beenakker. "Colloquium: Andreev reflection and Klein tunneling in graphene". *Reviews of Modern Physics* 80.4 (2008), p. 1337.

[105] Michael Victor Berry and RJ Mondragon. "Neutrino billiards: time-reversal symmetry-breaking without magnetic fields". *Proceedings of the Royal Society of London. A. Mathematical and Physical Sciences* 412.1842 (1987), pp. 53–74.

[106] FV Tikhonenko et al. "Transition between electron localization and antilocalization in graphene". *Physical Review Letters* 103.22 (2009), p. 226801.

[107] Edward McCann et al. "Weak-localization magnetoresistance and valley symmetry in graphene". *Physical Review Letters* 97.14 (2006), p. 146805.

[108] Luis Brey and HA Fertig. "Electronic states of graphene nanoribbons studied with the Dirac equation". *Physical Review B* 73.23 (2006), p. 235411.

[109] F Sols, F Guinea, and AH Castro Neto. "Coulomb blockade in graphene nanoribbons". *Physical Review Letters* 99.16 (2007), p. 166803.

[110] Katsunori Wakabayashi et al. "Electronic states of graphene nanoribbons and analytical solutions". *Science and Technology of Advanced Materials* 11.5 (2010), p. 054504.

[111] Kyoko Nakada et al. "Edge state in graphene ribbons: Nanometer size effect and edge shape dependence". *Physical Review B* 54.24 (1996), p. 17954.

[112] Mitsutaka Fujita et al. "Peculiar localized state at zigzag graphite edge". *Journal of the Physical Society of Japan* 65.7 (1996), pp. 1920–1923.

[113] Kyle A Ritter and Joseph W Lyding. "The influence of edge structure on the electronic properties of graphene quantum dots and nanoribbons". *Nature Materials* 8.3 (2009), pp. 235–242.

[114] Katsunori Wakabayashi and Sudipta Dutta. "Nanoscale and edge effect on electronic properties of graphene". *Solid State Communications* 152.15 (2012), pp. 1420–1430.

[115] Hosik Lee et al. "Magnetic ordering at the edges of graphitic fragments: Magnetic tail interactions between the edge-localized states". *Physical Review B* 72.17 (2005), p. 174431.

[116] Young-Woo Son, Marvin L Cohen, and Steven G Louie. "Half-metallic graphene nanoribbons". *Nature* 444.7117 (2006), pp. 347–349.

[117] Federico Muñoz-Rojas, Joaquın Fernández-Rossier, and JJ Palacios. "Giant magnetoresistance in ultrasmall graphene based devices". *Physical Review Letters* 102.13 (2009), p. 136810.

[118] Melinda Y Han et al. "Energy band-gap engineering of graphene nanoribbons". *Physical Review Letters* 98.20 (2007), p. 206805.

[119] Liying Jiao et al. "Narrow graphene nanoribbons from carbon nanotubes". *Nature* 458.7240 (2009), pp. 877–880.

[120] Liying Jiao et al. "Facile synthesis of high-quality graphene nanoribbons". *Nature Nanotechnology* 5.5 (2010), pp. 321–325.

[121] Xinran Wang et al. "Graphene nanoribbons with smooth edges behave as quantum wires". *Nature Nanotechnology* 6.9 (2011), pp. 563–567.

[122] Chenggang Tao et al. "Spatially resolving edge states of chiral graphene nanoribbons". *Nature Physics* 7.8 (2011), pp. 616–620.

[123] Xiaolin Li et al. "Chemically derived, ultrasmooth graphene nanoribbon semiconductors". *Science* 319.5867 (2008), pp. 1229–1232.

[124] Leonhard Grill et al. "Nano-architectures by covalent assembly of molecular building blocks". *Nature Nanotechnology* 2.11 (2007), pp. 687–691.

[125] Amina Kimouche et al. "Ultra-narrow metallic armchair graphene nanoribbons". *Nature Communications* 6.1 (2015), pp. 1–6.

[126] Matthias Koch et al. "Voltage-dependent conductance of a single graphene nanoribbon". *Nature Nanotechnology* 7.11 (2012), pp. 713–717.

[127] Junzhi Liu et al. “Toward cove-edged low band gap graphene nanoribbons”. *Journal of the American Chemical Society* 137.18 (2015), pp. 6097–6103.

[128] Pascal Ruffieux et al. “Electronic structure of atomically precise graphene nanoribbons”. *ACS Nano* 6.8 (2012), pp. 6930–6935.

[129] Shiyong Wang et al. “Quantum dots in graphene nanoribbons”. *Nano Letters* 17.7 (2017), pp. 4277–4283.

[130] Akimitsu Narita et al. “New advances in nanographene chemistry”. *Chemical Society Reviews* 44.18 (2015), pp. 6616–6643.

[131] Arieh Aviram and Mark A Ratner. “Molecular rectifiers”. *Chemical Physics Letters* 29.2 (1974), pp. 277–283.

[132] Hongkun Park et al. “Nanomechanical oscillations in a single-C 60 transistor”. *Nature* 407.6800 (2000), pp. 57–60.

[133] M Di Ventra, ST Pantelides, and ND Lang. “First-principles calculation of transport properties of a molecular device”. *Physical Review Letters* 84.5 (2000), p. 979.

[134] Prashant Damle et al. “Current-voltage characteristics of molecular conductors: two versus three terminal”. *IEEE Transactions on Nanotechnology* 99.3 (2002), pp. 145–153.

[135] Ch Joachim et al. “Electronics using hybrid-molecular and mono-molecular devices”. *Nature* 408.6812 (2000), p. 541.

[136] Gianaurelio Cuniberti, Giorgos Fagas, and Klaus Richter. “Introducing molecular electronics: A brief overview”. Springer, 2006, pp. 1–10.

[137] Abraham Nitzan and Mark A Ratner. “Electron transport in molecular wire junctions”. *Science* 300.5624 (2003), pp. 1384–1389.

[138] Yoram Selzer and David L Allara. “Single-molecule electrical junctions”. *Annu. Rev. Phys. Chem.* 57 (2006), pp. 593–623.

[139] Mickael L Perrin, Enrique Burzurı, and Herre SJ van der Zant. “Single-molecule transistors”. *Chemical Society Reviews* 44.4 (2015), pp. 902–919.

[140] Ronald Hanson et al. “Spins in few-electron quantum dots”. *Reviews of Modern Physics* 79.4 (2007), p. 1217.

[141] Jiwoong Park et al. “Coulomb blockade and the Kondo effect in single-atom transistors”. *Nature* 417.6890 (2002), pp. 722–725.

[142] H Van Houten, CWJ Beenakker, and AAM Staring. “Coulomb-blockade oscillations in semiconductor nanostructures”. *Single Charge Tunneling*. Springer, 1992, pp. 167–216.

[143] Daniel Loss and David P DiVincenzo. “Quantum computation with quantum dots”. *Physical Review A* 57.1 (1998), p. 120.

[144] David P DiVincenzo et al. “Universal quantum computation with the exchange interaction”. *Nature* 408.6810 (2000), pp. 339–342.

[145] Mark S Byrd and Daniel A Lidar. “Comprehensive encoding and decoupling solution to problems of decoherence and design in solid-state quantum computing”. *Physical Review Letters* 89.4 (2002), p. 047901.

[146] Jeremy Levy. "Universal quantum computation with spin-1/2 pairs and Heisenberg exchange". *Physical Review Letters* 89.14 (2002), p. 147902.

[147] L-A Wu and DA Lidar. "Power of anisotropic exchange interactions: Universality and efficient codes for quantum computing". *Physical Review A* 65.4 (2002), p. 042318.

[148] Lian-Ao Wu and Daniel A Lidar. "Universal quantum logic from Zeeman and anisotropic exchange interactions". *Physical Review A* 66.6 (2002), p. 062314.

[149] Florian Meier, Jeremy Levy, and Daniel Loss. "Quantum computing with spin cluster qubits". *Physical Review Letters* 90.4 (2003), p. 047901.

[150] Jordan Kyriakidis and Stephen J Penney. "Coherent rotations of a single spin-based qubit in a single quantum dot at fixed Zeeman energy". *Physical Review B* 71.12 (2005), p. 125332.

[151] Leo P Kouwenhoven, DG Austing, and Seigo Tarucha. "Few-electron quantum dots". *Reports on Progress in Physics* 64.6 (2001), p. 701.

[152] E Burzurı, R Gaudenzi, and HSJ van der Zant. "Observing magnetic anisotropy in electronic transport through individual single-molecule magnets". *Journal of Physics: Condensed Matter* 27.11 (2015), p. 113202.

[153] James O Thomas et al. "Understanding resonant charge transport through weakly coupled single-molecule junctions". *Nature Communications* 10.1 (2019), pp. 1–9.

[154] Jakub K Sowa et al. "Beyond Marcus theory and the Landauer-Büttiker approach in molecular junctions: A unified framework". *The Journal of Chemical Physics* 149.15 (2018), p. 154112.

[155] Hans-Andreas Engel and Daniel Loss. "Detection of single spin decoherence in a quantum dot via charge currents". *Physical Review Letters* 86.20 (2001), p. 4648.

[156] Hans-Andreas Engel and Daniel Loss. "Single-spin dynamics and decoherence in a quantum dot via charge transport". *Physical Review B* 65.19 (2002), p. 195321.

[157] Ronald Hanson. "Electron spins in semiconductor quantum dots". PhD thesis. TU Delft, Delft University of Technology, 2005.

[158] Gloria Platero and Ramón Aguado. "Photon-assisted transport in semiconductor nanostructures". *Physics Reports* 395.1-2 (2004), pp. 1–157.

[159] R Hanson et al. "Single-shot readout of electron spin states in a quantum dot using spin-dependent tunnel rates". *Physical Review Letters* 94.19 (2005), p. 196802.

[160] Frank HL Koppens et al. "Driven coherent oscillations of a single electron spin in a quantum dot". *Nature* 442.7104 (2006), p. 766.

[161] Jan A Mol et al. "Graphene-porphyrin single-molecule transistors". *Nanoscale* 7.31 (2015), pp. 13181–13185.

[162] David H Cobden et al. "Spin splitting and even-odd effects in carbon nanotubes". *Physical Review Letters* 81.3 (1998), p. 681.

[163] Leonardo Martini et al. "Structure-dependent electrical properties of graphene nanoribbon devices with graphene electrodes". *Carbon* 146 (2019), pp. 36–43.

[164] Jose I Gonzalez et al. "Quantum mechanical single-gold-nanocluster electroluminescent light source at room temperature". *Physical Review Letters* 93.14 (2004), p. 147402.

[165] Moon-Ho Jo et al. "Signatures of molecular magnetism in single-molecule transport spectroscopy". *Nano Letters* 6.9 (2006), pp. 2014–2020.

[166] Alexander S Zyazin et al. "Electric field controlled magnetic anisotropy in a single molecule". *Nano Letters* 10.9 (2010), pp. 3307–3311.

[167] Alexander S Zyazin et al. "High-spin and magnetic anisotropy signatures in three-terminal transport through a single molecule". *Synthetic Metals* 161.7-8 (2011), pp. 591–597.

[168] M Misiorny et al. "Probing transverse magnetic anisotropy by electronic transport through a single-molecule magnet". *Physical Review B* 91.3 (2015), p. 035442.

[169] E Burzurı et al. "Direct observation of magnetic anisotropy in an individual Fe_4 single-molecule magnet". *Physical Review Letters* 109.14 (2012), p. 147203.

[170] Enrique Burzurı et al. "Franck–Condon blockade in a single-molecule transistor". *Nano Letters* 14.6 (2014), pp. 3191–3196.

[171] Max Koole, Jan C Hummelen, and Herre SJ van der Zant. "Spin excitations in an all-organic double quantum dot molecule". *Physical Review B* 94.16 (2016), p. 165414.

[172] Romain Vincent et al. "Electronic read-out of a single nuclear spin using a molecular spin transistor". *Nature* 488.7411 (2012), p. 357.

[173] Naoto Ishikawa, Miki Sugita, and Wolfgang Wernsdorfer. "Quantum tunneling of magnetization in lanthanide single-molecule magnets: bis (phthalocyaninato) terbium and bis (phthalocyaninato) dysprosium anions". *Angewandte Chemie International Edition* 44.19 (2005), pp. 2931–2935.

[174] Stefan Thiele et al. "Electrically driven nuclear spin resonance in single-molecule magnets". *Science* 344.6188 (2014), pp. 1135–1138.

[175] Ferry Prins et al. "Room-temperature gating of molecular junctions using few-layer graphene nanogap electrodes". *Nano Letters* 11.11 (2011), pp. 4607–4611.

[176] CS Lau et al. "Nanoscale control of graphene electrodes". *Physical Chemistry Chemical Physics* 16.38 (2014), pp. 20398–20401.

[177] Hatef Sadeghi et al. "Conductance enlargement in picoscale electroburnt graphene nanojunctions". *Proceedings of the National Academy of Sciences* 112.9 (2015), pp. 2658–2663.

[178] Emanuel Lörtscher. "Wiring molecules into circuits". *Nature Nanotechnology* 8.6 (2013), p. 381.

[179] David H Cobden and Jesper Nygård. "Shell filling in closed single-wall carbon nanotube quantum dots". *Physical Review Letters* 89.4 (2002), p. 046803.

[180] Sander J Tans et al. "Electron–electron correlations in carbon nanotubes". *Nature* 394.6695 (1998), pp. 761–764.

[181] Ferdinand Kuemmeth et al. "Coupling of spin and orbital motion of electrons in carbon nanotubes". *Nature* 452.7186 (2008), pp. 448–452.

[182] Tsuneya Ando. "Spin-orbit interaction in carbon nanotubes". *Journal of the Physical Society of Japan* 69.6 (2000), pp. 1757–1763.

[183] T Pei et al. "Hyperfine and spin-orbit coupling effects on decay of spin-valley states in a carbon nanotube". *Physical Review Letters* 118.17 (2017), p. 177701.

[184] Edward A Laird, Fei Pei, and Leo P Kouwenhoven. "A valley–spin qubit in a carbon nanotube". *Nature Nanotechnology* 8.8 (2013), pp. 565–568.

[185] Fei Pei et al. "Valley–spin blockade and spin resonance in carbon nanotubes". *Nature Nanotechnology* 7.10 (2012), pp. 630–634.

[186] Karsten Flensberg and Charles M Marcus. "Bends in nanotubes allow electric spin control and coupling". *Physical Review B* 81.19 (2010), p. 195418.

[187] Gábor Széchenyi and András Pályi. "Current hot spot in the spin-valley blockade in carbon nanotubes". *Physical Review B* 88.23 (2013), p. 235414.

[188] MP Nowak, B Szafran, and FM Peeters. "Resonant harmonic generation and collective spin rotations in electrically driven quantum dots". *Physical Review B* 86.12 (2012), p. 125428.

[189] Hugh Olen Hill Churchill et al. "Relaxation and Dephasing in a Two-Electron C 13 Nanotube Double Quantum Dot". *Physical Review Letters* 102.16 (2009), p. 166802.

[190] Jan Fischer, Björn Trauzettel, and Daniel Loss. "Hyperfine interaction and electron-spin decoherence in graphene and carbon nanotube quantum dots". *Physical Review B* 80.15 (2009), p. 155401.

[191] S Nadj-Perge et al. "Spin–orbit qubit in a semiconductor nanowire". *Nature* 468.7327 (2010), pp. 1084–1087.

[192] JWG Van den Berg et al. "Fast spin-orbit qubit in an indium antimonide nanowire". *Physical Review Letters* 110.6 (2013), p. 066806.

[193] Hendrik Bluhm et al. "Dephasing time of GaAs electron-spin qubits coupled to a nuclear bath exceeding 200 μs". *Nature Physics* 7.2 (2011), pp. 109–113.

[194] Brett M Maune et al. "Coherent singlet-triplet oscillations in a silicon-based double quantum dot". *Nature* 481.7381 (2012), pp. 344–347.

[195] G De Lange et al. "Universal dynamical decoupling of a single solid-state spin from a spin bath". *Science* 330.6000 (2010), pp. 60–63.

[196] Dante Gatteschi, Roberta Sessoli, and Lorenzo Sorace. "Magnetic bistability in lanthanide-based molecular systems: the role of anisotropy and exchange interactions". *Handbook on the Physics and Chemistry of Rare Earths*. Vol. 50. Elsevier, 2016, pp. 91–139.

[197] S Hill et al. "Detailed single-crystal EPR line shape measurements for the single-molecule magnets Fe 8 Br and Mn 12- acetate". *Physical Review B* 65.22 (2002), p. 224410.

[198] Ivano Bertini, Claudio Luchinat, and Giacomo Parigi. "Magnetic susceptibility in paramagnetic NMR". *Progress in Nuclear Magnetic Resonance Spectroscopy* 40.3 (2002), p. 249.

[199] Karl Ridier et al. "Polarized neutron diffraction as a tool for mapping molecular magnetic anisotropy: local susceptibility tensors in CoII complexes". *Chemistry–A European Journal* 22.2 (2016), pp. 724–735.

[200] Fadi El Hallak, Joris Van Slageren, and Martin Dressel. "Torque detected broad band electron spin resonance". *Review of Scientific Instruments* 81.9 (2010), p. 095105.

[201] Eric Heintze et al. "Dynamic control of magnetic nanowires by light-induced domain-wall kickoffs". *Nature Materials* 12.3 (2013), p. 202.

[202] Andrea Cornia et al. "Magnetic anisotropy of Mn12-acetate nanomagnets from high-field torque magnetometry". *Chemical Physics Letters* 322.6 (2000), pp. 477–482.

[203] Guglielmo Ventura and Lara Risegari. *The art of cryogenics: low-temperature experimental techniques*. Elsevier, 2010.

[204] Edmund Clifton Stoner. "Collective electron ferronmagnetism". *Proceedings of the Royal Society of London. Series A. Mathematical and Physical Sciences* 165.922 (1938), pp. 372–414.

[205] IL Kurland, IL Aleiner, and BL Altshuler. "Mesoscopic magnetization fluctuations for metallic grains close to the Stoner instability". *Physical Review B* 62.22 (2000), p. 14886.

[206] J Weis et al. "Competing channels in single-electron tunneling through a quantum dot". *Physical Review Letters* 71.24 (1993), p. 4019.

[207] Abraham Savitzky and Marcel JE Golay. "Smoothing and differentiation of data by simplified least squares procedures." *Analytical Chemistry* 36.8 (1964), pp. 1627–1639.

[208] H Kamerlingh Onnes. "The resistance of pure mercury at helium temperatures". *Commun. Phys. Lab. Univ. Leiden, b* 120 (1911).

[209] Martin N Wilson. "Superconducting magnets" (1983).

[210] Bernd T Matthias, Theodore H Geballe, and VB Compton. "Superconductivity". *Reviews of Modern Physics* 35.1 (1963), p. 1.

[211] Stephen Timoshenko. *Strength of Materials: Part 2, Advanced Theory and Problems*. van Nostrand, 1956.

[212] Donald Bruce Montgomery. "Solenoid magnet design. The magnetic and mechanical aspects of resistive and superconducting systems" (1969).

[213] AJ Middleton and CW Trowbridge. "Mechanical stress in large high field magnet coils." *pp 140-9 of Proceedings of the Second International Conference on Magnet Technology, Oxford, England, 1967. Hadley, H.(ed.). Chilton, Eng., Rutherford Laboratory, 1967.* Rutherford High Energy Lab., Chilton, Eng. 1968.

[214] Stefan Thiele. *Read-Out and Coherent Manipulation of an Isolated Nuclear Spin: Using a Single-Molecule Magnet Spin-Transistor*. Springer, 2015.

[215] Wei Han et al. "Graphene spintronics". *Nature Nanotechnology* 9.10 (2014), pp. 794–807.

[216] Indrani Choudhuri, Preeti Bhauriyal, and Biswarup Pathak. "Recent advances in graphene-like 2D materials for spintronics applications". *Chemistry of Materials* 31.20 (2019), pp. 8260–8285.

[217] Luigi Malavolti et al. "Erratic magnetic hysteresis of TbPc 2 molecular nanomagnets". *Journal of Materials Chemistry C* 1.16 (2013), pp. 2935–2942.

[218] Fu-Sheng Guo et al. "Magnetic hysteresis up to 80 kelvin in a dysprosium metallocene single-molecule magnet". *Science* 362.6421 (2018), pp. 1400–1403.

[219] Jennifer J Le Roy et al. "Tailored homo-and hetero-lanthanide porphyrin dimers: a synthetic strategy for integrating multiple spintronic functionalities into a single molecule". *Chemical Science* 9.45 (2018), pp. 8474–8481.

[220] Wolfgang Kläui. "The coordination chemistry and organometallic chemistry of tridentate oxygen ligands with π-donor properties". *Angewandte Chemie International Edition in English* 29.6 (1990), pp. 627–637.

[221] Matteo Mannini et al. "Magnetic behaviour of TbPc 2 single-molecule magnets chemically grafted on silicon surface". *Nature Communications* 5.1 (2014), pp. 1–8.

[222] Yoji Horii et al. "Elongation of magnetic relaxation times in a single-molecule magnet through intermetallic interactions: a clamshell-type dinuclear terbium (iii)-phthalocynaninato quadruple-decker complex". *Chemical Communications* 53.61 (2017), pp. 8561–8564.

[223] Stefan Stoll and Arthur Schweiger. "EasySpin, a comprehensive software package for spectral simulation and analysis in EPR". *Journal of Magnetic Resonance* 178.1 (2006), pp. 42–55.

[224] Akihiko Tsuda, Hiroyuki Furuta, and Atsuhiro Osuka. "Completely fused diporphyrins and triporphyrin". *Angewandte Chemie International Edition* 39.14 (2000), pp. 2549–2552.

[225] Tian Pei et al. "Exchange-induced spin polarization in a single magnetic molecule junction". *Submitted* (2021).

[226] Bart Limburg et al. "Anchor Groups for Graphene-Porphyrin Single-Molecule Transistors". *Advanced Functional Materials* 28.45 (2018), p. 1803629.

[227] Steven G Bratsch. "Standard electrode potentials and temperature coefficients in water at 298.15 K". *Journal of Physical and Chemical Reference Data* 18.1 (1989), pp. 1–21.

[228] Andrea Candini et al. "Graphene spintronic devices with molecular nanomagnets". *Nano Letters* 11.7 (2011), pp. 2634–2639.

[229] AA Shylau, JW Kłos, and IV Zozoulenko. "Capacitance of graphene nanoribbons". *Physical Review B* 80.20 (2009), p. 205402.

[230] John Robertson. "High dielectric constant oxides". *The European Physical Journal Applied Physics* 28.3 (2004), pp. 265–291.

[231] Pascal Gehring et al. "Distinguishing lead and molecule states in graphene-based single-electron transistors". *ACS nano* 11.6 (2017), pp. 5325–5331.

[232] Supriyo Datta. *Quantum transport: atom to transistor*. Cambridge university press, 2005.

[233] PL Stiller et al. "Magnetic field control of the Franck-Condon coupling of few-electron quantum states". *Physical Review B* 102.11 (2020), p. 115408.

[234] Renaud Leturcq et al. "Franck–Condon blockade in suspended carbon nanotube quantum dots". *Nature Physics* 5.5 (2009), pp. 327–331.

[235] S Sapmaz et al. "Tunneling in suspended carbon nanotubes assisted by longitudinal phonons". *Physical Review Letters* 96.2 (2006), p. 026801.

[236] Guoqing Zhou et al. "Electron–Phonon Scattering Is Much Weaker in Carbon Nanotubes than in Graphene Nanoribbons". *The Journal of Physical Chemistry Letters* 10.22 (2019), pp. 7179–7187.

[237] AN Pasupathy et al. "Vibration-assisted electron tunneling in C140 transistors". *Nano Letters* 5.2 (2005), pp. 203–207.

[238] Chit Siong Lau et al. "Redox-dependent Franck–Condon blockade and Avalanche transport in a graphene–fullerene single-molecule transistor". *Nano Letters* 16.1 (2016), pp. 170–176.

[239] Daniel Sánchez-Portal et al. "Ab initio structural, elastic, and vibrational properties of carbon nanotubes". *Physical Review B* 59.19 (1999), p. 12678.

[240] AV Savin and Yu S Kivshar. "Localized vibrations of graphene nanoribbons". *Low Temperature Physics* 42.8 (2016), pp. 703–710.

[241] Johannes S Seldenthuis et al. "Vibrational excitations in weakly coupled single-molecule junctions: A computational analysis". *ACS nano* 2.7 (2008), pp. 1445–1451.

[242] Filip K Malinowski et al. "Spin of a multielectron quantum dot and its interaction with a neighboring electron". *Physical Review X* 8.1 (2018), p. 011045.

[243] Floris A Zwanenburg et al. "Spin states of the first four holes in a silicon nanowire quantum dot". *Nano Letters* 9.3 (2009), pp. 1071–1079.

[244] SD Liles et al. "Spin and orbital structure of the first six holes in a silicon metal-oxide-semiconductor quantum dot". *Nature Communications* 9.1 (2018), pp. 1–7.

[245] RCC Leon et al. "Coherent spin control of s-, p-, d-and f-electrons in a silicon quantum dot". *Nature Communications* 11.1 (2020), pp. 1–7.

[246] Johannes Güttinger et al. "Spin states in graphene quantum dots". *Physical Review Letters* 105.11 (2010), p. 116801.

[247] IS Burmistrov et al. "Mesoscopic Stoner instability in open quantum dots: suppression of Coleman-Weinberg mechanism by electron tunneling". *Physical Review Letters* 124.19 (2020), p. 196801.

[248] Alexander A Balandin. "Low-frequency 1/f noise in graphene devices". *Nature Nanotechnology* 8.8 (2013), pp. 549–555.

[249] Tibor Grasser. "Stochastic charge trapping in oxides: From random telegraph noise to bias temperature instabilities". *Microelectronics Reliability* 52.1 (2012), pp. 39–70.

[250] Stefan Machlup. "Noise in semiconductors: spectrum of a two-parameter random signal". *Journal of Applied Physics* 25.3 (1954), pp. 341–343.

[251] Sheng-Shiuan Yeh, Wen-Yao Chang, and Juhn-Jong Lin. "Probing nanocrystalline grain dynamics in nanodevices". *Science Advances* 3.6 (2017), e1700135.

[252] Herbert A Sturges. "The choice of a class interval". *Journal of the American Statistical Association* 21.153 (1926), pp. 65–66.

[253] Sung Ho Jhang. "Analysis of random telegraph noise observed in semiconducting carbon nanotube quantum dots". *Synthetic Metals* 198 (2014), pp. 118–121.

[254] TM Buehler et al. "Observing sub-microsecond telegraph noise with the radio frequency single electron transistor". *Journal of Applied Physics* 96.11 (2004), pp. 6827–6830.

[255] Zuo Li et al. "Random telegraph noise from resonant tunnelling at low temperatures". *Scientific Reports* 8.1 (2018), pp. 1–9.

[256] Paweł Puczkarski et al. "Low-frequency noise in graphene tunnel junctions". *ACS Nano* 12.9 (2018), pp. 9451–9460.

[257] Jasper P Fried et al. "Large amplitude charge noise and random telegraph fluctuations in room-temperature graphene single-electron transistors". *Nanoscale* 12.2 (2020), pp. 871–876.

[258] Fei Liu et al. "Giant random telegraph signals in the carbon nanotubes as a single defect probe". *Applied Physics Letters* 86.16 (2005), p. 163102.